Advanced Organic Vapor Cycles for Improving Thermal Conversion Efficiency in Renewable Energy Systems

By

Tony Ho

A dissertation submitted in partial satisfaction of the

requirements for the degree of

Doctor of Philosophy

in

Engineering – Mechanical Engineering

in the

Graduate Division

of the

University of California, Berkeley

Committee in charge:

Professor Ralph Greif, Co-Chair
Professor Samuel S. Mao, Co-Chair
Professor Van P. Carey
Professor Per F. Peterson

Spring 2012

Abstract

Advanced Organic Vapor Cycles for Improving Thermal Conversion Efficiency in Renewable Energy Systems

by

Tony Ho

Doctor of Philosophy in Mechanical Engineering

University of California, Berkeley

Professor Ralph Greif, Co-Chair
Professor Samuel S. Mao, Co-Chair

The Organic Flash Cycle (OFC) is proposed as a vapor power cycle that could potentially increase power generation and improve the utilization efficiency of renewable energy and waste heat recovery systems. A brief review of current advanced vapor power cycles including the Organic Rankine Cycle (ORC), the zeotropic Rankine cycle, the Kalina cycle, the transcritical cycle, and the trilateral flash cycle is presented. The premise and motivation for the OFC concept is that essentially by improving temperature matching to the energy reservoir stream during heat addition to the power cycle, less irreversibilities are generated and more power can be produced from a given finite thermal energy reservoir. In this study, modern equations of state explicit in Helmholtz energy such as the BACKONE equations, multi-parameter Span-Wagner equations, and the equations compiled in NIST REFPROP 8.0 were used to accurately determine thermodynamic property data for the working fluids considered. Though these equations of state tend to be significantly more complex than cubic equations both in form and computational schemes, modern Helmholtz equations provide much higher accuracy in the high pressure regions, liquid regions, and two-phase regions and also can be extended to accurately describe complex polar fluids. Calculated values of saturated liquid and vapor density and vapor pressure were then compared to values listed in the NIST Chemistry WebBook to ensure accuracy for the temperature range of interest. Deviations from the NIST WebBook were typically below 1%; a comparison of first law efficiencies for an ideal basic Rankine cycle yielded less than 0.4% difference between calculations using the Helmholtz-explicit equations of state and NIST REFPROP. Also by employing the BACKONE and Span-Wagner equations, the number of potential aromatic hydrocarbon and siloxane working fluids that are appropriate for high and intermediate temperature applications is expanded considerably.

A theoretical investigation on the OFC is conducted using the aforementioned Helmholtz-explicit equations of state for 10 different aromatic hydrocarbon and siloxane working fluids for intermediate temperature finite thermal energy reservoirs (~300^{o}C). Results showed that aromatic hydrocarbons to be the better suited working fluid for the ORC and OFC due to less "drying" behavior and also smaller turbine volumetric flow ratios resulting in simpler turbine designs. The single flash OFC is shown to achieve utilization efficiencies that are comparable to

the optimized basic ORC (~0.63) which is used as a baseline. It is shown that the advantage of improved temperature matching during heat addition was effectively negated by irreversibilities introduced into the OFC during flash evaporation. Several improvements to the basic OFC are proposed and analyzed such as introducing a secondary flash stage or replacing the throttling valve with a two-phase expander. Utilization efficiency gains of about 10% over the optimized basic ORC can be achieved by splitting the expansion process in the OFC into two steps and recombining the liquid stream from flash evaporation prior to the secondary, low pressure, expansion stage. Results show that the proposed enhancements had a more pronounced effect for the OFC using aromatic hydrocarbon working fluids (5-20% utilization efficiency improvement) than for siloxane working fluids (2-4%). The proposed modifications were aimed towards reducing irreversibility in flash evaporation; it was observed for siloxanes that the primary source of irreversibility was due to high superheat at the turbine exhaust because of the highly "drying" nature of the fluid. Though an order of magnitude analysis, results showed that the OFC and ORC to require similar heat transfer surface areas.

For low temperature thermal energy reservoirs (80-150^{o}C) applicable to non-concentrated solar thermal, geothermal, and low grade industrial waste heat energy, alkane and refrigerant working fluids possess more appropriate vapor pressures. The optimized single flash OFC was again shown to generate comparable power per unit flow rate of the thermal energy reservoir than the optimized basic ORC. With some of the previously proposed design modifications though, the OFC can produce over 60% more power than the optimized ORC. For low temperature applications, the minimum temperature difference between streams in the heat exchanger, or pinch temperature, becomes an important design parameter. Reduction of the pinch temperature even slightly can yield significantly higher gains in power output, but will also increase required heat exchanger surface area and subsequently capital costs.

A high-level design of a liquid-fluoride salt (NaF-NaBF4) cooled solar power tower plant is presented; liquid-fluoride salt is used rather than current molten nitrate salts to increase the receiver temperature and subsequently allow for higher efficiency gas power cycles to be used. Graphite or direct energy storage in the salt itself is proposed. The power block component of this heliostat-central receiver plant is a combined cycle system consisting of a topping Brayton cycle with intercooling, reheat, and regeneration and a bottoming low-temperature modified OFC. The combined cycle is designed with dry cooling in mind, such that operation in desert climates are more suitable. The combined cycle design is shown to increase power block efficiencies by 6%-8% over the Brayton cycle with intercooling, reheat, and regeneration alone. An estimated 30% annual average total solar-to-electric conversion efficiency is possible with this system design, which is comparable to some of the most efficient high temperature solar power tower designs to date. Theoretically, power block efficiencies over 60% are possible; however, emission losses from the isothermal central receiver would limit the plant's operational temperature range. Results show that for high efficiency solar power towers to be realized, high temperature non-isothermal, or partitioned, receivers operating efficiently above 1000^{o}C are necessary. Other potential areas of renewable energy system integration for the OFC include a co-generation solar thermal-photovoltaic system that employs highly concentrated, densely packed photovoltaic cells using single-phase or two-phase cooling. The thermal energy absorbed by that coolant could then be used as the working fluid in a separate OFC to further produce power in co-generation with the concentrated photovoltaics.

Dedication

This dissertation is dedicated to my mother and father, Tracy and Yick Han Ho; I owe everything to their love, their hard work and sacrifices, and the character that they have instilled in me.

This dissertation is also dedicated in loving memory of my grandfather.

Table of Contents

List of Figures

List of Tables

Nomenclature

A_s	Surface area [m^2]
A, B, A^*, B^*	Fluid specific constants in generalized cubic equation of state
A, B, C	Empirical fluid specific constants in Antoine vapor equations
a	Helmholtz free energy [J/kg]
C_{solar}	Solar concentration ratio
c_p	Isobaric heat capacity [J/kg K]
d_i, g_i, n_i, p_i, t_i,	Equation of state specific constants
h	Enthalpy [J/kg]
h_{conv}	Convective heat transfer coefficient [W/m^2K]
ΔH_v	Heat of vaporization [J/kg]
I_{coll}	Annual average collectable solar radiation per unit surface area ($300W/m^2$)
I_{exp}	Number of exponential terms in equation of state
I_{pol}	Number of polynomial terms in equation of state
J	Iterative step-width size parameter
k	Specific heat ratio
$\dot{m}$	Mass flow rate [kg/s]
n	Watson relation constant
P	Pressure [Pa]
q	Vapor quality
$\dot{Q}$	Heat transfer rate [W]
Q_{add}	Heat addition [W]
R	Ideal gas constant (8.314 J/mol K)
r	Residual
r_p	Turbine pressure ratio
s	Entropy [J/kg]
SP	Turbine Size Parameter [m]
T	Temperature [K]
T_0	Fluid specific characteristic temperature [K]
ΔT_{LM}	Log mean temperature difference
u,w	Equation of state specific constants in generalized cubic equation of state
U	Overall heat transfer coefficient [W/m^2K]
V	specific volume [m^3/kg]
$\dot{V}$	Volumetric flow rate [m^3/s]
VDW	Van Der Waals
VFR	Turbine Volumetric Flow Ratio
W_i, Ω_i	Wagner equation fluid specific constant
W_{net}	Net Power [W]
X	Iterative values in regula falsi method
Z	Compressibility factor
ZT	Thermoelectric figure of merit

Greek Symbols

α	Total reduced Helmholtz energy
α^0	Ideal Gas component of Helmholtz energy
α^R	Residual component of Helmhotlz energy
γ	Packing fraction constant
δ	Reduced density
ε	Utilization efficiency
η_I	1st law efficiency
$\eta_{II,int}$	Internal 2nd law efficiency
$\eta_{II,ext}$	External 2nd law efficiency
η_{add}	Heat addition exergetic efficiency
κ	Constant for estimating initial temperature (eq. 2.48)
ξ	Packing fraction
ρ	Density [kg/m^3]
ρ_0	Fluid specific characteristic density [kg/m^3]
σ	Stefan-Boltzmann constant (5.67×10^{-8}W/m^{2}K^4)
τ	Inverse reduced temperature
ϕ	Constant for estimating saturated liquid density (eq. 2.53)
φ	Anisotropy parameter
χ	Exergy [J/kg]
ω	Acentric factor

Subscripts and Superscripts

0	Ideal gas property
A	Nonpolar attractive term
Br	Brayton
BWR	Benedict-Webb-Rubin
c	Property at fluid's critical point
calc	Calculated
cold	Cold side/stream or cold salt temperature
cp	Fluid specific constants for ideal gas specific heat correlations
D	Dipole term
d	Dead state
est	Initial estimate
f	Working fluid
H	High cycle value (corresponding to turbine inlet)
H	Hard sphere term
hot	Hot side/stream or Hot salt temperature
i, j	Index number
in	Inlet
isen	Isentropic process
L	Liquid
OFC	Organic Flash Cycle
ORC	Organic Rankine Cycle

opt	Optical
out	Outlet
PB	Power block
Pol	Polar term
Q	Quadrupole term
R	Experimental reference property
rec	Receiver
r	Reduced property to corresponding critical property
ref	Reference state
s	Stream from finite thermal energy reservoir
sat	Saturated
V	Vapor
z	Constants to determine packing fraction in hard sphere term
δ	Partial derivative with respect to reduced density
σ	Along saturated vapor curve
τ	Partial derivative with respect to inverse reduced temperature

Acknowledgements

The research presented in this dissertation could not have been completed without the help and support of some key individuals whom I am very grateful to. I first would like to first acknowledge and thank my research advisers Professor Ralph Greif and Professor Samuel S. Mao for their academic and professional advice and mentorship. I have truly enjoyed and appreciated their expertise, their patience, and the overall experience of working with them, and I want to thank them for all that they have done to help further my graduate education here at Berkeley. I also would like to thank Professor Van P. Carey and Professor Per F. Peterson for sitting on my qualifying examination and on my dissertation committee, as well as their input and recommendations to this dissertation.

I want to recognize Professor Li Zhao, Wang Xiaodong, and the rest of Professor Zhao's research team for the unforgettable visiting scholar experience at Tianjin University; I not only gained much experimental research experience but also learned quite a lot culturally as well. I also want to thank Mark Miles for the opportunity to work along the way with him on some unique projects. I greatly appreciate the kindness and support shown by Professor Catherine Bordel and Donna Sakima of the Berkeley Physics Department for their help in shaping me to become a better teacher. Lastly, I would like to thank my family for their support and the friends I have met at Berkeley for making this all a wonderful experience.

1 Introduction

1.1 Background on thermal energy conversion systems

As energy demands continue to rise, researchers continue to search for alternative energy sources to generate electricity, as well as improve existing methods to maximize efficiency. To meet the ever higher global energy demands of the future, a greater reliance on electricity generated from renewable energy sources such as solar thermal and geothermal energy will become an inevitable necessity. In addition to renewable sources, thermal energy that in the past would have been released and lost to the ambient such as hot exhaust exiting a gas turbine and industrial waste heat, are now being reexamined as potential power sources and areas for improving efficiency.

Two devices often used for thermal energy conversion to electricity include thermoelectric devices and heat engines. Thermoelectric devices benefit from being quiet, small, possessing low environmental impact, and being highly reliable due to their solid state nature **[**1**]**. However, to date they have not yet been able to achieve or demonstrate efficiencies similar to mechanical heat engines and will need to advance significantly before comparable efficiencies are realized **[**2**]**. In fact, a recent publication by Vining suggested that not only are the efficiencies for thermoelectric devices not comparable to mechanical heat engines presently, but it is doubtful that the efficiencies will ever be comparable in the foreseeable future for a wide range of thermal energy sources. Vining's plot comparing the present and estimated future efficiencies for thermoelectric devices and the efficiencies currently attainable with mechanical heat engines is shown Fig 1.1 **[**2**]**.

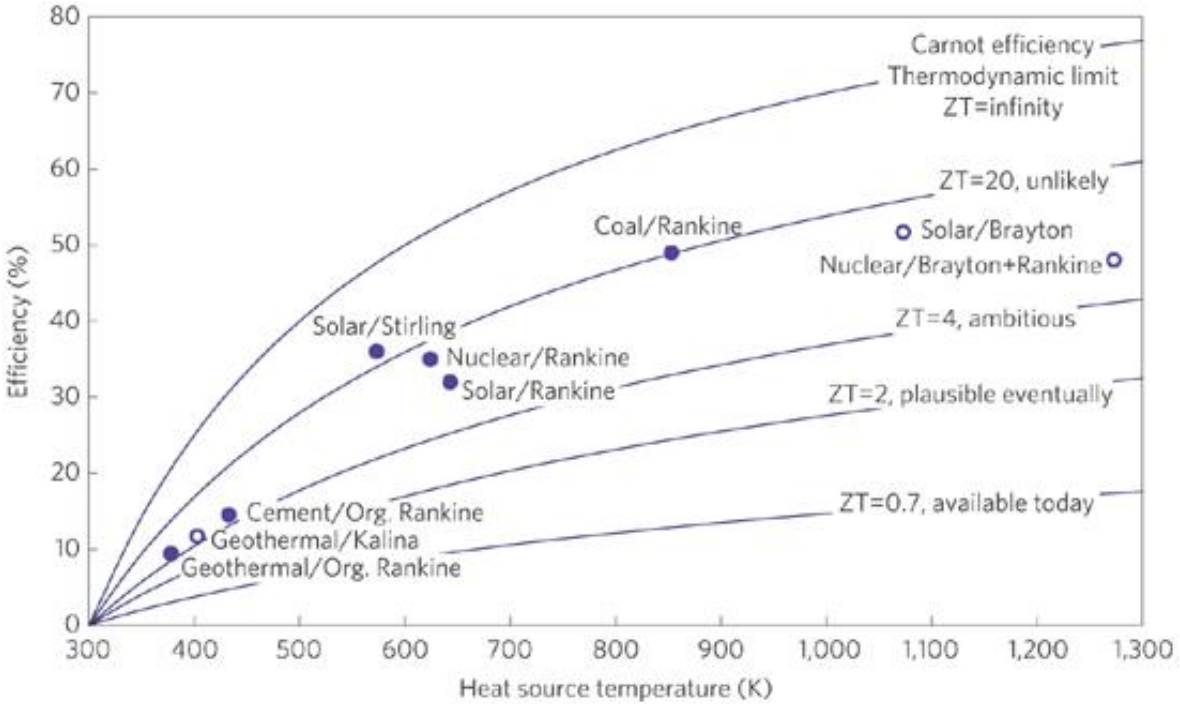

Figure 1.1: Comparison of mechanical heat engines and estimates for present and future thermoelectric devices. Reprinted by permission from Macmillan Publishers Ltd: *Nature Materials* [2], copyright 2009.

In Fig. 1.1, ZT is the so-called "Figure of Merit" which is a dimensionless parameter made up of the combination of the thermoelectric material's thermal conductivity, electrical resistivity, Seebeck coefficient, and absolute temperature **[**2**]**. Research on improving thermoelectrics is heavily dependent on discovering thermoelectric materials that can increase the Figure of Merit. Since the early 1990s though, only a few instances of Figure of Merits greater than 2 have ever been reported in the literature **[**2**]**. Commercial implementation of thermoelectrics has been limited to power generation in remote areas **[**2**]**. Aside from low Figures of Merit, thermoelectrics are also more costly than traditional mechanical heat engines. Table 1.1 shows the estimated capital costs from the U.S. Department of Energy (DOE) for various thermal energy conversion technologies applicable to waste heat recovery in 2008. Note that the U.S. DOE projects that the capital costs for a thermoelectric generation system for industrial waste heat recovery to exceed the costs of mechanical heat engines by about an order of magnitude **[**3**]**.

Table 1.1: Heat recovery and energy conversion technologies and their estimated capital costs **[**3**]**

Thermal Energy Conversion Technology	Temperature Range	Typical Sources of Waste Heat	Estimated Capital Costs
Traditional Steam Rankine Cycle[a]	Intermediate-High	Exhaust from gas turbines, reciprocating engines, incinerators, and furnaces	$1100-$1400/kW[d]
Kalina Cycle[d]	Low-Intermediate	Gas turbine exhaust, boiler exhaust, cement kilns	$1100-$1500/kW[d]
Organic Rankine Cycle[c,e]	Low-Intermediate	Gas turbine exhaust, boiler exhaust, heated water, cement kilns	$1500-$3500/kW[d]
Thermoelectric Generation[b]	Intermediate-High	Not yet demonstrated in industrial applications	$20,000-$30,000/kW[b]
Piezoelectric Generation[b]	Low	Not yet demonstrated in industrial applications	$10,000,000/kW[b]
Thermal Photovoltaics	Intermediate-High	Not yet demonstrated in industrial applications	N/A

[a]Sean Casten. Update on US Steam Turbine technology. Presented to Canadian District Energy Association 8th Annual Conference. 20 June 2003.
[b]BCS Inc. Engineering Scoping Study of Thermoelectric Generator Systems for Industrial Waste Heat Recovery.
[c]Daniel Duffy. "Better Cogeneration through Chemistry: the Organic Rankine Cycle."
[d]Nark Mirolli. "The Kalina Cycle for Cement Kiln Waste Heat Recovery Power Plants." Cement Industry Technical Conference. 15-20 Mary 2005.
[e]Organic Rankine Cycle for Electricity Generation. [Online] http://www.stowa-selectedtechnologies.nl
[f]Cunningham P. Waste Heat/Cogen Opportunities in the Cement Industry. Cogeneration and Competitive Power Journal 2002:17; 31-50.

Fig. 1.1 shows that for low temperature finite thermal sources such as geothermal and waste heat recovery, thermoelectrics may in the future approach efficiencies of current mechanical heat engines such as the Organic Rankine Cycle (ORC) and the Kalina cycle. Vining **[**2**]** suggests that if Figure of Merits close to ~4 are realized, it is possible that for low power generation and

distributed power markets, thermoelectrics may be preferred over mechanical heat engines because of their small size. However, for large scale centralized utilities generating power from fuels such as nuclear, Concentrated Solar Power (CSP), and coal, Fig. 1.1 shows that it is unlikely that thermoelectrics will be able to compete with mechanical heat engines in the foreseeable future. Vining states that realistically, thermoelectrics are more or less confined to niche applications such as vehicle heat recovery and air conditioning; even in these applications though, thermoelectrics still face considerable obstacles before their widespread adoption **[**2**]**.

The conversion of thermal energy to useful power using a mechanical heat engine has been studied for centuries now and continues to be improved upon with new and innovative designs to plant components and system configurations. There are many types of different mechanical heat engines, the more well known being the vapor Rankine, gas Brayton, Otto, Diesel, Stirling, and Ericsson cycles, all of which are typically covered in most undergraduate thermodynamics textbooks such as ref. **[**4,5**]**. Although the concept of heat engines is well established, the introduction of new and unconventional working fluids and novel cycle configurations continue to push the limits of cycle design and corresponding cycle efficiencies. Vapor cycles in particular are versatile in that they can be designed to take advantage of low and intermediate temperature energy resources such as solar thermal, geothermal, and industrial waste heat, but also can be used as a complement to high temperature Brayton gas cycles in so-called "combined cycles." In the remainder of this introductory chapter, a review of advanced vapor power cycles that have been proposed in the literature or implemented in practice is presented. The motivation for a new proposed cycle concept is then given with the crux of the dissertation dedicated to the analysis and discussion of results for the proposed cycle applied to thermal energy reservoirs over a wide range of initial temperatures.

1.2 Review of advanced vapor power cycles for finite thermal sources

In the following section, a brief description of the traditional simple steam Rankine cycle is given as well as a review of advanced vapor power cycles that have been proposed such as the ORC, the Kalina cycle and other zeotropic cycles, the supercritical and transcritical cycle, and the trilateral flash cycle. These advanced cycles are often geared toward energy reservoirs where the reservoir temperature and its thermal energy decreases dramatically as heat is transferred from the reservoir to the power cycle; hence they are often termed finite thermal energy reservoirs. Finite thermal energy reservoirs include renewable energies such as solar thermal energy, where thermal energy is obtained from a heated fluid circulating in a solar field, and geothermal energy, where energy is obtained from hot brine that has been extracted from a geothermal well. Waste heat sources from industrial processes and gas turbine exhaust are often also classified as finite thermal energy reservoirs. In the following sections, it is examined why the steam Rankine cycle is not appropriate for many of these energy reservoirs and how advanced vapor cycles attempt to address these difficulties.

1.2.1 Steam Rankine cycle

The first widely used heat engine (an atmospheric heat engine that used steam) was developed by Thomas Newcomen in the 1700s. In 1765 James Watt, a Scottish mechanical engineer, improved upon the steam engine then patented the Boulton and Watt steam engine in 1775 **[**6**]**.

Since then the steam Rankine cycle has seen numerous improvements in pump, heat exchanger, and turbine technology; nearly 90% of the world's electricity still continues to be generated by a form of the steam Rankine cycle **[**7**]**. Presently, the highest live steam temperatures allowed are about 620^{o}C due to metallurgical limits **[**4**]**. Typical large scale steam Rankine plants operate near 550^{o}C and have thermal efficiencies in the mid 30% range; however, some modern supercritical coal plants have overall plant efficiencies exceeding 40% **[**8**]**. The basic steam Rankine cycle configuration and its Temperature-Entropy (T-S) diagram is shown in Fig. 1.2

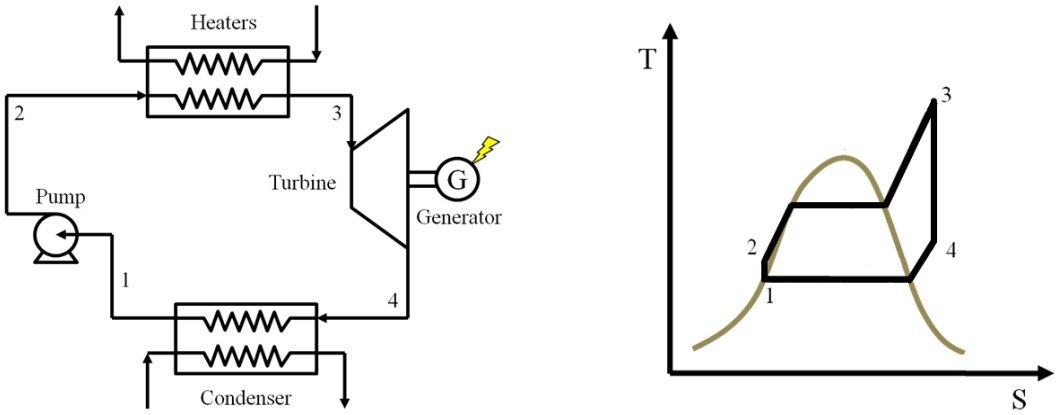

Figure 1.2: Plant schematic and T-S diagram for basic pure fluid ORC, zeotropic Rankine cycle, and transcritical Rankine cycle [9**].**

The basic, ideal steam Rankine cycle begins with saturated water at state 1 pumped to a high pressure at state 2 and then heated isobarically to superheated steam at state 3. The superheated steam can then be expanded to state 4 though a turbine to generate power and then condensed back to saturated water at state 1. Although Fig. 1.2 shows isentropic expansion for the pump and turbine, in reality these devices are not reversible and an isentropic efficiency parameter is used for the pump and turbine accounts for these irreversibilities. Improvements to the basic Rankine cycle include the use of reheating and regeneration using feedwater heaters **[**4**]**. For bottoming steam Rankine cycles in combined cycle plants, multiple pressure heat addition at two or three pressures is often utilized in order to minimize temperature mismatch to the topping cycle's gas turbine exhaust. This is almost always done when the inlet gas temperature to the Heat Recovery Steam Generator (HRSG) is high, which is often the case for heavy duty simple gas turbines where the turbine exit temperature is typically higher than 500^{o}C **[**4**]**. When fuel costs are inexpensive and/or one wants to reduce initial capital costs, single pressure HRSG may also be used; however, the decreased temperature matching inevitably results in less energy being transferred from the waste heat stream, thus decreasing total efficiency and increasing gas stack temperatures **[**10**]**. At gas inlet temperatures above 593^{o}C to the HRSG, multi-pressure steam cycles with reheat also become feasible **[**10**]**. Ultimately, a thermoeconomic analysis such as those described in ref. **[**11**,**12**]** are required to determine the optimal balance of total costs (plant-installed capital costs, fuel costs, operating and maintenance costs, etc. **[**10**]**) and efficiency for a given scenario.

Although the predominant power cycle used, the steam Rankine cycle does have some significant disadvantages in a number of situations. For example, if heat rejection to a low heat sink temperature (below normal boiling point) is available, the steam would need to be brought down to a pressure below atmospheric pressure. This requires deaerators to remove air and other

non-condensable gases that leak into the system in the last turbine stages and the condenser. For small scale power production, the introduction of additional plant components may not warrant the capital cost. The low pressure steam turbine may also become impractically large or at the very least, inefficient because of steam's large turbine volumetric flow ratio at low pressures [8]. For high power level generation above 10MW, steam turbines are able to achieve ~80% isentropic efficiency, but for small scale power production (10-100kW) the steam turbine isentropic efficiencies ranges 50% to as low as 25%. A turbine with the same power level utilizing a molecularly heavier fluid though can reach much higher isentropic efficiencies of about 60-75% [13]. A heavier organic fluid can also solve the problem of air leakage as many organic fluids have vapor pressures above atmospheric even at room temperature. For low temperature resources below 370^{o}C, thermal efficiencies also decrease to the point where steam cycles are no longer cost effective or efficient [14]. Superheating is also necessary to avoid moisture formation in the latter stages of the turbine or special reinforcing material is necessary on wet turbine's blades to avoid erosion caused by the water droplets forming [15]. For combined cycles, HRSGs will often incorporate superheating as the gas turbine exit temperature is typically high enough that it can be done fairly easily. However, for low temperature and/or low power applications when multiple pressure heat addition may not be practical, superheating will significantly lower thermal efficiency because the boiling temperature, and thereby the average heat addition temperature, is lower [13]. In addition, capital costs will also be greater for systems using superheating because of the increased heat surface area needed for the superheater caused by poor vapor heat transfer coefficients. Multi-stage reheating and expansion is also a possibility to avoid expansion into the vapor dome, but it dramatically increases the size and complexity of the HRSG [16] and is only feasible at high gas turbine exit temperatures [10]. Due to interest in low temperature renewable thermal resources such as geothermal and non-concentrated solar thermal, vapor power cycles using working fluids other than steam were aggressively developed in the 1970s, including the so-called Organic Rankine Cycle.

1.2.2 Organic Rankine Cycles (ORC)

As mentioned previously, steam cycles become less efficient and more expensive than ORCs at temperature below 370^{o}C [13,17]. Aside from smaller more efficient turbines, organic working fluids also have the added advantage of higher vapor pressures at room temperatures making air leakage into the system and subsequent deaerators for removing air and non-condensable gases unnecessary. Although organic fluids require more stringent sealing and ventilation due to flammability and toxicity concerns, no significant health or safety issues were observed in a study conducted by Marciniak et al. [17] that included working fluids such as methanol, 2methylpyridine/H_2O, Fluorinol 85, R11, R113, and toluene.

There are several solar ORC plants operating presently including the solar powered Coolidge Deep-Well Irrigation System in Arizona which uses a toluene working fluid [13] and another 1MWe CSP plant also in Arizona that uses a n-pentane working fluid [18]. In 2004, about 155 geothermal binary plants were in operation utilizing a number of organic working fluids including butane, pentane, isopentane, propane, etc. [15]. Present ORC manufacturers including ORMAT, Turboden, UTC, and Koehler-Ziegler offer packaged ORC power generation modules using working fluids such as silicone oil, n-pentane, R245fa, R134a, and other hydrocarbons [18]. Fig. 1.3 shows the cycle configuration and T-S diagram for the ORC using a pure fluid, a

zeotropic cycle using a fluid mixture, and a transcritical cycle using a pure fluid [9]. Note that the cycle configuration and T-S diagram for the ORC is actually exactly the same as that for the steam Rankine cycle of Fig. 1.1; therefore, the ORC should not be regarded as a "new" cycle but a slight deviation of the Rankine cycle that uses an organic working fluid instead of steam.

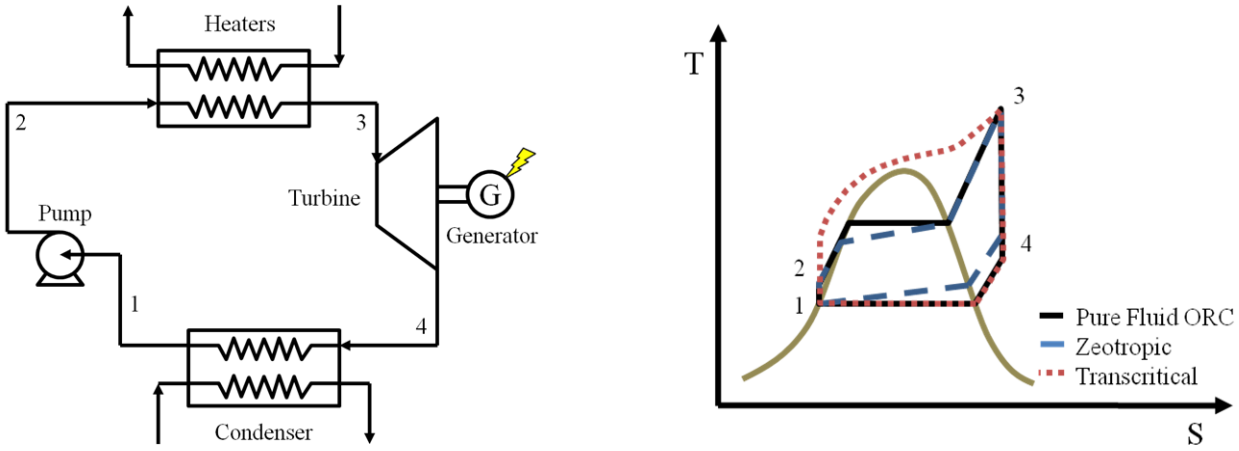

Figure 1.3: Plant schematic and T-S diagram for basic pure fluid ORC, zeotropic Rankine cycle, and transcritical Rankine cycle [9].

A number of other ORC working fluids for a wide range of operating temperature ranges have also been proposed by researchers as well. Saleh et al. [19] proposed a number of refrigerants and hydrocarbons for subcritical and transcritical ORCs with internal heat exchangers. Tchanche et al. [20] examined similar working fluids for a low temperature solar ORC below 90^{o}C with results showing R134a and R152a to be the most suitable fluids. Hettiarachichi et al. [21] optimized the basic ORC to an objective function comprised of the ratio of total heat transfer area to total new power generated; they concluded that ammonia, R123, and n-pentane to be the working fluids that gave the best balance of cost and performance for low-temperature geothermal ORC applications. Hung et al. [14], Chen et al. [22], and Tchache et al. [23] have all published comprehensive reviews of ORCs related studies for a number of different low temperature thermal energy sources. There are considerably fewer studies for intermediate and high temperature ORC applications than for low temperatures in the literature. Recently, Fernández et al. [24] examined siloxanes as potential working fluids for high temperature regenerative subcritical and supercritical ORCs. Lai et al. [25] similarly examined subcritical and transcritical high temperature ORCs with internal heat exchangers using siloxanes and aromatic hydrocarbons. Chacarteui et al. [26] analyzed the effect of different ORC cycle configurations utilizing aromatic hydrocarbons and refrigerant working fluids for a combined Brayton-ORC system. Thus far, the majority of the ORC studies in the literature have focused on the application and suitability of different working fluids for specific operating temperatures relevant to particular thermal energy reservoirs. Few studies have focused on the systematic categorization and prediction of working fluid performance to avoid carrying out complete and detailed thermodynamic power plant analysis. Aljundi et al. [27] studied how the working fluid's critical temperature correlated with the resulting ORC efficiency; they found that higher critical temperatures weakly correlated to higher thermal and exergetic efficiencies. Sunter and Carey [28] used the Redlich-Kwong fluid model to develop a broad thermodynamic similarity framework based on fluid critical temperature that is applicable to various working fluids for solar thermal Rankine cycles. Their results on the contrary showed thermal efficiency to

increase with lower fluid critical temperature [28]. Papadopoulos et al. [29] constructed a computer-aided-molecular-design optimization technique using chemical and molecular group contribution methods that systematically generates the general molecular structure for optimal ORC working fluids. Using this hypothetical molecule structure, they can then compare to existing working fluids to predict performance metrics.

One of the main working fluid properties that heavily influence ORCs is the working fluid's saturated vapor curve slope on a T-S diagram. Water and other "wet" fluids such as propane and R134a have negatively sloped saturated vapor curves on a T-S diagram. When isentropically expanded from a saturated vapor state, the final state will always be a two-phase mixture within the vapor dome for "wet" fluids. This is why for wet steam turbines, expensive reinforcing material is necessary on the last stages of the low pressure turbine to protect the blades from erosion caused by liquid droplets that form. Another option is to superheat the "wet" fluid to a substantial degree such that expansion to the condenser pressure results in a superheated vapor state, as shown for the ORC in Fig. 1.3. This is not ideal as superheating decreases the average heat addition temperature, since the boiler pressure is reduced, and increases the average heat rejection temperature, both which lowers cycle efficiency based on Carnot considerations. For "isentropic" fluids such as R11, the slope of their saturated vapor curve is infinite and isentropic expansion from a saturated vapor state still results in a saturated vapor state. For "dry" fluids such as toluene, their saturated vapor curve slope is positive and isentropic expansion from a saturated vapor state will always yield a superheated vapor. Ideally, an "isentropic" working fluid would provide the best balance between not requiring reinforcing material for the turbine blades while also not having substantial superheat at the turbine exit.

The prediction of the saturated vapor curve without the use of detailed equations of state and T-S plots is a useful tool in identifying potential working fluid candidates. Tabor and Bronicki [30] used Maxwell relations and the Clausius-Clapeyron equation to determine the theoretical relationship for the slope of the saturated vapor curve on a T-S diagram, shown in eq. (1.1),

$$\left(\frac{\partial T}{\partial s}\right)_{\sigma} = \frac{1}{\frac{c_p}{T} - \left(\frac{\partial V}{\partial T}\right)_p \left(\frac{\Delta H_v}{T \Delta V}\right)} \tag{1.1}$$

where T is temperature, s is entropy, c_p is specific heat under constant pressure, V is specific volume, P is pressure, ΔH_v is the heat of vaporization, ΔV is the vaporization volume change, and the subscript σ denotes along the saturated vapor curve. Simplifying for an ideal gas, eq. (1.1) becomes eq. (1.2).

$$\left(\frac{\partial T}{\partial s}\right)_{\sigma} = \frac{1}{c_p - \left(\frac{\Delta H_v}{T}\right)} \tag{1.2}$$

Using a statistical mechanics argument, more complex molecules have greater number of vibrational degrees of freedom and subsequently higher specific heats. Therefore, it can be roughly inferred that the greater the number of atoms for a particular fluid molecule, the more positive the saturated vapor curve slope (the actual contributions to a molecule's specific heat

though also rely on inter-atomic forces as well as the atoms' masses) [30]. Tabor and Bronicki estimated a c_p of ~88J/mol·K would roughly yield an "isentropic" fluid. Assuming an incompressible liquid and using the Watson relation [31], Liu et al. [32] derive a simplified expression for the slope of the saturated vapor curve shown in eq. (1.3),

$$\left(\frac{\partial T}{\partial s}\right)_{\sigma} = \frac{c_p}{T_H} - \frac{\frac{nT_{rH}}{1-T_{rH}} + 1}{T_H^2}\Delta H_V \tag{1.3}$$

where T_H is the turbine inlet temperature, T_{rH} is the reduced turbine inlet temperature, and n is recommended to be 0.375 or 0.38 [31]. Their results showed that molecules having strong hydrogen bonds interactions and high heats of vaporization often are "wet" fluids, such as water and ammonia.

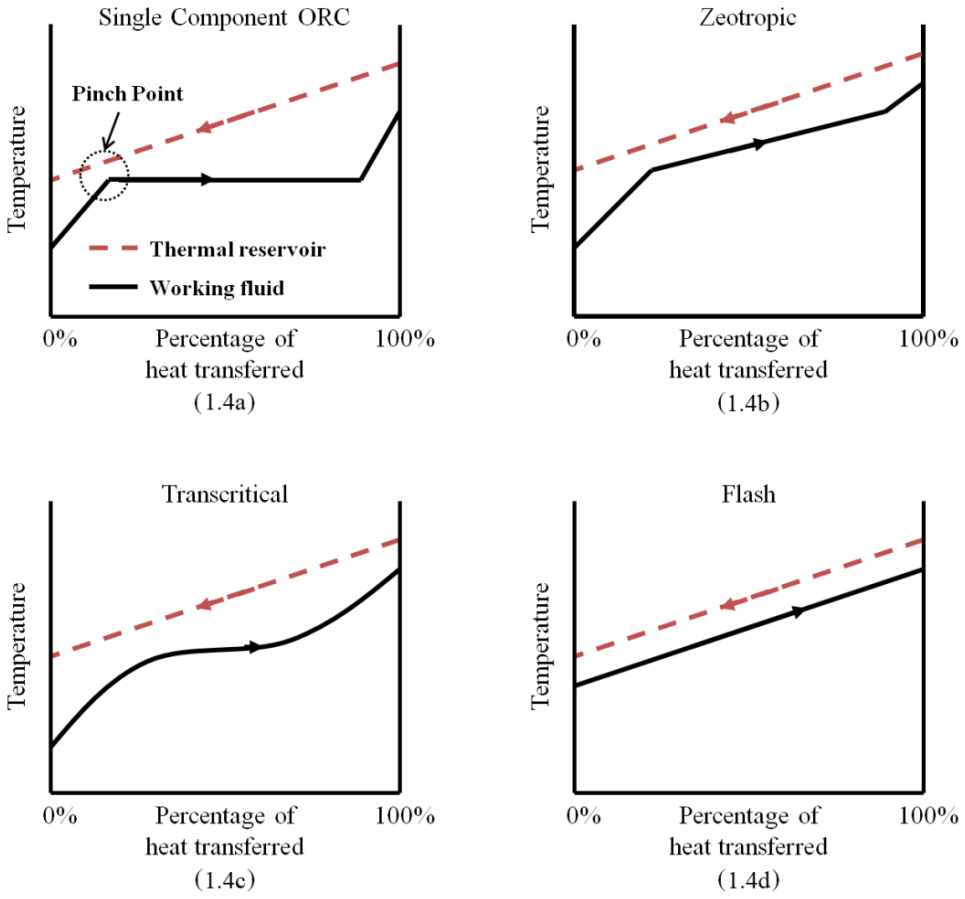

Figure 1.4: Variation in stream temperatures during heat addition process for single component, zeotropic, transcritical and flash cycles [9].

One of the major sources of irreversibilities for ORCs stem from the heat addition process. The thermal energy source and working fluid must be separated by some temperature difference in order for heat transfer to occur; however, heat transfer across a finite temperature difference inherently causes irreversibilities. Therefore, it is important to maintain good temperature

matching between the heat exchanger streams to minimize these types of irreversibilities [33]. A large degree of temperature mismatching often does occur when the thermal source is single-phase and possesses a near linear temperature profile along the heat exchanger. For an ORC using a pure working fluid though, the working fluid is first heated as a liquid, undergoes liquid-vapor phase change, and if necessary, is further superheated as a vapor thereafter. Its temperature profile will first be near linear, then constant during phase change, and then near linear again, as shown in Fig. 1.4a.

Temperature mismatching causes a pinch point to form, reduces heat exchanger effectiveness, and destroys potential work or exergy [34]. The exergy destruction caused by temperature mismatching can be represented qualitatively as the area of the plot between the thermal energy reservoir and working fluid stream in Fig. 1.4. As mentioned previously, heat is often added to the bottoming steam cycle at 2 or 3 pressures in modern HRSGs in combined cycle plants to reduce the aforementioned temperature mismatching. The temperature profile for a typical dual pressure HRSG is shown in Fig. 1.5.

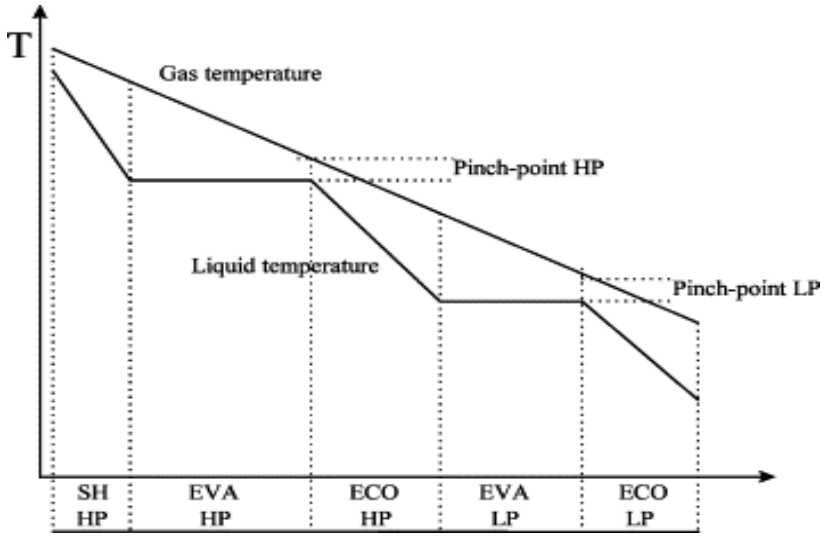

Figure 1.5: Temperature profiles for a dual pressure HRSG. Reprinted with permission from Elsevier: *Energy*, copyright 2002 [35].

Note that the temperature profiles follow each other much closer than that in Fig. 1.4a, thus allowing more heat to be transferred to the HRSG. This results in ~10% higher thermal efficiency for a dual pressure HRSG compared to a single pressure HRSG and 13% more for a triple pressure HRSG [35]. The temperature of the gas turbine exhaust stream out of the HRSG is also lower because more energy is transferred to the bottoming cycle. For example, the General Electric STeam And Gas (STAG) product line, the stack gas temperature decreases from approximately 171^{o}C for a single pressure non-reheat HRSG to 127^{o}C and 93^{o}C stack gas temperature for a dual and triple pressure non-reheat HRSG, respectively [10]. Some ORCs have also proposed multiple pressure heat addition to improve temperature matching; however, for low power generation or for low temperature energy resources, the additional heat exchangers and pumps required for heat addition at multiple pressures is not practical for ORCs and HRSGs alike. In addition, HRSGs using steam face additional problems at low temperatures and low power applications concerning large and inefficient turbines due to steam having low

molecular weight [13], as previously mentioned. To minimize temperature mismatching, researchers have proposed a number of possible solutions that include utilizing unconventional working fluids and innovative cycle configurations and designs which are discussed in the following sections.

1.2.3 Zeotropic vapor cycles

The use of zeotropic mixtures, mixtures of more than one type of pure fluid, as working fluids in vapor cycles has been proposed by a number of researchers as a possible method to improve temperature matching [36-42]. Zeotropic mixtures exhibit a unique characteristic known as a "temperature glide," which results in a variation in temperature during isobaric phase change. This is because the different components of the fluid mixture have will initiate phase change at different temperatures [43]. For example, ammonia and water are a common binary mixture used in power cycles and refrigeration cycles; its equilibrium phase diagram is shown in Fig. 1.6 at a pressure of 1MPa, where the red bubble point line represents saturated liquid states and the blue dew point line represents saturated vapor states.

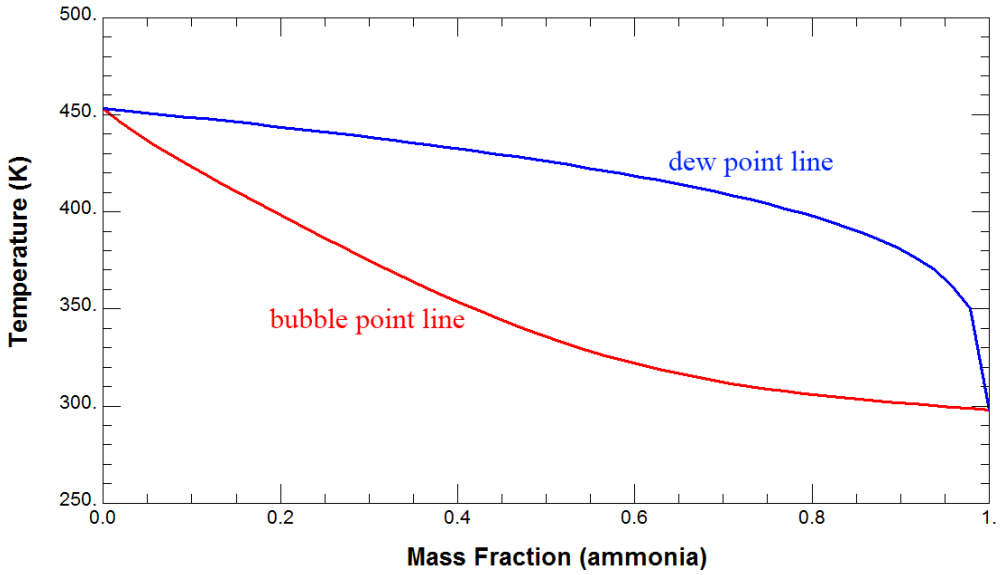

Figure 1.6: Equilibrium phase diagram for a water-ammonia binary mixture at 1MPa

Note that for the water and ammonia mixture, an intersection between the bubble line and dew line, or azeotropic point, is not formed. For azeotropic mixtures, isobaric phase change occurs at a constant temperature much like for a pure fluid. When the mixture does not have an azeotropic point, the mixture is termed a zeotropic mixture. Using Fig. 1.6 as an example, for a certain mixture composition, increasing temperature isobarically at 1MPa raises the liquid fluid's temperature until it reaches a saturated liquid state at the bubble line. Increasing the temperature further past the bubble line causes part of the fluid to vaporize; near the bubble point line it is mostly the more volatile component that begins vaporizing, in this case ammonia. As the temperature continues to increase and approach the dew point line, the majority of the more volatile ammonia component has already vaporized and the less volatile water component is now vaporizing. The specific component concentration of the liquid and vapor phases of the mixture

can be determined using the lever rule [43]. Once the mixture reaches the dew point line, the mixture has completely vaporized and is now at a saturated vapor state. Due to the temperature difference between the bubble point line and the dew point line, a so-called "temperature glide" exists during vaporization. This temperature glide can produce a better temperature match to the finite thermal reservoir by avoiding isothermal phase change. As shown in Fig. 1.4b, the zeotropic working fluid's temperature glide follows the temperature profile of the thermal reservoir more closely than the ORC's temperature profile. This reduces the irreversibilities in the heat addition process and can potentially improve the net power output and utilization efficiency [15]. Care must be taken in selecting the proper mixture composition to produce the closest temperature match possible; this is a subject of much theoretical and experimental research in minimizing pinch points and maximum temperature differences between zeotropic working fluids and the heat transfer fluid [34,44-46]

Although the temperature glide can improve temperature matching, there are some difficulties associated with using zeotropic mixtures in vapor cycles though. One disadvantage of using a mixture working fluid instead of a pure working fluid is that the mixtures will always have a lower convective heat transfer coefficients compared to the pure components for a given apparent heat transfer driving temperature difference [47]. This phenomenon arises because boiling reduces the quantity of the more volatile liquid near the liquid-vapor interface, thus near the interface, the remaining liquid must have a higher boiling point and temperature locally. Therefore, the actual temperature difference near the interface is lower than the apparent temperature difference and thus a lower heat transfer coefficient results [47]; this is sometimes referred to as the "diffusion resistance" to heat transfer for mixtures [48]. Another obstacle is that while the temperature glide improves temperature matching in the heat addition process; this same temperature glide also appears during heat rejection in the condenser after turbine expansion. This causes a higher average heat rejection temperature and becomes a detriment to the zeotropic vapor cycle by lowering efficiency due to Carnot considerations. This effect was observed by Wang et al. [37] for a theoretical low temperature solar ORC that used three different zeotropic mixtures of R245fa/R152a.

Despite these challenges, a number of researchers continue to explore vapor cycles with zeotropic working fluids. Chen et al. [49] screened a large number of potential zeotropic working fluid mixtures in conjunction with a supercritical Rankine cycle; an exergy analysis showed the temperature glide during heat rejection to be advantageous for non-isothermal condensation though it makes the cycle deviate from the ideal trilateral cycle [50] or the Maximum Power Cycle [42]. Herberle et al. [51] examined R227ea/R245fa and isobutene/isopentane mixtures for conversion of low grade geothermal energy to electricity. Angelino and di Paliano [39] performed a theoretical analysis on a zeotropic Rankine cycle with an internal heat exchanger using hydrocarbon and siloxane working fluids; their results showed similar performance to an ORC employing pure fluids. Recently Bao et al. [52] suggested an auto-cascade Rankine cycle for low temperature solar thermal energy that introduces a secondary circuit where the fluid is reheated prior to turbine expansion. Their approach is similar to that of other successful zeotropic Rankine cycles, where some type of an additional circulation loop is necessary in order to further utilize the high temperature working fluid at the high pressure vapor turbine exit. In the next sections, a brief summary of three other successful zeotropic vapor cycles is described.

1.2.3.1 The Kalina cycle

The Kalina cycle was invented by Russian engineer Alexander Kalina in 1983 originally for waste heat recovery [41]. The conventional version of the Kalina cycle uses a 70%/30% ammonia/water mixture as the primary working fluid; in an attempt to capture the energy in the vapor turbine exhaust and reduce the heat rejection temperature, a distiller-condenser-subsystem (DCSS) is introduced. The typical Kalina cycle is shown in Fig. 1.7 with the DCSS outlined in a dotted blue line [53]. In the DCSS, the working fluid changes composition multiple times, with a mixture very lean in ammonia being employed to reduce the condensing temperature [53,54]. Since the advent of the original Kalina cycle decades ago, numerous derivatives of the original cycle have been designed for specific applications such as geothermal energy [55], solar thermal energy [41], waste heat recovery [56], and combined cycle systems [57]. Claims of efficiency improvement by 10% to 50% over the conventional steam Rankine cycle for the Kalina cycle have been made [54]; however, some have disputed the actual increase in efficiency and put the increase in efficiency to be only about 3% [22]. The Kalina cycle does require fair amounts of precision for the mixing and distilling processes, as well as small pinch temperatures which will result in larger heat exchangers. Despite its complexity, presently the Kalina cycle is second only to the ORC in terms of popularity in actual implementation and is seen as the primary alternative to the ORC.

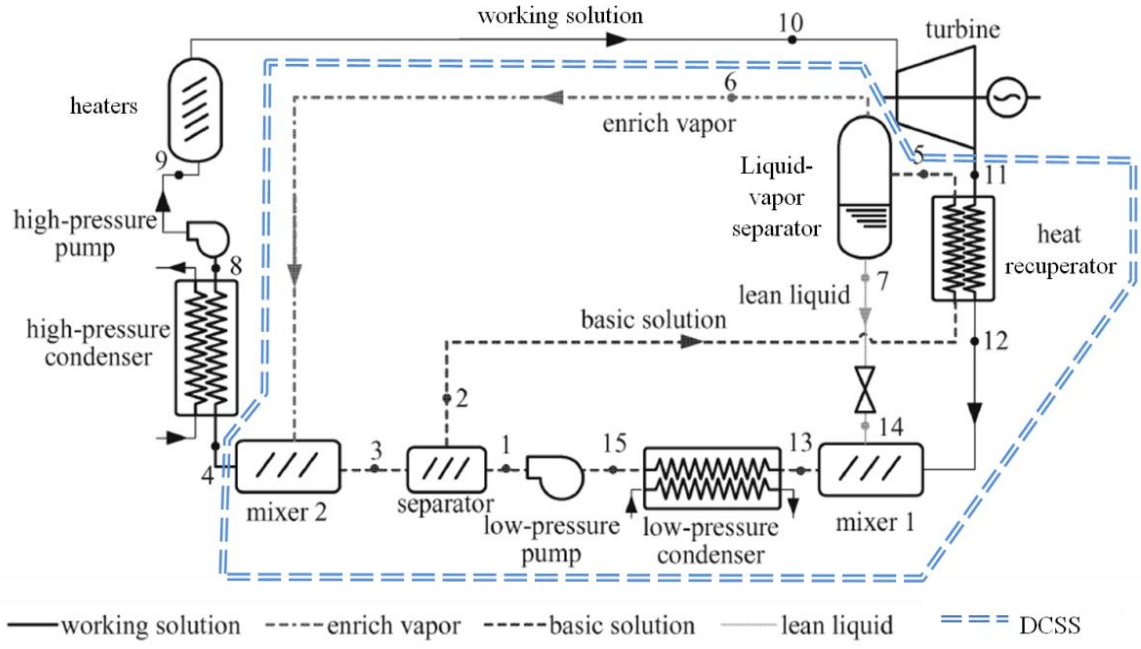

Figure 1.7: Schematic of Kalina cycle with distiller condenser subsystem (DCSS). Reprinted with permission from Springer Science and Business Media: *Frontiers in Energy and Power Engineering in China*, copyright 2008 [53].

1.2.3.2 The Maloney-Robertson cycle

Predating the Kalina cycle, was an ammonia-water vapor power cycle designed by Maloney and Robertson [58]. Results from their analysis determined that the steam Rankine cycle was more efficient in all the cases they examined. The Maloney-Robertson cycle was slightly less complex

than the Kalina cycle; however, it did require changing the mixture to a composition that was leaner in the volatile component prior to heat rejection to again lower the condensing temperature. Ibrahim and Klein [42] furthered the design study by examining the Maloney-Robertson cycle with a superheater and over a wider range of operating temperatures and pressures. Their results showed the Kalina cycle to more closely match the ideal Maximum Power cycle than the Maloney-Robertson cycle. However, their results also showed that for smaller heat exchanger sizes, the Maloney-Robertson cycle produced more power than the conventional Kalina cycle.

1.2.3.3 Combined power and cooling cycles

Rather than using the additional loop to produce additional power, some researchers have proposed a combined power and refrigeration or cooling cycle design. In these cycle designs, the heat rejected by the power cycle is used in an absorption refrigeration cycle. This can be a very advantageous design for industries such as food and beverage where power and refrigeration can both be produced from a waste heat stream. Vijayarghavan [59] modeled and examined a combined power and cooling cycle using a binary ammonia-water mixture and mixtures of a variety of organic working fluids for moderate and low temperature geothermal and solar thermal energy. His results showed the basic cycle to possess adequate exergetic efficiencies but poor resource utilization efficiencies; a number of configuration design changes were then subsequently recommended. Xu, Goswami et al. [60] proposed a combined ammonia/water Rankine power cycle and absorption refrigeration cycle that utilized absorption condensation; their simulation results show that the capital costs for a solar thermal system is significantly reduced by implementing their cycle. In fact, Goswami et al. are one of the leading researchers in combined power and refrigeration cycles and have numerous publications in the area [61-67], particularly for cycles using ammonia-water working fluids.

1.2.4 Transcritical and supercritical cycles

Another method that has been suggested is to avoid the phase change region completely by transferring heat at pressures above the critical pressure. This would essentially avoid the temperature mismatching encountered in the constant temperature phase change process that occurs inside the vapor dome. A cycle that operates partly under supercritical conditions is known as a transcritical cycle, whereas a cycle operating completely in the supercritical regime is known as a supercritical cycle; however, these two terms have been used interchangeably in the literature. Working fluids that are often suggested for such cycles include carbon dioxide, helium, refrigerants, and alkanes. An illustration of the improved temperature matching for a transcritical cycle is shown in Fig. 1.4c. Although theoretically the transcritical cycle has merit, the design of a suitable supercritical turbine for fluids other than water is still in the developmental phases [68]. A fluid under supercritical conditions can possess both liquid and vapor behaviors; thus tailoring a turbine specifically to one specific condition; i.e. liquid or vapor behavior, becomes problematic [69] and the development of an appropriate supercritical turbine design remains ongoing.

A number of theoretical studies have been performed for transcritical and supercritical cycles. Feher [70] conducted one of the earlier studies on supercritical cycles; a general method for

supercritical cycle analysis is given along with suggestions for improvements including regeneration. Feher concluded that in principle any working fluid could be used in the supercritical cycle; at the time though, abundant thermodynamic data over a wide range of temperatures and pressures was limited to only a few working fluids such as water and CO_2. Gu and Sato [71] examined the suitability of a propane regenerative transcritical cycle for a hypothetical low temperature geothermal source modeled after an existing binary plant; their results show that their cycle design produced greater power than other designs from a previous study [72]. Gu and Sato later expanded their study to also include R125 and R134a working fluids [73]. Mikielewicz et al. [74] examined 20 different organic fluids using REFPROP 8.0 for a subcritical and a transcritical cycle for domestic combined heat and power (CHP); their results showed better performance from ethanol, R123, and R141b working fluids. Karellas et al. [75] examined the subcritical and transcritical cycle for R134a, R227ea, R236fa, and R245fa working fluids and their suitability for different finite thermal energy applications such as biomass combustion, waste heat recovery from internal combustion engines, and geothermal energy. Schuster et al. [76] optimized the basic subcritical ORC and transcritical cycle for maximum power production and minimum required heat transfer area for a number of refrigerant and alkane working fluids; their study also provided a detailed analysis on different power cycle efficiency definitions based on exergy and the ideal Triangular cycle. By far though, the most popular transcritical and supercritical cycle working fluid suggested in the literature for finite thermal energy sources is CO_2.

1.2.4.1 CO_2 transcritical cycle

Due to its inexpensiveness, availability, inertness, and stability, CO_2 is by far the most often proposed working fluid for a transcritical or supercritical cycle [70]. Chen et al. [77] used computational analysis with Engineering Equation Solver (EES) to compare the performance of a transcritical CO_2 cycle to a R123 ORC for waste heat recovery; their results showed the CO_2 transcritical cycle to generate slightly more power from the same finite thermal energy source than the R123 ORC. Cayer et al. [78] also examined a transcritical CO_2 with and without an internal heat exchanger for low temperature waste heat recovery of a industrial exhaust gas stream; an exergy and pinch analysis was also presented along with estimated required heat exchanger surface areas. In a subsequent publication, Cayer et al. [79] conducted a parametric study on system parameters such as thermal and exergetic efficiency, specific net power output, heat exchanger sizing, and system costs for CO_2, ethane, and R125. Guo et al. [80] compared natural working fluids such as CO_2 to synthetic working fluids in a transcritical cycle for low temperature geothermal and found R125 to provide higher performance than CO_2 for geothermal resources above 90^oC and R32 and R143a to also be better at temperatures above 100^oC. Zhang et al. [68,81-84] have conducted numerous studies on the CHP application of the CO_2 transcritical cycle to solar thermal energy for the distributed or domestic production of power and hot water. In Zhang et al.'s experimental study [84], a throttling valve was used to simulate a turbine because again, to date no supercritical CO_2 is available. This again highlights that although the CO_2 transcritical cycle has promising potential, the design, construction, and implementation of an inexpensive, easily manufacturable, and reliable turbine will ultimately determine its practical value.

1.2.5 Trilateral flash cycle

The trilateral flash cycle [50,69,85,86], another proposed method to improve temperature matching, faces similar challenges to that of the transcritical cycle described in the previous section. Smith et al **[**69**,**87**,**88**]** first introduced the trilateral flash cycle where heat addition to the power cycle occurs completely while the working fluid is a single-phase liquid, thereby avoiding isothermal phase change as shown in Fig. 1.4d. As shown in Fig. 1.4d, this configuration enables near perfect temperature matching to the fluid stream from the finite thermal energy source. Once the working fluid is heated to a saturated liquid state, work is then extracted using a two-phase expander. Smith et al. initially proposed a number of different working fluids for the trilateral flash cycle including water, pentane, R12, and R113 **[**69**]**. Later working fluid mixtures of pentane/neo-pentane were also proposed and analyzed **[**87**]**. Similar to the transcritical cycle, the design of a reliable and efficient two-phase expander is still ongoing, though recent strides are being made for screw-type [88-91] and scroll-type expanders and reciprocating engines **[**86**]**.

1.3 Motivation for the Organic Flash Cycle (OFC)

To avoid the requirement of a two-phase expander though, the single-phase liquid could be throttled to a two-phase mixture after heat addition. The liquid and vapor components of the mixture could then be separated and power could be generated from the saturated vapor using a conventional and readily available ORC turbine. By using this type of configuration, a two-phase turbine is no longer necessary, while the near perfect temperature matching between streams shown in Fig. 1.4d is still maintained. This resulting cycle is somewhat similar to the flash steam cycle that utilizes high temperature and pressure geofluid that has been extracted in the liquid state from a geothermal well. Once extracted, the high pressure, high temperature liquid geofluid is brought to a lower pressure by a throttling or flashing process producing a liquid-vapor mixture **[**15**]**. One major disadvantage of the steam flash cycle though, is that the steam after expansion contains a significant amount of moisture because water is again a "wet" fluid and exhibits a negatively sloped saturated vapor curve on a T-S diagram. As mentioned previously, isentropic expansion of a "wet" fluid from its saturated vapor state will always produce a two-phase mixture with liquid droplets forming. In reality large steam turbines often have isentropic efficiencies of 80% to 90%; however, saturated steam cycles in geothermal and nuclear power industries still require special wet steam turbines that have expensive reinforcing materials to protect the turbine blades from erosion and damage caused by the liquid droplets that form **[**15**]**.

Expansion of a saturated vapor into the vapor dome can be avoided if an "isentropic" or "dry" fluid with an infinite or positively sloped saturated vapor curve on a T-S diagram was used instead of steam. In addition to having smaller turbine volumetric flow ratios and correspondingly smaller sizes, the turbine cost would also be significantly reduced for the Organic Flash Cycle (OFC) since blade reinforcing materials are no longer necessary. Although uncontrolled expansion of the working fluid generates considerable irreversibilities during the throttling or flashing process **[**4**]**, the reduction in exergy destruction during heat addition could ultimately provide a net gain in the OFC's power output as a whole. It is under this premise that a comprehensive thermodynamic and exergetic analysis was conducted to evaluate the effectiveness of the OFC employing an organic "isentropic" or "dry" fluid. The organic working

fluid under consideration is dependent on the initial temperature of the finite thermal energy source. With an optimized system configuration and appropriate cycle working fluid selection, the OFC could potentially generate significantly more power from a given finite thermal energy reservoir than the conventional ORC. Besides the environmental benefits of improving the efficiency with which these energy sources are utilized, the OFC may also have a faster return on investment, thus encouraging a more widespread adoption of renewables and waste heat recovery technologies.

1.4 Outline of dissertation

From the aforementioned motivations for this research, the outline of this dissertation is now briefly described. In chapter 2, the modern equations of state explicit in Helmholtz energy used in this study to accurately determine the thermodynamic data for power cycle analysis are presented. Siloxane, aromatic hydrocarbon, alkane, and refrigerant working fluids analyzed in chapter 2 represent a variety of nonpolar and polar fluids with varying molecular complexity. To verify the accuracy and robustness of the Helmholtz equations of states, the calculated saturated liquid and vapor density and vapor pressure values are compared to those listed in the online NIST Chemistry WebBook over a range of temperatures and pressures relevant to this study.

In chapter 3, the configuration of the basic OFC is described in detail; it is proposed as a method to increase power production by better temperature matching to the finite thermal energy reservoir. Here, the suitability of the OFC for intermediate temperature energy resource applications near ~300^{o}C such as one-axis solar thermal, geothermal, and high grade waste heat is examined. Ten different aromatic hydrocarbons and siloxanes are investigated as potential working fluid candidates for the OFC. Discussion is also presented on how the different working fluids affect preliminary turbine design. The OFC is then compared to the optimized basic ORC, a zeotropic ammonia-water Rankine cycle, and a transcritical CO_2 cycle.

A number of improvements to the OFC based on results from the previous chapter are analyzed and discussed in chapter 4. Although the OFC improved the heat addition exergetic efficiency, a considerable amount of irreversibility is generated during flash evaporation and throttling processes. A comparison of performance of the OFC with the proposed improvements and the optimized ORC is presented. Discussion is also given on the advantages of increased power output versus the disadvantages of more plant components and increased complexity of the proposed designs.

In chapter 5, the OFC and its proposed enhancements are investigated for low temperature resources such as non-concentrated solar thermal, geothermal, and low grade industrial waste heat energy. Here, alkanes and refrigerants are determined to be the more suitable working fluids because of their more appropriate vapor pressures in the temperature range of interest. Discussion is also given on how the minimum temperature difference between streams, or pinch temperature, is an especially important design parameter for low temperature applications.

A high-level plant design for a solar power tower is proposed in chapter 6. Liquid-fluoride salt coolant is preferred over nitrate salts to push the operating temperatures of the heliostat-central receiver system higher. The power block consists of a combined topping Brayton cycle with

intercooling, reheat, and regeneration and a bottoming low-temperature modified OFC. Power block and total system efficiencies are examined for different central receiver temperatures. In the final chapter, a summary of the study's main results are given with some conclusions drawn based on those results; some possible directions for future research on the OFC are also presented.

2 Description of thermodynamic properties of potential pure working fluids using modern Helmholtz-explicit equations of state

2.1 Introduction

The majority of studies of vapor power cycles for solar thermal and waste heat applications have been limited to the working fluids in NIST REFPROP 8.0 [92]. Many of the fluids in REFPROP are typically used in the oil and natural gas refining process and refrigeration industry and therefore, possess low critical temperatures when compared to water, which has a critical temperature of 374°C. When only considering fluids from REFPROP, the number of fluids that could potentially be suitable for a subcritical vapor cycle is then limited to low temperature energy reservoirs. For intermediate and high temperature thermal energy reservoirs such as heated solar fluid circulating in a parabolic trough field which can reach temperatures up to 400°C [93], fluids with higher critical temperatures should be considered. Therefore, there is a desire to expand the pool of potential working fluids beyond just those in REFPROP. To analyze the suitability of these other potential working fluids, a method of accurately determining thermodynamic property data of pure polar and nonpolar working fluids will be necessary. The equations of state that will be used should possess high order accuracy, yet require only a few fluid specific parameters to enable quick screening. This may require that the equations have some physical basis applicable to a large number of different working fluids, rather than be purely empirical. With the equation of state rooted in some physical basis, there is also an opportunity for analyzing why certain working fluids perform better than others by examining the fluid specific parameters and gain molecular-level insights.

A large number of equations of state have been developed by researchers over the years; they range from the very basic such as van Der Waals cubic equations of state and the adaptations of it such as the Redlich-Kwong-Soave [94] and the Peng-Robinson [95] equations to the very complex such as the Modified Benedict-Webb-Rubin Equations [96] and modern multi-parameter equations of state, some of which are employed in REFPROP [92]. Cubic equations of state are often very simple and require only two to three fluid specific parameters. Typically they are cast in the general form shown in eq. (2.1) [96],

$$P = \frac{RT}{V-B} - \frac{A}{V^2 + uBV + wB^2} \tag{2.1}$$

where A and B are fluid specific constants dependent on the fluid's critical temperature T_c and pressure P_c, and u and w are dependent on the specific cubic equation being used (i.e. $u = 1$ and $w = 0$ for Redlich-Kwong-Soave) [96]. Similar to the original van Der Waals equation, in the generalized cubic equation of state shown in eq. (2.1), the first term represents the repulsive forces and reduced volume cause by the physical finite space occupied by the molecules and the second term represents attractive dispersion forces between molecules [4]. A is often temperature dependent and can also have an additional dependency on the fluid's acentric factor ω. The acentric factor is fluid specific and represents the fluid molecule's nonsphericity and has been included in many cubic equations to generally improve the accuracy in predicting saturated liquid and vapor properties for nonpolar hydrocarbons [96]. Cubic equations are simple in their form, easy to implement computationally, and can often be solved non-iteratively which

generally makes applying them very straightforward. However, their relative ease of use and simplicity comes at the cost of accuracy. They often perform poorly at high pressures and become less accurate for subcooled liquids; this is because of the inherent limitation on density that it can be no more complex than cubic **[**96**]**. Another disadvantage of cubic equations is that they are limited in their application to nonpolar molecules, since polar molecules rarely obey corresponding states theories with only three parameters **[**96**]**. The present study for vapor power cycles will include many calculations within the two-phase regime and subcooled liquid regime; therefore, accurate predictions of thermodynamic property data at these states are required. It was thus concluded that cubic equations of state do not provide sufficient enough accuracy for this particular study in examining vapor cycles.

Helmholtz-explicit equations of state, similar to some of those used in REFPROP, are attractive because they offer highly accurate predictions of thermodynamic property data. However these equations are often very complex and almost always require iterative procedures to solve. The main drawback though of some equations of states is the extensive data sets that are required to correlate and obtain the large number of fluid-specific parameters and coefficients **[**97**]**. The fluid specific equations would also need to be programmed individually which would require a significant amount of time for each potential fluid. A compromise between accuracy and simplicity can be found with the BACKONE family of equations of state [19,97,98] and the Span-Wagner equations [99-102].

The BACKONE equations require only a small data set and are applicable to nonpolar, dipolar, and quadrupolar fluids. The Span-Wagner equations similarly require a small data set to be fit to and are broadly applicable to nonpolar and weakly polar fluids including aromatic hydrocarbons and siloxanes **[**103**,**104**]**. Unlike the aforementioned cubic equations which are explicit in pressure, the BACKONE and Span-Wagner equations are explicit in Helmholtz energy a, as a function of temperature T and density ρ. The main advantage of using equations that are explicit in Helmholtz energy is that all thermodynamic properties can be determined from the Helmholtz energy and its partial derivatives with respect to temperature and density. This makes programming the computational algorithms for equations explicit in Helmholtz energy more systematic and straightforward compared to those explicit in pressure **[**99**]**. The BACKONE equations require only three to five fluid specific parameters to characterize the fluid; these parameters include a characteristic density ρ_0, temperature T_0, and an anisotropy parameter φ. If the fluid is dipolar or quadrupolar then the fluid's reduced dipole moment μ^{*2} or reduced quadrupole moment Q^{*2} is also required **[**98**]**. The Span-Wagner equation in contrast typically requires 12 fluid specific parameters for the residual portion. In the following sections, a discussion is presented on the details and implementation of the BACKONE and Span-Wagner equations. A comparison of the predictions from these equations to those from NIST REFPROP for some reference fluids is also presented.

2.2 Modern equations of state explicit in Helmholtz energy

2.2.1 BACKONE equations of state

As previously mentioned, the BACKONE equations of state are part of a larger family of modern equations of state known as Helmholtz equations **[**99**]**. The BACKONE equations have been used in a variety of thermodynamic analyses in the literature and provide a method to accurately

determine thermodynamic properties [19,98,99,105-108]. Most modern equations of state including those in the NIST REFPROP program are Helmholtz equations. These equations are typically written in reduced Helmholtz energy $\alpha(T, \rho) = a(T, \rho)/RT$, where R is the universal gas constant; note that Helmholtz energy is written as a function of its natural variables, temperature and density **[**109**]**. The total reduced Helmholtz energy can be split into parts consisting of the ideal gas reduced Helmholtz energy α^0 and the residual reduced Helmholtz energy α^R. The ideal gas part gives the contribution to Helmholtz energy from an ideal gas at the specified temperature and density and the residual part corrects for how the real fluid deviates from an ideal gas description **[**99**]**. The BACKONE equations further splits up the residual component into the contributions from different intermolecular interactions consisting of the repulsive forces due to the molecule's hard spheres α^H, the nonpolar attractive dispersion forces α^A, and the polar interactions α^{Pol}. The polar contribution is made up of the contributions due to dipole interactions α^D and quadrupole interactions α^Q **[**98**]**. The different contributions to the total Helmholtz energy for the BACKONE equations are summarized in eq. (2.2).

$$\frac{a(T,\rho)}{RT} = \alpha(T,\rho) = \alpha^0 + \alpha^R = \alpha^0 + \left(\alpha^H + \alpha^A + \alpha^{Pol}\right) = \alpha^0 + \left(\alpha^H + \alpha^A + \left[\alpha^D + \alpha^Q\right]\right) \qquad (2.2)$$

By breaking the total Helmholtz energy into its components, one sees that the BACKONE equations are at least in part physically based and assumes the different intermolecular interactions each contributes additively to the total Helmholtz energy **[**98**]**. The following sections provide a detailed description of the methods and correlations used to determine each of the contributions to the reduced Helmholtz energy. The procedure of evaluating thermodynamic properties from Helmholtz energy and its partial derivatives with respect to temperature and density is also given. Afterwards, the algorithms and computational schemes used to determine thermodynamic properties from different combinations of initially known properties frequently used in power cycle analysis such as pressure and enthalpy are discussed.

2.2.1.1 Ideal gas contribution

Starting from the combined first and second law of thermodynamics and the definition of Helmholtz energy, the ideal gas contribution to Helmholtz energy is given in eq.(2.3),

$$a^0 = h^0 - RT - Ts^0 \qquad (2.3)$$

where h and s is enthalpy and entropy, respectively, and the superscript 0 denotes that the property is for an ideal gas. The ideal gas enthalpy and entropy in eq. (2.3) can be replaced with expressions given in eq. (2.4) and (2.5).

$$h^0 = h^0_{ref} + \int_{T_{ref}}^{T} c_p^0 dT \qquad (2.4)$$

$$s^0 = s^0_{ref} + \int_{T_{ref}}^{T} \frac{c_p^0}{T} dT - R\ln\left(\frac{\rho T}{\rho_{ref} T_{ref}}\right) \qquad (2.5)$$

In eq. (2.4) and (2.5), $c_p^{\,0}$ is the ideal gas heat capacitance and the subscript *ref* denotes the property at an arbitrary reference state. Combining those equations, the ideal gas contribution to the reduced Helmholtz energy is shown in eq. (2.6) where temperature and density have been replaced with inversed reduced temperature $\tau = T_0/T$ and reduced density $\delta = \rho/\rho_0$ **[**99**,**110**]**.

$$\alpha^0 = \frac{a^0}{RT} = \frac{h_{ref}^0 \tau}{RT_0} - 1 + \ln\left(\frac{\delta \tau_{ref}}{\delta_{ref} \tau}\right) - \frac{s_{ref}^0}{R} - \frac{\tau}{R}\int_{\tau_{ref}}^{\tau} \frac{c_p^0}{\tau^2} d\tau + \frac{1}{R}\int_{\tau_{ref}}^{\tau} \frac{c_p^0}{\tau} d\tau \tag{2.6}$$

For this present analysis, the reference state was set to T_{ref} = 298.15K and P_{ref} = 101.325kPa, where the ideal gas enthalpy and entropy are taken to be zero at this reference state. The substance specific, ideal gas heat capacitances are taken from available correlations published in the literature [96,110-113]. The general form of the molar ideal gas heat capacitance can often be written in the general form shown in eq. (2.7) [31,96],

$$c_p^0 = A_{cp} + B_{cp}T + C_{cp}T^2 + D_{cp}T^3 + E_{cp}T^4 = A_{cp} + B_{cp}\frac{T_0}{\tau} + C_{cp}\frac{T_0^{\,2}}{\tau^2} + D_{cp}\frac{T_0^{\,3}}{\tau^3} + E_{cp}\frac{T_0^{\,4}}{\tau^4} \tag{2.7}$$

where A_{cp}, B_{cp}, C_{cp}, D_{cp}, E_{cp} are fluid specific constants. Using eq. (2.6) and (2.7) together, the ideal gas contribution to the Helmholtz energy can be determined.

Again, the main advantage of using equations of state explicit in Helmholtz energy is the ability to determine all other properties from the Helmholtz energy, and its partial derivatives with respect to temperature and density. These relationships can be derived from the well known Maxwell Relationships and basic thermodynamic calculus. For power cycle analysis, besides temperature and density, properties such as pressure, enthalpy, and entropy are important. These properties as a function of reduced Helmholtz energy are shown in eq. (2.8), (2.9), and (2.10) respectively; the derivations of these equations can be found in Appendix B **[**99**]**.

$$P(T,\rho) = \rho RT\left(\delta\alpha_\delta\right) \tag{2.8}$$

$$h(T,\rho) = RT\left(\delta\alpha_\delta + \tau\alpha_\tau\right) \tag{2.9}$$

$$s(T,\rho) = R\left(\tau\alpha_\tau - \alpha\right) \tag{2.10}$$

Note that these equations are written with the notation shown in eq. (2.11) and (2.12).

$$\left(\frac{\partial\alpha}{\partial\delta}\right)_\tau = \alpha_\delta \tag{2.11}$$

$$\left(\frac{\partial\alpha}{\partial\tau}\right)_\delta = \alpha_\tau \tag{2.12}$$

Since the contributions are additive in the BACKONE equations, the derivative of the total reduced Helmholtz energy is the sum of derivative of the individual components of reduced Helmholtz energy. Using eq. (2.6), the derivatives of the ideal gas reduced Helmholtz energy with respect to reduced density and temperature are determined to be eq. (2.13) and (2.14).

$$\alpha_{\delta}^{0} = \delta^{-1} \tag{2.13}$$

$$\alpha_{\tau}^{0} = \frac{h_{ref}^{0}}{RT_0} - \frac{1}{\tau} - \frac{1}{R}\int_{\tau_{ref}}^{\tau} \frac{c_p^0}{\tau^2} d\tau \tag{2.14}$$

From eq. (2.6), (2.13), and (2.14) the ideal gas contributions can be calculated.

2.2.1.2 Residual contribution

The expression for the residual contribution to the reduced Helmholtz energy often takes on the general form shown in eq. (2.15) **[**99**]**,

$$\alpha^R(\tau,\delta) = \sum_{i=1}^{I_{pol}} n_i \tau^{t_i} \delta^{d_i} + \sum_{i=I_{pol}+1}^{I_{pol}+I_{exp}} n_i \tau^{t_i} \delta^{d_i} \exp\left(-g_i \delta^{p_i}\right) \tag{2.15}$$

where I_{pol} and I_{exp} is the number of polynomial and exponential terms respectively, and n_i, t_i, d_i, g_i, and p_i are constants dependent on the specific Helmholtz equation selected.

2.2.1.2.1 Hard-Sphere/Repulsive Contribution

For the BACKONE equations, the residual contribution is composed of contributions from the repulsive hard-sphere, attractive dispersion, and polar interactions. The effects of intermolecular repulsion that are represented in the hard-sphere contributions can be accurately determined theoretically using modern perturbation theories **[**99**]**. The hard-sphere contribution to reduced Helmholtz energy is given by eq. (2.16),

$$\alpha^H = \left(\varphi^2 - 1\right)\ln\left(1-\xi\right) + \frac{\left(\varphi^2 - 3\varphi\right)\xi - 3\varphi\xi^2}{\left(1-\xi\right)^2} \tag{2.16}$$

where φ is the anisotropy parameter of the fluid and ξ is the packing fraction given by eq. (2.17) with the constants in the equation given as $n_Z = 0.1617$, $a_Z = 0.689$, and $\gamma = 0.3674$ **[**99**]**.

$$\xi = n_Z \delta \left[a_Z + \left(1 - a_Z\right)\tau^{-\gamma} \right]^{-1} \tag{2.17}$$

The details of the derivation for the contribution from the hard-sphere terms can be found in ref. **[**114**]** by Saager et al.

Determining the derivatives of the hard-sphere terms is somewhat more complex than for the ideal gas terms because the packing fraction ξ is dependent on both density and temperature. Therefore, to calculate the derivatives, the packing fraction is differentiated with respect to density and temperature and then the chain rule is employed. These results are summarized in eq. (2.18) through (2.22) **[**99**]**.

$$\left(\frac{\partial \alpha^H}{\partial \delta}\right)_\tau = \alpha_\delta^H = \left(\frac{d\alpha^H}{d\xi}\right)\left(\frac{\partial \xi}{\partial \delta}\right)_\tau \tag{2.18}$$

$$\left(\frac{\partial \alpha^H}{\partial \tau}\right)_\delta = \alpha_\tau^H = \left(\frac{d\alpha^H}{d\xi}\right)\left(\frac{\partial \xi}{\partial \tau}\right)_\delta \tag{2.19}$$

$$\left(\frac{d\alpha^H}{d\xi}\right) = \left(\varphi^2 - 1\right)\ln\left(1-\xi\right) + \frac{\left(\varphi^2 + 3\varphi\right)\xi - 3\varphi\xi^2}{\left(1-\xi\right)^2} \tag{2.20}$$

$$\left(\frac{\partial \xi}{\partial \delta}\right)_\tau = n_Z\left[a_Z + \left(1-a_Z\right)\tau^{-\gamma}\right]^{-1} \tag{2.21}$$

$$\left(\frac{\partial \xi}{\partial \tau}\right)_\delta = n_Z\delta\frac{\left(1-a_Z\right)\gamma\tau^{-(\gamma+1)}}{\left[a_Z + \left(1-a_Z\right)\tau^{-\gamma}\right]^2} \tag{2.22}$$

With these relationships, the contributions from the short-range, repulsive hard-body terms can be determined.

2.2.1.2.2 Nonpolar Attractive-Dispersion Contribution

The contribution to the reduced Helmholtz energy from attractive dispersion forces α^A was determined by Müller et al. **[**97**,**98**]**; it has been modified here to eq. (2.23) so that it fits the general form given by eq. (2.15).

$$\alpha^A = \sum_{i=1}^{19} n_i \tau^{t_i} \delta^{d_i} + \sum_{i=20}^{28} n_i \tau^{t_i} \delta^{d_i} \exp\left(-\delta^{p_i}\right) \tag{2.23}$$

Using experimental data for methane, oxygen, and ethane, Müller et al. determined the constants n_i, t_i, d_i, and p_i in ref. **[**97**]**; they have been reproduced in Table A.1 of Appendix A for convenience. These constants, with the exception of n_i, are substance independent; the constants n_i are dependent on the substance specific anisotropy parameter φ. The derivatives of the nonpolar attractive contribution to reduced Helmholtz energy with respect to temperature and density is given by eq. (2.24) and (2.25) **[**99**]**.

$$a_\delta^A = \sum_{1}^{19} n_i d_i \delta^{d_i - 1}\tau^{t_i} + \sum_{20}^{28} n_i \delta^{d_i - 1}\left(d_i - p_i\delta^{p_i}\right)\tau^{t_i}\exp\left(-\delta^{p_i}\right) \tag{2.24}$$

$$a_\tau^A = \sum_{1}^{19} n_i d_i \delta^{d_i} t_i \tau^{t_i - 1} + \sum_{20}^{28} n_i \delta^{d_i} t_i \tau^{t_i - 1}\exp\left(-\delta^{p_i}\right) \tag{2.25}$$

These equations combined with those for the repulsive and ideal gas terms, give the Helmholtz equations for nonpolar substances. For fluids with dipolar and quadrupolar moments, additional contributions are required.

2.2.1.2.3 Dipolar and Quadrupolar Contributions

For fluids exhibiting dipoles or quadrupoles, additional contributions from the molecule's polar interactions need to be included. The contribution to the reduced Helmholtz energy from dipole and quadrupole interactions are given in eq. (2.26) and (2.27), respectively **[**97**,**99**,**115**]**.

$$\alpha^D = \sum_{i=1}^{28} n_i \left(1.13\tau\right)^{t_i} \delta^{d_i} \exp\left(-g_i\delta^2\right) \tag{2.26}$$

$$\alpha^Q = \sum_{i=1}^{17} n_i \left(1.13\tau\right)^{t_i} \delta^{d_i} \exp\left(-g_i\delta^2\right) \tag{2.27}$$

The constants have been modified to fit the general form given by eq. (2.15); their values have been reproduced in Table A.2 and Table A.3 for convenience **[**97**,**99**,**115**]**. Similar to the nonpolar attractive contribution, all the constants in eq. (2.26) and (2.27) are fluid independent except constants n_i, which depend on the reduced dipole moment μ^{*2} and reduced quadrupole moment Q^{*2}, respectively. The derivatives to the dipole and quadrupole contributions are calculated and given in eq. (2.28) through (2.31).

$$a_\delta^D = \sum_{1}^{28} n_i\delta^{d_i-1}\left(d_i - 2g_i\delta^{p_i}\right)\left(1.13\tau\right)^{t_i} \exp\left(-g_i\delta^2\right) \tag{2.28}$$

$$a_\tau^D = \sum_{1}^{28} n_i\delta^{d_i} t_i \left(1.13\tau^{t_i-1}\right)\exp\left(-g_i\delta^2\right) \tag{2.29}$$

$$a_\delta^Q = \sum_{1}^{17} n_i\delta^{d_i-1}\left(d_i - 2g_i\delta^{p_i}\right)\left(1.13\tau\right)^{t_i} \exp\left(-g_i\delta^2\right) \tag{2.30}$$

$$a_\tau^Q = \sum_{1}^{17} n_i\delta^{d_i} t_i \left(1.13\tau^{t_i-1}\right)\exp\left(-g_i\delta^2\right) \tag{2.31}$$

With these relationships, the Helmholtz energy for polar fluids can be determined from only one to two additional fluid specific parameters: the reduced dipole and/or quadrupole moments.

2.2.2 Span-Wagner equations of state

For the Span-Wagner multi-parameter equations of state for nonpolar and weakly polar substances, the reduced Helmholtz energy is split into its ideal gas component and residual components similar to the BACKONE equations **[**101**,**102**]**. The ideal gas component is exactly the same as that used for the BACKONE equations shown in section 2.1.1. For convenience, the results of ideal gas component of the reduced Helmholtz energy and the derivative of the reduced Helmholtz energy with respect to temperature and density are shown in eq. (2.32), (2.33), and (2.34) respectively.

$$\alpha^0 = \frac{a^0}{RT} = \frac{h_{ref}^0\tau}{RT_0} - 1 + \ln\left(\frac{\delta\tau_{ref}}{\delta_{ref}\tau}\right) - \frac{s_{ref}^0}{R} - \frac{\tau}{R}\int_{\tau_{ref}}^{\tau}\frac{c_p^0}{\tau^2}d\tau + \frac{1}{R}\int_{\tau_{ref}}^{\tau}\frac{c_p^0}{\tau}d\tau \tag{2.32}$$

$$\alpha_\delta^0 = \delta^{-1} \tag{2.33}$$

$$\alpha_\tau^0 = \frac{h_{ref}^0}{RT_0} - \frac{1}{\tau} - \frac{1}{R}\int_{\tau_{ref}}^{\tau} \frac{c_p^0}{\tau^2} d\tau \tag{2.34}$$

The residual component of the reduced Helmholtz energy for Span-Wagner equations is shown in eq. (2.35); note that it follows the general functional form given previously in eq. (2.15).

$$\alpha^R(\tau,\delta) = \sum_{i=1}^{6} n_i \tau^{t_i} \delta^{d_i} + \sum_{i=7}^{12} n_i \tau^{t_i} \delta^{d_i} \exp\left(-\delta^{p_i}\right) \tag{2.35}$$

Unlike the BACKONE equations, the Span-Wagner equations do not further divide the residual component into the attractive, repulsive, and polar components. In eq. (2.35), n_i are fluid specific coefficients which can be found for a number of different fluids in ref. [101-104]. The other variables are constants specific to just the Span-Wagner equations and are listed in the appendix in Table A.4 and Table A.5. The total reduced Helmholtz energy is found by summing the ideal gas and residual components. The derivative of the Span-Wagner residual component of Helmholtz energy with respect to density and temperature is given in eq. (2.36) and (2.37) respectively.

$$\alpha_\delta^R = \sum_{i=1}^{6} n_i \tau^{t_i} d_i \delta^{d_i-1} + \sum_{i=7}^{12} n_i \tau^{t_i} \delta^{d_i-1}\left(d_i - p_i \delta^{p_i}\right)\exp\left(-\delta^{p_i}\right) \tag{2.36}$$

$$\alpha_\tau^R = \sum_{i=1}^{6} n_i t_i \tau^{t_i-1} \delta^{d_i} + \sum_{i=7}^{12} n_i t_i \tau^{t_i-1} \delta^{d_i} \exp\left(-\delta^{p_i}\right) \tag{2.37}$$

Similar to the BACKONE equations, by using different combinations of temperature, density, Helmholtz energy, and its partial derivatives, all remaining thermodynamic properties can be determined.

2.2.3 Computational algorithms and schemes employed

From the Gibb's Phase Rule, pure fluids require only two properties to determine all other remaining intensive properties **[**109**]**. Equations of state explicit in Helmholtz energy are, as expected, functions of their natural variables: temperature and density. As such, the relationships presented thus far have all been predicated on the temperature and density at the particular state being known a priori. However, in power cycle analysis, property calculations from an initial known pair of properties other than temperature and density are often required. Common initial known property pairs from which all other remaining properties are determined from include temperature and pressure, pressure and enthalpy, pressure and entropy, pressure and vapor quality, and temperature and vapor quality; where vapor quality refers to the vapor mass or mole fraction. Determining the properties from an initially unknown temperature and/or density adds significant additional complexities for Helmholtz equations because an iterative solution is required **[**99**]**. Very often, the majority of the complications stem from determining initial guesses for temperature and density to start the iterative solving process. In the next sections, the methods to solve the Helmholtz-explicit equations of state from initially known property pairs other than temperature and density are developed. Where appropriate, the discussion includes how to determine properties in both the fluid's homogenous regions and its two-phase regions.

2.2.3.1 Solutions from a known Temperature and Pressure (T, P)

Single-phase property calculations from a known temperature and pressure require an initial guess of density to begin the iterative process. The initial starting estimate for density can be determined by solving a simpler, cubic equation of state such as the Redlich-Kwong-Soave equation **[**94**]**. The Redlich-Kwong-Soave equation has the general form of cubic equations shown in eq. (2.1) with $u = 1$, $w = 0$, and A and B defined by eq. (2.38) and (2.39), respectively **[**96**,**99**]**.

$$A = \frac{0.42748 R^2 T_c^2}{P_c}\left[1 + m\left(1 - \tau^{-1/2}\right)\right]^2 \tag{2.38}$$

$$m = 0.48 + 1.574\omega - 0.176\omega^2$$

$$B = \frac{0.08664 R T_c}{P_c} \tag{2.39}$$

Using the compressibility factor $Z = P/(\rho RT)$, the Redlich-Kwong-Soave equation can be rewritten in the form of eq. (2.40),

$$Z^3 - Z^2 + Z\left(A^* - B^* - B^{*2}\right) - A^* B^* = 0 \tag{2.40}$$

where $A^* = AP/R^2T^2$ and $B^* = BP/R$ **[**96**,**99**]** T. If the temperature and pressure are known a priori, Z can be solved for explicitly in eq. (2.40), yielding either one or three real roots. In the case of three real roots, the largest root is the vapor phase compressibility, the smallest root is the liquid phase compressibility, and the middle root has no real physical meaning **[**116**]**. To determine whether the liquid or vapor root is of interest, one must first determine whether the given temperature and pressure is in the liquid or vapor phase. This can be done by first determining the saturation pressure for the given temperature and then comparing it to the given pressure. If the given pressure exceeds the saturation pressure, the liquid phase root is used; if the given pressure is less than the saturation pressure, the vapor phase root is used. The saturation pressure P_{sat} as a function of temperature can be calculated from the well known and accurate Wagner equation, shown in eq. (2.41) [96,117-119],

$$P_{sat} = P_c \exp\left(\frac{T_c}{T}\sum_{i=1}^{4} W_i\left[1 - T/T_c\right]^{\Omega_i}\right) \tag{2.41}$$

where the constants W_i and Ω_i are fluid dependent constants that can be found in the literature. After comparing the Wagner equation with a variety of other vapor pressure equations, Reid et al. recommends the Wagner equation because it yielded reasonable estimates for reduced temperatures of 0.5 to the critical temperature and was found to be superior in all instances **[**96**]**.

Once the compressibility is known, the initial estimate for density $\rho_{est} = P/(ZRT)$ can be determined. With this initial guess, the iterative solving process can begin by solving for pressure using the Helmholtz equations with the given temperature and initial estimate for density. The residual r can be calculated using eq. (2.42), where P is the given known pressure and P_{calc} is the pressure calculated from the Helmholtz equation using the estimated density.

$$r(\rho) = P_{calc}(T, \rho) - P \tag{2.42}$$

Once the residual goes to zero or to an arbitrarily small value, convergence is achieved and the remaining thermodynamic properties can be solved for with the now known temperature, density, Helmholtz free energy, and its derivatives using the relations and methods outlined in section 2.1 and 2.2 **[**99**]**. Span recommends using the regula falsi or the false position method, shown in eq. (2.43), as the iterative algorithm to solve Helmholtz-explicit equations of state.

$$x_{j+1} = x_j - r(x_j)\frac{x_j - x_{j-1}}{r(x_j) - r(x_{j-1})} \tag{2.43}$$

The regula falsi method is preferred because, unlike the Newton-Raphson method, the regula falsi method does not require the derivative of the residuum which can be difficult to calculate analytically and slow to calculate numerically **[**99**]**. However, the regula falsi method does require two initial estimates of x for the iterative procedure to start. For single-phase property calculations starting from a known temperature and pressure, Span recommends for the two initial estimates for density: $\rho_{1,2} = \rho_{est}$ (1±0.05) **[**99**]**. The author, however, found the computational program to be much more stable for states far away from the critical point using $\rho_1 = \rho_{est}$ (1+0.25) and $\rho_2 = \rho_{est}$ (1-0.05). To guarantee convergence and improve stability, the modified regula falsi algorithm eq. (2.44) should be used instead of eq. (2.43) in instances when both $r(x_j)\cdot r(x_{j-1}) > 0$ and $r(x_j)\cdot r(x_{j-2}) < 0$.

$$x_{j+1} = x_j - r(x_j)\frac{x_j - x_{j-2}}{r(x_j) - r(x_{j-2})} \tag{2.44}$$

Fig. 2.1 on the following page shows a flow chart for the iterative solution process used to determine temperature and density from a known temperature and pressure. This computational algorithm is applicable for solving equations of state explicit in Helmholtz energy when only the temperature and pressure is known.

2.2.3.2 Solutions from a known Pressure and Enthalpy (P, h)

Prior to beginning the iterative procedure, it needs to be determined whether the state resides in the single or two-phase region. If the pressure is below the critical pressure, the saturation temperature T_{sat} is first solved using eq. (2.41) with the given pressure; this was done using the built-in iterative solver MATLAB function "fzero" **[**120**]**. The saturated liquid h_L and vapor enthalpy h_V were then determined by calculating the properties of the fluid at a temperature value just barely less than and greater than T_{sat} at the given pressure. Depending on if the value of the given enthalpy h is greater than the saturated vapor enthalpy, less than the saturated liquid enthalpy, or in between the saturated liquid and vapor enthalpies, then it can be concluded the state is in the vapor, liquid, or two-phase regime, respectively.

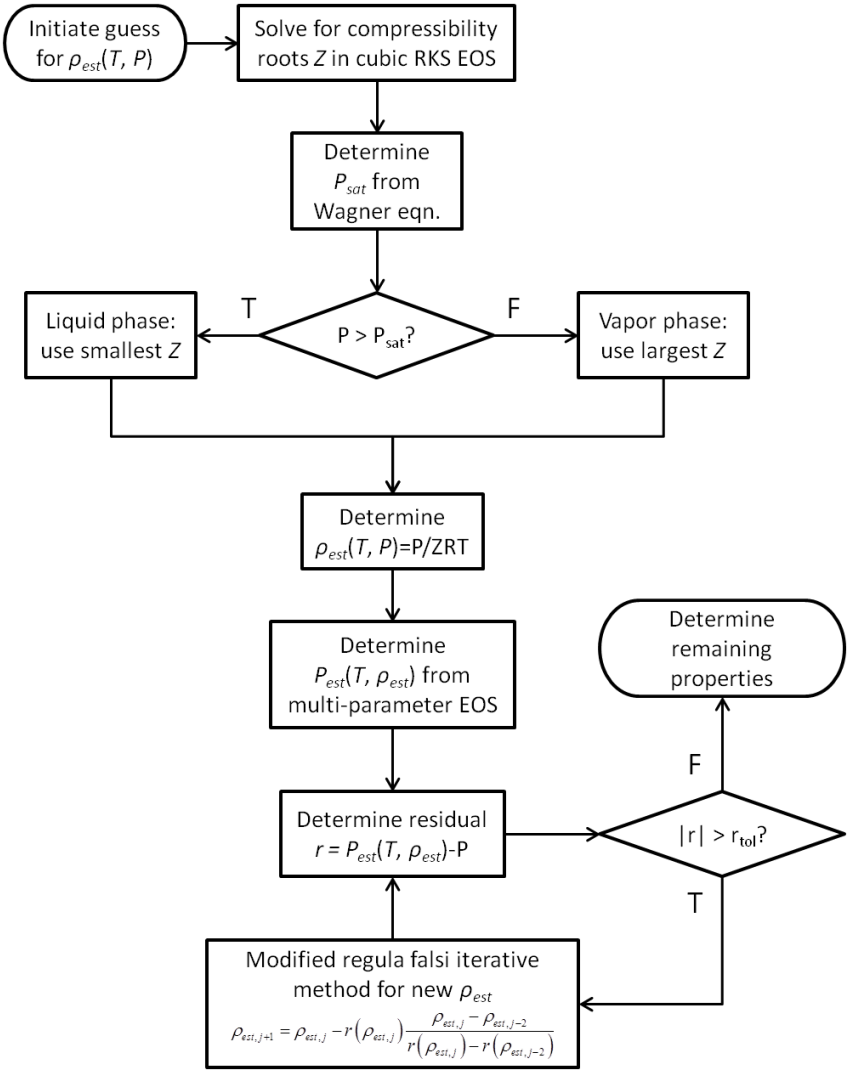

Figure 2.1: Flow chart for iterative solution process from a known temperature and pressure

If the state is in the two-phase regime, the fluid's equilibrium temperature is the saturation temperature that has already been calculated and the fluid's vapor quality q can be determined using eq. (2.45).

$$q = \frac{h - h_L}{h_V - h_L} \tag{2.45}$$

The density can then be calculated by using an analogous equation for volume, and rearranging to eq. (2.46).

$$\rho = \left(q\rho_V^{-1} + \left[1 - q\right]\rho_L^{-1} \right)^{-1} \tag{2.46}$$

Now that the temperature and density are solved for, the remaining thermodynamic properties are determined by using the methods described in sections 2.1 and 2.2.

If the state is in the single-phase state, a reasonable initial guess for temperature first needs to be obtained since the fluid is not necessarily at its saturation temperature. If the given pressure is greater than the fluid's critical pressure, $T_{est,0}$ can be determined by solving Van der Waals equation in eq. (2.47) using the given pressure and the critical density ρ_c **[**99**]**.

$$T_{est,0} = \frac{\left(P + a_{VDW}\rho_c^2\right)\left(\rho^{-1} - b_{VDW}\right)}{R} \tag{2.47}$$

Using temperature $T_{est,0}$ and the given pressure P, the corresponding enthalpy $h_{est,0}$ at can be determined using the procedure discussed in section 2.3.1. If the given enthalpy h is larger than $h_{est,0}$, then the actual temperature is greater than $T_{est,0}$, and vice versa. In either case, $T_{est,1}$ and each subsequent T_{est} needs to be calculated using eq. (2.48),

$$T_{est,i+1} = \left(1+\kappa\right)T_{est,i} \tag{2.48}$$

where Span recommends values κ = 0.2 for $h > h_{est,0}$ and κ = -0.1 for $h < h_{est,0}$ **[**99**]**. Bounds for temperature are needed; therefore, the procedure of using eq. (2.48) and calculating the corresponding $h_{est,i}$ is repeated until the product of the current and previous iteration's residual is less than zero, where the residual is defined in eq. (2.49) **[**99**]**.

$$r\left(T_{est,i}\right) = h_{est,i}\left(T_{est,i}, P\right) - h \tag{2.49}$$

Once $r(T_{est,i})\ r(T_{est,i-1}) < 0$, $T_{est,i-1}$ and $T_{est,i}$ are used as the two initial guesses to start the modified regula falsi algorithm, and the next iteration's estimate for temperature $T_{est,i+1}$ is determined by the modified regula falsi algorithm instead of eq. (2.48). Iterations for temperatures are continued until the residual reaches zero or an arbitrarily small number. For calculations from pressure and enthalpy described in this section, note that each iteration's solution for enthalpy from a given pressure and estimated temperature are determined from a complete iterative solution based on temperature and pressure (section 2.3.1) **[**99**]**; therefore, pressure and enthalpy calculations typically require longer times for convergence than calculations from temperature and pressure.

If the fluid is in the single-phase region and the given pressure is below the critical pressure, $T_{est,0}$ is taken to be the calculated saturation temperature. If $h>h_V$, the state is in the vapor region, h_V is used as $h_{est,0}$, and the actual temperature is greater than the saturation temperature; otherwise if $h<h_L$, the state is in the liquid region, h_L is used as $h_{est,0}$, and the actual temperature is less than the saturation temperature. For the former case, eq. (2.48) is used to determine the next iteration's estimated temperature with κ = 0.2. For the latter case, Span recommends using a self adapting step width in eq. (2.50), where T_{triple} is the fluid's triple point temperature **[**99**]**.

$$T_{est,i+1} = \left(1 - \frac{T_{sat}\left(P\right) - T_{triple}}{JT_{sat(P)}}\right) \tag{2.50}$$

Although Span recommends $J \approx 5$ as a reasonable value **[**99**]**, the author found that values of $J \approx 20$ provided greater stability and did not significantly increase computational time even though the step widths were smaller. Similar to $P>P_{crit}$ cases, the procedure of calculating the estimated temperature and the corresponding enthalpy $h_{est,i}$ is repeated until the temperature is bounded when $r(T_{est,i})\ r(T_{est,i-1}) < 0$, where r is determined from eq. (2.49). The modified regula falsi algorithm is then used to calculate $T_{est,i+1}$, and iterations repeat until the residual goes to zero or to an arbitrarily small number **[**99**]**. Once the solution converges, the known temperature and pressure can be used to determine all remaining properties using the algorithms and methods described in section 2.3.1. The computational algorithm for determining a solution from a known pressure and enthalpy is summarized in the flowchart shown in Fig. 2.2.

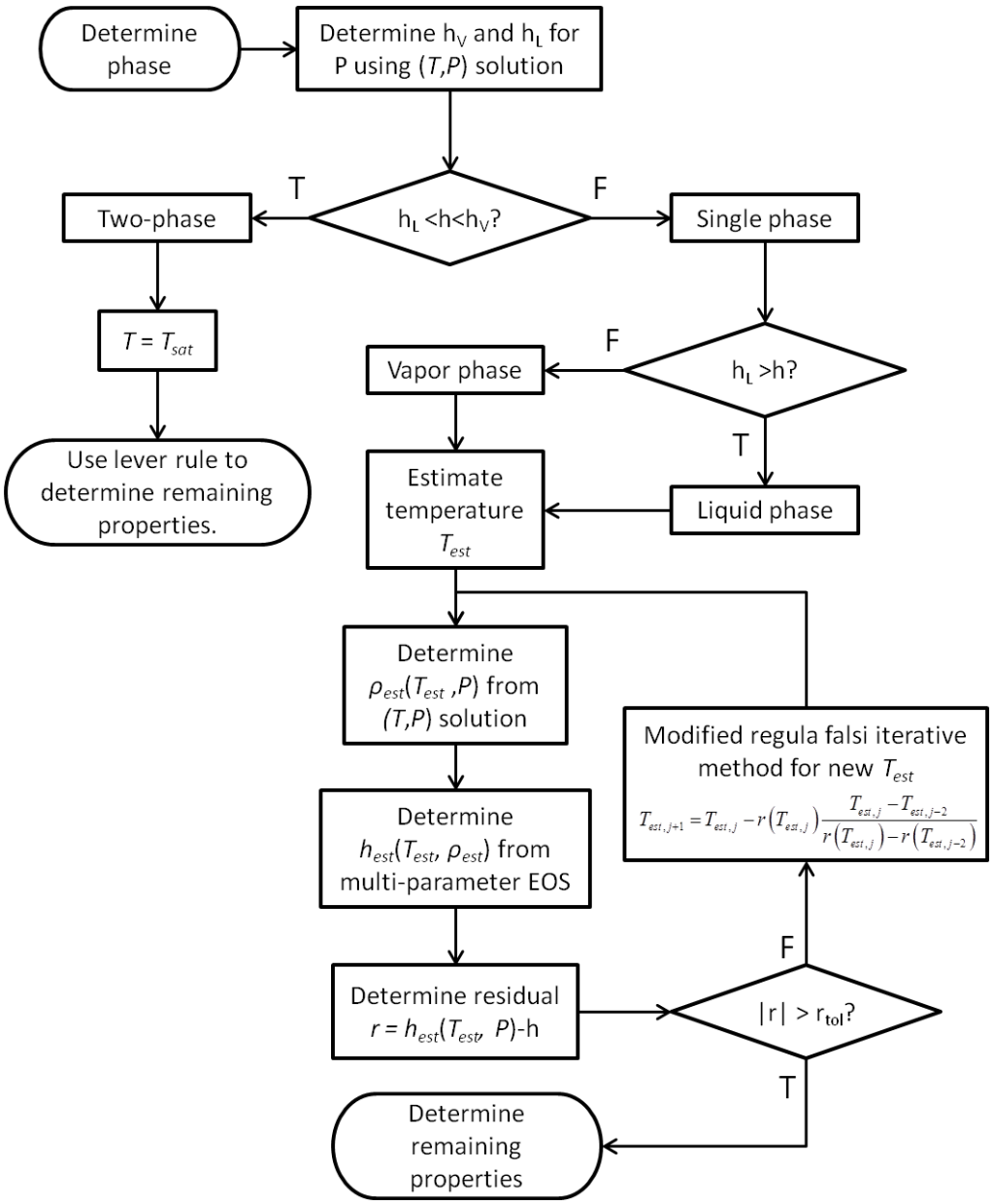

Figure 2.2: Flow chart for iterative solution process from a known pressure and enthalpy

2.2.3.3 Solutions from a known Pressure and Entropy (P, s)

The method and algorithms for property calculations from a known pressure and entropy are very similar to those in section 2.3.2 for a known pressure and enthalpy. In fact, the equations from section 2.3.2 can be used with enthalpy being replaced with entropy. The flow chart for this computational algorithm would also be more or less the same as for Fig. 2.2, with enthalpy replaced with entropy. The residual in eq. (2.49) now becomes eq. (2.51) for calculations from a known pressure and entropy **[**99**]**.

$$r\left(T_{est,i}\right) = s_{calc}\left(T_{est,i}, P\right) - s \tag{2.51}$$

If the pressure is below the critical pressure, the conditions for the liquid and vapor phase are the same as before, such that if $s>s_V$ the fluid is in the vapor state, if $s<s_L$ the fluid is in the liquid state, and if $s_L<s<s_V$ the fluid is in the two-phase region. The same equations in section 2.3.2 can be used to perform the iterations required for bounding the temperature. Afterwards, the two temperature bounds are used in the modified regula falsi algorithm to solve for the temperature of that state. Lastly, the given pressure and solved temperature are used to solve for the remaining thermodynamic properties using the methods described in section 2.3.1 **[**99**]**.

2.2.3.4 Solutions from known Temperature/Quality (T,q) or known Pressure/Quality (P,q)

For a known temperature and quality, it is concluded that the state is in the two-phase region. The pressure can be calculated using the Wagner equations, because the equilibrium pressure in the two-phase region is the vapor pressure of the fluid. The saturated liquid and vapor properties can then be determined using the procedure described in section 2.3.2 for states in the two-phase regime. Using the lever rule **[**4**]**, the remaining thermodynamic properties can be calculated.

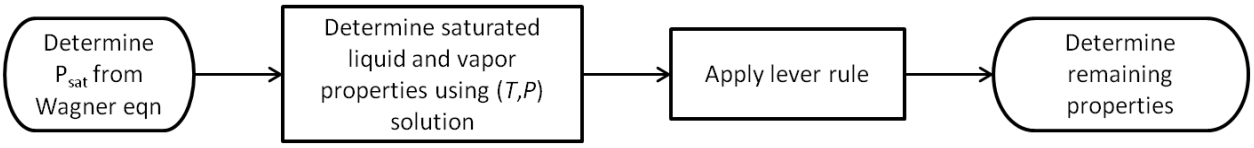

Figure 2.3: Flow chart for solution from known temperature or pressure and quality

For a known pressure and quality, the solution method is very similar. The saturation temperature can be found by iteratively by solving the Wagner saturated pressure equation, eq. (2.41). The saturated liquid and vapor properties would then again be determined using the procedure outlined above and the lever rule would then be applied to determine the liquid-vapor mixture properties. The flow chart for this computational algorithm is shown in Fig. 2.3.

2.3 Results – Comparison of the BACKONE and Span-Wagner equations to NIST Reference equations of state

The objective of using the BACKONE equations and Span-Wagner equations in this present study is to expand the number of possible working fluids that could be included in the analysis of vapor power cycles for a wide range of finite thermal energy reservoirs. Therefore, the BACKONE and Span-Wagner equations need to be verified for their reliability and accuracy with available reference data. In this study, results generated from NIST Chemistry WebBook

[121**]** are taken as the reference data and compared with results obtained from the BACKONE and Span-Wagner equations. A sample of different siloxanes, aromatic hydrocarbons, alkanes, and refrigerants were used to compare data from the NIST Chemistry WebBook to the predictions from the Helmholtz-explicit equations of state for saturated liquid and vapor densities, and vapor pressure. The selected fluids and are listed in Table 2.1.

Table 2.1: Select working fluids for comparison to NIST Chemistry WebBook

Fluid Type	Fluid	Equation of State	Reference
Siloxanes	MD4M (tetradecamethylhexasiloxane)	Span-Wagner	**[**99**,**103**]**
	D5(decamethylcyclopentasiloxane)		**[**99**,**103**]**
	MD3M (Dodecamethylpentasiloxane)		**[**99**,**104**]**
	D6 (Dodecamethylcyclohexasiloxane)		**[**99**,**104**]**
	MM (hexamethyldisiloxane)		**[**99**,**103**]**
	D4 (Octamethylcyclotetrasiloxane)		**[**99**,**103**]**
Aromatic Hydrocarbons	toluene	BACKONE	[97-99,108]
	ethylbenzene		[97-99,108]
	butylbenzene		[97-99,108]
	o-xylene		[97-99,108]
	m-xylene		[97-99,108]
	p-xylene		[97-99,108]
Alkanes	pentane	BACKONE	[97-99,107]
	butane		[97-99,107]
	cyclopentane		[97-99,107]
	cyclohexane		[97-99,107]
	hexane		[97-99,107]
Refrigerants	R113	Span-Wagner	[99-102]
	R123	Span-Wagner	[99-102]
	R141b	BACKONE	[97-99,107]
	R245ca	BACKONE	[97-99,107]

Siloxanes and aromatic hydrocarbons have high critical temperatures and are considered for high or intermediate temperature energy resources. Alkanes and refrigerants have lower critical temperatures and therefore would be considered for low temperature thermal resources. Temperatures below 300K are not expected to be encountered as the heat sink available is assumed to be near ambient conditions. For the fluids using the BACKONE equations, all the selected aromatic hydrocarbons and alkanes are at least quadrupolar; whereas R245ca and R141b exhibit both dipole and quadrupole moments. The percent error between the BACKONE or Span-Wagner predictions and from the NIST Chemistry WebBook for saturated liquid and vapor densities and vapor pressure are plotted for the siloxanes in Fig. 2.4, 2.5, and 2.6; aromatic hydrocarbons in Fig. 2.7, 2.8, and 2.9; alkanes in Fig. 2.10, 2.11, and 2.12; and refrigerants in Fig. 2.13, 2.14, and 2.15; respectively.

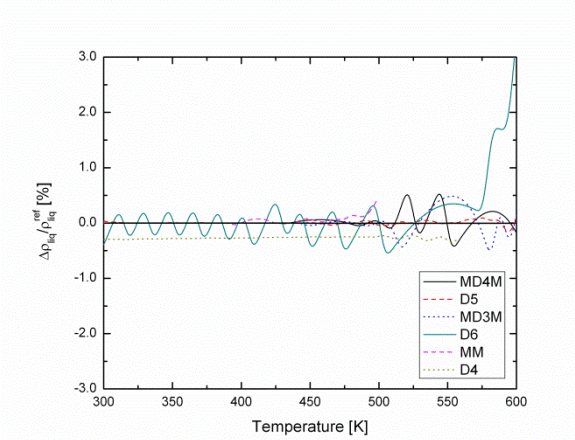

Figure 2.4: Percent difference in saturated liquid density between Span-Wagner and NIST Chem WebBook for select siloxanes.

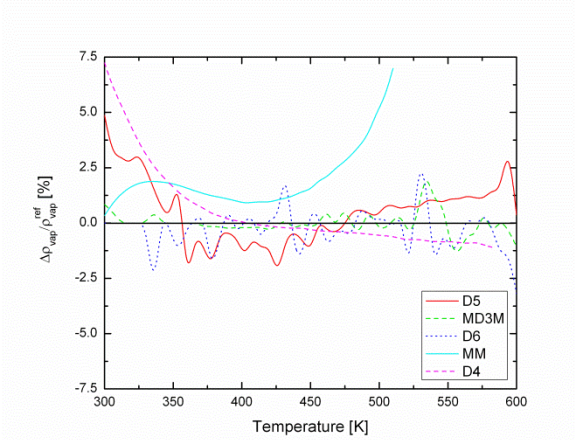

Figure 2.5: Percent difference in saturated vapor density between Span-Wagner and NIST Chem WebBook for select siloxanes.

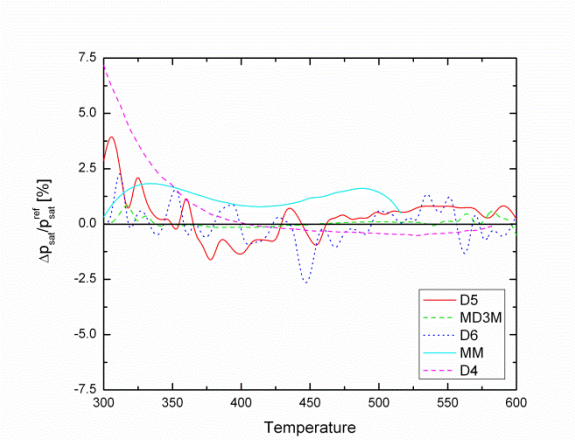

Figure 2.6: Percent difference in vapor pressure between Span-Wagner and NIST Chem WebBook for select siloxanes.

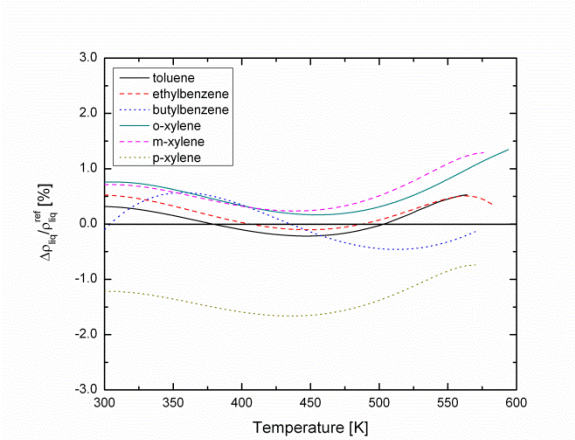

Figure 2.7: Percent difference in saturated liquid density between BACKONE and NIST Chem WebBook for select aromatic hydrocarbons.

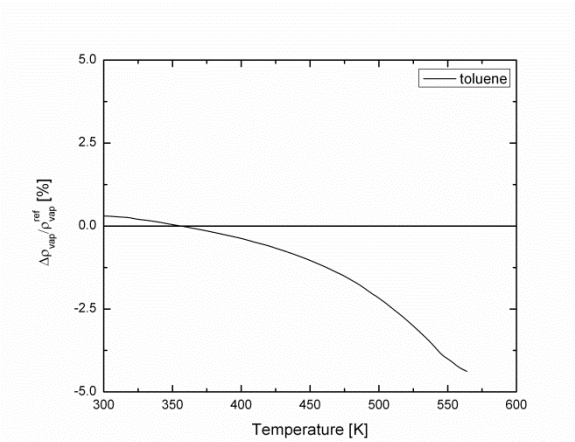

Figure 2.8: Percent difference in saturated vapor density between BACKONE and NIST Chem WebBook for select aromatic hydrocarbons.

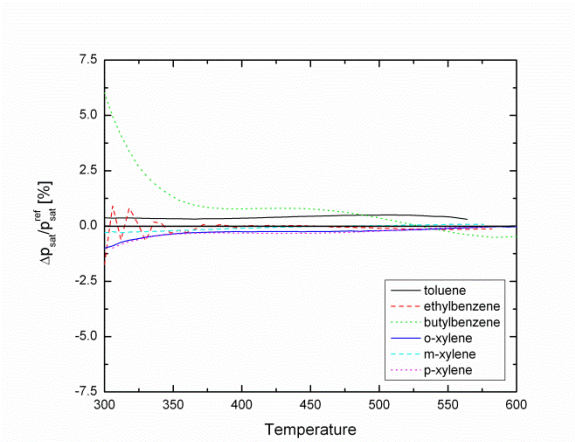

Figure 2.9: Percent difference in vapor pressure between BACKONE and NIST Chem WebBook for select aromatic hydrocarbons.

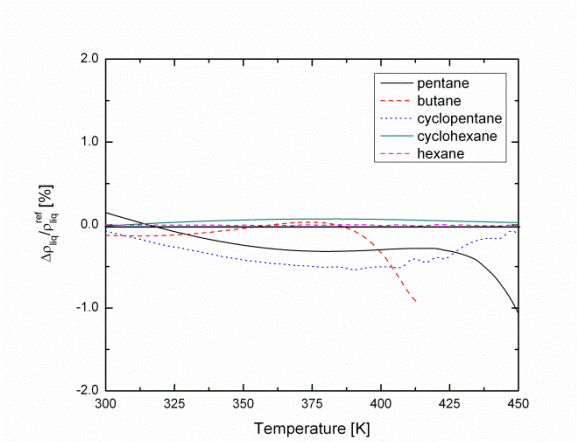

Figure 2.10: Percent difference in saturated liquid density between BACKONE and NIST Chem WebBook for select alkanes.

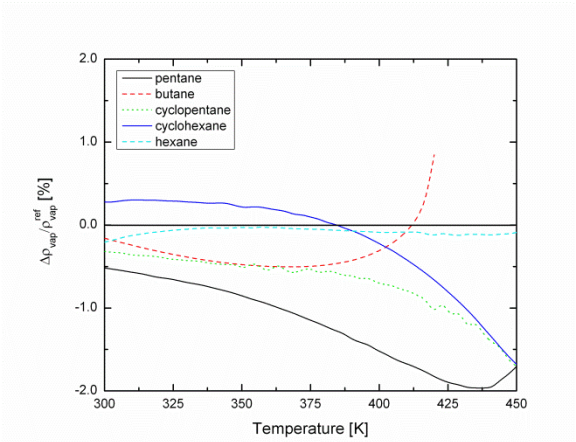

Figure 2.11: Percent difference in saturated vapor density between BACKONE and NIST Chem WebBook for select alkanes.

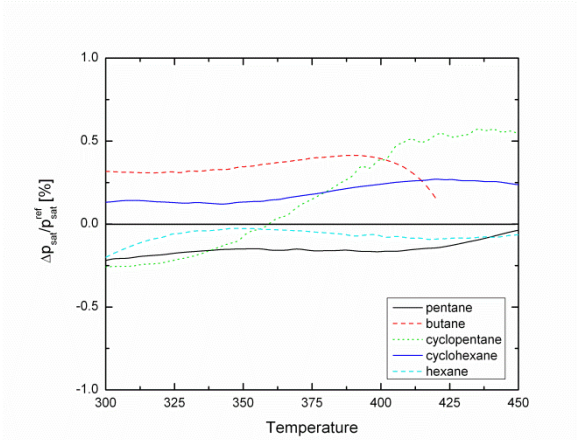

Figure 2.12: Percent difference in vapor pressure between BACKONE and NIST Chem WebBook for select alkanes.

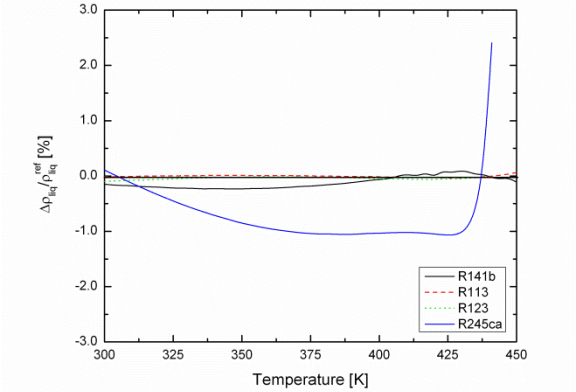

Figure 2.13: Percent difference in saturated liquid density between Helmholtz-explicit EOS and NIST Chem WebBook for select refrigerants.

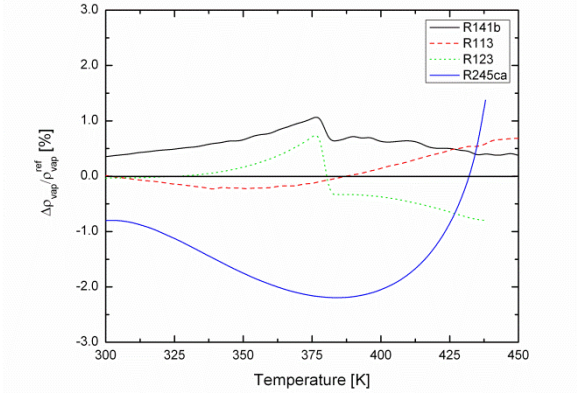

Figure 2.14: Percent difference in saturated vapor density between Helmholtz-explicit EOS and NIST Chem WebBook for select refrigerants.

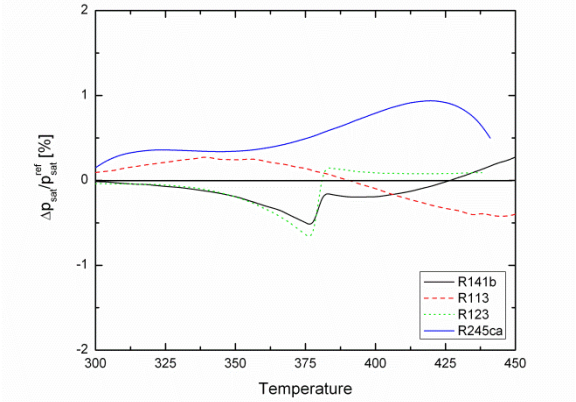

Figure 2.15: Percent difference in vapor pressure between Helmholtz-explicit EOS and NIST Chem WebBook for select refrigerants.

Fig. 2.4, 2.7, 2.10, and 2.13 show that for the temperature ranges examined, the maximum percent difference between the predicted saturated liquid density predicted by Helmholtz-explicit EOS and that from the NIST Chem WebBook was limited to ±3%. The greatest percent errors were seen for siloxanes; however, it should be noted that the data listed in NIST Chem WebBook for siloxanes had considerably large uncertainties associated with the listed saturated liquid and vapor densities and vapor pressure values **[**121**]**. For the selected aromatic hydrocarbons besides toluene, the NIST Chem WebBook did not have saturated liquid or vapor densities listed. Using a known experimental density $\rho^R_{s,L}$ at a reference temperature T^R, eq. (2.52) and (2.53) can be used to estimate saturated liquid density **[**31**]**.

$$\rho_{s,L} = \rho^R_{s,L}\left(0.29056 - 0.08775\omega\right)^{\phi} \tag{2.52}$$

$$\phi = \left(1 - T/T_c\right)^{2/7} - \left(1 - T^R/T_c\right)^{2/7} \tag{2.53}$$

From Fig. 2.5, 2.8, 2.11, and 2.14 show the maximum percent difference between saturated vapor density values predicted by the Helmholtz-explicit EOS and the NIST Chem WebBook to be less than ±7.5%. Aside from toluene, the NIST Chem WebBook again did not list saturated vapor density values for the selected aromatic hydrocarbons. To the author's knowledge, there exists no simple correlation similar to eq. (2.52) and (2.53) for saturated vapor density; therefore, only a comparison for toluene can be drawn. Fig. 2.6, 2.9, 2.12, and 2.15 show that the maximum percent difference between the saturated vapor pressure was limited to within ±7.5%. The sharp step shown in Fig. 2.14 and 2.15 for the R141b and R123 curves near 380K is due to the transition from using the Antoine equation to the Wagner equation to calculate vapor pressure. Antoine-type equations often take the form shown in eq. (2.54) where *A*, *B*, and *C* are empirical constants.

$$\ln P_{sat} = A - \frac{B}{T - C} \tag{2.54}$$

This method of using several vapor pressure equations is recommended when a single correlation is not available to cover the entire range of pressures of interest **[**31**]**.

Results showed that the Helmholtz-explicit equations became less accurate near the critical region and for reduced temperatures below 0.60; this is expected as the Wagner equations used to predict the vapor pressure are reasonable only down to reduced temperature of 0.5 **[**96**]**. For almost all equations of state, the greatest difficulties encountered are often accurately predicting properties near the critical point. To improve the accuracy in the critical region, some Helmholtz equations of state utilize so called modified Gaussian Bell shaped terms **[**99**]**. However, the analysis in this present study examines only subcritical vapor cycles; therefore, the presently examined equations are suitable for this analysis as states in the critical region will not be encountered in this study. For analyzing transcritical vapor cycles though, an equation of state that includes Gaussian Bell shaped terms to increase accuracy in the critical region would most likely need to be employed.

Using the BACKONE and Span-Wagner equations, a simple thermodynamic analysis can be conducted on an ideal simple vapor cycle shown in Fig. 2.16 that rejects heat to a thermal reservoir at 30^{o}C (303K). Results for the first laws efficiency η, the ratio of net work to heat

input, are compared to values obtained using NIST REFPROP. Note that no siloxanes and most of the aromatic hydrocarbons are included in this comparison as REFPROP 8.0 did not include these fluids in its database. NIST REFPROP has been verified to be highly accurate; the maximum uncertainties for density and vapor pressure obtained from the equations of state used in REFPROP are listed in Table A.6 of Appendix A for a representative sample of fluids **[**92**]**. Assuming no superheating prior to expansion, Fig. 2.17 shows the percent difference in first law efficiency for turbine inlet temperatures T_3 from 80°C (353K) to $0.96T_{crit}$.

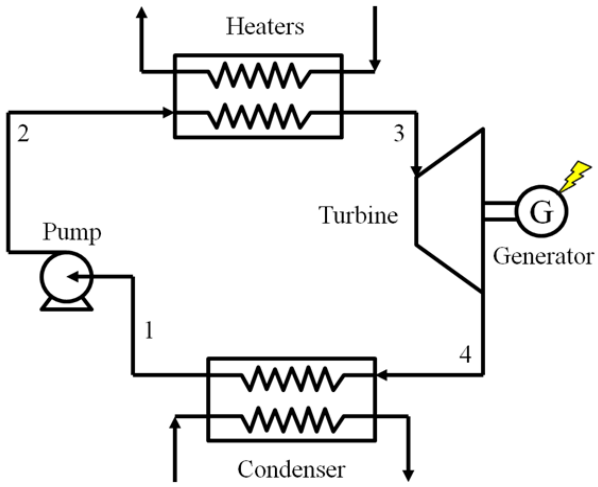

Figure 2.16: Schematic of ideal simple vapor cycle.

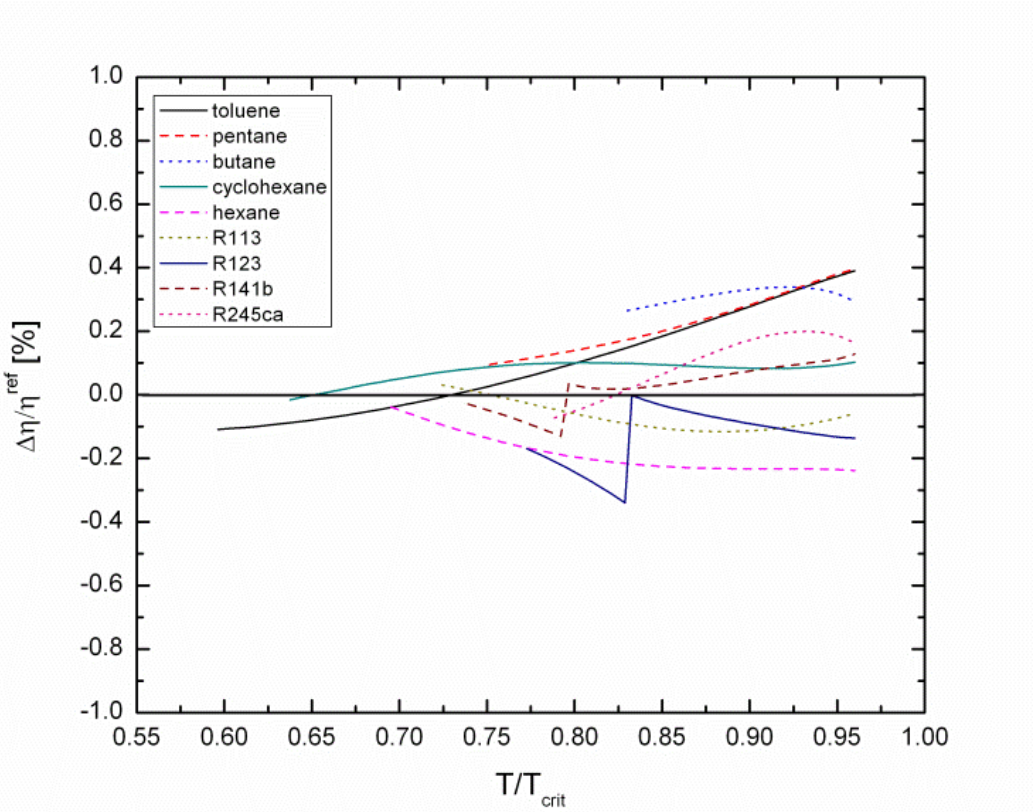

Figure 2.17: 1st Law efficiency percent difference for ideal simple vapor cycle.

As shown in Fig 2.17, the calculated values for efficiency determined from the Helmholtz-explicit EOS are all within ±0.4% of that calculated from REFPROP. The prominent step change seen for R123 and R141b can again be attributed to switching to the Wagner vapor equation from the Antoine equation, since multiple vapor pressure equations were used for these two fluids. For molecules exhibiting more complex polar interactions than dipole and quadrupole, the BACKONE equations may have difficulty adequately modeling the fluid behavior. It's likely that more sophisticated or fluid specific equations of state with more polynomial and exponential terms in the residual will be required, because the BACKONE equations are not capable of describing the complex polar molecular interactions. Similarly, the Span-Wagner equation has 12 residual terms and has been used to describe nonpolar and weakly polar molecules.

2.4 Conclusions

Modern equations of state explicit in Helmholtz energy, such as the BACKONE equations, provide a method to accurately predict thermodynamic property data for various states. Although significantly more complex than cubic equations, both in form and computational schemes, Helmholtz equations provide much higher accuracy in the high pressure regions, liquid regions, and two-phase regions and also can be extended to accurately describe polar fluids. It was shown that the BACKONE equations, in conjunction with the Wagner equations, are capable of describing nonpolar, dipolar, and quadrupolar fluids with high accuracy for reduced temperatures of 0.65 to 0.96. For the present study concerning subcritical vapor power cycles, the BACKONE and Span-Wagner equations greatly expands the number of fluids beyond those in the REFPROP library that can be investigated. Results showed the BACKONE and Span-Wagner equations provided good to excellent agreement to reference equations of state from REFPROP. In addition, due to the physical basis of the BACKONE and Span-Wagner equations, there is a potential that physical insight can be gained through examining why certain working fluids outperform others.

3 The Organic Flash Cycle (OFC) for energy conversion of intermediate temperature finite thermal resources

3.1 Introduction and description of relevant intermediate temperature heat sources

The inclusion of electricity production from energy sources beyond conventional fossil fuels will become inevitably necessary in order to meet increasing global energy demands. Efficient and cost-effective utilization of renewable energy sources such as solar thermal and geothermal energy will lessen the reliance on fossil fuels and reduce the emission of pollutants and potential climate changing agents. In addition, greater care must be taken to improve efficiency of all processes and reduce the amount of energy that is wasted or unused. In many industries such as the ceramic [122], cement [123-125], metallurgical [126], paper and pulp [127,128], food and beverage, and oil refining industries [128], process heat containing significant amounts of energy is vented and lost to the environment. This high quality waste energy though has the potential to be efficiently converted to electricity; doing so would reduce thermal pollution and overall plant operating costs as the electricity generated from the waste heat could be used to at power the plant itself or be sold back to the grid. In addition to industrial processes, energy from the exit stream of gas turbines in high temperature Brayton cycles could also be used to generate electricity; in fact, utilizing this energy is the premise in many combined cycle plants [26,129]. These sources of thermal energy are often termed "finite thermal energy reservoirs" because the source temperature decreases dramatically as heat is transferred to the power cycle.

In addition to the aforementioned waste heat sources, one-axis concentrating solar thermal (collectors such as linear Fresnel lens and parabolic troughs) and high grade geothermal energy are also in the temperature range of 200-400^{o}C [26,122-126,128-131]. For applications in this temperature range, vapor cycles are the most suitable power cycle [13]; however, the traditional steam working fluid is unsuitable for low temperature energy sources below 370^{o}C due to a number of complications that include high turbine volumetric flow ratios, low vapor pressures in the condenser, and low thermal efficiencies caused by low boiler pressures that are required for superheating the steam and avoiding moisture from forming during the final expansion stages in the turbine [13,19,24,132]. High volume flow ratios requires larger, more complicated, and more expensive turbines; low vapor pressures in the condenser requires deaerators to remove air that leaks into the system [13]. Liquid droplets and moisture forming in the turbine during expansion erodes and damages the turbine blades [13,15]; aside from expensive, reinforced blades being necessary, it is also known that turbine isentropic efficiency decreases linearly with the fluid's average moisture content as specified by the so-called "Baumann rule" [15]. Organic working fluids on the other hand can overcome many of these obstacles and have been utilized in the Organic Rankine Cycle (ORC). Organic fluids have turbine volume ratios that can be an order of magnitude smaller than steam [19], they have higher vapor pressures compared to steam [13], and because the majority of them are "dry" or "isentropic" fluids they do not require superheating prior to expansion in order to avoid droplet formation in the turbine [19,22]. "Dry" and "isentropic" fluids exhibit a positively or infinitely sloped saturated vapor curve respectively on a T-S diagram. Unlike "wet" fluids like water that have a negatively sloped vapor curve, isentropic expansion from a saturated vapor state for "dry" and "isentropic" fluids will always result in a saturated vapor or superheated vapor; therefore, no liquid droplets are expected to form [22,36,37].

One major challenge for ORCs is temperature matching while the thermal energy source stream transfers energy to the ORC working fluid stream. Temperature matching to the source stream during heat addition is important in minimizing the irreversibilities caused by heat transfer across a finite temperature difference **[**33**,**34**]**. When using the ORC to produce electricity from a finite thermal reservoir though, temperature mismatching often is inevitable because the source stream is single-phase and possesses a near linear temperature profile along the heat exchanger. For an ORC employing a pure working fluid though, the fluid is heated first as a liquid, then vaporized, and if necessary, further superheated as a vapor. The resulting temperature profile along the heat exchanger for the ORC will first be near linear, then constant during phase change, and then near linear again. This temperature mismatching between streams is ultimately the largest source of the cycle irreversibility and lost exergy (potential work) **[**133**]**. This has led to much research into innovative methods to produce closer temperature matches between the energy source and working fluid. A comprehensive review of many of these proposed methods can be found in ref. [9,22]; they include the transcritical and supercritical ORCs and CO_2 Rankine cycles [49,78,134], zeotropic Rankine cycles **[**36**,**37**]**, the Kalina cycle [41,54], and the Trilateral Flash Cycle **[**69**]**. Two of the more often suggested methods are adding heat while the fluid is above the critical pressure or using a multi-component mixture working fluid instead of a pure one component fluid. In the former case isothermal phase change is avoided because heat addition occurs above the critical pressure and the fluid avoids the vapor dome completely; in the latter case, during phase change the working fluid mixture also changes temperature because the different components of the mixture vaporize at different temperatures for a common pressure.

3.2 Description of the Organic Flash Cycle (OFC)

In **Error! Reference source not found.** 3.1, a basic ORC plant layout and its temperature-entropy (T-S) diagram are shown again for convenience. Also shown are the T-S diagrams for a Rankine cycle using a zeotropic mixture and for a transcritical Rankine cycle. A schematic of the proposed OFC configuration and its T-S diagram are shown in Figure 3.2.

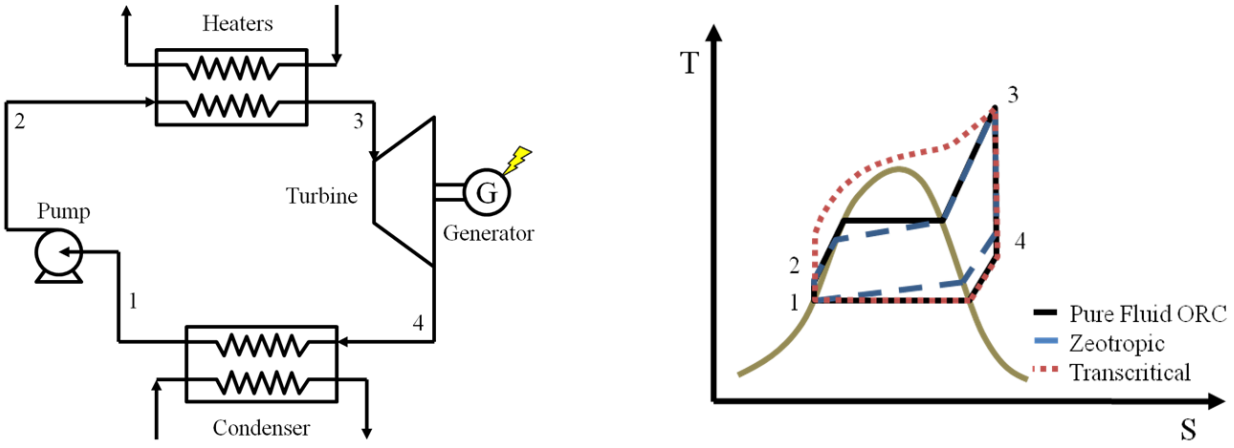

Figure 3.1: Plant schematic and T-S diagram for basic pure fluid ORC, zeotropic Rankine cycle, and transcritical Rankine cycle [9].

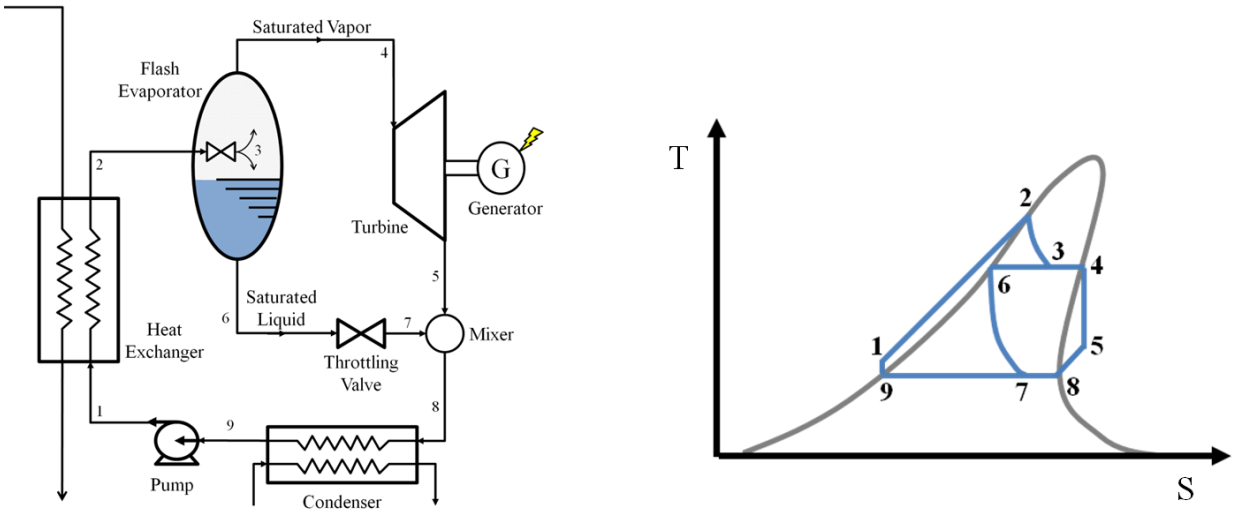

Figure 3.2: Plant schematic and T-S diagram for Single Flash OFC [9].

Note that in **Error! Reference source not found.** a "wet" fluid had been assumed, as the slope of the saturated vapor curve is negative, whereas in Figure 3.2, a "dry" fluid has been assumed as the slope of the saturated vapor curve is positive. It can be seen from Figure 3.2 that the OFC design is only slightly more complex than the basic Rankine cycle. The OFC brings the saturated liquid working fluid at a low pressure at state 9 to a high pressure at state 1 as shown in Figure 3.2 using a feed pump. In reality, state 9 would be slightly subcooled to prevent pump cavitation. Next, from states 1 to 2, the high pressure liquid absorbs heat from the finite thermal source and is then throttled, or flash evaporated, to a lower pressure liquid-vapor mixture at state 3. The mixture is separated into its saturated vapor and liquid components at states 4 and 6, respectively. From states 4 to 5, the saturated vapor is expanded to the condensing pressure and work is extracted. The saturated liquid is brought to the condenser pressure using a throttling valve from states 6 to 7. The liquid and vapor are then recombined in the mixer and then condensed back to a low pressure saturated liquid from states 8 to 9. It should be noted that energy in the saturated liquid can be further utilized by using an internal heat exchanger (IHE) as is often done in ORCs **[**37**]**. The flashing process could also be performed in two steps to extract more work; this is sometimes done in higher temperature geothermal plants to boost power output **[**15**]**.

3.3 Methods of analysis

3.3.1 Equations of state

To determine the thermodynamic properties of different working fluids, accurate equations of state are necessary. Since increases in efficiency by even just a few percent is important, simple equations of state such as cubic ones do not possess enough accuracy for analysis in this study. Instead a combination of modern equations of state such as the semi-empirical BACKONE equations **[**97**,**98**]**, the multi-parameter Span-Wagner equations **[**99**,**103**,**104**,**135**]**, and the equations of state compiled in REFPROP 8.0 **[**92**]** were employed to determine thermodynamic states and property data. A detailed discussion of Helmholtz-explicit equations of state is given in Chapter 2; for convenience a brief overview of these equations of state are presented here.

The BACKONE and Span-Wagner equations of state are explicit in Helmholtz energy and are functions of density and temperature; they can also be cast into the general form shown in eq. (3.1) **[**99**]**,

$$\frac{a(T,\rho)}{RT} = \alpha(T,\rho) = \alpha^0 + \alpha^R \tag{3.1}$$

where a is the Helmholtz free energy, R is the universal gas constant, T is temperature, ρ is density, and α, α^0, and α^R are the total, ideal gas component, and residual component of the reduced Helmholtz energy. The ideal gas portion of the reduced Helmholtz energy is well known and given in eq. (3.2) **[**99**,**110**]**,

$$a^0 = \frac{h^0_{ref}\tau}{RT_0} - 1 + \ln\left(\frac{\delta\tau_{ref}}{\delta_{ref}\tau}\right) - \frac{s^0_{ref}}{R} - \frac{\tau}{R}\int_{\tau_{ref}}^{\tau}\frac{c^0_p}{\tau^2}d\tau + \frac{1}{R}\int_{\tau_{ref}}^{\tau}\frac{c^0_p}{\tau}d\tau \tag{3.2}$$

where h is enthalpy, s is entropy, the subscript *ref* denotes the property at an arbitrary reference state, and $c_p{}^0$ is the ideal gas isobaric heat capacity, which can be determined theoretically from statistical thermodynamics or, as was done in this study, it can be approximated using power law correlations that are available for a number of fluids in ref. **[**96**,**103**,**104**,**135**]**. τ and δ are inverse reduced temperature and reduced density and are given in eq. (3.3),

$$\tau = T_0/T; \qquad \delta = \rho/\rho_0 \tag{3.3}$$

where T_0 and ρ_0 are a fluid specific characteristic temperature and density. The residual portion of the reduced Helmholtz energy can be cast in the general form shown in eq. (3.4),

$$\alpha^R(\tau,\rho) = \sum_{i=1}^{I_{pol}} n_i \tau^{t_i}\delta^{d_i} + \sum_{i=I_{pol}+1}^{I_{pol}+I_{exp}} n_i \tau^{t_i}\delta^{d_i}\exp\left(-g_i\delta^{p_i}\right) \tag{3.4}$$

where n_i, t_i, d_i, g_i, and p_i are constants dependent on the specific Helmholtz-explicit equation of state selected and I_{pol} and I_{exp} are the number of polynomial and exponential terms, respectively **[**99**]**. The BACKONE equations are termed semi-empirical as they possess some theoretical basis to the residual contribution. For the BACKONE equations, the residual contribution is further split into contributions from the hard body repulsive forces using perturbation theories, the attractive-dispersive intermolecular forces for nonpolar molecules, and a term accounting for dipolar or quadrupolar interactions for polar molecules [97-99]. The Span-Wagner equations are empirical multi-parameter equations of state that utilize optimized empirical data to determine the coefficients in eq. (3.4) **[**99**,**103**,**104**,**135**]**.

Thermodynamic properties such as pressure, enthalpy, entropy, etc. can be determined directly from a combination of temperature, density, Helmholtz energy, and partial derivatives of Helmholtz energy with respect to temperature and/or density. The derivations of these and other thermodynamic properties are covered in great detail in chapter 2 and in ref. **[**99**]**. Due to the Helmholtz energy being defined in terms of its natural variables of density and temperature, determining thermodynamic states from other combinations of properties such as temperature

and pressure or pressure and enthalpy requires complicated iterative procedures. Examples of some of the iterative techniques often used are also discussed in chapter 2 and ref. **[**99**]**. For the working fluids considered in this study, the authors verified the calculated vapor pressure and saturated liquid and vapor density values from the BACKONE and Span-Wagner equations by comparing with values given on the online NIST Chemistry WebBook as shown in the previous chapter **[**121**]**. For the conditions of interest, excellent agreement was obtained between the NIST data tables and the equations of state utilized in this study. The BACKONE and Span-Wagner equations of state have also been utilized in several other advanced vapor cycle studies in the literature [19,24,25].

Besides the BACKONE and Span-Wagner equations, NIST REFPROP 8.0 is also utilized in this study. In REFPROP 8.0, thermodynamic properties can be calculated for a large number of refrigerants and hydrocarbons typically used in combustion and refrigeration processes. Depending on the selected working fluid, the program will either apply an equation of state explicit in Helmholtz energy, the modified Benedict-Webb-Rubin equation of state, or an Extended Corresponding States (ECS) model **[**92**]**. The equations of states utilized in REFPROP are all highly accurate and have been incorporated in other ORC investigations in the literature as well **[**34**,**36**,**129**]**. EES is also another often used computational tool that compiles equations of state for ORC design and other technical applications [77,78].

3.3.2 Thermodynamic analysis and efficiency definitions

One thermodynamic property that is particularly useful in power analysis is potential work or exergy χ, defined in eq. (3.5),

$$\chi = h - T_d s \tag{3.5}$$

where the subscript *d* designates the property at the dead state [**4**]. The dead state in this study is taken to be the conditions of the ambient environment. Two parameters that are often used to determine power cycle effectiveness are the first law and internal second law efficiencies defined in eq. (3.6) and (3.7) respectively,

$$\eta_I = W_{net} / Q_{add} \tag{3.6}$$

$$\eta_{II,\text{int}} = \frac{W_{net}}{\dot{m}_f \left(\chi_{f,out} - \chi_{f.in} \right)} \tag{3.7}$$

where W_{net} is the net power produced by the cycle, Q_{add} is the heat transfer rate during the heat addition process, $\dot{m}_f$ is the working fluid flow rate, and $\chi_{f,in}$ and $\chi_{f,out}$ are the working fluid exergy before and after heat addition, respectively. From eq. (3.6) and (3.7), it is noted that η_I is the ratio of net work produced to the heat added, whereas $\eta_{II,int}$ is the ratio of the net work produced to the potential work added. However these parameters do not completely quantify how well a cycle performs in applications such as waste heat reclamation or as a bottoming cycle for high temperature solar thermal if the energy in the thermal energy source stream is discarded or unused. This unused exergy in the source stream is known as "lost exergy" **[**76**]**. In applications where the energy from the source stream is not used further after transferring heat to the power

cycle, the primary objective is to maximize the amount of heat transferred to the power cycle from the source stream and simultaneously maximize the power produced from this transferred energy. The 1st law and internal 2nd law efficiencies, however, only consider how efficient the cycle is with respect to producing work from a given amount of energy or exergy that it absorbs. These parameters do not consider how effective the cycle is at absorbing the energy or exergy from the thermal source. Therefore, a power cycle could have very high 1st and internal 2nd law efficiencies, but produce little power because not much energy is absorbed from the thermal source. In some applications such as combined heat and power, energy in the finite thermal heat source needs to be used conservatively because it is to be used further after transferring heat to the power cycle. In such a case, the efficiency parameter of primary interest is the external 2nd law efficiency shown in eq. (3.8); note this efficiency is similar to the internal 2nd law efficiency but it also accounts for the exergy destruction due to heat transfer across a finite temperature difference from the source to the power cycle.

$$\eta_{II,ext} = \frac{W_{net}}{\dot{m}_s \left(\chi_{s.in} - \chi_{s,out} \right)} \tag{3.8}$$

In many waste heat applications though, where energy left in the source stream is discarded or unused after heat is transferred to the vapor cycle, a more appropriate parameter is the utilization efficiency ε, defined in eq. (3.9) **[**15**,**76**,**136**,**137**]**,

$$\varepsilon = \frac{W_{net}}{\dot{m}_s \left(\chi_{s,in} - \chi_{s,d} \right)} \tag{3.9}$$

where $\dot{m}_s$ represents the source flow rate, $\chi_{s,in}$ is the source's inlet exergy, and $\chi_{s,d}$ is the source's exergy at the dead state. Note that in defining the utilization efficiency in eq. (3.9), the source's exergy at the dead state is used rather than the source's exergy at the exit of the heat exchanger. This parameter is appropriate when assuming that after the source stream has transferred heat to the vapor cycle for power production, whatever remaining exergy from the source stream goes unused and is eventually lost to the environment. This is often the case for waste heat and bottoming cycles. Although theoretically another cycle could be applied, practically this secondary cycle would not be cost-effective with respect to either the capital cost to install it or the power produced because the source stream to this cycle would be at such a low temperature. For solar thermal applications, it is also useful to return the solar heat transfer fluid to the solar field as close to ambient temperatures as possible to reduce heat losses in the receiver thus achieving high receiver efficiencies which contributes to the overall system efficiency. The utilization efficiency is a ratio of how much power is produced to the amount of work theoretically possible from a given finite thermal source. In this study, the utilization efficiency parameter can also be thought of as a nondimensional parameter for power as the same energy source with some initial exergy will be specified. Note this definition of utilization efficiency is the product of the internal 2nd law efficiency $\eta_{II,int}$ and the heat addition exergetic efficiency η_{add} as shown in eq. (3.10),

$$\varepsilon = \frac{W_{net}}{\dot{m}_s \left(\chi_{s,in} - \chi_{s,d} \right)} = \left[\frac{W_{net}}{\dot{m}_f \left(\chi_{f,out} - \chi_{f,in} \right)} \right] \left[\frac{\dot{m}_f \left(\chi_{f,out} - \chi_{f,in} \right)}{\dot{m}_s \left(\chi_{s,in} - \chi_{s,d} \right)} \right] = \eta_{II,\text{int}} \eta_{add} \tag{3.10}$$

where the subscript *f,in* and *f,out* designate the working fluid at its inlet and outlet of the heat exchanger. Utilization efficiency is maximized when the system is efficient at both absorbing energy from the finite thermal source as well as converting it to useful work.

A number of simplifying assumptions that are used in power plant analysis have been employed in this study **[**4**]**. Frictional losses in the piping and heat exchanger have been considered small and negligible; the heat addition and condensing processes are therefore assumed to be isobaric. Changes in the working fluid's kinetic and potential energies have also been considered negligible. The steady flow devices in the vapor cycle are all considered to be well insulated and do not lose significant energy to the surroundings. Throttling valves are assumed to be isenthalpic devices [4,15]. Mixing chambers and separators are assumed to be isobaric, adiabatic, and have no work interactions **[**4**]**. The turbine and feed pump are assumed to deviate from ideal isentropic behavior by isentropic efficiencies of η_{turb} and η_{pump}, respectively. The construction of energy balances across different steady flow devices is well known and the details can be found in ref. **[**4**,**5**]**. A computational program was constructed in MATLAB to model a variety of different working fluids for the OFC. An analysis is made to compare the internal and external second law, utilization, and heat addition exergetic efficiencies of the OFC to those obtained for optimized basic ORC and an ammonia-water zeotropic Rankine cycle **[**38**,**41**,**42**,**53**]** and to a CO_2 transcritical cycle [68,77,78], two of the more often suggested power cycles in the literature.

3.4 Results and discussion

3.4.1 Results for the basic ORC

Aromatic hydrocarbon and siloxane working fluids have often been proposed for ORCs utilizing a high or intermediate temperature finite thermal source [25,39,138,139]. A list of the fluids analyzed in this study has been compiled in Table 3.1, along with the equation of state that was used and its corresponding references. Note in Table 3.1, aromatic hydrocarbons are first listed and then siloxanes. The finite thermal source is modeled as hot water initially at 300^{o}C flowing at a steady rate of 1kg/s. The ambient temperature is assumed to be 30^{o}C and a minimum pinch temperature difference of at least 10^{o}C in the heat exchanger is assumed necessary to facilitate heat transfer between the two streams. The temperature of the working fluid at the condenser outlet is set to the ambient temperature plus the pinch (40^{o}C) in both the ORC and OFC. Isentropic efficiencies of 85% are assumed for the feed pumps and turbines. Design parameters of the basic ORC include the turbine inlet temperature and pressure and the working fluid flow rate. Therefore to maximize the utilization efficiency and power production, ORC optimization is required with respect to both the turbine inlet temperature and pressure and the corresponding maximum flow rate that would still yield a minimum 10^{o}C temperature difference between streams during heat addition.

Table 3.1: List of working fluids analyzed for OFC, ORC, zeotropic, and transcritical vapor cycles **[9]**.

Fluid Name	Vapor Cycle	T_{crit} [K]	Equation of State and Reference
toluene	OFC/ORC	591.75	REFPROP [92]
ethylbenzene	OFC/ORC	617.20	BACKONE [97-99,105-108]
butylbenzene	OFC/ORC	660.05	BACKONE [97-99,105-108]
o-xylene	OFC/ORC	630.33	BACKONE [97-99,105-108]
m-xylene	OFC/ORC	617.05	BACKONE [97-99,105-108]
p-xylene	OFC/ORC	616.23	BACKONE [97-99,105-108]
tetradecamethylhexasiloxane (MD4M)	OFC/ORC	653.2	Span-Wagner [99-104]
decamethylcyclopentasiloxane (D5)	OFC/ORC	619.2	Span-Wagner [99-104]
dodecamethylpentasiloxane (MD3M)	OFC/ORC	628.36	Span-Wagner [99-104]
dodecamethylcyclohexasiloxane (D6)	OFC/ORC	645.78	Span-Wagner [99-104]
0.7/0.3 ammonia-water (NH_3-H_2O)	Zeotropic	505.82	REFPROP [92]
carbon dioxide (CO_2)	Transcritical	304.13	REFPROP [92]

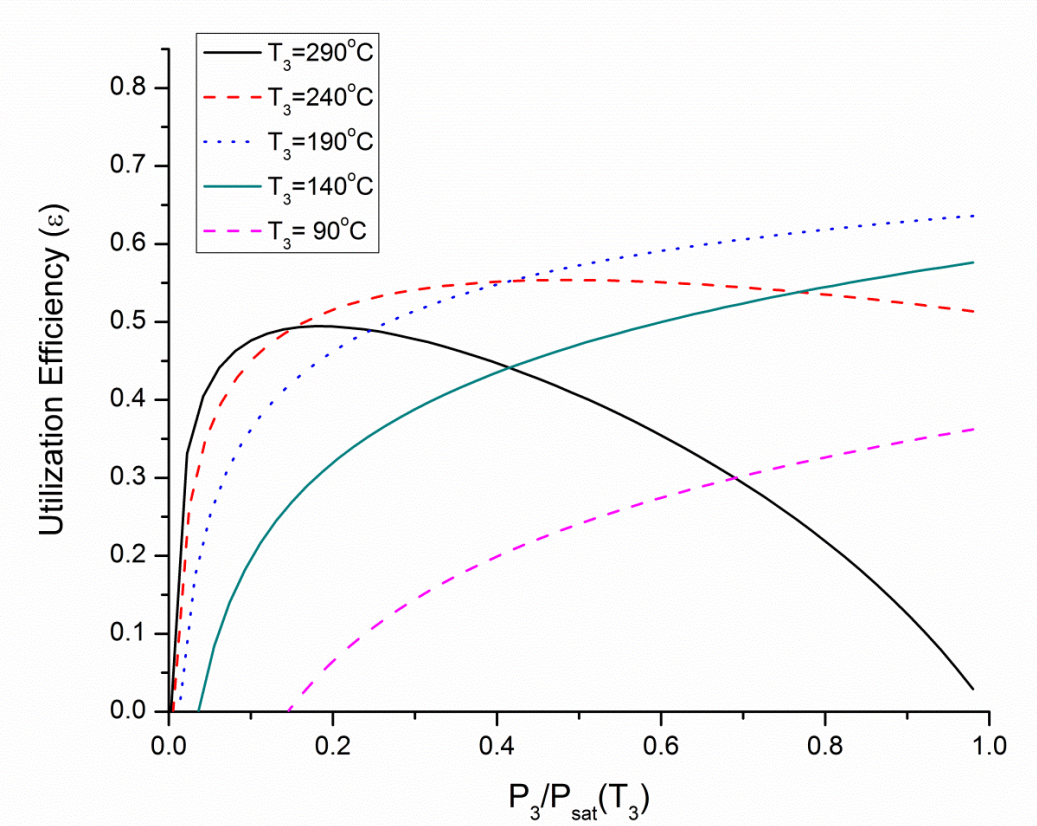

Figure 3.3: Utilization efficiency for a toluene ORC for varying turbine inlet temperature and pressure [9].

Using a toluene working fluid as an example, Fig. 3.3 shows the utilization efficiency as a function of the turbine inlet pressure ratio for several turbine inlet temperatures. As shown in Fig. 3.3, the utilization efficiency is strongly dependent on both the inlet turbine temperature and pressure at state 3 of Fig. 3.2. Depending on the turbine inlet temperature, the shape of the utilization efficiency curve is vastly different. At a 290^{o}C turbine inlet temperature, the maximum utilization efficiency is reached when the fluid is significantly superheated at state 3. At higher pressures, little power is produced from the thermal energy source because poor heat addition exergy efficiencies are encountered, which are a result of poor temperature matching, low cycle flow rate, and little energy being transferred to the ORC. For turbine inlet temperatures of 240^{o}C and 190^{o}C, one sees that the maximum of the utilization efficiency curves in Figure 4 begin to increase and shift towards the right. Utilization efficiency actually increases with lower turbine inlet temperature because state point 3 is becoming less superheated and consequently, state point 4 at the turbine exit is less superheated and heat rejection occurs at a lower temperature which increases the internal 2nd law efficiency.

High superheat at the turbine exit is a particular concern for "dry" working fluids as they tend to have significant superheat after expansion through a turbine because of their positively sloped saturated vapor curve on a T-S diagram. As the turbine inlet temperature is further decreased to 140^{o}C and 90^{o}C, the curves maintain the same shape, but the maximum of the curves begin to decrease. The average heat addition temperature is now approaching the average heat rejection temperature of the cycle and poor efficiency results based on Carnot considerations. These general trends just described were observed for all the working fluids in this study. For the fluids considered, because they are "dry" fluids, the maximum utilization efficiency was achieved at an inlet turbine temperature significantly below the initial temperature of the heat source.

As noted previously, the utilization efficiency is the appropriate efficiency parameter for situations in which the finite thermal energy source stream is not used further after transferring heat to the power cycle **[**76**,**136**,**137**]**. In some cases though, the heat source stream is valuable and useful for applications such as providing building heat; in such a scenario, the more appropriate parameter becomes the external 2nd law efficiency because energy left in the source stream will still be used in a different application. Using a toluene working fluid as an example again, Fig. 3.4 shows the external 2nd law efficiency as a function of turbine inlet pressure ratio for several turbine inlet temperatures. Note that the general behavior of the curves is very similar to that of Fig. 3.3, and the preceding observations on the trends in Fig. 3.3 are also applicable to Fig. 3.4. In the present study, the basic ORC was optimized to maximize either utilization efficiency or external 2nd law efficiency; the thermodynamic state at point 3 and corresponding cycle mass flow rate for the ORC optimized to both variables are shown in Table 3.2. Also given in Table 3.2 is the pressure at state 1 for the basic ORC; note this state also corresponds to state 9 of the OFC as well. Table 3.2 shows that for some of the working fluids considered, the turbine inlet conditions for maximum utilization efficiency and maximum external 2nd law efficiency do not correspond.

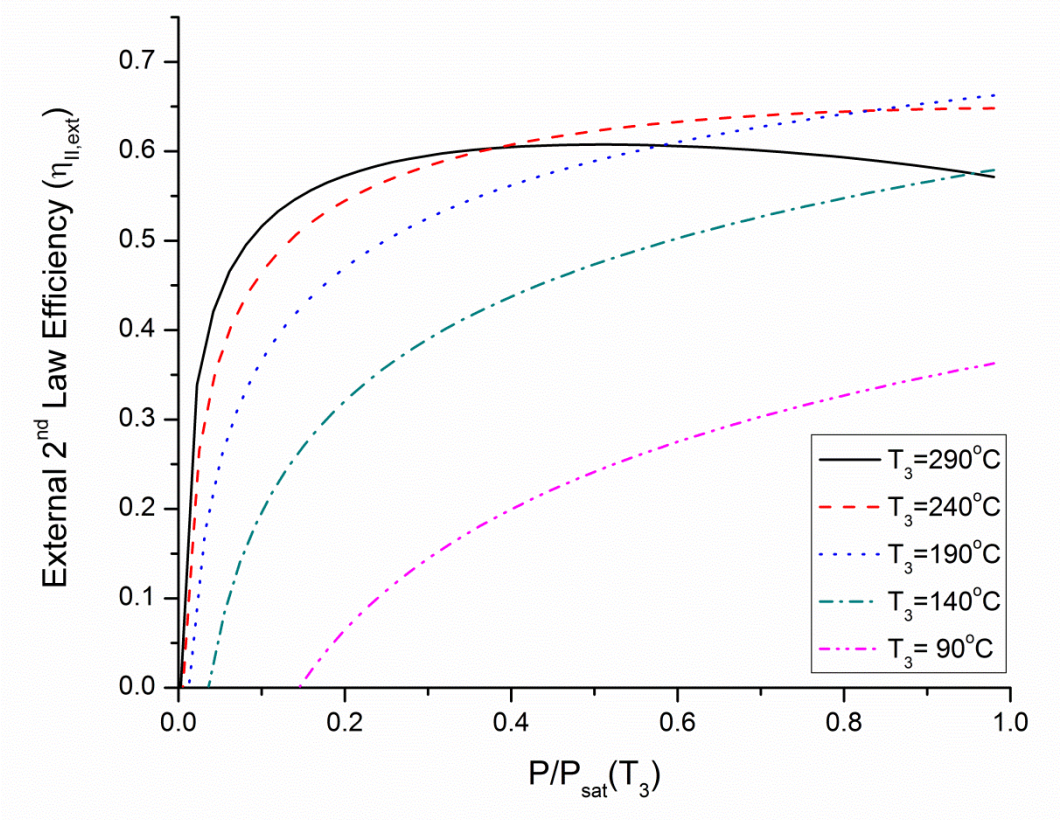

Figure 3.4: External 2nd law efficiencies for a basic toluene ORC for varying turbine inlet temperature and pressure [9].

Table 3.2: Thermodynamic states for key points and mass flow rates of the optimized ORC for different working fluids **[9]**.

Fluid Name	P_1* [kPa]	Optimized to ε		Optimized to $\eta_{II,ext}$	
		T_3† [K]	$\dot{m}_{ORC}$ [kg/s]	T_3† [K]	$\dot{m}_{ORC}$ [kg/s]
toluene	7.867	454	1.69	478	1.44
ethylbenzene	2.852	451	1.72	476	1.45
butylbenzene	0.3965	452	1.74	468	1.55
o-xylene	2.302	455	1.60	468	1.47
m-xylene	2.506	453	1.67	471	1.48
p-xylene	2.621	454	1.68	468	1.53
MD4M	0.0050	509	2.31	504	2.35
D5	0.0771	506	2.47	499	2.54
MD3M	0.0237	508	2.28	503	2.33
D6	0.0125	509	2.45	505	2.50

*$P_1 = P_{sat}(T_1$=40°C), also corresponds to OFC at $P_9 = P_{sat}(T_9 = 40°C)$ as a saturated liquid
†State point 3 is a saturated vapor ($q_3 = 1$) for the ORC optimized to either ε or $\eta_{II,ext}$

Assuming a saturated vapor at the turbine inlet, Fig. 3.5 shows the external 2nd law efficiencies and corresponding utilization efficiency or nondimensional power output. For aromatic hydrocarbons, Fig. 3.5 shows that there are a range of potential turbine inlet conditions where there is a balance between maximizing power generation and external 2nd law efficiency. This is shown specifically for toluene by the top right quadrant formed by the dotted vertical and horizontal lines indicating maximum utilization efficiency and internal 2nd law efficiency respectively. The balance between maximizing efficiency and power generation is well known in the field of endoreversible and finite time thermodynamics and further discussion on this topic can be found in ref. **[**140**]**.

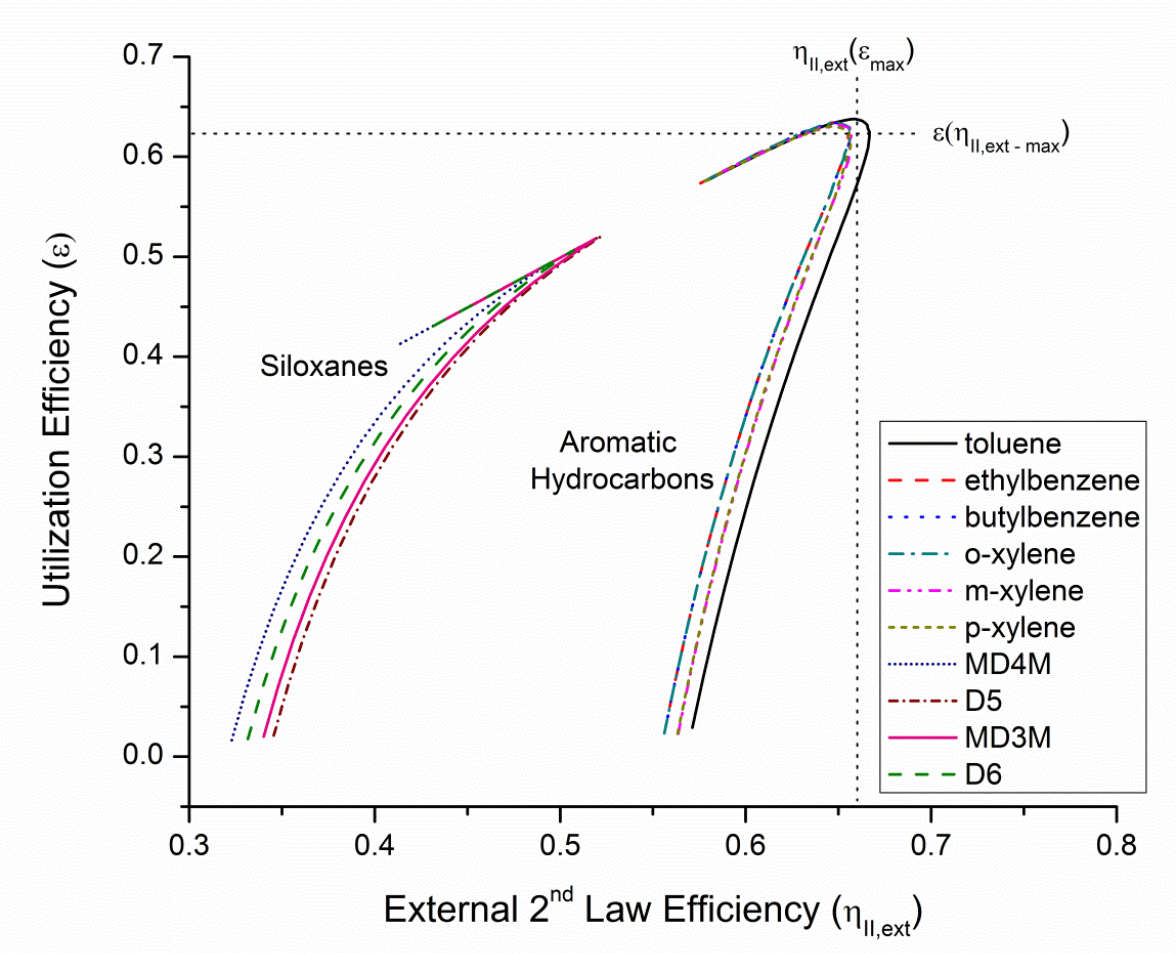

Figure 3.5: Utilization efficiency versus external 2nd law efficiency for basic ORC at a saturated vapor state at turbine inlet [9].

Fig. 3.6 shows utilization efficiency as a function of the ratio of the turbine inlet pressure to the fluid saturation pressure at the temperature for maximum utilization efficiency as given in Table 3.2. Note again for all the curves, utilization efficiency and thus power generation, reaches a maximum when the working fluid is at a saturated vapor state at the turbine inlet. Using eq. 3.6, the optimized ORC's first law efficiency was also calculated and it was observed that increasing first law efficiency for the optimized basic ORC correlated with decreasing fluid critical temperature. Though Sunter and Carey **[**28**]** conducted a thermodynamic similarity study on

solar thermal Rankine cycles and investigated completely different working fluids, they too also observed that lower fluid critical temperatures corresponded to higher first law efficiencies.

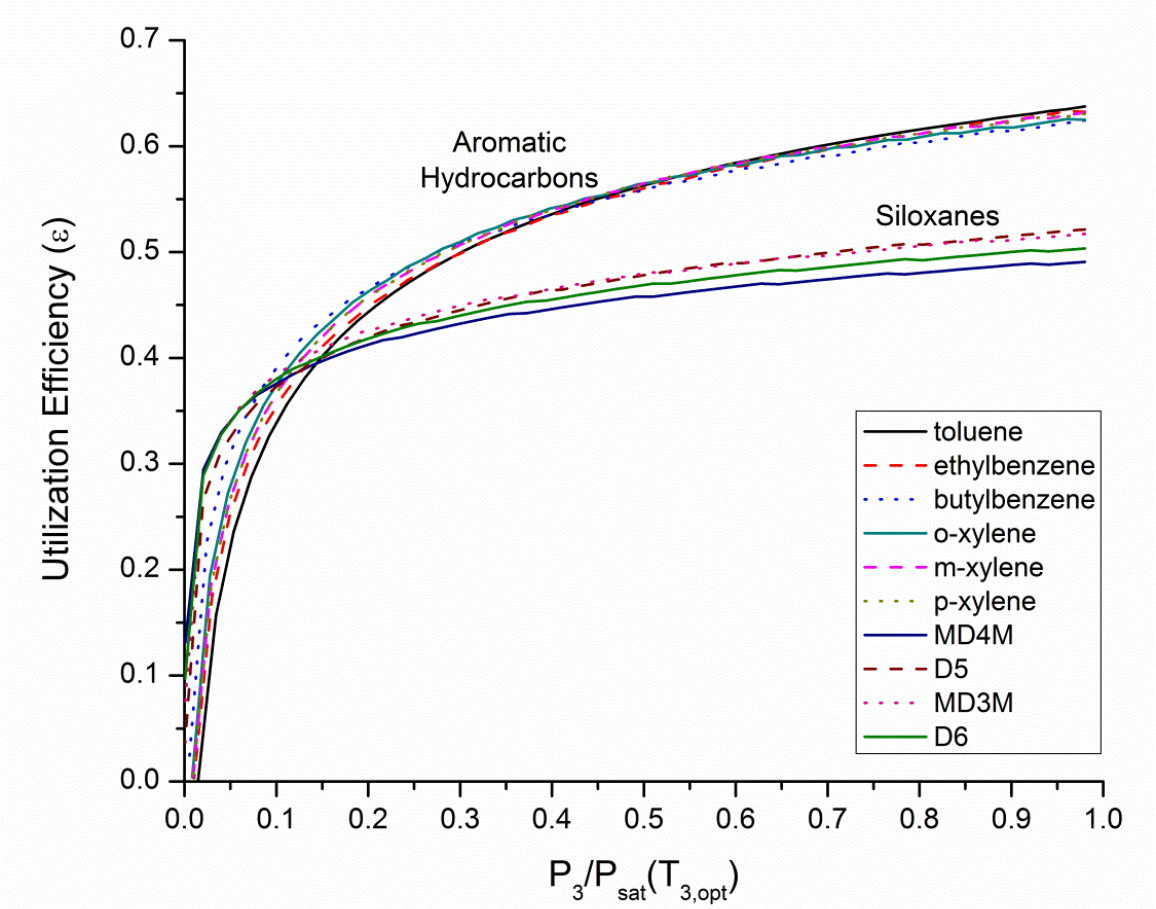

Figure 3.6: Utilization efficiency for basic ORC at varying inlet turbine pressures and T_3 from Table 2 for a particular working fluid [9].

Fig. 3.6 shows that aromatic hydrocarbons achieved significantly higher utilization efficiencies than siloxanes. This difference in performance can be attributed in large part to the molecular structure of siloxanes as compared to aromatic hydrocarbons. Using a statistical thermodynamics argument, Tabor and Bronicki [30] showed that more complex molecules exhibit a more "drying" behavior and possess a less positively sloped saturated vapor curve on a T-S diagram. Siloxanes are more complex and thus exhibit more "drying" behavior. After expansion from a saturated vapor state, siloxanes will then be at a higher temperature and superheated to a greater degree than their aromatic hydrocarbon counterparts. However, in the basic ORC this high temperature, superheated vapor with considerable exergy is simply cooled in the condenser and the potential work it possessed is not utilized. Some ORC studies have suggested an internal heat exchanger (IHE) to reuse energy from the turbine exhaust to preheat the fluid leaving the feed pumps [25,37]. This improves the internal 2nd law efficiency since the amount of energy absorbed from the external source is reduced, while the net work produced remains constant. However, an IHE does not improve the utilization efficiency or maximum power generation [136,141]. This is because the exergetic efficiency of the heat addition process decreases as a result of less energy being transferred from the finite thermal source, and energy

from the source that is not utilized is calculated as wasted potential work or "lost exergy" [**76**]. The IHE does improve the external 2nd law efficiency though because even though less energy from the heat source stream is transferred to the power cycle, the power cycle is not penalized for this because it is assumed that the remaining energy will be used in the next application. This difference in usefulness of an IHE again points to the importance of identifying the context with which the vapor power cycle is to be operated in so that the appropriate efficiency parameter is used in the design and analysis of the power cycle.

3.4.2 Results for the OFC

The OFC cycle analysis begins with determining the optimal state for the fluid to be throttled to so that the utilization efficiency is maximized. This is done in concert with determining the temperature at the inlet of the flash evaporator and its corresponding maximum flow rate that still provides the minimum 10^{o}C temperature difference between streams of the heat exchanger. Through some simplifications, DiPippo determined analytically the optimal state using the "equal-temperature-split rule" **[**15**]**. Here, an iterative method is employed to determine the optimal state with which to flash the fluid to. Table 3.3 gives, for maximum utilization efficiency, some important thermodynamic states for the OFC including state 3, the state the fluid should be flash evaporated to.

Table 3.3: Optimal thermodynamic state 3 to flash evaporate to for the OFC in terms of temperature T_3 and vapor mass quality q_3 and corresponding cycle mass flow rate **[**9**]**.

Fluid Name	T_2† [K]	T_3 [K]	q_3	$\dot{m}_{OFC}$ [kg/s]
toluene	559	457	0.87	1.92
ethylbenzene	561	453	0.89	1.90
butylbenzene	563	452	0.94	1.85
o-xylene	562	452	0.86	1.90
m-xylene	561	453	0.87	1.92
p-xylene	561	453	0.87	1.93
MD4M	557	507	1.00	2.31
D5	558	509	1.00	2.43
MD3M	552	502	1.00	2.33
D6	557	507	1.00	2.46

†State point 2 for the optimized OFC is a saturated liquid ($q_2 = 0$)

Fig. 3.7 shows a plot of the resulting maximum utilization efficiencies for the OFC and the percentage difference compared to the maximum utilization efficiency for the optimized ORC determined earlier in Fig. 3.6. Fig. 3.7 shows the OFC to exhibit comparable performance to the optimized ORC in terms of the utilization efficiency, with the OFC generating about 0% to 2.5% less power than the optimized ORC. Results show that the advantages resulting from increasing the exergetic efficiency during the heat addition process to be comparable to the disadvantages of introducing the throttling process in flash evaporation and the added irreversibilities that it generates.

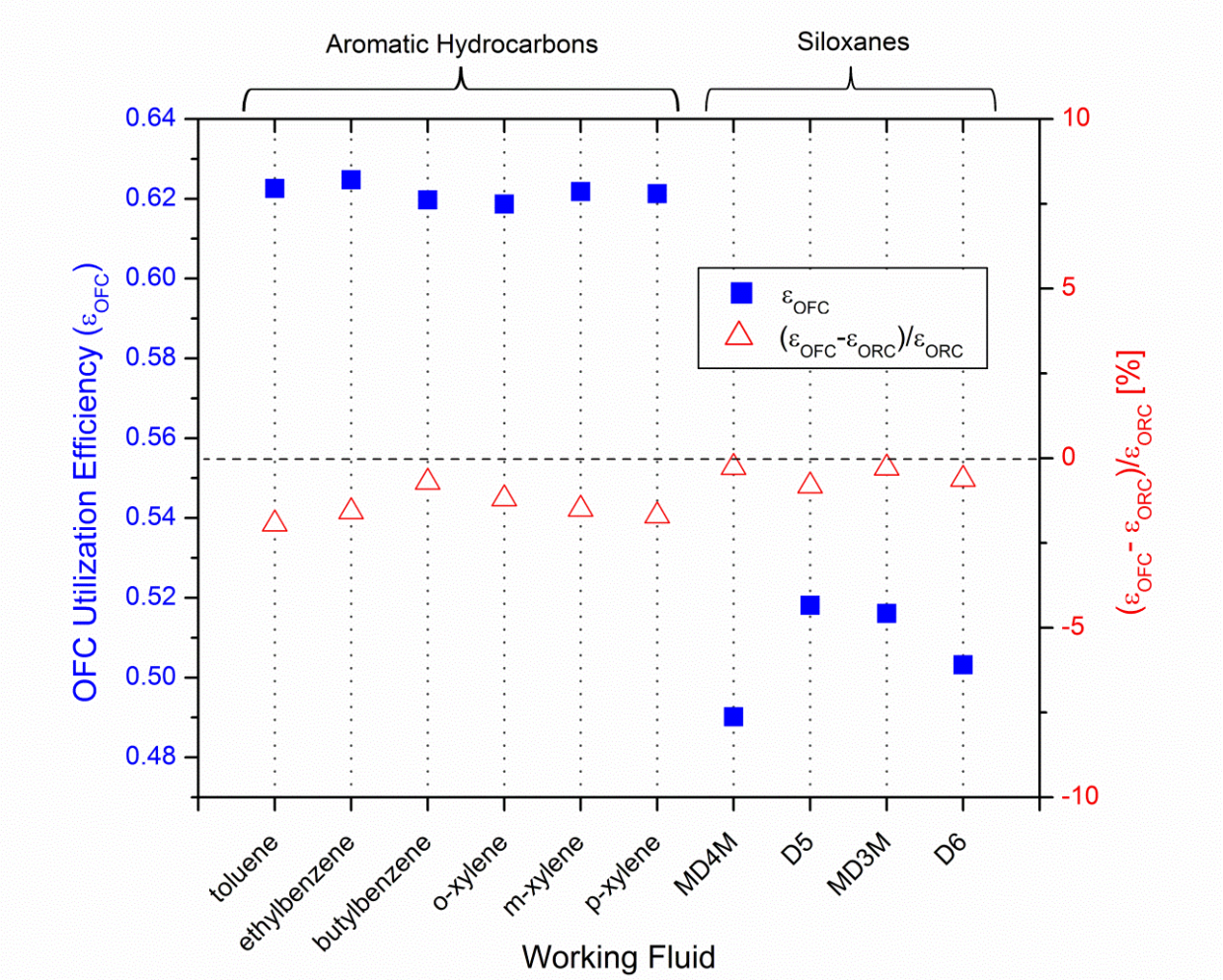

Figure 3.7: OFC utilization efficiencies and the percent difference in utilization efficiency for OFCs compared to the optimized ORC [9].

The exergetic efficiency of the heat addition process for the optimized ORC averaged ~75% for aromatic hydrocarbons, whereas for siloxanes it neared 89%. This high heat addition exergetic efficiency for siloxanes can be attributed to their molecular complexity which gives siloxane molecules many degrees of freedom and in turn makes the specific heat for siloxanes very high. Their high specific heat causes the majority of the heat that is absorbed in the cycle to go towards heating the siloxane from a subcooled state at the pump exit (state 1) to a saturated liquid state. The energy required to vaporize the siloxane working fluid is actually fairly small compared to the necessary sensible heat; this is actually advantageous in the ORC as it allows the siloxane temperature profile to match that of the energy source fairly well resulting in high heat addition exergetic efficiency. Unfortunately, as mentioned previously, their molecular complexity also makes the fluid very "drying;" this contributes to very high superheat at the turbine exit and low internal 2nd law efficiencies which then limits the total power generated. This is the primary reason why aromatic hydrocarbons, which are less "drying," exhibited better performance than siloxanes for the OFC, as shown in Figure 3.7.

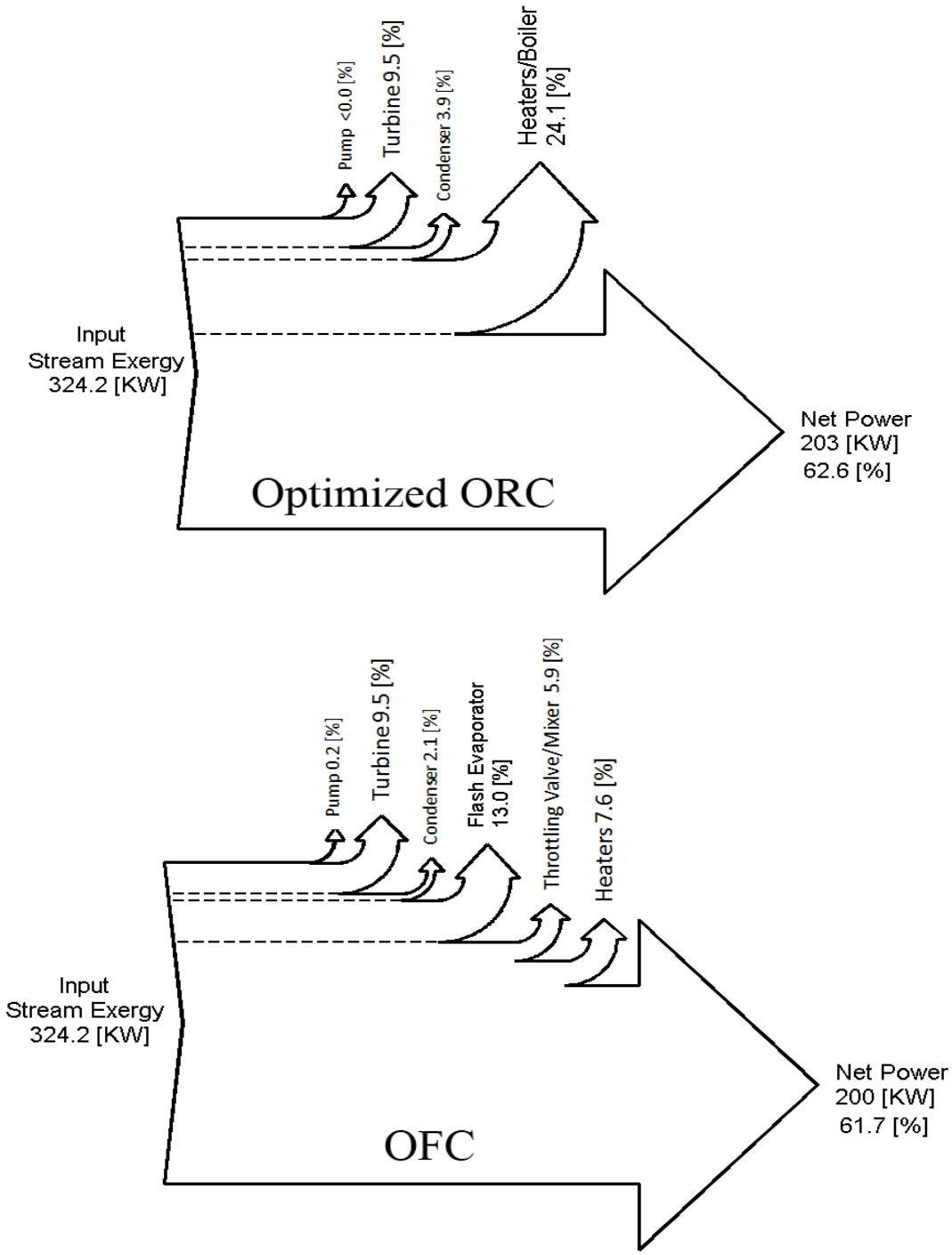

Figure 3.8: Exergy Sankey diagrams for an optimized ORC and OFC using an o-xylene working fluid

Fig. 3.8 shows the exergy Sankey diagrams for an optimized ORC and OFC using an o-xylene working fluid as an example. Note that for the OFC, the heat addition process only destroys 7.6% of the initial exergy, whereas for the optimized ORC the heat addition process destroys 24.1% of the initial exergy and is by far the greatest cause of irreversibility. This was seen for all

aromatic hydrocarbons examined where the heat addition exergetic efficiency was slightly over 90%, approximately a 20% improvement over the optimized ORC. For siloxanes in the OFC, the heat addition exergetic efficiency was approximately 92%, which only amounts to about a 3% improvement over the optimized ORC. Although the OFC did improve temperature matching, the gains in heat addition efficiency over the optimized ORC are marred by the considerable exergy destruction in flash evaporation, throttling and mixing processes. Further improvements on the OFC design will need to target these components and increase the exergetic efficiency of these processes.

3.4.2.1 Turbine Considerations

In addition to power output, practical considerations such as the design of a suitable turbine or expander should be taken into consideration when selecting a working fluid. Neglecting Reynolds number effects, Macchi et al. **[**142**]** used similarity arguments to show that the efficiency of a particular turbine stage can be approximated quite well from the Volumetric Flow Ratio (*VFR*) and the Size Parameter (*SP*) defined in eq. (3.11) and (3.12), respectively **[**142**]**.

$$VFR = \left(\dot{V}_{out} / \dot{V}_{in}\right)_{isen} \tag{3.11}$$

$$SP = \sqrt{\dot{V}_{out}} \Big/ \left(\Delta h\right)_{isen}^{0.25} \tag{3.12}$$

In eq. (3.11) and (3.12), $\dot{V}_{out}$and $\dot{V}_{in}$ are the volumetric flow rates at the turbine stage exit and inlet, Δh is the enthalpy drop across the stage, and the subscript *isen* denotes an isentropic process. *VFR* is essentially the turbine expansion ratio and can also be thought of as a compressibility parameter; *SP* is a dimensional parameter which is an approximate indication of the turbine's actual size **[**141**,**142**]**. Table 3.4 gives the *VFR* and *SP* for the optimized ORC and OFC for the working fluids considered.

Table 3.4: Turbine Size Parameter (*SP*) and Volumetric Flow Ratio (*VFR*) for conditions for optimized ORC and OFC **[**9**]**.

Fluid Name	OFC		ORC optimized to ε		ORC optimized to $\eta_{II,ext}$	
	SP [m]	*VFR*	*SP* [m]	*VFR*	*SP* [m]	*VFR*
toluene	0.132	62.1	0.133	58.4	0.120	93.7
ethylbenzene	0.210	86.9	0.212	83.2	0.191	140
butylbenzene	0.522	197	0.522	198	0.487	291
o-xylene	0.242	96.8	0.239	104	0.233	137
m-xylene	0.221	91.8	0.221	91.2	0.205	135
p-xylene	0.217	88.8	0.217	90.8	0.205	122
MD4M	3.70	1.09×10^{4}	3.70	1.15×10^{4}	3.73	1.01×10^{4}
D5	1.06	2.39×10^{3}	1.07	2.23×10^{3}	1.09	1.89×10^{3}
MD3M	1.82	4.20×10^{3}	1.80	4.87×10^{3}	1.82	4.31×10^{3}
D6	2.46	6.23×10^{3}	2.46	6.55×10^{3}	2.49	5.93×10^{3}

For single stage axial turbines, isentropic efficiencies of at least 80% are only possible for a *VFW* below ~50 **[**143**,**144**]**. Note that for all the working fluids in this study, the *VFW* was determined to be above this threshold; this indicates that an axial turbine of at least 2 stages would be necessary to achieve the isentropic efficiencies of 85% which had been assumed in this study. Siloxanes in particular have *VFR*s from 2-3 orders of magnitude greater than aromatic hydrocarbon working fluids indicating that multiple stages beyond 2 stages would likely be necessary in order to achieve reasonable isentropic efficiencies. In addition, MD4M and D6 have very high *VFR*s compared to all the other working fluids. When considering the high cost of multi-stage turbines, using these working fluids may not actually be cost justified in practice. Note in Table 3.4 that the *SP* and *VFR* are very similar between the optimized ORC and OFC; this would confirm that turbine technology already available for the ORC are also likely suitable for the OFC.

3.4.2.2 Potential improvements to the OFC

Fig. 3.7 shows that the single flash OFC exhibits only comparable utilization efficiencies to the optimized ORC; however, there are a number of potential improvements that could raise the OFC utilization efficiency considerably. One method could be to use two separate flash steps instead of only one, similar to the double flash steam cycle that is applied to higher temperature geothermal resources **[**15**]**. This double flash OFC would also then have two turbines, one high pressure turbine for saturated vapor from the first flash step, and then a second low pressure turbine for vapor gathered from the secondary flash step. Introducing a secondary flash step reduces the irreversibilities associated with the flash evaporation process; for geothermal resources, double flash steam cycles have reported 15% to 20% more power generated compared to a single flash steam cycle for the same geofluid. Another potential improvement could be to replace the throttling valve with a two-phase expander; this concept has been discussed and is of a particular interest in the refrigeration and oil refining industries. Replacing the throttling valve with a two-phase expander would significantly improve the OFC, as a previous source of irreversibility has now become a source of power generation. Reheat loops using the liquid from the first flash step for aromatic hydrocarbons or reverse feedwater heaters to reduce vapor superheat at the turbine exit for siloxanes are also potential areas for improvement.

3.4.3 Comparing the OFC with other proposed cycles

A variety of modifications to the basic ORC have been proposed by researchers to improve temperature matching, heat addition exergetic efficiency, and system utilization efficiency. Two frequently suggested approaches are employing binary mixtures or operating the cycle partly supercritical. An analysis was conducted to compare the performance of the proposed OFC to that for a basic ammonia-water Rankine cycle and a basic transcritical CO_2 Rankine cycle.

3.4.3.1 Comparing the OFC to a basic ammonia-water Rankine cycle

For comparison, a basic Rankine cycle using an ammonia-water mixture 0.70/0.30 mass ratio was analyzed. This particular zeotropic fluid is chosen because it is the mixture that is used in the widely known Kalina cycle. Figure 3.9 shows the exergetic efficiency of the heat addition process, the internal 2nd law efficiency, and the utilization efficiency for the ammonia-water Rankine cycle as a function of the expansion ratio (P_3/P_4) and turbine inlet pressure (P_3). Only conditions that produced vapor qualities greater than or equal to 0.85 after expansion have been presented, as too much moisture would erode and damage the steam turbine blades **[**145**]**. Note

that for the ammonia-water Rankine cycle which utilizes a "wet" fluid, the turbine inlet temperature is set to the maximum 290°C. This was done to ensure that at higher boiler pressures, the mixture is still superheated enough at the turbine inlet to avoid expansion into the vapor dome at the turbine exit.

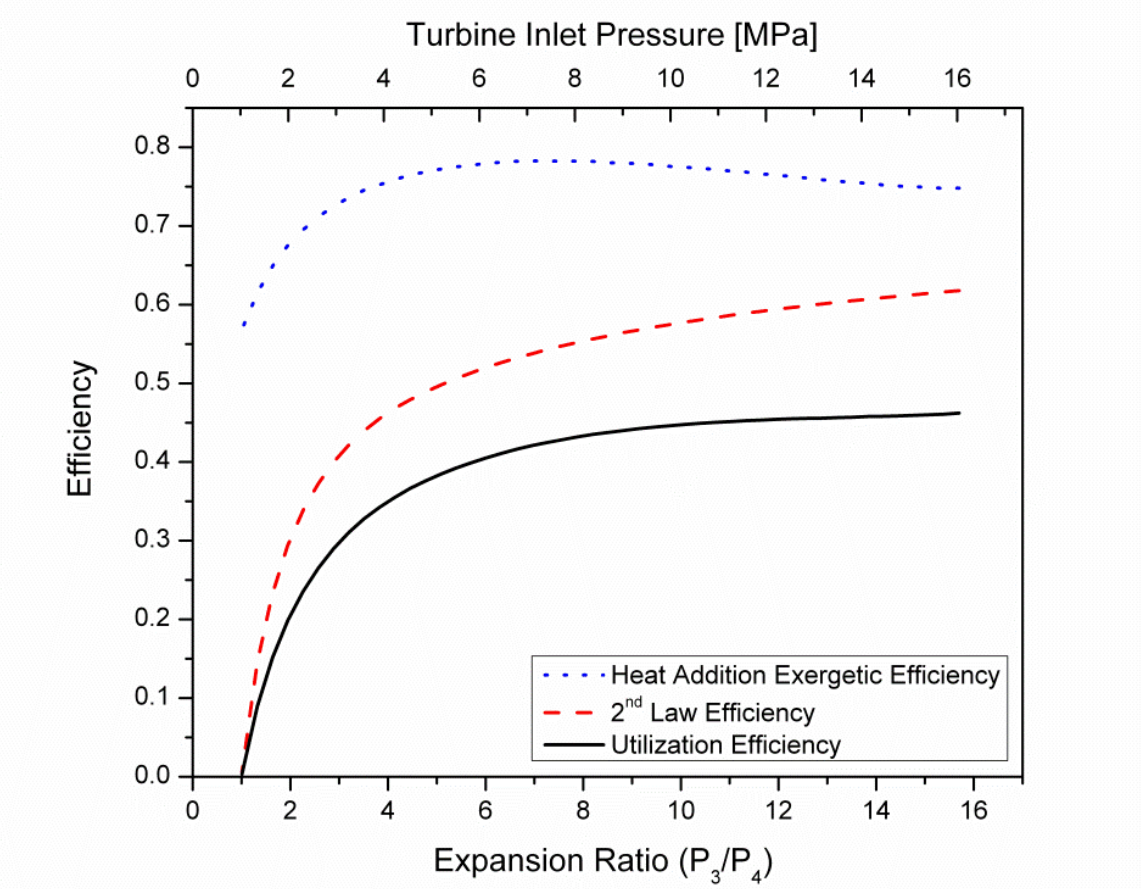

Figure 3.9: Zeotropic water-ammonia Rankine cycle (0.30/0.70 mass ratio) performance parameters [9].

Fig. 3.9 shows that the zeotropic ammonia-water Rankine cycle achieves comparable heat addition exergetic efficiency to the optimized ORC at about 75%. The temperature glide exhibited by zeotropic fluids has been shown here to not noticeably improve temperature matching during heat addition compared to the optimized ORC. This result, however, may be due to a poor selection of mixture concentration; a detailed design of a zeotropic cycle would select concentration ratios and mixtures that it matches the temperature profile of the energy source very closely. From Fig. 3.9, the maximum utilization efficiency obtained was only about 0.46, which is considerably below that obtained for the optimized ORC. The low utilization efficiency can be attributed to the same temperature glide property researchers exploit to improve heat addition efficiency. After expansion, zeotropic fluids are at a much higher temperature than their pure fluid counterparts because of the temperature glide. The high temperature, high exergetic content of the exhaust stream is then lost in the condenser. Similar results were seen by Wang et al. **[**37**]** for a low temperature solar ORC. Their results showed that the pure fluid R245fa ORC outperformed ORCs using three different zeotropic mixtures of R245fa/R152a.

The Kalina cycle attempts to reclaim this exergy by using a distiller-condenser-subsystem (DCSS), which changes the working fluid composition multiple times in different loops [53,54]. The system schematic for the Kalina cycle is reproduced in Fig. 3.10 for convenience. The increase in efficiency over the conventional steam Rankine cycle by the Kalina cycle has been reported as high as 50% [54] or as low as 3% [22]. In either case, Fig. 3.10 shows that one disadvantage to the Kalina cycle is the greater complexity and greater number of plant components than the ORC or OFC. Also, the Kalina cycle requires precision in the mixing and distilling processes, as well as potentially very small pinch temperatures. Fig. 3.9 shows yet another major obstacle for an ammonia-water Rankine cycle is the high operating pressures. Care must be taken to select the proper fluids and concentration ratio to ensure better temperature matching, as well as reducing the disadvantages of the temperature glide during the condensing process.

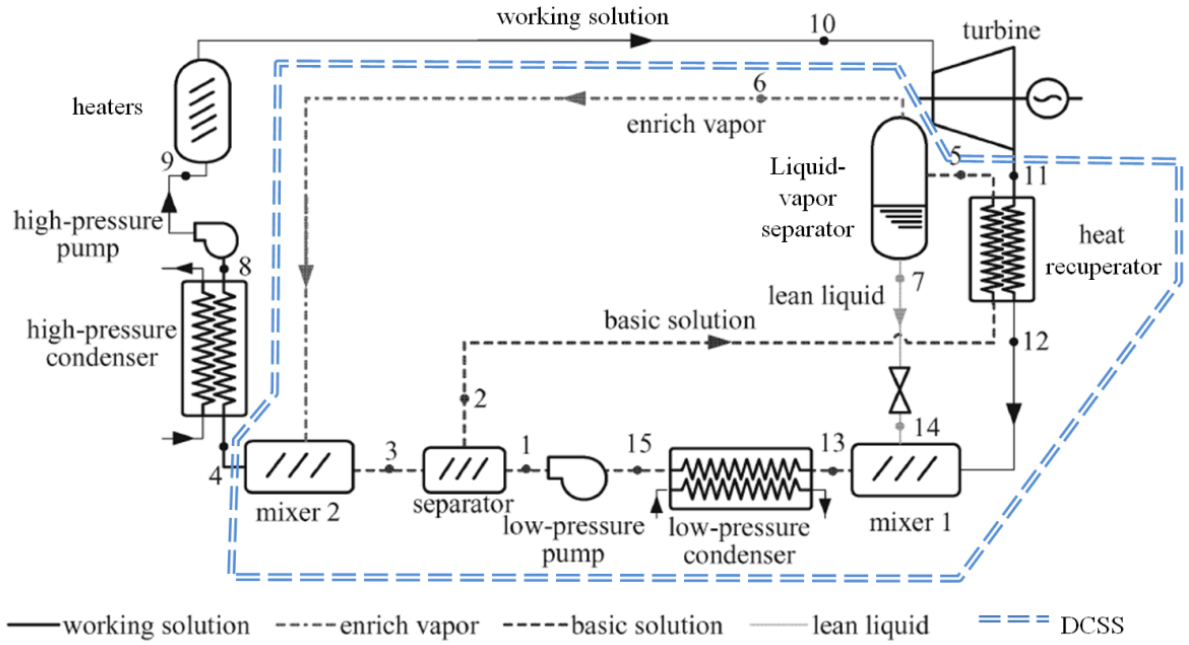

Figure 3.10: Schematic of Kalina cycle with distiller condenser subsystem (DCSS). Reprinted with permission from Springer Science and Business Media: *Frontiers in Energy and Power Engineering in China*, copyright 2008 [53].

3.4.3.2 Comparing the OFC to the transcritical CO_2 Cycle

Operating the Rankine cycle partially in the supercritical regime is another method that researchers have suggested to improve temperature matching. CO_2 is often cited as a working fluid for such a cycle due to its inexpensiveness, availability, and stability [68,77,78]. Performance parameters for a simple transcritical CO_2 Rankine cycle are plotted in Fig. 3.11. Note that for the CO_2 cycle, the assumed cold thermal reservoir temperature is reduced to 20°C from 30°C, which had been used in the analysis of all the preceding cycles thus far. The temperature reduction of the cold thermal reservoir is necessary to achieve subcritical condensing of CO_2.

From Fig. 3.11, the heat addition process's exergetic efficiency for the transcritical CO_2 cycle is observed to be about 75% to 80%. This increase in exergetic efficiency compared to the optimized ORC is again due to supercritical heating that avoids isothermal phase change that occurs in the two-phase region. By adding heat to CO_2 above the critical pressure, better temperature matching to the finite thermal source is achieved. Although the exergetic efficiency of the heat addition process is slightly higher for the transcritical CO_2 cycle compared to the optimized ORC, it should be noted that it is still less than the greater than 90% exergetic efficiency achieved by the OFC.

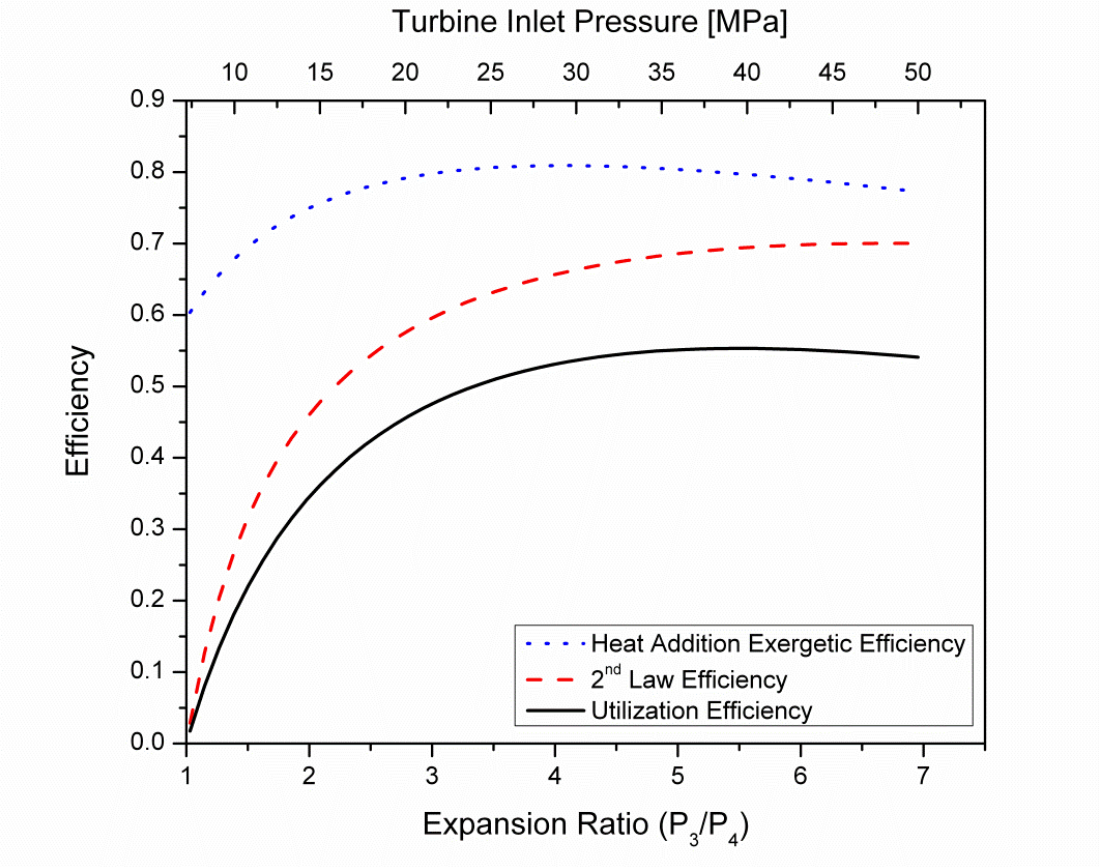

Figure 3.11: Performance parameters for a transcritical CO_2 Rankine cycle [9].

In this study, the maximum utilization efficiency achieved by the simple transcritical CO_2 cycle was about 0.55, which is about 13% less than the maximum achieved by the OFC and optimized ORC, 0.62 and 0.63, respectively. Similar to the ammonia-water Rankine cycle, very high operating pressures are encountered for a transcritical CO_2 cycle, as shown in Fig. 3.11. The OFC and optimized ORC on the other hand are both completely subcritical and thus operate under much lower pressures. Yet another obstacle for the transcritical CO_2 cycle is the aforementioned design of a suitable supercritical CO_2 turbine which is still under development **[**68**]**.

3.4.4 Required heat transfer surface area

For ORCs, heat exchangers by far make up the lion's share of the initial investment cost **[**146**,**147**]** of the plants and the total heat exchanger surface area is frequently used in studies as a

metric to compare initial capital costs for different ORC designs [78,136,146-150]. Here, approximations for the total heat transfer area required for the optimized basic ORC and the OFC are compared. Using the well known Log Mean Temperature Method **[**151**]**, for an ideal countercurrent heat exchanger, the total heat transfer rate $\dot{Q}$ is equal to the product of the overall heat transfer U, the heat exchanger surface area A, and the log mean temperature difference ΔT_{LM} , as shown in eq. (3.13) **[**151**]**.

$$\dot{Q} = UA_s \Delta T_{LM} \tag{3.13}$$

The log mean temperature difference for a countercurrent heat exchanger is shown in eq. (3.14),

$$\Delta T_{LM} = \frac{\left[\left(T_{hot,in} - T_{cold,out}\right) - \left(T_{hot,out} - T_{cold,in}\right)\right]}{\ln\left[\left(T_{hot,in} - T_{cold,out}\right) / \left(T_{hot,out} - T_{cold,in}\right)\right]} \tag{3.14}$$

where $T_{hot,in}$ and $T_{hot,out}$ are the temperature at the inlet and outlet for the hot stream and $T_{\text{cold,in}}$ and $T_{cold,out}$ are the temperature at the inlet and outlet for the cold stream in the heat exchanger **[**151**]**. Note that for the ORC, the surface area for the preheater, boiler, and superheater need to be calculated separately as the overall heat transfer coefficient will be significantly different for each of these heat exchangers because of the heat transfer coefficients corresponding to liquid, two-phase, or vapor flow. Similarly, if the fluid is superheated at the turbine exit, the two separate surface area calculations need to be done for the condenser. For the OFC, the fluid remains in single-phase liquid throughout heat addition so only one surface area calculation is necessary. The total heat transfer area for the cycle is then determined by summing up the surface areas of each of the individual heat exchanger components for the cycle.

From results of the previous thermodynamic analysis in section 3.4.1 and 3.4.2, the log mean temperature difference and the total heat transfer rate of the individual heat exchangers can be calculated by determining the thermodynamic states of the fluid at the appropriate conditions of interest. The overall heat transfer coefficient for a heat exchanger is a function of a number of different variables tied to the characteristics of the flow of the two streams and the geometry and material of the heat exchangers. Determining the overall heat transfer coefficient requires the selection or design of a specific heat exchanger which is beyond the scope and also is not the primary focus of this study. Therefore, a simplified order of magnitude analysis is adopted here to compare approximate heat transfer areas. Due to the relatively low operating pressures of the ORC and OFC for these particular refrigerants (critical pressures are below 5MPa), it assumed that the heat exchanger pipe walls are thin and the pipe conductive resistance is negligible compared to the convective resistance. Therefore, for this simplified analysis, the overall heat transfer coefficient can be found from the inverse sum of the convective resistances as shown in eq. (3.15),

$$U = \left[\frac{1}{h_{conv,hot}} + \frac{1}{h_{conv,cold}}\right]^{-1} \tag{3.15}$$

where $h_{conv,hot}$ and $h_{conv,cold}$ are the convective heat transfer coefficients for the hot and cold stream to the pipe wall, respectively **[**151**]**. General order of magnitude approximations shown

in Table 3.5 for convective heat transfer coefficients based on the flow regime were used in lieu of determining heat transfer coefficients specific to flow characteristics for a particular heat exchanger [151,152]. Results for the overall heat transfer coefficient for combinations of streams of different phase regimes are given in Table 3.6 and were verified to be comparable to values reported in the literature [148,153].

Table 3.5: Order of magnitude approximations for convective heat transfer coefficients for different phase regimes [151,152]

Flow regime	Convective heat transfer coefficient
Liquid	10^3 W/m^{2}K
Two-phase	10^4 W/m^{2}K
Vapor	10^2 W/m^{2}K

Table 3.6: Order of magnitude approximation for overall heat transfer coefficient for different combinations of streams

Flow regime combination for heat exchanger streams	Overall heat transfer coefficient
Liquid – Liquid	500 W/m^{2}K
Liquid – Two-phase	909 W/m^{2}K
Liquid – Vapor	90.9 W/m^{2}K
Vapor – Two-phase	99.0 W/m^{2}K
Vapor – Vapor	50.0 W/m^{2}K

Note that from Tables 3.5 and 3.6, the lower heat transfer coefficient dominates in determining the overall heat transfer coefficient. This is significant in that although two-phase heat transfer coefficients are very high, the overall heat transfer coefficient in the boiler will be limited by the phase of the finite thermal heat source stream. This is also significant if a superheater is used, where significantly more heat transfer area is required to compensate for low vapor heat transfer coefficients. For heat addition, Fig. 3.12 shows that the OFC requires more heat exchanger surface area for aromatic hydrocarbons and comparable surface area of siloxanes. For aromatic hydrocarbons, the OFC absorbs more energy from the finite thermal source, has a lower log mean temperature difference between the streams, and the ORC is able to utilize high heat transfer coefficients in the boiler. Since the optimized ORC is a saturated vapor prior to expansion through the turbine, it does not require the use of a superheater in the design and does not encounter the correspondingly low vapor heat transfer coefficients. As mentioned previously, siloxanes actually showed very close temperature matching as the energy required for vaporization was small compared to the energy required for the sensible heating to a saturated liquid. Therefore, the temperature profiles and required heat transfer surface areas for the siloxane ORC and OFC are similar.

As shown in Fig. 3.12, the OFC requires slightly less de-superheater and condenser heat transfer surface area than the optimized ORC. Results showed that the optimized ORC required roughly

20%-30% more surface area for the de-superheater than the OFC. Although the two cycles' total heat rejection rates were similar, the OFC was significantly less superheated at state 9 of Fig. 3.2 than the optimized ORC at state 4 of Fig. 3.1. The low vapor superheat for the OFC is due primarily to the OFC's vapor turbine exhaust being mixed with the throttled saturated liquid from the flash evaporator. Therefore during heat rejection, a greater fraction of the total heat rejected occurs in the de-superheater for the optimized ORC than the OFC where low heat transfer coefficients are observed. For the OFC, the majority of the energy is rejected while the working fluid is a two-phase mixture in the condenser, allowing the OFC to take advantage of the high two-phase heat transfer coefficients and subsequently require less heat transfer surface area for the heat rejection process.

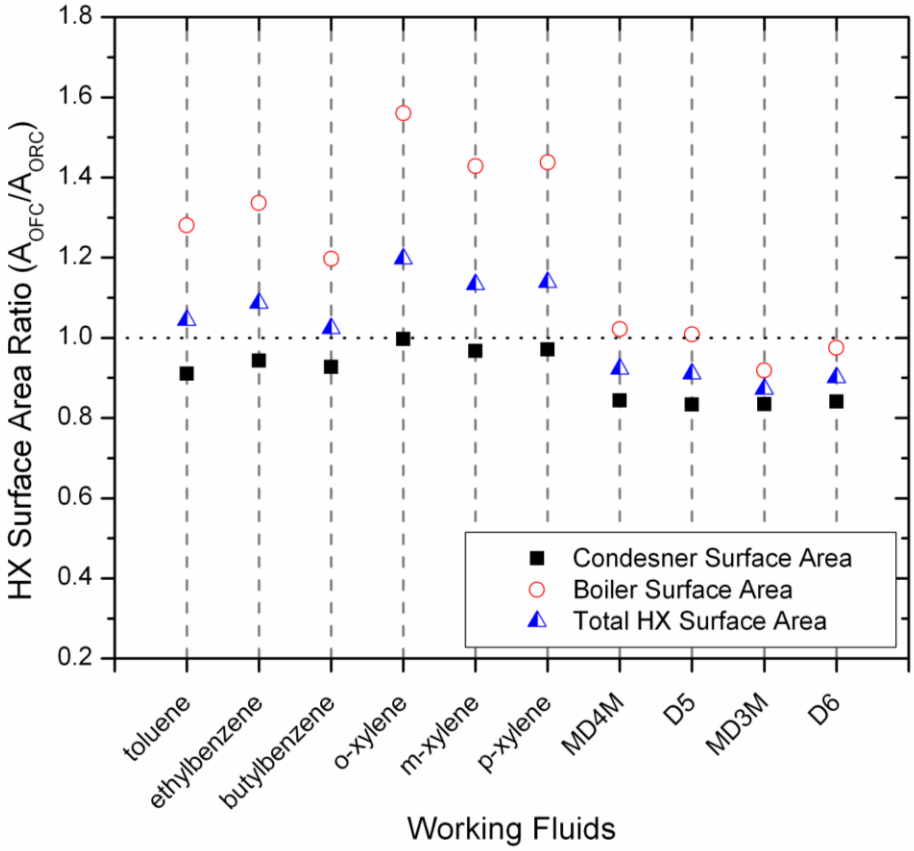

Figure 3.12: Required heat exchanger surface area for the OFC compared to the optimized basic ORC for various different working fluids

Summing the total heat exchanger surface area for heat addition and heat rejection for the cycle, Fig. 3.12 shows that the required heat exchanger surface area for the OFC and optimized basic ORC are again fairly comparable. Due to their comparable required heat exchanger surface area, the initial capital cost for the OFC compared to the optimized basic ORC would be similar or only slightly more (A_{OFC}/A_{ORC} ~ 0.9 to 1.2). In the following chapter, some enhancements are proposed for the OFC that do not change the temperature profiles in the preheater, but potentially could produce more power thus decreasing the heat rejection required in the condenser and the condenser surface area. The payback or return on investment then would be significantly less for the enhanced OFC as it can produce more power than the optimized basic ORC per finite thermal

energy source flow rate, but will require only comparable or slightly less heat transfer surface area or initial cost. One then can generate more power and all the while, recovering the initial cost in a similar or shorter time span.

3.5 Conclusions

A comparison of the Organic Flash Cycle to the optimized ORC and other advanced vapor cycles for high and intermediate temperature finite thermal sources was presented. The OFC concept is based upon the design principle of increasing utilization efficiency by increasing temperature matching and reducing exergy losses during the heat addition process. REFPROP, BACKONE, and Span-Wagner equations of states were used in conjunction with a detailed thermodynamic and exergetic analysis to determine the validity and merit of the OFC. A number of different aromatic hydrocarbons and siloxanes were analyzed as potential working fluids. For the working fluids examined, results showed the OFC to have comparable performance to the optimized ORC. Aromatic hydrocarbons were shown to outperform siloxanes as working fluids for both the OFC and optimized ORC. Aromatic hydrocarbons also had smaller turbine volumetric flow ratios making their turbines smaller and less complex. While the OFC also possessed the highest heat addition exergetic efficiency of the cycles analyzed, this advantage was negated by the exergy destruction introduced by the throttling valve in the flash evaporation process. The OFC and ORC were seen to have comparable required heat exchanger surface areas and subsequently initial capital costs. However, a number of improvements are possible for the OFC that could significantly increase net power generation. Research into these potential improvements to OFC and its possible applications to lower temperature thermal energy sources is warranted and will be discussed in the following subsequent chapters.

4 Enhancements to the Organic Flash Cycle (OFC) for improved power production from intermediate finite thermal resources

4.1 Introduction

In the previous chapter and prior works **[**9**]**, the Organic Flash Cycle (OFC) was proposed as a vapor power cycle where the working fluid remains completely in the liquid state during heat addition. In other words, heat is transferred to the OFC until the working fluid reaches a saturated liquid state ensuring near perfect temperature matching to the source stream. The fluid would then be flash evaporated to produce a two phase mixture; the saturated vapor would be separated and then expanded to produce power. For convenience, the cycle schematic and its associated T-S diagram is reproduced in Fig. 4.1 for a "dry" working fluid.

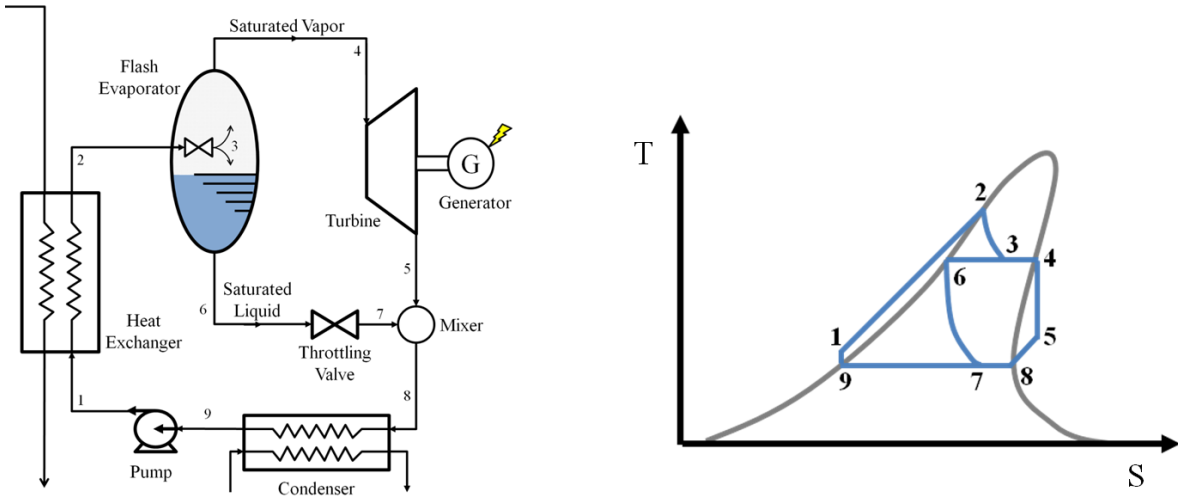

Figure 4.1: System schematic and T-S diagram for the basic OFC [9].

The original premise of the OFC was that the advantages of increased exergetic efficiency in the heat addition process due to better temperature matching to the energy reservoir stream would outweigh the disadvantages of the irreversibilities generated by uncontrolled expansion during the flash evaporation process. A finite thermal source initially at 300^{o}C was considered in the previous chapter to be a broad representation of the renewables such as one-axis solar thermal, high grade geothermal, and industrial waste heat energy sources. Ten different aromatic hydrocarbons and siloxanes were analyzed as potential working fluids using a combination of the BACKONE, Span-Wagner, and REFPROP equations of state. The OFC was compared to the optimized ORC and results showed that the two cycles possessed comparable performances and gave similar power production per unit finite thermal energy reservoir flow rate **[**9**]**. It was determined that although the OFC possessed higher heat addition exergetic efficiency, this did not overcome the exergy destruction introduced by the throttling valve in the flash evaporation process; the net effect being the basic OFC and optimized ORC had comparable net power outputs. In this present study, a number of potential improvements to the basic OFC are proposed and analyzed for improving power production.

4.2 Enhancements to the basic OFC

From the previous analysis **[**9**]**, it was observed that a major source of irreversibilities and exergy destruction in the basic OFC are from the flash evaporation process (state 2→3 in Fig. 4.1) and the liquid throttling process (state 6→7). These two processes respectively, caused about 13% and 6% of the total initial potential work in the finite thermal energy source stream to be lost when using aromatic hydrocarbon working fluids. In the following sections, several modifications to the basic OFC are proposed to mitigate the exergy destroyed in these two processes.

4.2.1 The double flash OFC

The motivation of the double flash OFC is similar to that of the well known double flash steam cycle in geothermal energy. By splitting the flash evaporation process into two steps instead of only one, more of the fluid is vaporized and consequently, more of the fluid can be expanded for power production **[**15**]**. Fig. 4.2 shows the system schematic for the double flash OFC and its corresponding T-S diagram.

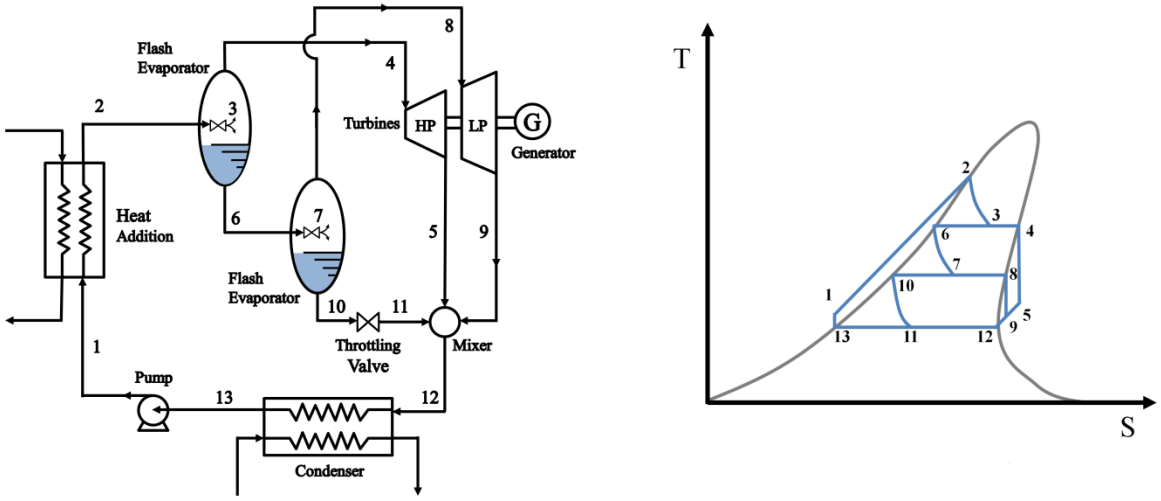

Figure 4.2: System schematic and T-S diagram for the double flash OFC.

Note that the expansion process now occurs in two stages, one at a high pressure after the first flash evaporation step (state 4→5 in Fig. 4.2) and a secondary expansion stage occurs at a lower, intermediate pressure after the second flash evaporation step (state 8→9). Geothermal studies have shown that by introducing a secondary flash step, the double flash steam cycle can generate 15% to 20% more power than the single flash steam cycle for the same geofluid source **[**15**]**.

4.2.2 The modified OFC

The schematic and T-S diagram for the modified OFC is shown in Fig. 4.3. From the preceding analysis **[**9**]**, results showed that the "drying" nature of the organic working fluids caused a substantial degree of superheat at the turbine exit, particularly for siloxanes. Siloxanes are molecularly complex, which have been shown to result in less positively sloped saturated vapor curves on a T-S diagram and correspondingly more superheat after expansion from a saturated

vapor state [30]. The modified OFC was designed with this observation in mind; the working fluid is first flashed to a two-phase mixture (state 2→3 in Fig. 4.3). Similar to the basic OFC, the two-phase mixture is separated (state 3→4 and 3→6), the saturated vapor is expanded through the high pressure turbine to an intermediate pressure (state 4→5), and the saturated liquid is throttled to the same intermediate pressure (state 6→7). The improvement to the basic OFC occurs next when the superheated vapor (state 5) and two-phase mixture (state 7) are combined in the mixer to produce a saturated vapor at the intermediate pressure (state 8), which is then expanded to the condenser pressure producing power.

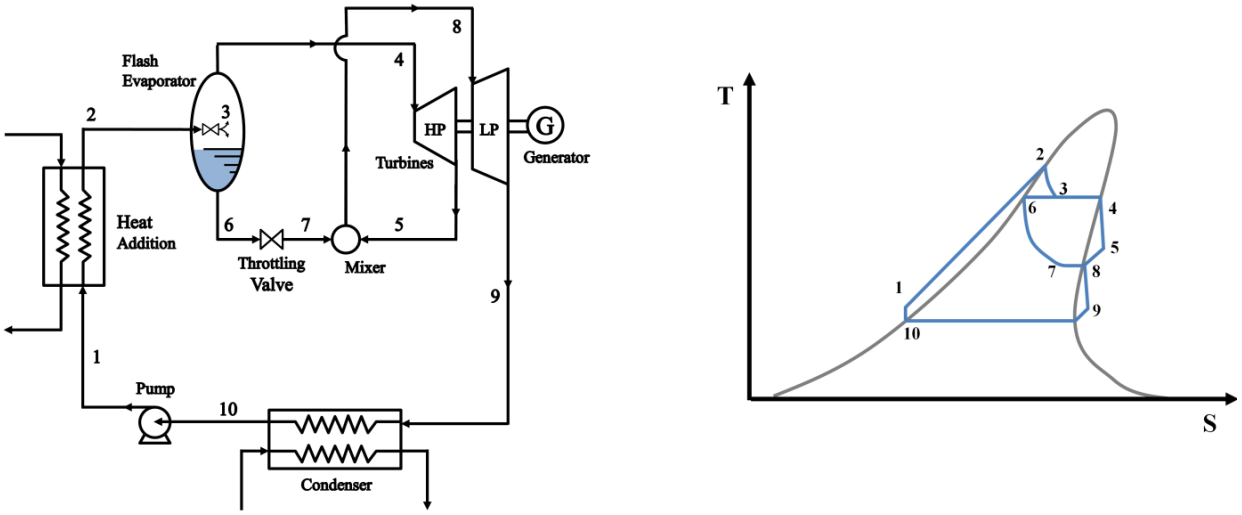

Figure 4.3: System schematic and T-S diagram for the modified OFC.

There are three distinct advantages to this design; the first being more of the fluid goes through the expansion process to produce power. In the basic OFC, saturated liquid separated after the flash evaporation step is throttled to the condensing pressure and never used to generate power and the energy it possessed was essentially lost in the condenser. In the modified OFC, the saturated liquid does produce work after it recombines with the high pressure turbine exhaust and is then expanded in the low pressure turbine (state 8→9). The second advantage that stems from this design is that the fluid is less superheated at the low pressure turbine exit; this can be seen more clearly in the T-S diagram of Fig. 4.3. Expansion to the condenser pressure from a saturated vapor at a lower pressure (e.g. state 8) will produce a state less superheated than expansion from a saturated vapor at a higher pressure (e.g. state 4). Effectively, the excess superheat due to expansion of a "dry" fluid has been used to vaporize more fluid and generate more power. Also, from Carnot considerations, the thermal efficiency of the cycle will increase because heat is now being rejected at a lower temperature since the fluid is less superheated prior to the condenser (state 9). These two advantages should allow for decreased exergy destruction in the condenser and throttling valve compared to the basic OFC. The third advantage of this design is that the fluid is flashed to a lower quality which results in the fluid being at a higher temperature and pressure prior to the high pressure turbine. This also results in reduced exergy destruction in the flash evaporation process since the separated liquid will still be used to produce power in the low pressure turbine.

4.2.3 The 2-phase OFC

Traditionally, the task of designing a reliable and efficient two-phase turbine has been a very challenging because it requires the turbine to be able to handle a fluid with both liquid and vapor behaviors. Tailoring the turbine specifically to one phase or the other is thus not appropriate in this case which has made it difficult to achieve a suitable design **[**69**]**. Presently, radial inflow turbine manufacturers have reported that isentropic efficiencies of about 70% can be achieved reliably in the two-phase regime **[**89**,**91**]**. Significant advances have also been achieved recently for screw-type and scroll-type expanders [86,131]. Smith et al. have designed, built, and tested a twin-screw machine for two-phase expansion that achieved isentropic efficiencies of about 70%; the device is claimed to be both simple and cheap to manufacture **[**90**]**. The attractiveness of 2-phase expanders is that they could potentially replace throttling valves, thereby producing useful work where a source of irreversibility had previously existed. In particular, the refrigeration **[**154**]** and liquefied natural gas (LNG) **[**155**]** industries are highly interested in this technology. In the proposed 2-phase OFC, the flash evaporation throttling valve (state 2→3 in Figure 1) in the basic OFC is replaced with a two-phase expander. The system schematic and T-S diagram of the 2-phase OFC are shown in Figure 4.4.

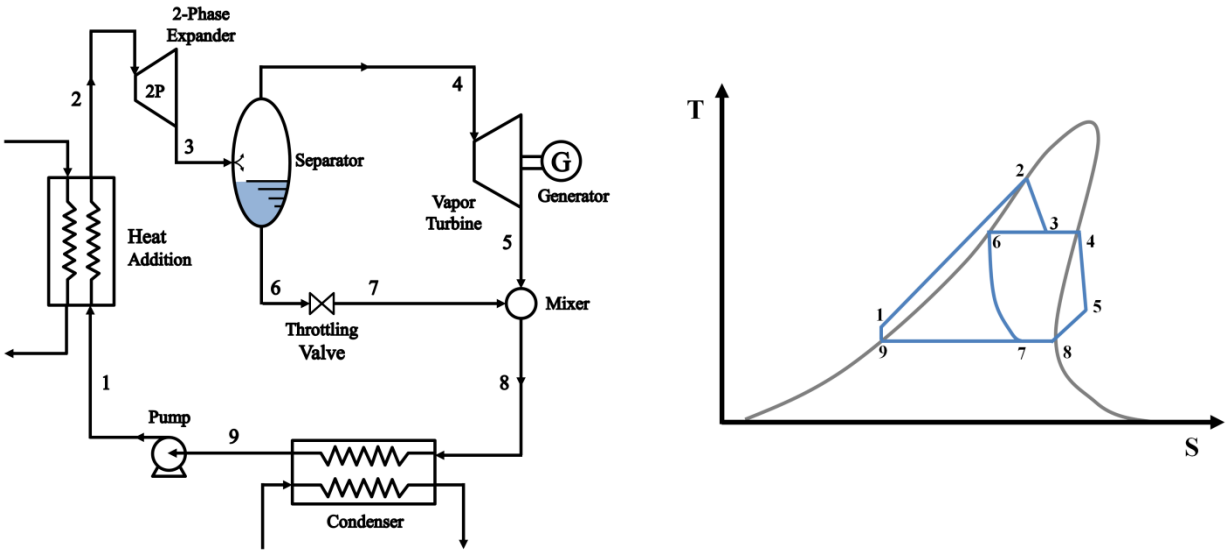

Figure 4.4: System schematic and T-S diagram for the 2-phase OFC.

The resulting cycle resembles the so-called "Smith Cycle" which used an n-pentane working fluid **[**91**]**. Results from Smith et al. showed increases in power output up to 30% over the conventional ORC for the same geothermal source **[**91**]**. Since two-phase expanders are still very much in the research and development phase, in the present analysis, a range of possible isentropic efficiencies from 5% to 70% for a hypothetical 2-phase expander have been assumed.

4.2.4 The modified 2-phase OFC

Combining the enhancements introduced in section 4.2.2 and 4.2.3, the modified 2-phase OFC replaces the throttling valve in the flash evaporation process with a 2-phase expander. It also uses two separate vapor expansion stages to de-superheat the exhaust from the high pressure

turbine, generating more vapor to produce power. The system schematic and corresponding T-S diagram for the modified 2-phase OFC is shown in Fig. 4.5.

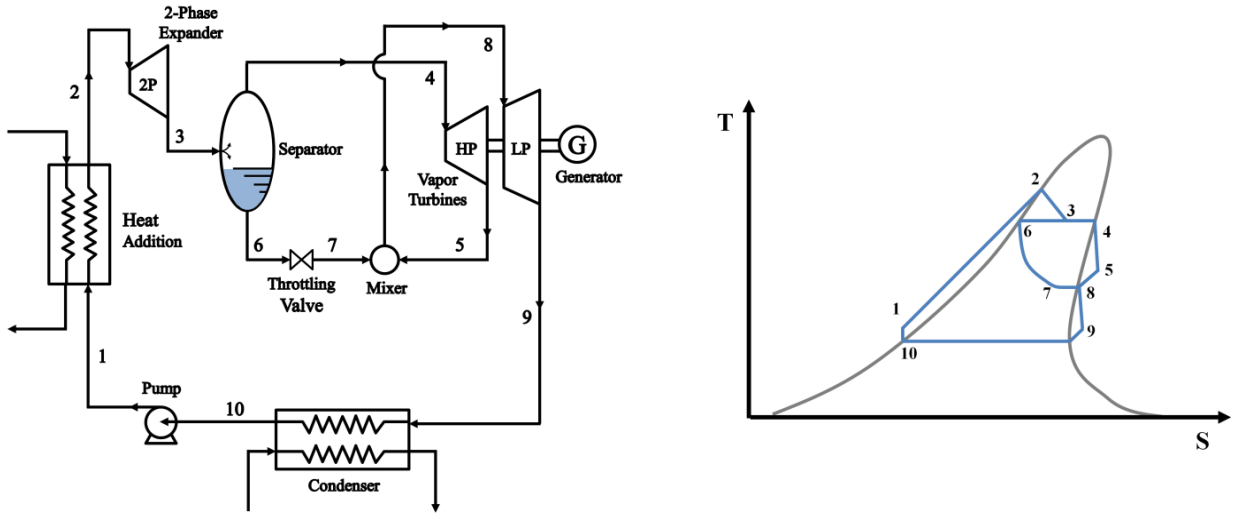

Figure 4.5: System schematic and T-S diagram for the modified 2-phase OFC.

This system is likely to produce the most power; however, it is noted that it is also the most complex of the enhancements suggested. There are a total of three expanders in the system: the 2-phase expander and the high pressure and low pressure vapor turbines. The increase in power output will need considered in respect to the cost of additional equipment when determining the merits of the modified 2-phase OFC and the other enhancements to OFC that have been proposed here.

4.3 Methods of analysis

4.3.1 Equations of state and thermodynamic/exergetic analysis

In chapter 2 and previous works **[**9**]**, a combination of modern equations of state was used to calculate working fluid thermodynamic properties. These equations of state included the BACKONE equations [25,97,98], the Span-Wagner equations [99,103,104,135], and the equations of state compiled in REFPROP 8.0 **[**92**]**. A very brief overview is again provided here; greater details on the applications of these equations of state can be found in chapter 2 and ref. **[**9**]**. Helmholtz explicit equations of state like the BACKONE and Span-Wagner equations can often be cast into the general form shown in eq. (4.1) **[**99**]**,

$$\frac{a(T,\rho)}{RT} = \alpha(T,\rho) = \alpha^0 + \alpha^R \tag{4.1}$$

where a is the Helmholtz free energy, R is the universal gas constant, T is temperature, ρ is density, and α, α^0, and α^R are the total, ideal gas component, and residual component of the reduced Helmholtz energy. The ideal gas portion can be determined relatively straightforward if the ideal gas heat capacity is known. The residual portion though is more complex and can be cast into the general form shown in eq. (4.2),

$$\alpha^R(\tau,\rho) = \sum_{i=1}^{I_{pol}} n_i \tau^{t_i} \delta^{d_i} + \sum_{i=I_{pol}+1}^{I_{pol}+I_{\exp}} n_i \tau^{t_i} \delta^{d_i} \exp\left(-g_i \delta^{p_i}\right) \tag{4.2}$$

where n_i, t_i, d_i, g_i, and p_i are constants dependent on the specific Helmholtz-explicit equation of state selected, δ and τ are respectively the reduced density and inverse reduced temperature with respect to the critical properties, and I_{pol} and I_{exp} are the number of polynomial and exponential terms, respectively **[**99**]**. The Span-Wagner equations use optimized empirical data to determine the coefficients in eq. (4.2), whereas the BACKONE equations use a combination of theoretical/physical basis and empirical data. The appeal of Helmholtz explicit equations of state is that thermodynamic properties can be determined just from a combination of temperature, density, Helmholtz energy, and partial derivatives of Helmholtz energy with respect to temperature and/or density. The disadvantage however, is that complex iterative schemes are necessary when starting from known properties other than temperature and density. The derivations of the thermodynamic properties and common iterative schemes can be found in ref. **[**99**]**. NIST REFPROP 8.0 uses an equation of state explicit in Helmholtz energy, a modified Benedict-Webb-Rubin equation of state, or an Extended Corresponding States (ECS) model depending on the fluid of interest **[**92**]**. REFPROP, BACKONE, and Span-Wagner have all been utilized in a number of ORC studies and these equations of state have been verified that they provide the necessary accuracy for technical analysis of vapor power cycle systems.

Exergy χ defined in eq. (4.3), is again an important variable to quantify a fluid's usefulness and the potentiality for producing work.

$$\chi = h - T_d s \tag{4.3}$$

In eq. (4.3), the subscript *d* designates the property at the dead state which has been taken to be the conditions of the surrounding environment which are assumed to be at 30^oC and atmospheric pressure. It is assumed the energy remaining in the source stream is lost to the environment after it has transferred energy to the power cycle. In this case, the goal again is to maximize the power output from the power cycle per unit flow rate of the finite thermal reservoir. In eq. (4.4), a nondimensional power parameter termed the utilization efficiency is given,

$$\varepsilon = \frac{W_{net}}{\dot{m}_s\left(\chi_{s,in} - \chi_{s,d}\right)} \tag{4.4}$$

where $\dot{m}_s$ represents the source flow rate, $\chi_{s,in}$ is the source's inlet exergy, and $\chi_{s,d}$ is the source's exergy at the dead state. The utilization efficiency is essentially a ratio of the actual power produced to the maximum theoretically power initially available in the thermal energy reservoir.

Common simplifying assumptions such as neglecting frictional losses in the piping and heat exchangers have been employed in this study [4,9]. It is also assumed that working fluid's kinetic and potential energies changes are small and negligible and that the cycle components are well insulated so they do not lose significant energy to the surroundings. Throttling valves are modeled as isenthalpic devices; mixing chambers and separators are assumed to be isobaric and adiabatic with no work interactions. Turbines and pumps are assumed to have 85% isentropic

efficiency. A thermodynamic model for the OFC and the proposed enhancements was constructed using MATLAB; the equations of states were also programmed into MATLAB to determine thermodynamic properties of the 10 working fluids considered in this study. These fluids are shown in Table 3.1 with the respective equation of state that was used also listed.

4.3.2 Optimization of the OFC with proposed enhancements

For the basic OFC, optimization entailed determining the conditions at state 3 of Figure 3.1 that would yield the greatest power output. Using some simplifying assumptions, the "equal-temperature-split-rule" was shown to be a good initial estimate for state 3 **[**15**]**; in the previous analysis **[**9**]**, the authors used an iterative algorithm to determine state 3 for the optimized basic OFC. For the double flash OFC, an extra degree of freedom makes the optimization more complex; however, the "equal-temperature-split-rule" again provides a good initial estimate to start the simultaneous iterative functions to determine the optimal states for state 3 and state 7 of Fig. 4.2. For the modified OFC, the fluid is set to a saturated vapor state before entering the low pressure turbine so that the fluid is minimally superheated prior to the condenser. The optimization procedure for the modified OFC is again more complex than the basic OFC because of the added degree of freedom in selecting the intermediate pressure between the high pressure turbine inlet and the condensing pressure. For the 2-phase OFC, the number of degrees of freedom is similar to that of the basic OFC. The modified 2-phase OFC also possesses an additional degree of freedom more than the basic OFC, and simultaneous iterative functions for state 3 and intermediate pressure at state 5, 7, and 8 of Fig. 4.5 are required to determine the optimal conditions for maximum power output. The proposed cycles were optimized with iterative functions available in the MATLAB optimization toolbox.

4.4 Results and discussion

The proposed enhancements to the OFC were studied for the 10 aromatic hydrocarbon and siloxane working fluids that had been suggested in the previous chapter for the single-flash OFC. An intermediate temperature finite thermal energy source in the form of a 1kg/s stream of water available initially at 300^{o}C is again assumed as it is representative of the previously discussed energy sources such as single-axis solar thermal technology. A heat sink is assumed to be available that allows for a minimum cycle temperature of 40^{o}C for the saturated liquid at the exit of the condenser. A minimum 10^{o}C temperature difference is assumed necessary to properly transfer energy in the heat exchangers; the mass flow rate of the power cycle is adjusted to the maximum value that produces maximum power while still maintaining a 10^{o}C pinch.

Fig. 4.6 show the resulting utilization efficiencies for the optimized basic ORC, OFC, double flash OFC, modified OFC, and 2-phase OFC and modified 2-phase OFC both with a 70% isentropic 2-phase expander. Fig. 4.7 shows the resulting percent increases or decreases in power output for the OFCs compared to the optimized ORC, which had been analyzed in detail in chapter 3 and in ref. **[**9**]**. From Fig. 4.6, it is observed that the modified 2-phase OFC produced the greatest power from the same finite thermal sources of all the cycles analyzed. This was true for all 10 working fluids examined; in addition, it can be seen that the proposed enhancements to the OFC had a much greater effect for aromatic hydrocarbon working fluids than for siloxanes.

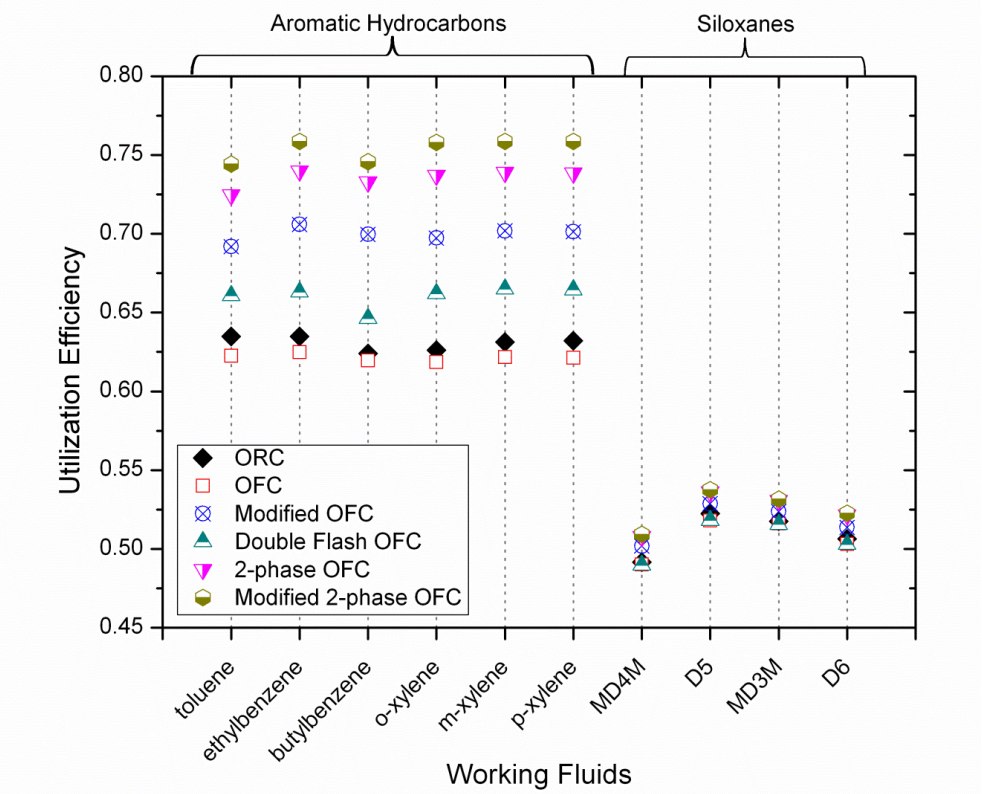

Figure 4.6: Utilization efficiencies for the optimized ORC and the OFC with proposed enhancements.

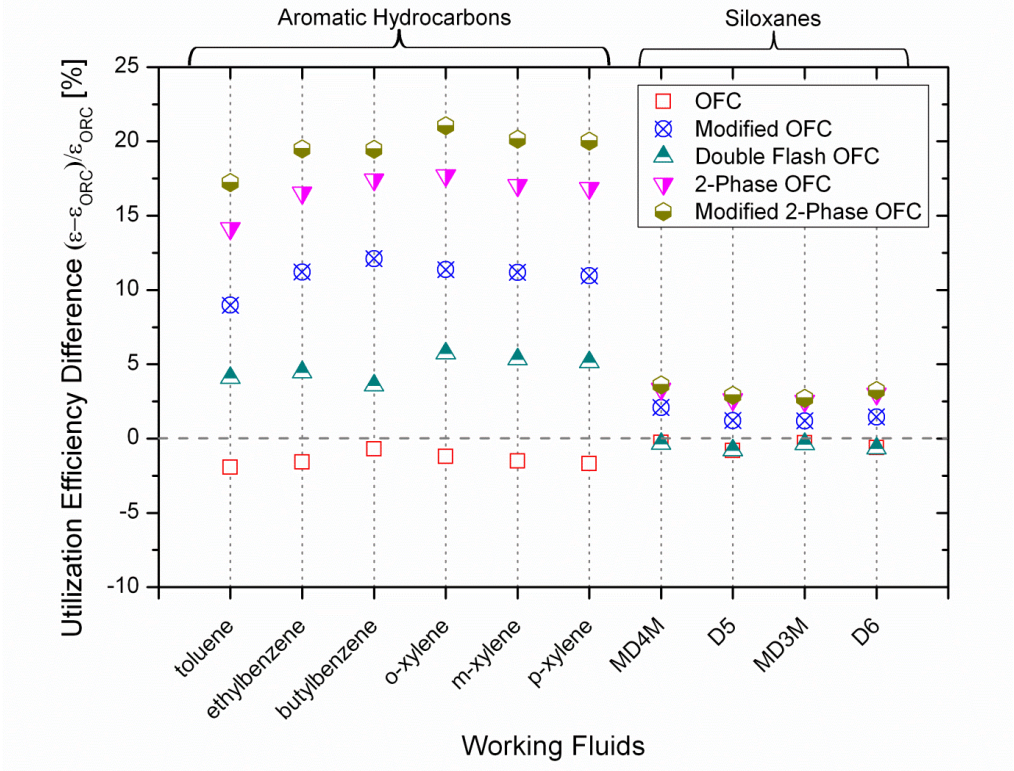

Figure 4.7: OFC percent difference in power output compared to the optimized ORC.

Tables 4.1 and 4.2 give the conditions at several important states for the optimized basic OFC and double flash OFC respectively. The main advantage of double flash OFC is the generation of additional vapor for power production. Comparing Tables 4.1 and 4.2, it can be seen that for aromatic hydrocarbon working fluids, the vapor produced from flash evaporation is at a higher temperature but lower quality than for the basic OFC. Although the total amount of fluid expanded are similar for the single flash OFC and double flash OFC, more power is produced because the first flash step results in a higher exergetic state. Results showed the exergy destruction from the flash evaporation processes decreased by approximately 20-30% for the double flash OFC compared to the single flash OFC. In theory, additional flash steps could be added, but the improvements in efficiency diminishes with each additional step and additional steps beyond a secondary flash would not be cost-justified **[**15**]**.

Table 4.1: Important state points for the basic OFC (from Fig. 4.1) **[**9**]**

Fluid Name	T_2† [K]	T_3 [K]	q_3	$\dot{m}_{OFC}$ [kg/s]
toluene	559	457	0.87	1.92
ethylbenzene	561	453	0.89	1.90
butylbenzene	563	452	0.94	1.85
o-xylene	562	452	0.86	1.90
m-xylene	561	453	0.87	1.92
p-xylene	561	453	0.87	1.93
MD4M	557	507	1.00	2.31
D5	558	509	1.00	2.43
MD3M	552	502	1.00	2.33
D6	557	507	1.00	2.46

†State point 2 for the optimized basic OFC is a saturated liquid ($q_2 = 0$). This value for T_2 and $\dot{m_{OFC}}$is applicable to the basic OFC and to the OFC with the proposed enhancements.

Table 4.2: Thermodynamic states for key points for the double flash OFC (from Fig. 4.2)

Fluid Name	T_3 [K]	q_3	T_7 [K]	q_7
toluene	494	0.66	410	0.56
ethylbenzene	489	0.68	407	0.56
butylbenzene	486	0.72	405	0.58
o-xylene	489	0.64	406	0.54
m-xylene	489	0.65	407	0.55
p-xylene	490	0.65	407	0.55
MD4M	507	1.00	-	-
D5	509	1.00	-	-
MD3M	502	1.00	-	-
D6	507	1.00	-	-

From Table 4.2, it is noted that for siloxanes, maximum power output was achieved for conditions where the working fluid was completely flash evaporated into a saturated vapor in the first step. In other words, for maximum power output for siloxanes, all the flow should be vaporized at state 3 and sent through the high pressure turbine. The optimal double flash OFC for siloxanes actually defaults to the optimized single flash OFC. This was a significant difference from aromatic hydrocarbons which showed the greater power output with two flash steps. For siloxanes, their vapor dome on a T-S diagram is actually very narrow due in part to their high molecular complexity and very "drying" behavior; therefore, the net change in specific entropy between saturated liquid and saturate vapor states is much smaller for siloxanes than for aromatic hydrocarbons. This property causes substantially less exergy to be destroyed during isenthalpic throttling from a saturated liquid to a saturated vapor for siloxanes. At lower temperatures, the vapor dome broadens and the exergetic losses during isenthalpic expansion increases. In a double flash OFC for siloxanes, less power would actually be produced because no additional vapor is actually being produced with two flash steps compared to single flash OFC for siloxanes; in addition, the two flash steps would actually be less efficient than a single one for this particular type of working fluid. Results for the single flash OFC actually showed that flash evaporation only contributed to approximately 4-5% of total exergy destruction/losses for siloxanes.

As noted in the previous chapter and ref. **[**9**]**, the majority of the exergy losses for siloxanes occur in the condenser because of their highly "drying" behavior that causes substantial superheat and high temperatures at the turbine exit (~190^{o}C turbine exhaust temperature for siloxanes compared to ~70^{o}C for aromatic hydrocarbons). Energy recovery from the turbine exhaust in the form of an additional power cycle or combined heat and power would be necessary for a siloxane OFC or ORC so that the high quality energy, due to its high temperature, is not wasted. In addition, siloxane working fluids may face challenges in the practical design of an inexpensive and simple turbine due to potentially very high turbine volumetric flow ratios which is discussed in the previous chapter and in ref. **[**9**]**, particularly for MD4M and D6.

Results from Figures 4.6 and 4.7 show that the modified OFC can produce significantly more power than the double flash OFC per unit flow rate from the same thermal energy reservoir. The modified OFC is also more attractive than the double flash OFC in terms of system simplicity because a second flash evaporator is not required. Table 4.3 gives some important state points for the optimized modified OFC. Note that when comparing Table 4.2 and 4.3, the temperature of state 3 and 7 for the double flash OFC is comparable to the temperature of state 3 and 8 for the modified OFC. This suggests similar exergy content in the fluid prior to entering the high pressure and low pressure turbines. However, the vapor quality at state 7 for the double flash OFC is significantly smaller than that for the saturated vapor at state 8 for the modified OFC vapor (q_8 = 1). The modified OFC configuration produces more power because all the flow is expanded through the low pressure turbine. In addition, less energy is lost in the condenser because the fluid is less superheated at the low pressure turbine exit and energy from the separated saturated liquid after flash evaporation is also utilized to produce power. This was the original motivation for the modified OFC as discussed in section 4.2.2.

Table 4.3: Thermodynamic states for key points for the modified OFC (from Fig. 4.3)

Fluid Name	T_3 [K]	q_3	P_8* [kPa]	T_8* [K]
toluene	495	0.65	180	405
ethylbenzene	494	0.64	109.9	412
butylbenzene	500	0.61	47.6	428
o-xylene	488	0.64	60.9	399
m-xylene	491	0.65	79.6	403
p-xylene	491	0.65	81.2	403
MD4M	539	0.54	65.5	514
D5	540	0.55	195.9	514
MD3M	540	0.55	133.7	515
D6	539	0.54	91.3	513

*State 8 corresponds to a saturated vapor state (q_8 = 1).

In Figures 4.6 and 4.7, a two-phase expander with a 70% isentropic efficiency was assumed for the 2-phase OFC and modified 2-phase OFC. This isentropic efficiency corresponds to results given by some two-phase expander studies [69,89-91]. To examine the how 2-phase expander efficiencies impacts total system efficiency, Fig. 4.8 and 4.9 show a range of hypothetical two-phase expander isentropic efficiencies for the 2-phase OFC and the resulting utilization efficiency and percent improvement over the optimized ORC.

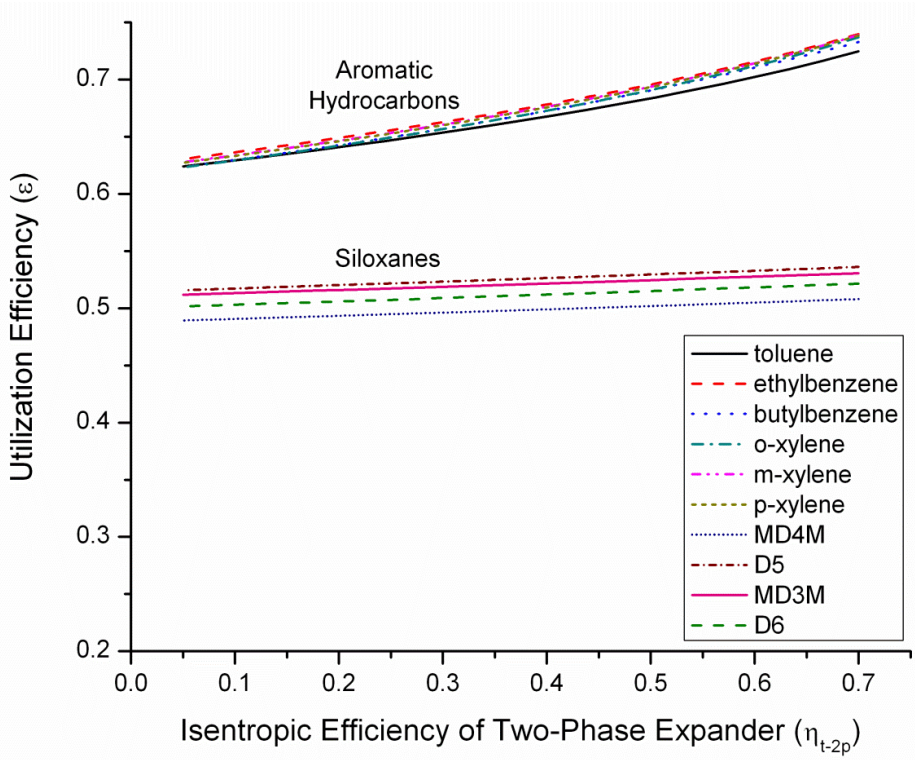

Figure 4.8: 2-phase OFC utilization efficiencies for varying 2-phase expander isentropic efficiency.

Note that the two-phase expander isentropic efficiency is of greater importance to aromatic hydrocarbons than siloxanes for improved performance. As mentioned previously, exergy destruction in the flash evaporation process only amounted to about 4-5% of total exergy destruction/losses for siloxanes. For siloxanes, there is less potential exergy to be recovered by replacing the throttling valve with a two-phase expander. Fig. 4.9 shows that a 2-phase expander of at least a 10-15% isentropic efficiency is necessary for an aromatic hydrocarbon 2-phase OFC to generate the same power as the optimized ORC. For a siloxane 2-phase OFC, a 2-phase expander of at least a 30% isentropic efficiency is necessary to reach the same power output as an optimized ORC. In practice, the necessary 2-phase isentropic expander efficiencies would need to be significantly higher than the previously listed values to justify the cost and complexity. DiPippo suggests that isentropic efficiencies of at least 75% are necessary before practical implementation of 2-phase expanders into binary geothermal plants is feasible **[**156**]**.

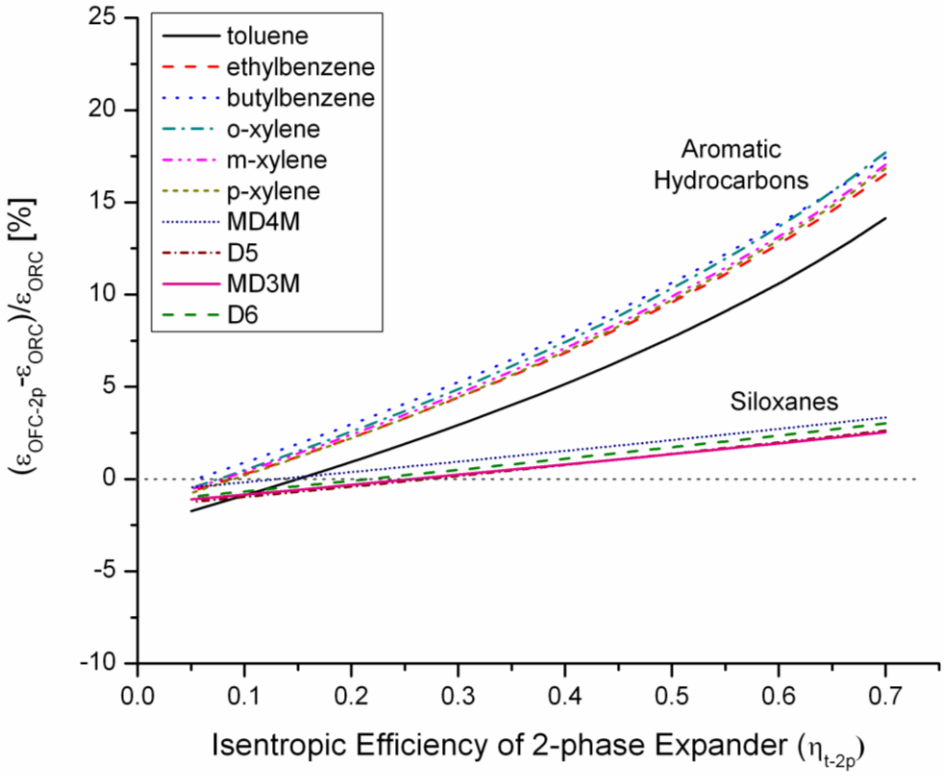

Figure 4.9: 2-phase OFC percent difference in utilization efficiency compared to the optimized ORC for varying 2-phase expander isentropic efficiency.

Combining the advantages of the modified OFC and the 2-phase OFC, the modified 2-phase OFC showed the greatest power output of the proposed enhancements in this study as shown by Fig. 4.6. For aromatic hydrocarbon working fluids, the modified 2-phase OFC produced approximately 76% of the theoretically available power initially in the finite thermal energy source. For the same finite thermal energy source, the modified 2-phase OFC produced approximately 20% more power than the optimized conventional ORC. Although this cycle does generate substantially more power, this needs to be evaluated in respect to the additional complexity and equipment costs. The modified OFC could be an attractive compromise between high power output and additional equipment costs. By only adding an additional low pressure

turbine to the basic OFC, a 10%-12% increase in power output compared to the optimized ORC is achievable for aromatic hydrocarbons without the requirement of a 2-phase expander. The heat exchangers for the modified OFC would also be less expensive than the basic OFC because more power is being produced which reduces the total heat rejection rate in the condenser and subsequently decreases the necessary heat transfer area for the condenser. Heat exchanger surface area is often used as a rough guide to total system cost in many ORC studies.

4.5 Conclusions

Several enhancements to the basic Organic Flash Cycle (OFC) were proposed to improve power output per specific flow rate of a given finite thermal energy reservoir. Some of the sources of inefficiencies in the basic OFC configuration included irreversibilities generated by the flash evaporation process and the considerably high exergy content at the vapor turbine exhaust due to significant vapor superheat. The BACKONE, Span-Wagner, and REFPROP equations of state were used to calculate the working fluid thermodynamic property data. Ten aromatic hydrocarbon and siloxane working fluids were reexamined from chapter 2 for the OFC with proposed enhancements such as double flashing, two-phase expanders, using energy in the separated liquid in a low pressure turbine and reducing vapor superheat prior to the condenser. Results showed that the modified OFC using aromatic hydrocarbons can produce approximately 10% higher power output than the optimized ORC. Combining this technique with presently available two-phase expander technology would yield approximately 20% greater power output than the optimized ORC for aromatic hydrocarbons. Results for the enhanced OFC for siloxanes were less promising as increases in power output ranged from only 2-4%. Based on results from this study, further research into other possible modifications of the OFC seems warranted for aromatic hydrocarbon working fluids. Research for the OFC for low temperature resources such as non-concentrating solar thermal may also have potential applications and are presented in the next chapter.

5 The applicability of the Organic Flash Cycle (OFC) for improved power production from low temperature finite thermal resources

5.1 Introduction

Low temperature thermal energy reservoirs has been continually cited as being one of the most abundant sources of energy both in terms of the number of possible resources and the total energy content available from these resources. The ability to generate cost-effective electricity from these resources would significantly raise system efficiencies and save fuel by basically recovering energy that otherwise would have been wasted. Thermal pollution and the production of global warming gases would also be significantly reduced because less heat is rejected by the system and less fuel is being consumed. A vast number of underutilized low temperature renewable energy resources such as non-concentrated solar thermal, low temperature geothermal, biomass, and waste heat from industrial processes, power plants, and buildings could then be used to generate electricity **[**157**]**. The lack of efficient, inexpensive methods of low temperature energy conversion though continues to be the primary cause of these resources remaining unutilized or underutilized. A preliminary study conducted at Lawrence Berkeley National Laboratory showed that a potential of nearly 100,000MW in electrical power could be generated from waste heat energy alone; this amount would be equivalent to about 19% of total present U.S. electricity consumption. This same study also estimated that this would result in a reduction of 400 million metric tons of CO_2 and 630,000 metric tons of NOx **[**158**]**. It is estimated that 20% to 50% of the input energy for industrial processes is ultimately lost as waste heat energy such as exhaust gases and cooling water **[**3**]**. Fig. 5.1 and Table 5.1 both show that of the recoverable waste heat resources from industrial processes and utilities, the majority of this energy is available at low temperatures below 300°F (~150°C) **[**159**]**. A number of non-concentrated solar thermal collectors also operate within this temperature range such as flat plate collectors (30°C-90°C), evacuated tube collectors (90°C-200°C), and solar ponds (70°C-90°C) **[**13**,**130**]**. The ability to effectively generate electricity from low temperature sources would also support a distributed energy grid.

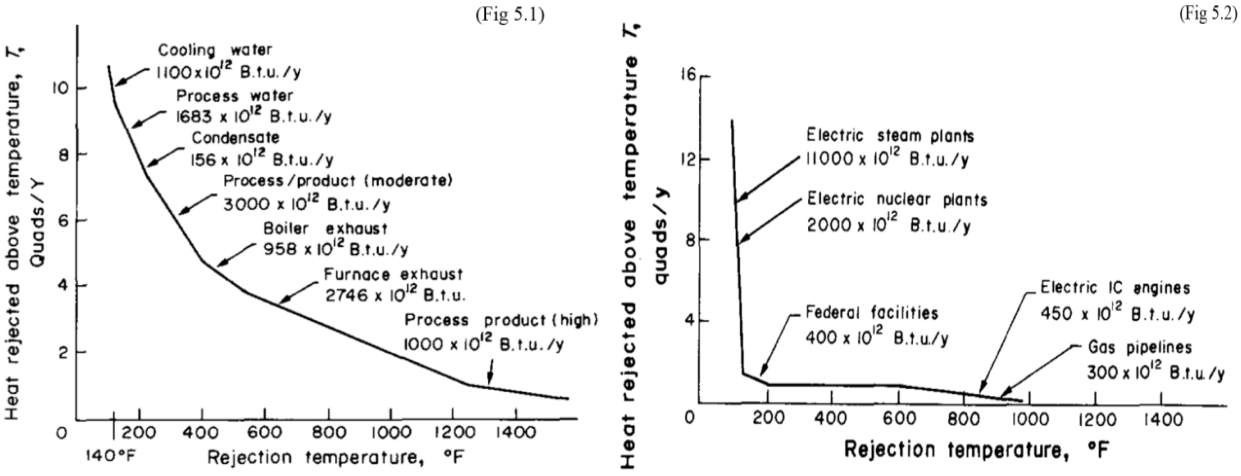

Figure 5.1: (a) Distribution of rejected industrial waste heat; (b) Distribution of rejected utility waste heat. Reprinted with permission from Elsevier: *Energy Conversion and Management*, copyright 1982 [**159**].

Table 5.1: Temperature ranges of some waste heat energy sources **[**3**]**.

Source	Temperature [^{o}C]
Exhaust gases from gas-fired boilers, ethylene furnaces, etc.	70-230
Process steam condensate	50-90
Cooling water from:	
Annealing furnaces	70-230
Internal combustion engines	70-120
Drying, baking, and curing ovens	90-230
Hot processed liquids/solids	30-230

The primary heat engine for low temperature heat resources has been Organic Rankine cycles (ORC), although recent research has shown that transcritical CO_2 vapor cycles and vapor cycles that utilize zeotropic mixtures such as the Kalina cycle may also be viable **[**3**]**. As discussed in previous chapters, these types of vapor cycles try to improve the exergetic efficiency of the heat addition process by enhanced temperature matching. By using a mixture that changes temperature during phase change as in the case of zeotropic Rankine cycles or by adding heat above the critical pressure as in transcritical cycles, isothermal phase change and the poor temperature matching that results can be avoided. However, as discussed in the preceding chapters, these cycles are not without their own challenges that have slowed their adoption and implementation. The Organic Flash Cycle (OFC) and the proposed enhancements that were suggested in chapter 4 are analyzed for their suitability for low temperature resources in the 80^{o}C to 150^{o}C regime.

In the previous chapters, aromatic hydrocarbons and siloxanes were introduced as potential working fluids for the OFC operating in the intermediate temperature range ~300^{o}C. These working fluids, however, would not be suitable in the low temperature range because of the resulting low condensing vapor pressures and their high volumetric turbine flow ratios. Low temperature resources are often harnessed for small scale power generation; therefore, large, expensive, multistage turbines would not be cost justified for this application. Extra equipment such as deaerators to remove air that leaks into the systems should also be avoided by selecting a working fluid whose vapor pressure is above atmospheric in the condenser. For low temperature resources, refrigerants and alkanes are the more often suggested working fluids for ORCs exactly for this reason [22,136,160,161]. Besides having desirable thermodynamic properties, it is also important that the cycle working fluid should have low Ozone Depletion Potential (ODP) and Global Warming Potential (GWP), toxicity, and flammability to mitigate the harmful environmental impacts in the case of working fluid leakage **[**162**]**. The fluid should also possess high chemical stability at the desired operating temperatures and low corrosiveness to prevent damage to piping and other plant equipment **[**163**]**.

In this chapter, the OFC is analyzed and compared to the optimized ORC for a number of alkane and refrigerant working fluids. The OFC with enhancements recommended in chapter 4 is also examined to see how these improvements improve the OFC performance relative to the

optimized ORC. A brief discussion of the corresponding turbine design for the different working fluids is also given.

5.2 Working fluids and methods of analysis

In Table 5.2 and Table 5.3, the alkane and refrigerant working fluids considered for low temperature power generation applications are given along with their corresponding critical temperature and vapor pressures at the minimum condenser temperature of 313K. The equations of state compiled in NIST REFPROP 8.0 are integrated with MATLAB to calculate thermodynamic properties for different state points of the low temperature vapor cycles. Aside from the fluids listed in Table 5.2 and 5.3, REFPROP also contains equations of state to calculate thermodynamic properties for a large number of common industrial refrigerants and hydrocarbons often encountered in combustion and refrigeration processes.

Table 5.2: Select properties for alkane working fluids

Working Fluid	Critical Temperature [K]†	Vapor Pressure at T=313K [kPa]
Nonane	594.55	1.4018
Octane	569.32	4.0954
Hexane	507.82	37.076
Heptane	540.13	12.245
Isohexane	497.70	50.428
Isopentane	460.35	150.79
Pentane	469.70	115.09
Cyclohexane	553.64	24.478

†From ref. **[**92**]**

Table 5.3: Select properties for refrigerant working fluids

Working Fluid	Critical Temperature [K] †	Vapor Pressure at T=313K [kPa]
R245ca	447.57	172.58
R365mfc	460.00	100.08
R113	487.21	77.837
R123	456.83	153.71
R141b	477.5	132.24

†From ref. **[**92**]**

Depending on the fluid, REFPROP will apply either an equation of state explicit in Helmholtz energy which has been discussed in detail in chapter 2, the modified Benedict-Webb-Rubin equation of state shown in one of its original forms in eq. (5.1), or an Extended Corresponding States (ECS) model for fluids with limited data **[**92**,**164**]**.

$$P = \rho RT + \left(B_{BWD} RT - A_0 - \frac{C_{BWR}}{T^2} + \frac{D_{BWR}}{T^3} - \frac{E_{BWR}}{T^4} \right) \rho^2 + \left(bRT - a - \frac{d}{T} \right) \rho^3 + \alpha \left(a + \frac{d}{T} \right) \rho^6 + \frac{c\rho^3}{T^2} \left(1 - \gamma\rho^2 \right) e^{-\gamma\rho^2} \tag{5.1}$$

In eq. (5.1), R is the universal gas constant, ρ the molar density, and A_{BWD}, B_{BWD}, a, b, etc. are the fluid specific parameters **[**164**]**. For the vast majority of the fluids listed in Tables 5.2 and 5.3 though, the equation of state used in REFPROP was a Helmholtz energy explicit equation. All the equations of states incorporated in REFPROP are verified to be highly accurate; in fact they represent the most accurate models currently available to the public. Due to their high reliability and accuracy, REFPROP have been incorporated in a number of ORC studies in the literature as well **[**34**,**36**,**129**]**. Aside from REFPROP, EES is also another often cited computational tool in ORC research and other technical applications [77,78].

As was done in the preceding analysis, it is assumed that the energy remaining in the low temperature thermal energy source is lost to the environment after it has transferred heat to the power cycle. Therefore, similar to the preceding analysis, the objective again is to maximize power output per unit flow rate of the low temperature finite thermal reservoir. The idea of exergy χ is again used as a variable to help quantify a fluid's availability to produce work at a given thermodynamic state. The nondimensional power parameter, utilization efficiency, is again used to compare the cycle's actual power produced to the amount of theoretical power available initially in the finite thermal energy reservoir. Both exergy and the utilization efficiency definitions are shown in eq. (5.2) and (5.3) respectively for convenience.

$$\chi = h - T_d s \tag{5.2}$$

$$\varepsilon = \frac{W_{net}}{\dot{m}_s \left(\chi_{s,in} - \chi_{s,d} \right)} \tag{5.3}$$

In eq. (5.2) and (5.3), the subscript d designates the property at the dead state, $\dot{m}_s$ is the energy source flow rate, $\chi_{s,in}$ is the source's inlet exergy, and $\chi_{s,d}$ is the source's exergy at the dead state. The conditions of the ambient environment are again assumed to be at 30^{o}C and atmospheric pressure and have been taken as the definition of the dead state.

Typical high-level power cycle analysis assumptions such as neglecting frictional losses in the piping and heat exchangers have been employed **[**4**,**9**]**. Changes in kinetic and potential energies are neglected and the steady flow devices in the vapor cycle are considered well insulated such that no significant energy is lost to the surroundings. As was done in the analysis in the preceding chapters, throttling valves are modeled as isenthalpic devices; mixing chambers and separators are modeled to be isobaric and adiabatic with no work interactions. The vapor turbines and feed pumps are assumed to possess 85% isentropic efficiency. Using REFPROP to model the difference working fluids thermodynamic properties, the low temperature optimized ORC, OFC, and the OFC with proposed enhancements from chapter 4 were modeled using MATLAB. REFPROP was interfaced with MATLAB using a ".mex" file available from NIST **[**92**]**.

5.3 Results and discussion

The low temperature optimized ORC and OFC were modeled for the 13 working fluids listed in Tables 5.2 and 5.3. A finite thermal energy reservoir is assumed to available as a 1kg/s stream of water initially at temperatures from 80°C-150°C, representing a wide spectrum of potential low temperature energy sources that have been discussed. The ambient environment is the assumed available heat sink; this allows for a reasonable assumption of a minimum cycle temperature of 40°C for the saturated liquid at the exit of the condenser. Again, the pinch temperature is assumed to be 10°C, this minimum temperature difference is verified at different points along the heat exchanger to ensure that a large enough temperature difference exists to adequately facilitate heat transfer between the streams. From a steady state 1st law analysis, the thermodynamic state points are determine and the mass flow rate of the power cycle is adjusted to the maximum value such that maximum power is produced while maintaining the aforementioned 10°C pinch. Optimization of the power cycle depends on the number of variable state points, such as turbine inlet pressure and temperature, flow rate, etc. A discussion of the number of degrees of freedom specific to each of the discussed power cycles for optimization can be found in section 4.3.2.

5.3.1 Optimized ORC

Similar to the analysis for intermediate temperatures finite thermal sources, the basic ORC is first optimized with respect to the available design parameters: mass flow rate, turbine inlet temperature, and turbine inlet pressure. A system schematic and T-S diagram for the basic ORC is reproduced in Fig. 5.2 for convenience. Note that in the T-S diagram in Fig. 5.2, a "dry" fluid has been assumed and the saturated vapor curve's slope is now positive, as oppose to Fig. 3.1 which assumed a "wet" working fluid. Also note, this T-S diagram accurately displays how the optimized ORC cycle looks for a "dry" fluid based on the results in section 3.4.1 where it was shown that for maximum utilization efficiency, the "dry" working fluid should be a saturated vapor prior to expansion. This behavior for the optimized ORC was also observed for the low temperature range as shown in Fig. 5.3 where the utilization efficiency is plotted against turbine inlet pressure ratio for several turbine inlet temperatures for a pentane ORC as an example.

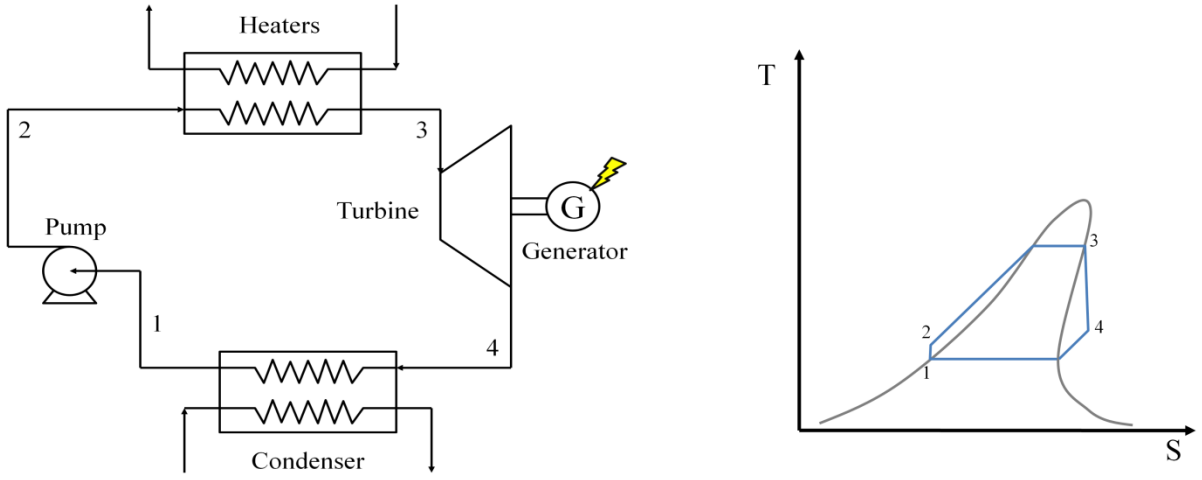

Figure 5.2: System schematic and T-S diagram for the optimized ORC using a "dry" fluid

Note that similar to Fig. 3.3, the optimum ORC at low temperature possesses a turbine inlet temperature much lower than the source temperature in Fig. 5.3. At turbine inlet temperatures close to the source temperature such as 130°C, the curves reach peak utilization efficiency when the fluid is highly superheated at state 3. At higher pressures, poor temperature matching and the pinch limitations restricts the cycle flow rate and ultimately the energy being transferred to the ORC.

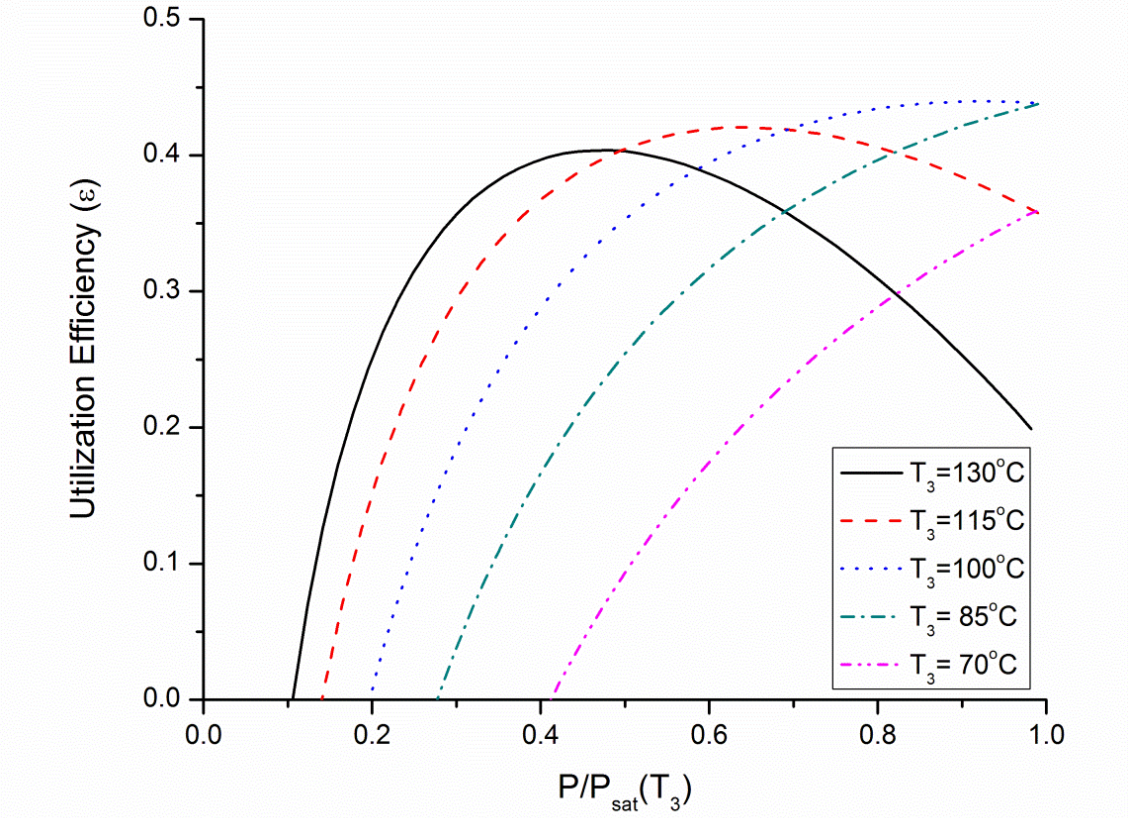

Figure 5.3: Utilization efficiencies for a pentane ORC with an initial source temperature of 150°C

As the turbine inlet temperature decreases, the maximum of the utilization efficiency curves in Figure 5.3 increase and shift towards the right. The maximums of the curves increase because the lower the superheat and the closer fluid is to a saturated vapor at state 3, the less superheated the fluid is at state 4 of Fig. 5.3. As in the intermediate temperature case, for the low temperature case high superheat in the turbine exhaust causes higher temperature heat rejection in the condenser and lowers cycle thermal efficiencies based on Carnot considerations. As the temperature at state 3 continues to decrease, the maximum of the curves begin to increase, but the maximum still occurs when the fluid is a saturated vapor at the turbine inlet. Reducing the turbine inlet temperature no longer reduces the turbine exhaust's superheat and the corresponding average heat rejection temperature anymore; instead, it now just lowers the average heat addition temperature which reduces efficiency. It is important to point out again this counterintuitive result that the condition for maximum power output per unit flow from the energy source occurs at a turbine inlet temperature significantly below the initial temperature of the heat source because of the nature of "dry" fluids being used.

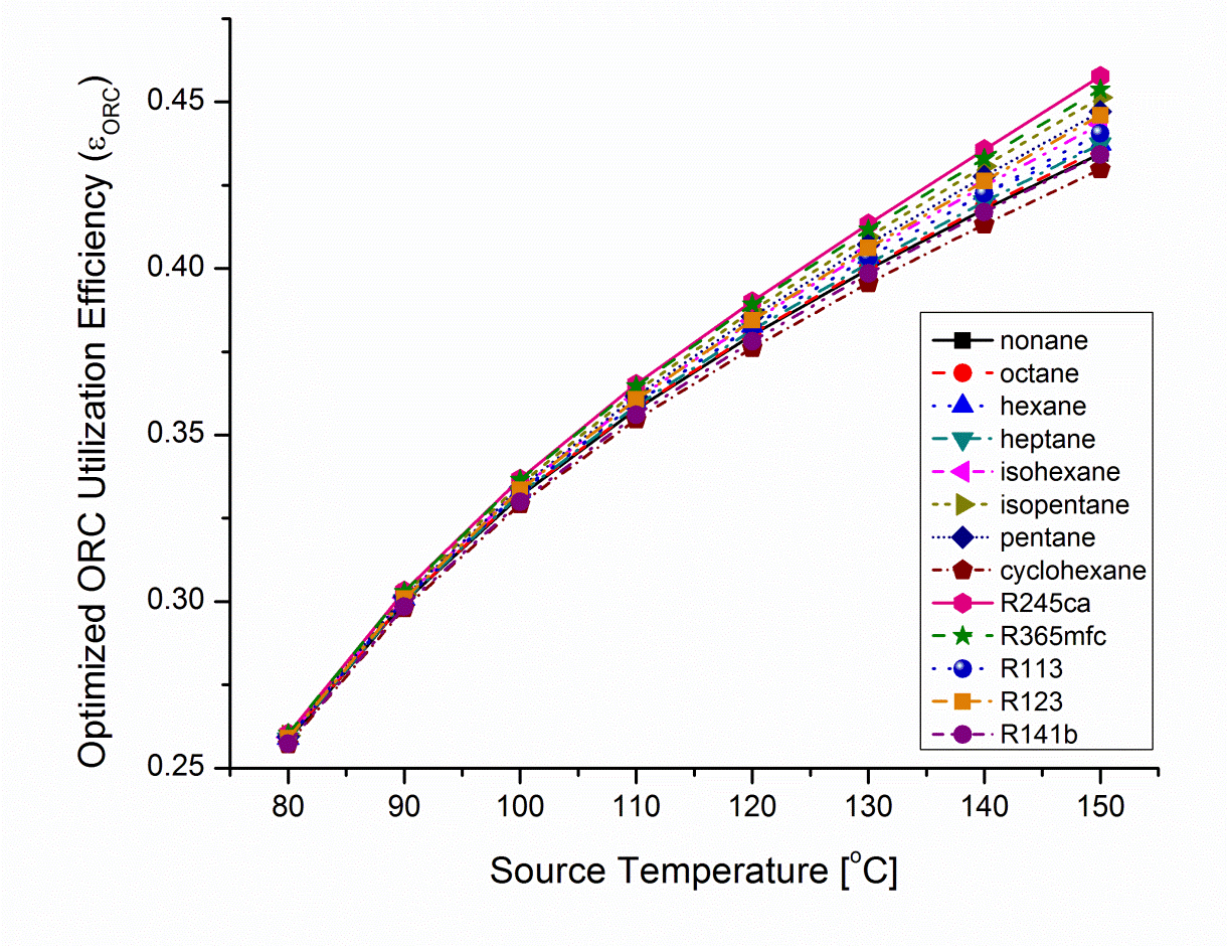

Figure 5.4: Utilization efficiencies for the optimized ORC at different initial finite thermal source temperatures

The ORC was optimized for each of the working fluids considered and the results are shown in Fig. 5.4 for initial finite thermal energy source temperatures from 80°-150°C. Unlike the results in Fig. 3.6 for the optimized intermediate temperature ORC that showed significant difference in performance between aromatic hydrocarbon and siloxane working fluid types, no large discernible difference in behavior or performance between alkanes and refrigerants is observed in Fig. 5.4. At higher source temperature, results from Fig 5.4 show R245ca, R365mfc, isopentane, and pentane to generate the greatest power output. These four fluids are all slightly less drying than some of the more complex alkanes such as octane and heptane, making the slope of their saturated vapor curve more positive. Expansion from a saturated vapor state results in less superheating and higher 2nd law internal efficiencies for the cycle.

At lower and lower source temperatures, the maximum power output for the different working fluids begins to approach each other. This is because at lower temperatures, the difference between the inlet and exit turbine temperature and pressure the working fluids becomes small as the differences in the working fluids' saturated vapor curve becomes less pronounced. Although fluids such as R245ca and pentane continue to produce more power, the difference begins to be a smaller and smaller portion compared to the total power generated for lower temperature

resources. This result would suggest that for low temperature energy resources such as solar ponds (70°C-90°C), the working fluid used in the optimized basic ORC makes little difference as far as thermodynamic performance. For these low temperature sources, greater importance should be placed on parameters such as environmental impact and heat transfer characteristics as the thermodynamic characteristics of the fluid and its effect on the optimized ORC seems to be minimal.

5.3.2 Optimized single flash OFC

As described in section 3.2, the OFC attempts to achieve higher net power output by increasing temperature matching to the energy source and thus the heat addition exergetic efficiency such that it is able to overcome the irreversibilities introduced into the system by flash evaporation. The cycle schematic and T-S diagram for the single flash OFC is reproduced in Fig. 5.5 for convenience.

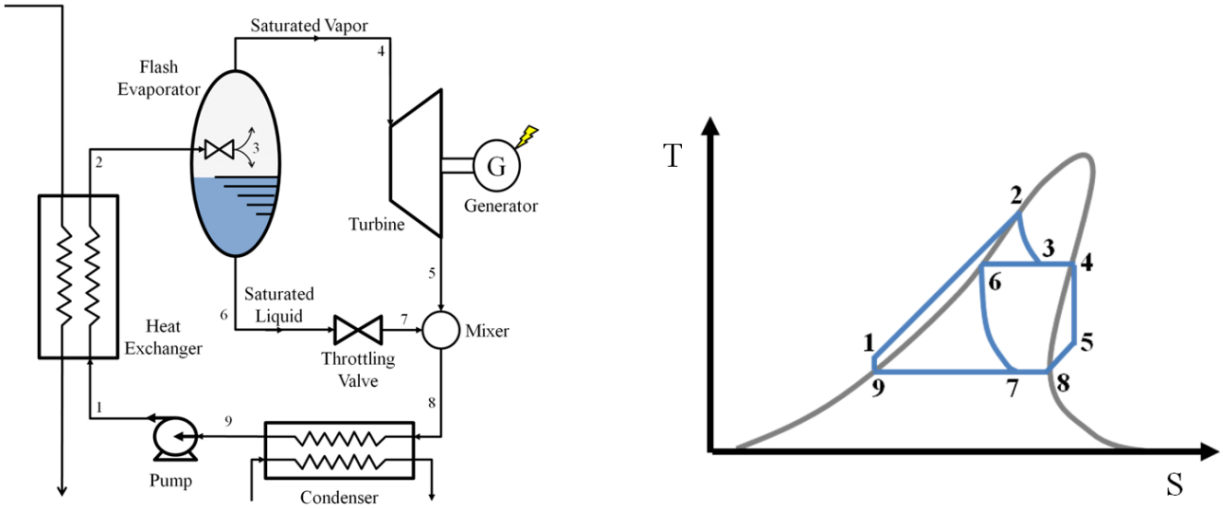

Figure 5.5: System schematic and T-S diagram for the single flash OFC.

As described in the preceding analysis, the "equal-temperature-split-rule" is a good initial estimate for determining the optimal state for the fluid to be throttled to (state 3) to maximize utilization efficiency **[**15**]**. The optimal state 3 is again determined iteratively with the results for maximum utilization efficiency shown in Fig. 5.6. Note in Fig. 5.6 that as the initial temperature of the thermal reservoir decreases, the vapor quality and subsequent fraction of the fluid that is expanded through the turbine also dramatically decreases. In fact, at thermal energy reservoir temperatures of 80°C, for a majority of the working fluids analyzed, only approximately 10% of the fluid will actually be used to produce power. The remaining saturated liquid after flash evaporation is unused and its energy is lost to the environment in the condenser. It seems that for low temperature sources, the inclusion of the enhancements discussed in chapter 4 will be particularly important.

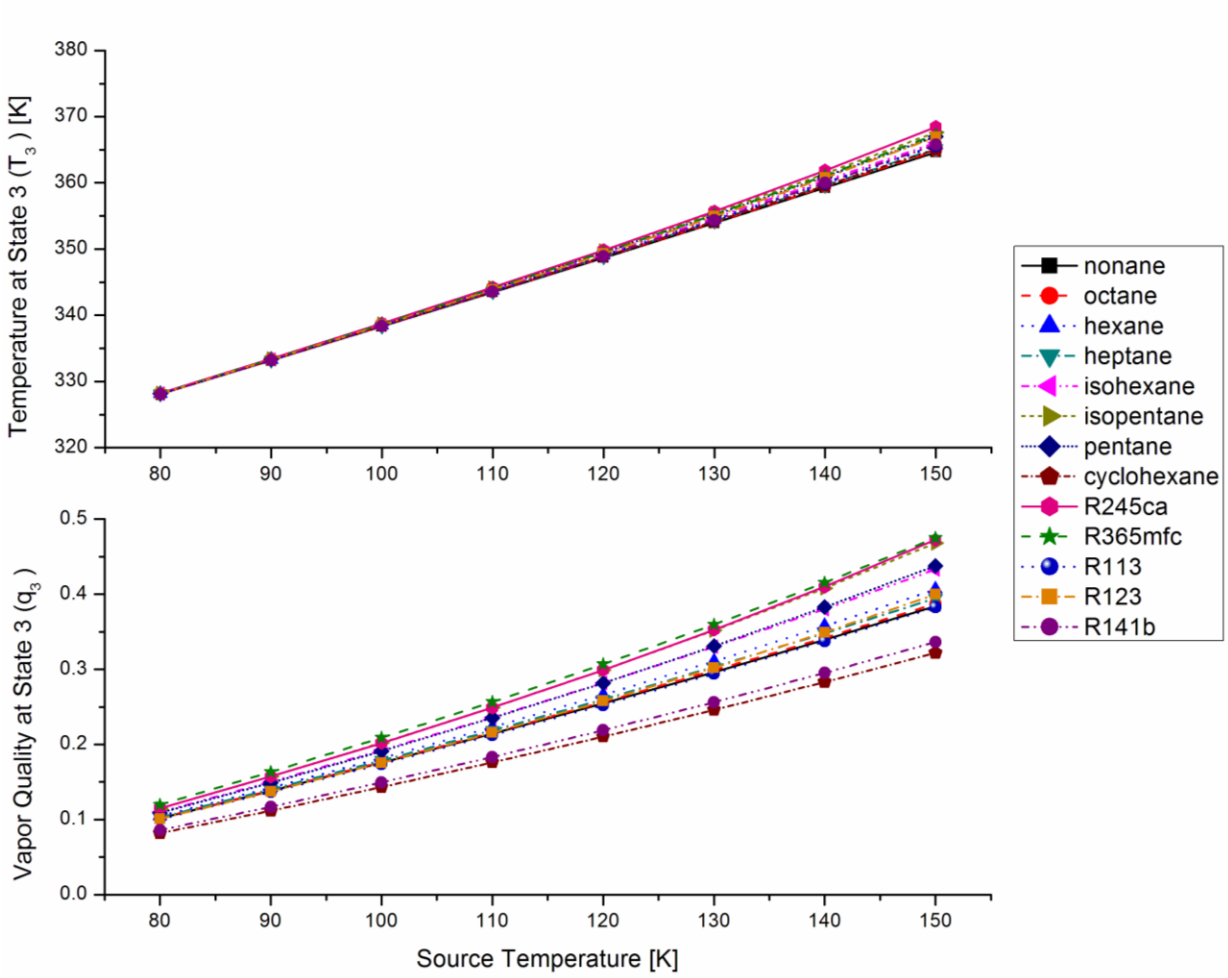

Figure 5.6: Temperature and vapor quality at state 3 for optimized single flash OFC.

In the intermediate temperature regime, Fig 3.8 showed that of the aromatic hydrocarbons and siloxane working fluids examined, the single-flash OFC achieved maximum utilization efficiencies that were only slightly below what was capable by the optimized basic ORC. In the low temperature regime though, Fig. 5.6 shows that depending on the working fluid, the range of performance is much greater. Depending on the working fluid, the single flash OFC can perform comparably to the optimized ORC, such as nonane and octane for example, or significantly below it in the case of R123and R245ca.

From Fig 5.6, it is noted that of the fluids examined, octane and nonane yielded the highest power output for the single flash OFC in the low temperature regime. The difference in performance between the different working fluids examined can be attributed to the differences in exergy destruction during the throttling process, which is plotted in Fig. 5.7. Note that for the fluids that encounter the greatest exergy destruction during the throttling processes also exhibit the lowest utilization efficiency. Assuming isenthalpic expansion and using the definition of the differential thermodynamic potential enthalpy and the chain rule, the change in exergy during the throttling process is given in eq. (5.4).

$$\dot{m}\chi = -\dot{m}T_0 \int ds = -\dot{m}T_0 \int \frac{V}{T}\frac{\partial P_{sat}}{\partial T} dT \qquad (5.4)$$

This expression however is quite complex to evaluate due to the volume and saturated pressure term for isenthalpic expansion. Instead, a qualitative analysis between the different fluids can be made in a more straightforward manner from the working fluid's Temperature-Enthalpy (T-H) diagram. From Fig. 5.6, it can be seen that the optimal temperature for state 3 behaves very closely to the "equal-temperature-split-rule" and the actual working fluid has little effect on the optimal temperature.

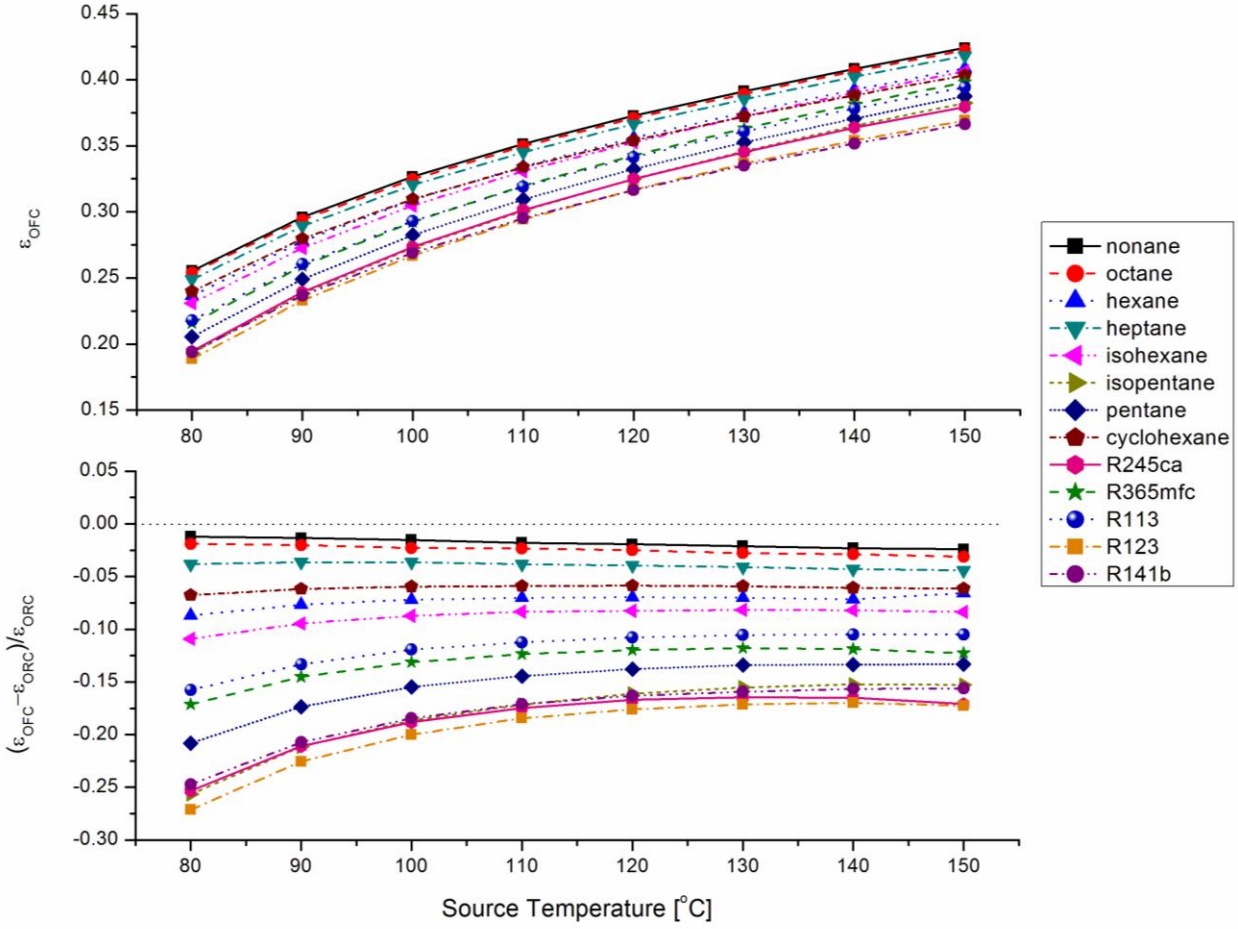

Figure 5.7: Utilization efficiencies for the optimized single flash OFC and the percent difference in utilization efficiency as compared to the optimized ORC at different initial finite thermal source temperatures

In Fig. 5.8, the T-H diagram for octane and R245ca are shown with isobars for every 50kPa. In Fig. 5.8, it is noted that the isobars inside the vapor dome for R245ca are spaced much closer together than for octane. Octane and R245ca both undergo isenthalpic expansion from a saturated liquid at state 2 that is near the initial temperature of the thermal reservoir to a similar temperature at state 3. In the 300-400K range, a unit change in temperature under constant enthalpy yields a much lower drop in pressure for octane than for R245ca. This corresponding larger drop in pressure in turn causes a larger reduction in exergy for R245ca as compared to

octane. This result suggests that higher exergy efficiencies can be achieved with fluids with small values of $(\partial P_{sat}/\partial T)$ in the temperature regime that flash evaporation is to take place.

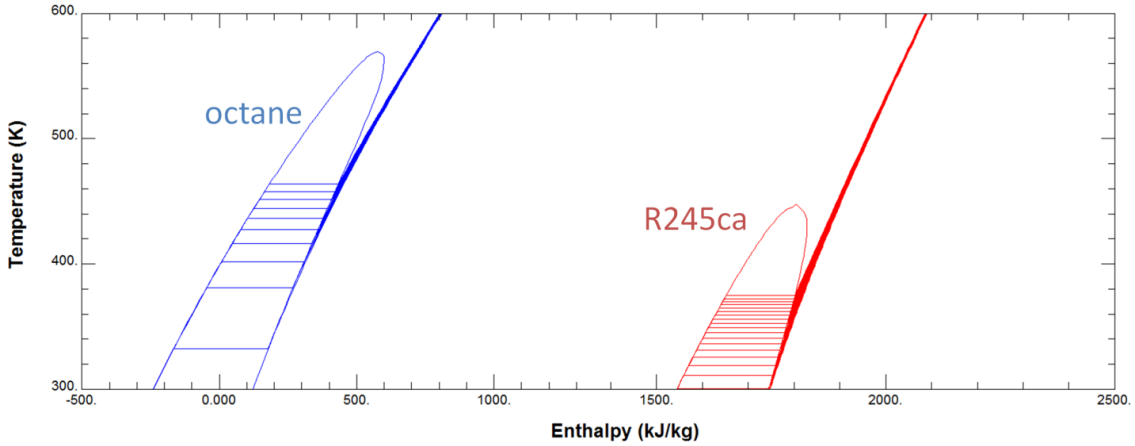

Figure 5.8: Temperature-Enthalpy diagrams for octane and R245ca

5.3.3 Double flash OFC

In section 4.2.1, it was proposed that more power could be generated using the saturated liquid from the first flash evaporation step by introducing an additional flash step. This secondary flash would produce more saturated vapor which would be expanded in a low pressure turbine; thus increasing net power output and reducing the amount of energy lost in the condenser. For convenience, the system schematic and T-S diagram for the double flash OFC is reproduced in Fig. 5.9.

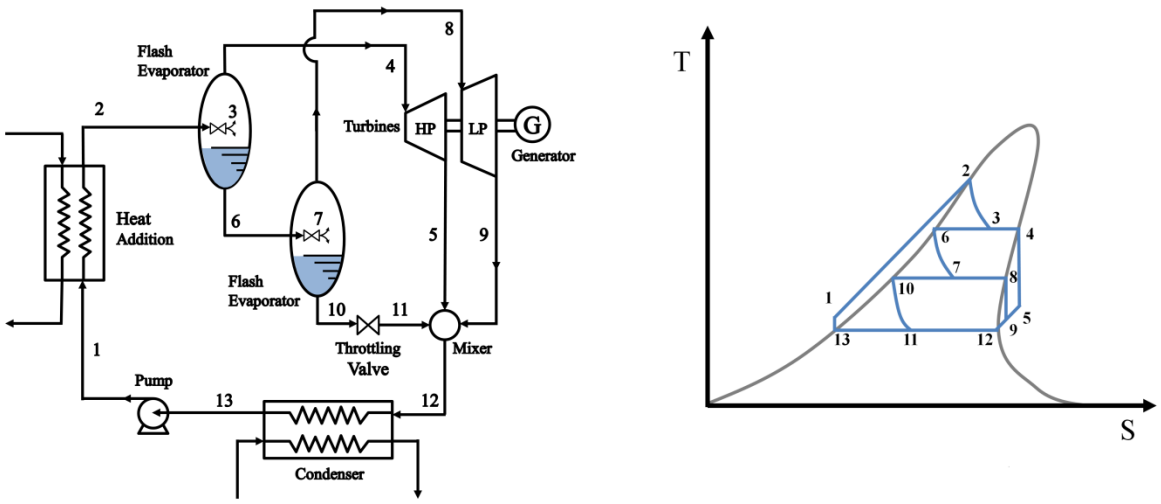

Figure 5.9: System schematic and T-S diagram for the double flash OFC.

This system design was based on an adaptation of the double flash steam cycle, which is frequently used in geothermal plants. For intermediate temperature resources, Fig. 4.7 showed that the double flash OFC increased net power output by approximately 5% over the optimized ORC using aromatic hydrocarbons. For low temperature resources, Fig. 5.10 shows that by

introducing a secondary flash step, the double flash OFC increased power output by as little as 2% to as much as 29% depending on the working fluid and the energy reservoir's initial temperature.

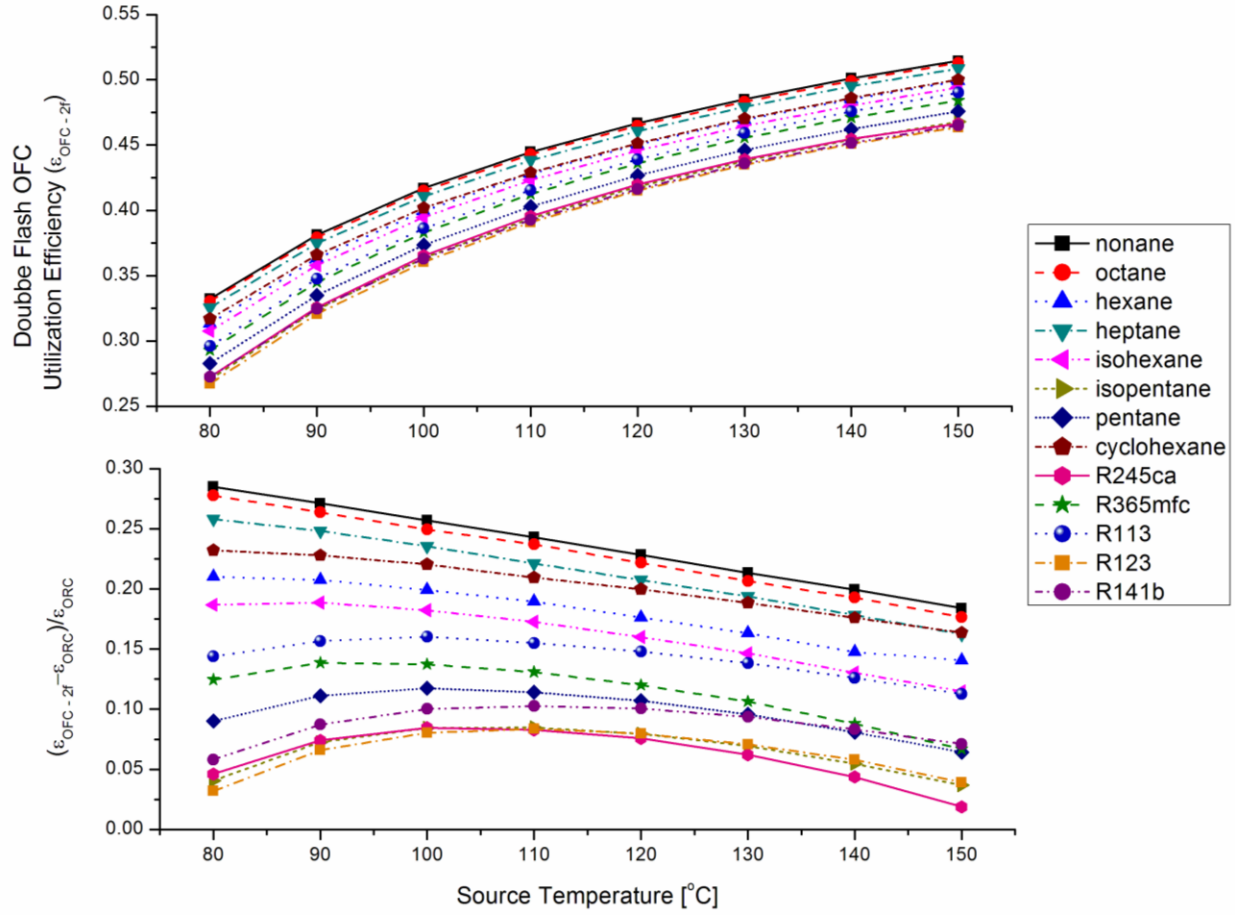

Figure 5.10: Utilization efficiencies for the optimized double flash OFC and the percent difference in utilization efficiency as compared to the optimized ORC.

In Fig. 5.10, double flash OFCs utilizing fluids such as octane and nonane have a significant higher improvement over fluids such as R245ca and R123. As discussed previously in section 5.3.2, nonane and octane are able to achieve higher exergetic efficiencies for the flash evaporation process than fluids such as R245ca because the isobars inside the vapor dome are spaced closer together, resulting in smaller pressure losses during flash evaporation for R245ca on a T-H diagram as shown in Fig. 5.8.

Results showed that the throttling valves of the single-flash OFC were the primary sources of exergy destruction in the cycle. The double flash OFC reduces these irreversibilities in the OFC because the fluid is expanded in two separate steps rather than in a single one. Results show that for all the working fluids examine, the introduction of the secondary flash step resulted in approximately 30% reduction in exergy losses associated with the flash evaporation processes as compared with the single flash OFC. As discussed before, additional flash steps would reduce

the irreversibility of flash evaporation even further, but practically speaking it likely would not be cost justified.

5.3.4 The low temperature modified OFC

In section 4.2.2, the modified OFC was proposed as a method to reduce the working fluid's substantial superheat prior to entering the condenser. In Fig. 4.3, the saturated liquid from flash evaporation is throttled and then combined with the superheated exhaust of the high pressure turbine. The flow rates from the throttling valve at state 7 and the high pressure turbine exit at state 5 are adjusted such that a saturated vapor was produced at state 8 at the low pressure turbine inlet. The modified OFC has a unique advantage in that it allowed for the excess superheat due to using a "dry" working fluid and the energy contained in the saturated liquid from flash evaporation to be used for generating power. An additional advantage was seen in that the pressure drop in the throttling valve was also reduced since expansion in the vapor turbines was now split into a high pressure and low pressure stage. More details on the advantages of the modified OFC design are given in section 4.2.2.

For aromatic hydrocarbons and siloxanes, these working fluids were superheated to a greater degree than alkane and refrigerant working fluids at the exit of the high pressure turbine because they are more molecularly complex and subsequently exhibit a more "drying" behavior. In addition, the higher temperatures the aromatic hydrocarbon and siloxane working fluid were heated to allowed for a greater fraction of vapor to be generated during flash evaporation. For low temperature thermal resources, the majority of the fluid remains a saturated liquid after flash evaporation. In fact, only 10% of the fluid is flashed to vapor for 80^{o}C energy sources as shown in Fig. 5.6. Therefore, the modified OFC in the form shown in Fig 3.3 for intermediate temperature thermal resources cannot be directly applied to low temperature energy sources because there is not enough vapor being generated nor is the vapor superheated enough such that recombination of the working fluid at the mixer can produce a saturated vapor prior to entering the low pressure turbine. Instead, the low temperature modified OFC was reconfigured and its system schematic and associated T-S diagram is shown in Fig.5.11.

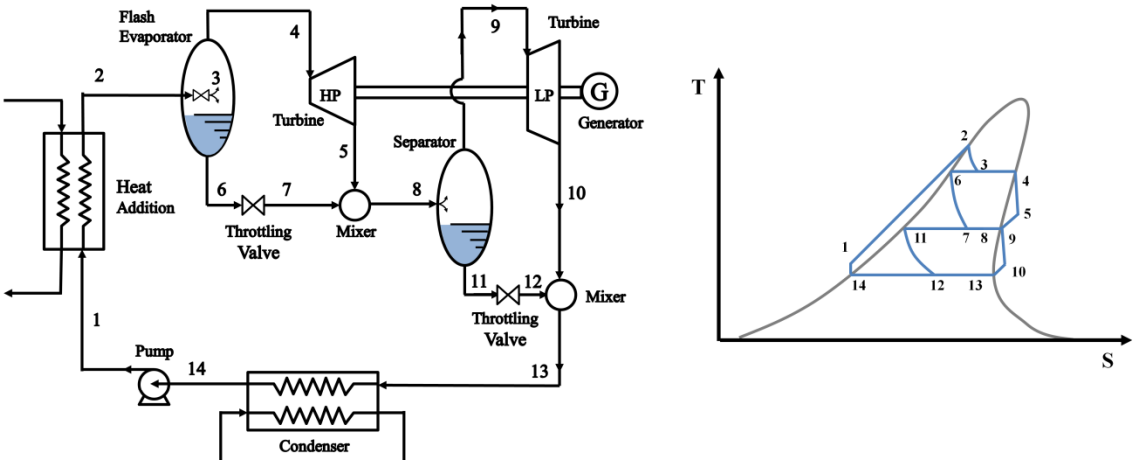

Figure 5.11: System schematic and T-S diagram for the low temperature modified OFC.

From Fig. 5.11, it can be seen that the original objective of the modified OFC is still maintained; that is, to use the excess superheat of the turbine exhaust for a dry fluid and the energy contained in the saturated liquid after flash evaporation to generate more power. Similar to Brayton cycles to maximize efficiency, the intermediate pressure was determined by setting the pressure drop ratios across each turbine equal. The temperature and vapor qualities at state 3 and state 8 of Fig. 5.11 given in Fig. 5.12.

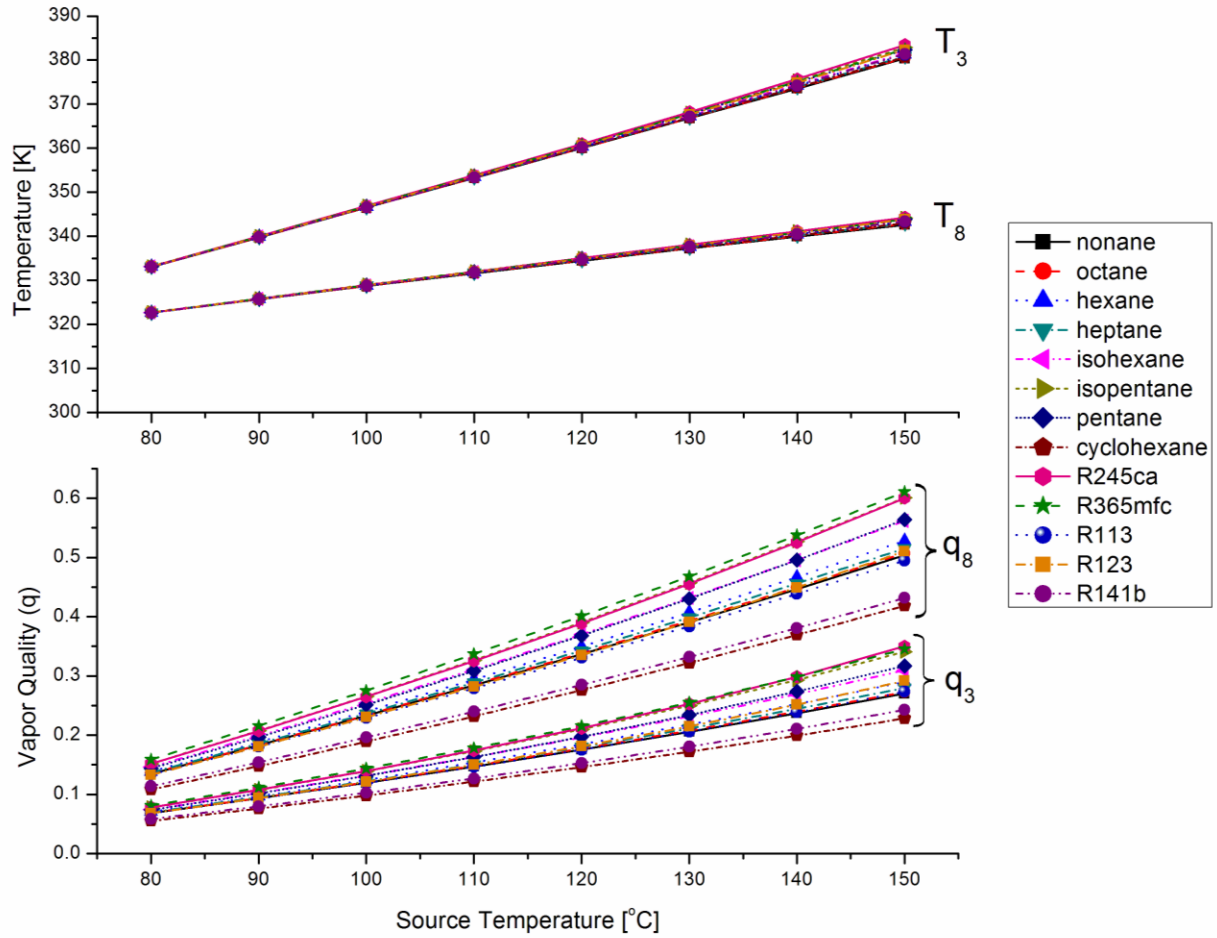

Figure 5.12: Temperature and vapor quality at state 3 and state 8 for the optimized low temperature modified OFC.

The utilization efficiency and the percent increase in power output for the low temperature modified OFC as compared to the optimized ORC is shown in Fig. 5.13. Similar to the OFC and the double flash OFC, nonane and octane showed the greatest utilization efficiency as a result of the higher exergetic efficiencies they exhibited during flash evaporation as discussed previously in section 5.3.2.

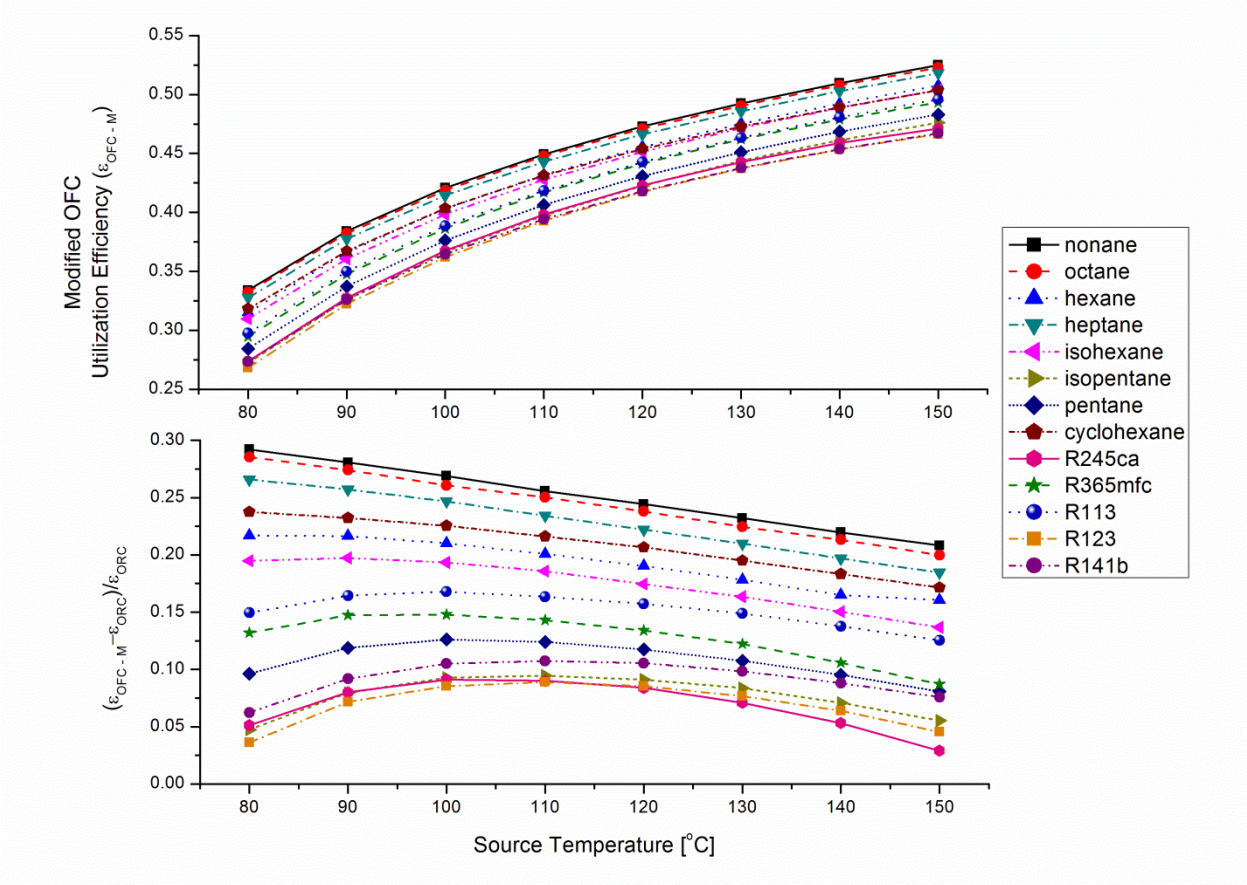

Figure 5.13: Utilization efficiencies for the optimized low temperature modified OFC and the percent difference in utilization efficiency as compared to the optimized ORC.

Unlike what was seen for intermediate temperature resources in Fig. 4.6 and 4.7 though, the net power output for the modified OFC was not shown to be significantly higher than the double flash OFC. Instead, the power outputs are fairly comparable. This can again be attributed to the less "drying" nature of alkane and refrigerant working fluids; they have less superheat at the high pressure turbine exit and thus recombination prior to the secondary flash step makes a less dramatic impact for these working fluids in the low temperature regime.

5.3.5 2-phase OFC

As discussed in section 4.2.3, replacing the throttling valve in the flash evaporator of the OFC with a two-phase expander would generate significantly more work. Essentially, a device that was responsible for the majority the cycle's exergy destruction is replaced with a device that produces additional power. For convenience, the 2-phase OFC's system schematic and T-S diagram is reproduced in Fig. 5.14 on the following page. As discussed previously, the design of a suitable two-phase expander is not without its own challenges as the expander would need to be able to handle both liquid and vapor behaviors of the fluid as it expands through the vapor dome. Despite these challenges though, much research into two-phase expanders is being conducted because of the potential for much improved efficiencies when replacing a throttling valve, particularly in the refrigeration, heating, venting, and air conditioning (HVAC), and LNG industries.

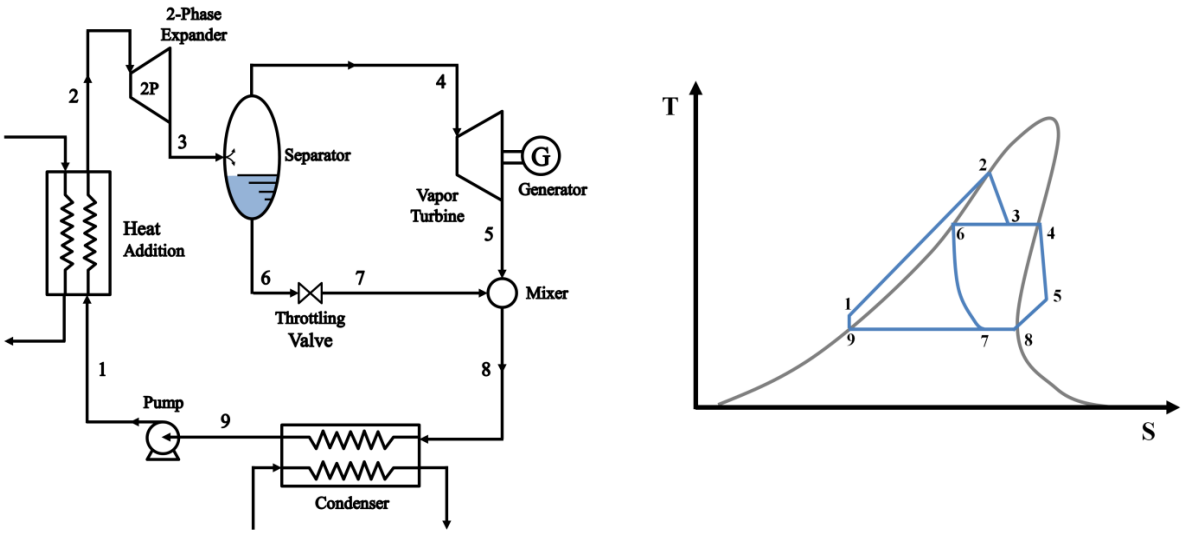

Figure 5.14: System schematic and T-S diagram for the 2-phase OFC.

For the alkane and refrigerant working fluids discussed, the utilization efficiency and percent improvement over the optimized ORC using a 2-phase OFC with a 70% isentropic efficiency two-phase expander was calculated and plotted in Fig. 5.15.

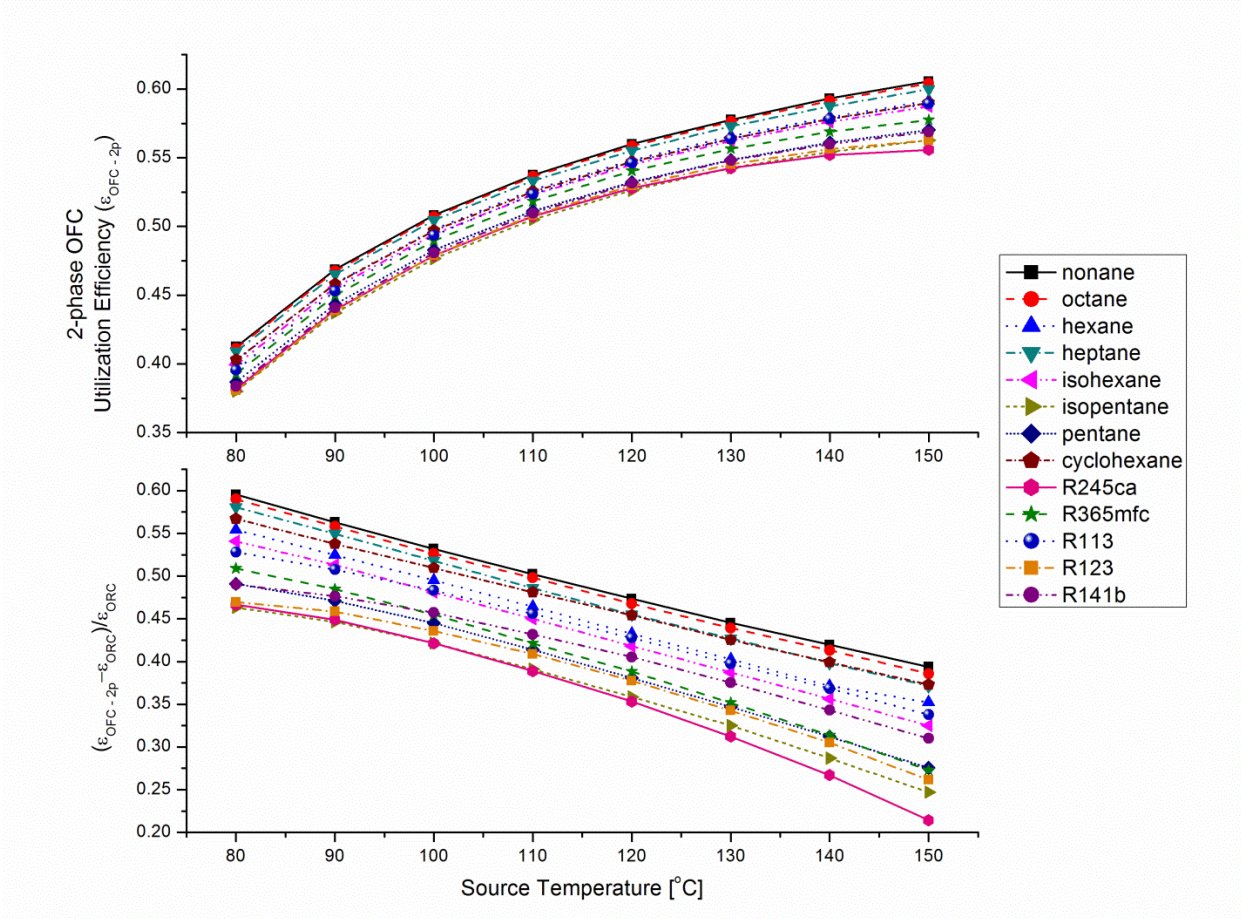

Figure 5.15: Utilization efficiencies for the optimized low temperature 2-phase OFC and the percent difference in utilization efficiency as compared to the optimized ORC

It is noted that in Fig. 5.15, the 2-phase OFC's percent increase in utilization efficiency over the optimized ORC are in the range of 20% to 60% depending on the fluid and initial temperature of the thermal energy reservoir. For intermediate temperature resources, Fig. 4.6 shows increases in utilization efficiency by only approximately 15%. This difference in efficiency gains can be attributed to the fact that for low temperature energy sources, the relative amount of exergy destruction in the primary flash evaporation process to the total initial exergy contained in the thermal reservoir is much greater. Therefore, the reduction of irreversibilities associated with uncontrolled expansion in the flash evaporation process creates a significantly greater impact for cycle utilization efficiency for low temperature resources than for intermediate and high temperature thermal energy sources.

A 70% isentropic efficiency was assumed for the two-phase expander in Fig. 5.13, which corresponds to isentropic efficiencies that are presently achievable on a reliable basis with radial inflow turbines [89,91] and advanced twin-screw expanders [90]. In particular, the twin-screw expander developed by Smith et al. [90] is also claimed to be low in cost and can be easily manufactured. Scroll expanders have also been shown to have potential as a viable two-phase expander [86,131]. In the context of low temperature energy sources, two-phase expanders with lower isentropic efficiencies while less desirable, will likely still generate a significantly higher power output than the optimized ORC.

5.3.6 Modified 2-phase OFC

Similar to section 4.2.4, the enhancements introduced by the low temperature modified and the 2-phase OFC can be combined to produce the low temperature modified 2-phase OFC. This cycle uses the turbine exhaust superheat to generate more saturated vapor for power production in the low pressure stage. A 2-phase expander also replaces the throttling valve in the flash evaporation process. The system schematic and corresponding T-S diagram for the low temperature modified 2-phase OFC is shown in Figure 5.16.

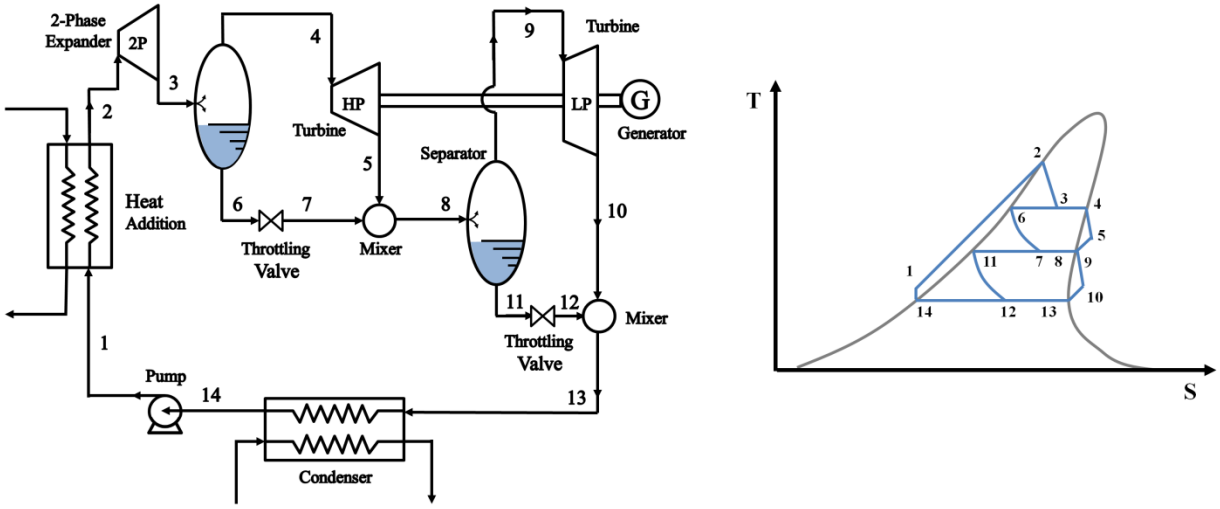

Figure 5.16: System schematic and T-S diagram for the low temperature modified 2-phase OFC.

Similar to the low temperature modified OFC, the high and low vapor turbine pressure ratios are set equal to each other. State 3 is determined by optimizing the cycle to maximize power generation for specific flow rate from the energy reservoir. Fig. 5.17 shows the utilization efficiencies for the low temperature modified 2-phase OFC and the percent improvement of this cycle over the optimized ORC.

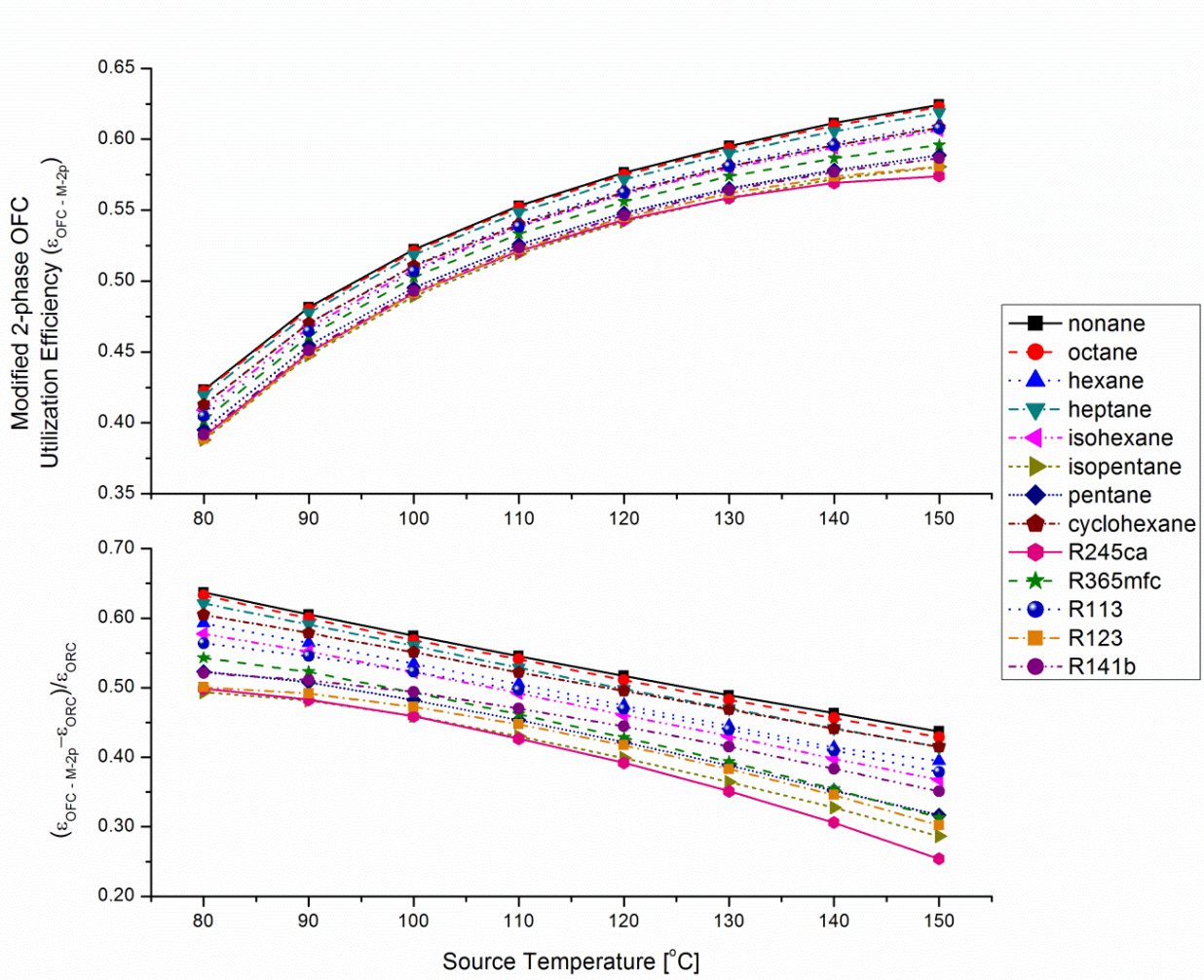

Figure 5.17: Utilization efficiencies for the optimized low temperature modified 2-phase OFC and the percent difference in utilization efficiency as compared to the optimized ORC

Similar to the results for intermediate temperature thermal energy reservoirs in Fig. 4.7, the modified 2-phase OFC exhibited the greatest utilization efficiencies of all the enhanced vapor cycles examined. However, it is noted that the modified 2-phase OFC only generates about 5% more power than the 2-phase OFC. However, the modified 2-phase OFC requires an additional low pressure vapor turbine and flash evaporator. In light of the extra equipment and complexities, it is likely that the 2-phase OFC would be preferred over the modified 2-phase OFC as long as a two-phase expander with reasonable isentropic efficiencies is available. As discussed in section 4.4, although the enhanced OFCs introduce greater complexities and plant equipment, the required condenser heat exchanger surface area, and consequently costs, should

ultimately decrease due to the more power being generated which results in less energy being rejected in the condenser.

5.4 Effect of pinch temperature difference

In the analysis thus far, a minimum 10°C temperature difference between hot and cold streams, or 10°C pinch, was assumed necessary in the heat exchangers to facilitate heat transfer. For power cycles using high and intermediate temperature energy sources, this pinch temperature is relatively small compared to the source's initial temperature. For low temperature resources, particularly for resources as low as 80°C, a 10°C pinch temperature creates a much greater impact and restriction on the cycle's heat addition. As an example, in Fig. 5.18 the utilization efficiency for a double flash OFC using R365mfc as a working fluid is shown for different pinch temperatures in the heat exchangers.

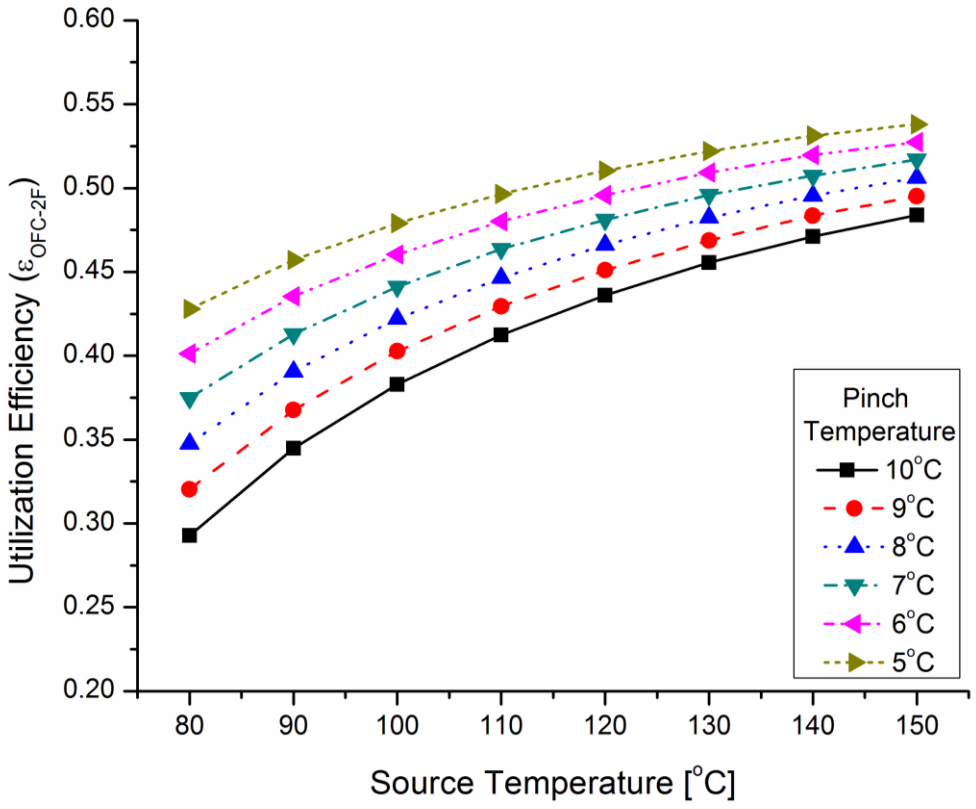

Figure 5.18: Utilization efficiencies for the optimized double flash OFC at different pinch temperatures using R365mfc as a working fluid.

As shown in Fig. 5.18, as the pinch temperature requirement decreases the utilization efficiency increases. This is expected as reducing the minimum temperature requirement in the heat exchangers decreases irreversibilities associated with heat transfer across a finite temperature difference. In other words, by decreasing the pinch temperature the heat addition exergetic efficiency increases and as a result, the utilization efficiency increases based on eq. (3.10). While decreasing the pinch temperature certainly increases net power output from a specific energy reservoir flow rate, it also increases the required surface area in the heat exchangers,

driving up equipment costs. As shown in eq. (3.13) and (3.14), by decreasing the temperature difference between streams, one is reducing the driving force of heat transfer in the heat exchanger and greater surface area is necessary for the same energy transfer rate to be maintained.

Another interesting result from the analysis is that as the energy reservoir's temperature decreases, the difference in power output for a cycle using a high pinch temperature such as 10°C as compared to a cycle with a low pinch temperature such as 5°C becomes more significant as the gap between the curves widen. This is more dramatically shown in Fig. 5.19, where the percent increase in utilization efficiency above a double flash OFC with a 10°C pinch temperature is plotted for smaller pinch temperatures.

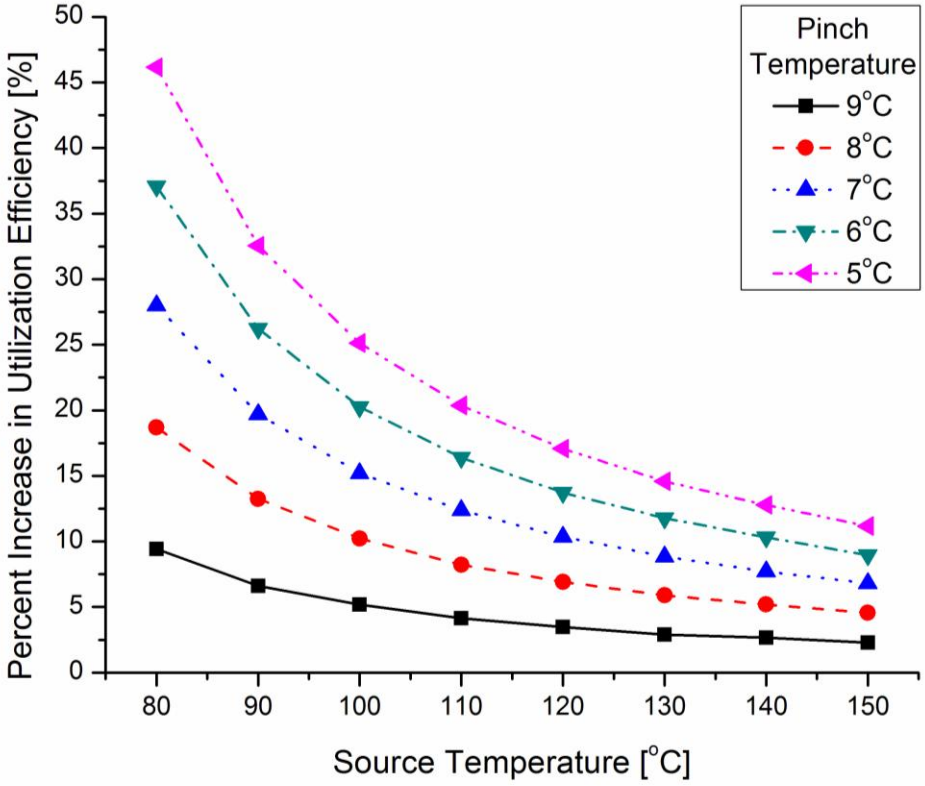

Figure 5.19: Percent difference in utilization efficiency for different pinch temperatures as compared to the optimized double flash OFC with a 10°C pinch using R365mfc as a working fluid.

As shown in Fig. 5.19, for an energy reservoir temperature of 80°C, by decreasing the pinch temperature from 10°C to 5°C, the power output increase by almost 50%. However, for a 150°C energy reservoir, that same change in pinch temperature approximately yields only a 10% increase in power output. This result suggests that at low temperatures, decreasing the pinch temperature requirements may make sense to achieve much higher performance whereas for higher temperatures the slight increase in performance may not justify the associated additional costs.

5.5 Vapor turbine considerations for alkane and refrigerant working fluids

Using an analysis similar to section 3.4.2.1, eq. (3.11) and (3.12) can be used to determine the turbine size parameter (*SP*) and turbine volumetric flow ratio (*VFR*) to give a preliminary estimate on the turbine characteristics for the OFC and the working fluids considered here in the low temperature regime. *SP* can be thought of as a dimensional parameter gauging how large the turbine is and *VFR* can be thought of as a compressibility parameter. It was noted that the *VFR*s determined in section 3.4.2.1 for aromatic hydrocarbons and siloxanes was well above ~50, the threshold for necessary for the possibility of at least 80% isentropic efficiency single-stage axial turbine design **[**142**,**143**]**. Table 5.4 gives the *SP* and *VFR* for the different working fluids considered for the vapor turbine in the single flash OFC shown in Fig. 5.5 and optimized ORC.

Table 5.4: Turbine Size Parameter (*SP*) and Volumetric Flow Ratio (*VFR*) for conditions for optimized ORC and OFC

Fluid Name	Optimized single flash OFC		Optimized ORC	
	SP [m]	*VFR*	*SP* [m]	*VFR*
nonane	1.84	10.19	1.85	10.01
octane	1.13	8.11	1.14	7.93
hexane	0.42	5.28	0.42	5.11
heptane	0.69	6.49	0.69	6.29
isohexane	0.36	5.02	0.37	4.77
isopentane	0.21	4.33	0.22	4.15
pentane	0.24	4.48	0.25	4.35
cyclohexane	0.55	5.27	0.55	5.13
R245ca	0.22	4.96	0.22	4.65
R365mfc	0.29	5.15	0.29	4.97
R113	0.39	4.53	0.40	4.37
R123	0.27	4.38	0.27	4.27
R141b	0.29	4.08	0.30	3.92

As shown in Table 5.4, the *VFR* for the low temperature OFC and ORC are well below the threshold limit of 50 and the design of a single stage axial-flow turbine with isentropic efficiency above 85% is theoretically possible **[**142**,**143**]**. Turbines with multiple stages would most likely not be cost-justified because of the quality of the thermal energy reservoir is low and less power is being produced compared to an intermediate or high temperature energy reservoir. Note the *VFR* for the alkane and refrigerant working fluids in the low temperature regime are at least an order of magnitude below that for alkanes and refrigerants shown in Table 3.4. The *SP* for the OFC and ORC are very close indicating the turbines for the two cycles would be of similar size. Pentane, isopentane, isohexane, R113, and R245ca have all been suggested as working fluids in other ORC studies; therefore, it would be expected that the vapor turbine used in those studies would be similarly applicable to the OFC and OFC variations.

5.6 Conclusions

The OFC and the proposed enhancements outlined in Chapter 4 were analyzed for their applicability to low temperature resources such as non-concentrated solar thermal energy and low grade waste heat and geothermal energy. Similar to results for intermediate temperature thermal resources, the optimized single flash OFC generated less maximum power that the optimized ORC. However, with the modifications suggested in Chapter 4, the enhanced OFCs can generate above 60% more power than the optimized ORC per specific flow rate from the same finite thermal energy reservoir. Although the low temperature modified 2-phase OFC produced the greatest power of the configurations considered, due to the additional complexity and plant equipment costs, it may not be the most desirable option. Instead, results showed that just replacing the throttling valve with two-phase expanders dramatically increases the overall power output of the OFC. Another important design consideration is the minimum pinch temperature in the heat exchangers, particularly for low temperature resources. Results showed that even small changes in the pinch temperature significantly affected net power output for low temperature energy sources; as the temperature of the energy source rises though, the pinch temperature has a smaller effect on utilization efficiency.

6 A combined air Brayton – toluene OFC for high temperature central receiver solar thermal plants

6.1 Introduction

The continuous fusion reaction of the sun is far and away the greatest source of energy available to earth; in fact, the amount of energy striking the earth from solar radiation in 30 minutes is equivalent to the total energy consumed annually by the entire globe [165]. It is no wonder that humans have continually strove to develop methods to harness this large energy source starting from prehistoric times when solar energy was used to dry and preserve food. Today, questions of long term sustainability and the harmful environmental consequences that coincide with the use of fossil fuels such as climate change, air and water pollution, and acid rain, have resulted in a resurgence in interest in renewable energies, such as concentrated solar power (CSP) [165]. CSP involves using tens to thousands of mirrors to reflect incident radiation upon a given surface. These mirrors can have no tracking, single-axis tracking, or two-axis tracking; it is through concentration that very high heat fluxes and temperatures can be achieved that are suitable for centralized large scale electricity production and solar furnaces for materials processing and endothermic reactions to form hydrocarbon fuels [165]. Although the technology to harness CSP for producing electricity has been an area of research for over 140 years, it was not until the 1980s that electricity generated from solar energy was first put onto the grid in response to the oil shortage crises of the 1970s [166]. In recent years a renewed focus has come from the scientific community that has been supported by multiple governmental agencies to research and develop concentrating solar thermal for cost competitive electricity generation [167].

Though the parabolic trough type collector remains the most mature CSP technology, these collectors use only one-axis tracking and are "line focusing" which limits the maximum temperatures they are able to achieve [168]. In fact, the majority of single-axis collectors often operate within the 200^{o}C to 400^{o}C and often employ a steam Rankine cycle as the mechanical heat engine in its power block [130]. For two-axis collectors that using "point-focusing" such as solar power towers, although more complex, the heliostats are able to track the sun's motion more effectively and focus the solar radiation very accurately upon the high temperature receiver. For solar power towers, very high concentrations ratios in the thousands are common and temperatures as high as 1500^{o}C are possible [165].

Solar power towers such as the Spanish Solar Tres and PS10 have demonstrated the commercial viability of high temperature solar thermal energy due in large part to the ability for energy storage; in both plants large tanks of hot molten salt are stored in containments so that electricity can be generated during the night and times of solar intermittence [166]. The molten nitrate salts that are used in the Solar Tres as the solar heat transfer fluid have temperature limits at ~600^{o}C where the salt begins to decompose [169] limiting the Solar Tres to maximum operating temperatures of 565^{o}C [166]. The PS10 uses air as a working fluid and operates at a higher temperature at 680^{o}C [166], but air is often a poor coolant because of its high volume and poor heat transfer characteristics. By using high-temperature liquid-fluoride salts, peak temperatures for solar power towers reaching 700^{o}C to 850^{o}C can be achieved without using air as a working

fluid [169]. In this temperature range, higher efficiency Brayton cycles can be utilized instead of steam Rankine cycles. Forsberg et al. [169] suggested a closed loop helium or nitrogen Brayton cycle with multiple reheat and intercooling stages for a high temperature liquid-fluoride salt solar power tower. It was estimated that by incorporating the Brayton cycle at higher temperatures that are afforded by liquid-fluoride salt coolants, potentially as high as a 20% to 30% increase in thermal energy conversion efficiency over present solar powers that utilize steam Rankine cycles is achievable [169].

An improvement upon a solar power tower operating with a gas Brayton cycle can be made by employing the so-called combined cycle concept where a bottoming steam Rankine cycle absorbs heat from a high temperature topping Brayton cycle to produce more electricity. Using advanced gas turbines that are capable of operating near 1500^{o}C, combined cycle have reported thermal conversion efficiencies approaching 60% [170]; and 50% efficiencies for combined cycles to be very typical [168,171,172]. As discussed in the previous chapters, because of the poor temperature matching of the vapor Rankine cycle, significant irreversibilities resulting from heat transfer across a finite temperature difference is encountered as energy is transferred from the gas turbine exhaust to the working fluid of the Rankine cycle. As mentioned previously, modern Heat Recovery Steam Generators (HRSG) in combined cycle systems will commonly employ heat addition at multiple pressure levels (generally 2-3) to reduce the degree of mismatching. If the gas turbine exhaust temperature is high enough, reheating may also be incorporated [10]. Combined cycles that employ heavy duty simple gas turbines without intercooling, reheating, and recuperation will almost always use multiple pressure HRSGs as the gas turbine exit temperature is often significantly above 500^{o}C which allows for high efficiency steam Rankine cycles to be utilized [4,26,173]. In fact, several studies have shown that introducing the combination of intercooling and/or recuperation in combined cycles often times actually lowers the total efficiency of the system even though it can increase the efficiency of the gas turbine when done with reheating [174-177]. This is due to the lower HRSG inlet temperatures because of intercooling and recuperation which reduces the efficiency of the bottoming steam cycle and is the dominant effect compared to the improved topping cycle efficiency. Reheating on the other hand for combined Brayton-steam Rankine cycles will increase combined cycle efficiency, because although the gas turbine exhaust temperature is higher, it improves the bottoming cycle significantly because of higher HRSG inlet temperatures. Polyzakis et al. [174] studied a number of different variations of the topping gas turbine cycle including simple, reheat, regeneration and intercooling; they concluded that when coupled to a steam Rankine cycle, the reheat Brayton cycle showed the most efficient performance. Da Cunha Alves also showed that energy from the higher exhaust temperatures are recovered by the bottoming cycle very efficiently; therefore, reheating without regeneration in the gas turbine does not decrease the combined cycle efficiency. Studies performed by Xiang et al. [178] and Franco et al. [35] have shown that increasing the inlet HRSG temperatures above ~600^{o}C though will decrease total combined cycle efficiency. This occurs because the bottoming cycle cannot increase its turbine inlet temperature any further due to aforementioned metallurgical limits and the topping gas cycle now becomes less efficient due to high gas turbine exit temperatures. If a high efficiency turbine that used recuperation and intercooling was to be fitted with a bottoming cycle though, multi-pressure HRSGs may not be suitable economically because of low gas turbine exit temperatures [173]. In fact, at low temperatures or low power applications, steam turbines become very large, inefficient, and expensive; it is in this context of combined cycles

that Organic Rankine Cycles (ORC) become viable and attractive compared to steam Rankine cycles [14,173]. High efficiency gas turbines using intercooling and recuperation that have low gas turbine exit temperatures [26,179] and micro-gas turbines that are of low power output (30-250kW) [180] thus seem the most attractive for implementing bottoming ORCs in combined cycles. For combustion cycles, too low of gas exhaust temperature causes toxic and/or corrosive combustion products to fall out of the exhaust; in nuclear and solar energy though, this is not a concern and actually more efficient cycles can be developed because more energy can be harvested from the fuel with lower gas stack temperatures. In chapter 4, enhancements to the Organic Flash Cycle (OFC) were proposed with results showing that the OFC could potentially generate 5% to 20% more power than the ORC per given flow rate of the finite thermal source, which in this case is energy from the topping gas cycle.

In this chapter, a combined air Brayton-toluene OFC is proposed as the power block component of a high temperature solar power system that utilizes liquid-fluoride salts. A theoretical thermodynamic model and analysis of the power block and a simplified analysis of the solar collector system is presented. Results from the analysis are discussed and compared to previous studies on solar power towers presented in the literature and current solar power plants that are in operation. Total system efficiency for the cycle configuration is also included. In addition, the primary obstacles to a high efficiency solar power tower and their potential solutions are identified.

6.2 Central receiver combined Brayton-OFC system

Combined cycles have been shown to be a method in significantly increase power block efficiencies in traditional fossil fuel plants. It has been shown in chapter 4 that the modified OFC could significantly increase the power generation as compared to the optimized ORC. In this chapter, a combined cycle featuring an air Brayton cycle with intercooling, reheating, and regeneration and a low-temperature toluene modified Organic Flash Cycle is proposed as the power block component to a high temperature solar power tower. Though some studies have concluded that a simple gas turbine with reheat to be optimal in combined cycles due to higher inlet temperatures to the HRSG [174,175], regeneration and intercooling does provide improved efficiency for the gas turbine. Overall combined cycle efficiency may also be higher if instead of a bottoming steam cycle, a cycle that could better utilize the low temperature exhaust from the intercooled, recuperated gas turbine was employed. The lower temperatures for inlet to the bottoming cycle from ~500-650^{o}C to ~350-400^{o}C is somewhat ideal for the intermediate temperature OFC studied in Chapter 3 and 4. As Chacartegui et al. [26] showed in a recent study, ORCs perform significantly worse than multi-pressure steam cycles for simple heavy duty gas turbines as they cannot take advantage of the high gas turbine exit temperatures. However, for high efficiency turbines such as the GE LM-6000 and recuperated turbines such as the Rolls-Royce WR 21 and the Solar Mercury 50, the ORC can show equivalent or slightly better efficiency than state of the art multi-pressure steam cycles [26]. This is particularly attractive because at low gas turbine exit temperatures, multi-pressure heat addition may not be attractive both technically and economically [173]. A study conducted by da Cunha Alves et al. [175] also showed that while intercooled cycles are not suitable for combined cycles with bottoming steam cycles because of low exhaust temperatures to the HRSG, ORCs may be able to uniquely take advantage of the lower exhaust temperatures. De Cunha Alves et al. also stated that water would be needed for intercooling, but in a design layout such as that in Fig. 6.1, the heat sink for

intercooling comes from the bottoming OFC and water is not necessary for intercooling. This combined cycle layout shown in Fig. 6.1 and its corresponding T-S diagram in Fig. 6.2 is similar to the one proposed by Najjar et al. **[**179**]**, except the bottoming ORC is replaced with a modified toluene OFC. The solar collection system would use a liquid fluoride salt (NaF-NaBF4) that will need to be pressurized for temperatures above 700°C to avoid boiling, but its components will remain stable and not decompose **[**169**]**. The heated salt could also serve as energy storage in the hot containment vessels similar to storage system used by the Solar Tres and PS10 such that electricity generation is possible at night. Forsberg et al. also suggested using graphite as a heat-storage medium as it is much less expensive than the fluoride salts for heat storage and it is also chemically compatible with the salts **[**169**]**.

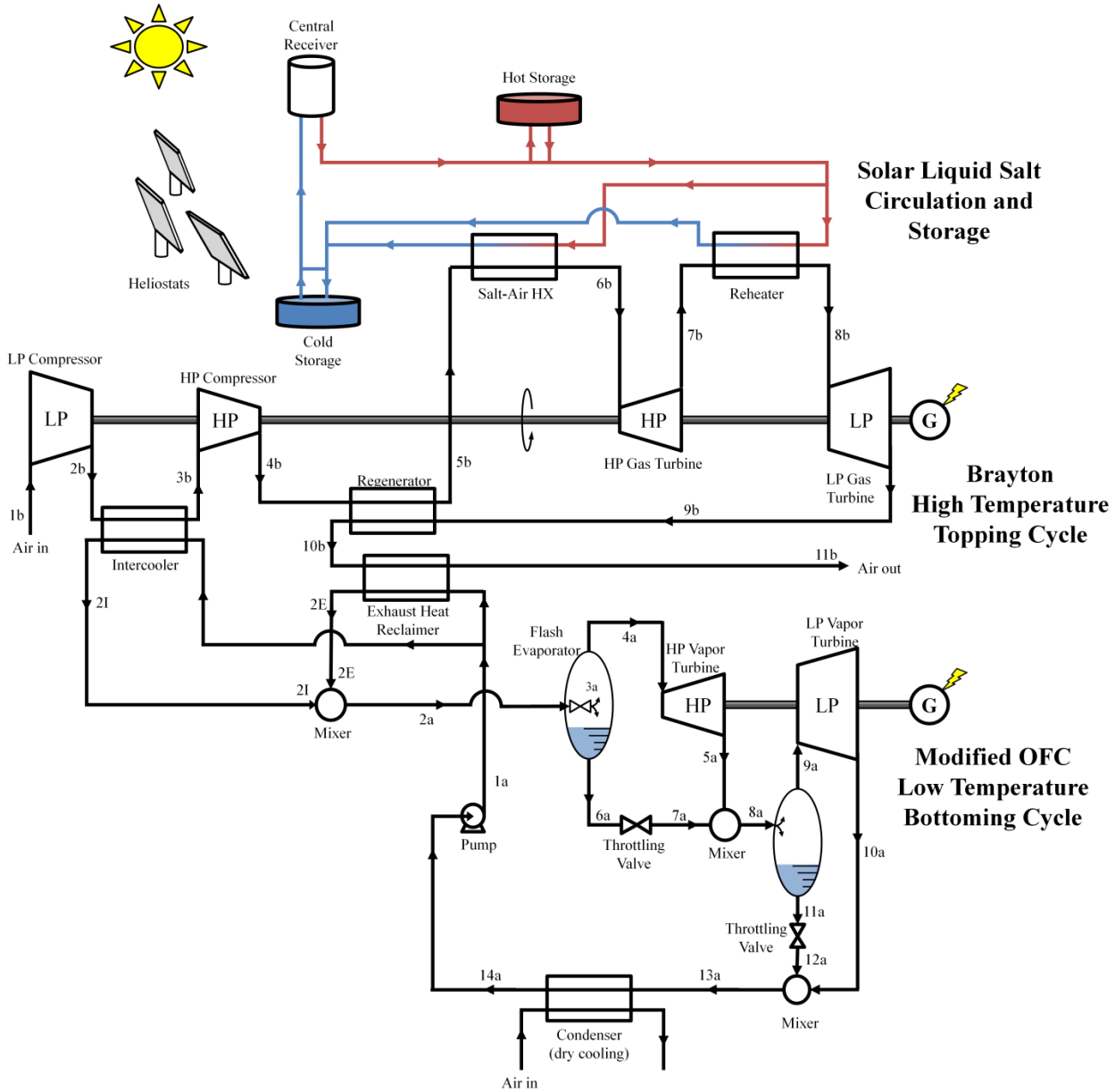

Figure 6.1: System schematic of the combined Brayton-OFC system for a solar power tower.

As shown in Figure 6.1, the bottoming OFC absorbs heat from the topping cycle at two different locations, in the exhaust heat reclaimer after the regenerator (state 9b→10b) and in between the low pressure (LP) and high pressure (HP) compressors at the intercooler (state 2b→3b). If the cycle configuration was for a Brayton cycle alone, cooling water or some type of heat sink would be necessary at the intercooler and exhaust. Therefore, not only does introducing the bottoming cycle generate more power, it also relaxes heat sink and cooling requirements. The high availability of solar radiation throughout the year coupled with low land costs makes deserts a natural place to locate CSP plants; unfortunately, deserts also have no lakes, rivers, or oceans nearby that can be cheaply and conveniently used as a heat sink. Therefore, CSP plants that reduce their cooling capacity requirements and further, could utilize use dry cooling or hybrid wet/dry cooling would be very attractive due to limited water resources **[**181**]**.

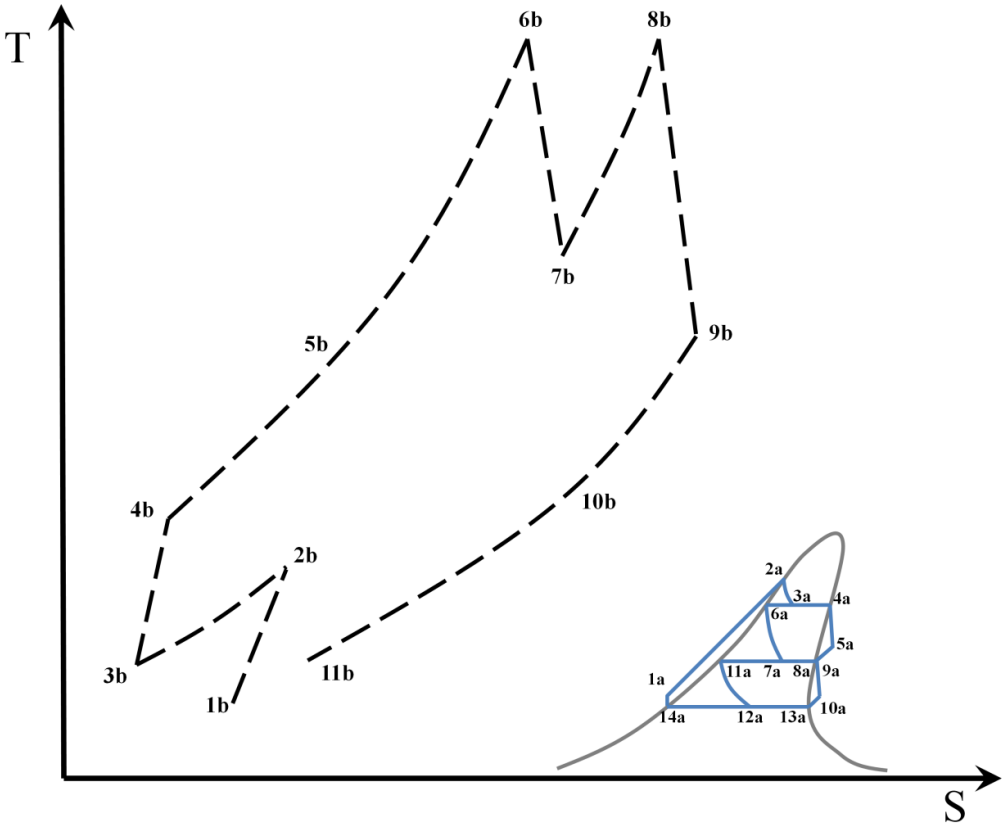

Figure 6.2: T-S diagram for combined Brayton-OFC system.

Unlike the closed helium or nitrogen Brayon cycle proposed in ref. **[**169**]**, the topping cycle shown in Fig. 6.1 and 6.1 is for an air open Brayton cycle. Since the working fluid is air, an open Brayton cycle can vent the exhaust heat at state 11b to the environment instead of cooling the working fluid prior to compression. The closed Brayton cycle proposed in ref. **[**169**]** does have its own advantages though. Helium has a larger specific-heat-ratio than air because it is a monatomic molecule versus air which is mostly composed of diatomic molecules; the specific-heat-ratio of helium is 1.66 as compared to 1.40 for air. Based on the well known relationship obtained from applying the cold air-standard assumptions on an ideal Brayton cycle, eq. (6.1) shows that the Brayton cycle first law efficiency increases for working fluids with larger specific-heat-ratios *k* **[**4**]**,

$$\eta_{I,Br} = 1 - \frac{1}{r_p^{(k-1)/k}} \tag{6.1}$$

where r_p is the pressure ratio across the turbine, typically between 5 to 20 **[**4**]**. Brayton cycles using working fluids other than air are still in the research and development phase though, with much of the research towards its applications for nuclear power **[**169**]**. In addition, closed cycles are better able to load follow and maintain design point efficiencies than open cycles during operation at part-load. During part load operation, the gas pressure in closed cycles is reduced to maintain the same flow velocities in the turbo machinery such that little inefficiencies arise compared to the design point. In open air cycles, operation at part-load requires the mass flow rates to be changed which has a much greater effect on the turbo machinery efficiency. Fig. 6.3 shows an example of three typical gas turbine relative efficiency curves from ref. **[**182**]** for part load operation as compared to design point.

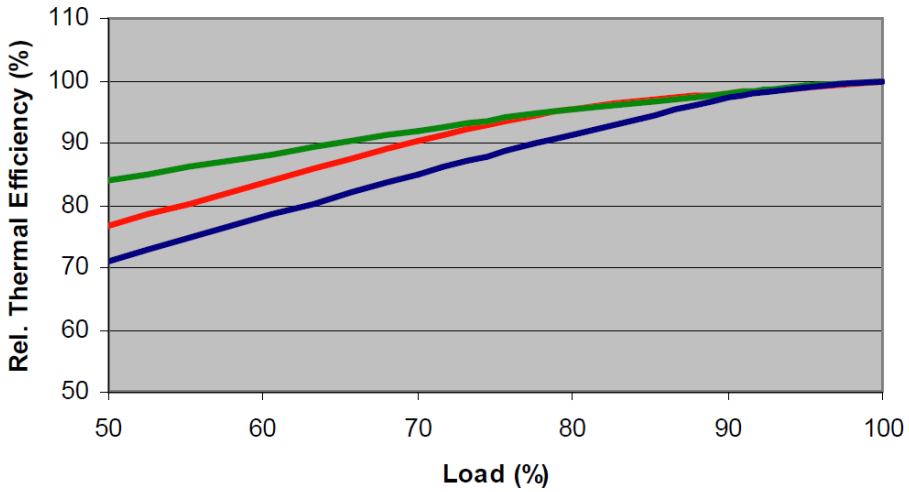

Fig. 6.3: Part load efficiencies for three typical gas turbines. Reprinted from Solar Turbines Presentation at EPA National CHP Turbine Technology and Regulatory Forum [**182**]**.**

The trends shown in Fig. 6.3 are somewhat typical of many gas turbines and the actual variations in part-load performance will ultimately be specific to the gas turbine and manufacturer. Part load performance for ORCs has been investigated in the literature by a number of researchers such as Gurgenci **[**183**]** and Muñoz et al. **[**173**]**. McMahan **[**152**]** gives generalized equations for ORC turbine and pump efficiencies as a function of the mass flow rate at part load divided by the flow rate at design point. Based on the generalized equations he presents **[**152**]**, even at 50% load, the turbo-machinery in the ORC still retain more than 75% of the isentropic efficiency at design point. Mass flow rate at part-load will also affect heat transfer characteristics in the boiler and condenser as well **[**152**]**. Aside from mass flow rate, the variations in heat source and heat sink temperatures will also affect part-load operation **[**183**]**. For the most part though, ORCs have been touted for excellent part-load operation **[**149**]**. Since ORC turbo machinery was shown in the previous chapters to have similar characteristics as the OFC's, it can be expected the OFC to have similar performance at part-load. ORCs are often used in situations where off-design conditions are the norm such as in solar energy and geothermal energy **[**183**]**. Solar energy in particular is sensitive to reduced load because of solar intermittence from for example

cloud cover or unclean heliostats that can cause the receiver temperatures to fluctuate. Thermal storage in high concentration plants somewhat reduces the effects, but present CSP plants have thermal storage only available for ~10-15 hours typically to account for night time power production. Combining a CSP plant with a gas-firing option to supplement during solar intermittence or peak demands has also been particularly attractive and is often done in many 1D axis CSP plants. By using a supplementary fuel source, the heat load going into the combined cycle can be maintained even during solar intermittence.

For the bottoming OFC, toluene was selected as the working fluid as it has been demonstrated in theory and in practice to be safe so long as adequate sealing and ventilation precautions are taken **[**17**]**. ORCs operating with a toluene working fluid have also shown the fluid to be thermally stable and more efficient than a steam working fluid for the temperature ranges considered for bottoming Brayton cycles **[**13**,**22**]**. Results from Table 3.4, the literature **[**13**,**143**]**, and actual practice has shown that simpler, less expensive turbine designs with fewer stages than steam are possible with molecularly heavier organic fluids such as toluene.

6.3 Methods of analysis

6.3.1 Power block analysis

As mentioned previously, air was selected as the working fluid for the topping Brayton cycle. NIST REFPROP 8.0 **[**92**]** was used to model air as a mixture of nitrogen, oxygen, and argon (0.7812, 0.2096, and 0.0092 by mole, respectively). REFPROP applies a Helmholtz explicit equation of state for air to determine thermodynamic properties at different states, the equation of state applied is suitable up to 2000K and 2000MPa with uncertainties typically bellow 0.5%. For the bottoming toluene OFC, the Helmholtz explicit equations of state that have been discussed extensively in chapters 2 and 3 are again employed.

Similar to the preceding analyses, small changes in the working fluids' kinetic and potential energies have been neglected. For the vapor cycle, frictional losses in the piping and heat exchanger have been neglected **[**4**,**9**]**, which has been done in the preceding chapters. However for the air Brayton cycle, the significant pressure losses are encountered in the heat exchangers and piping that cannot be ignored; in this analysis a 10% pressure reduction, a typical value that has been used in the literature [26,168,172], is assumed after compression. Heat exchangers and other steady flow devices in the Brayton and vapor cycle are assumed to be well insulated and no significant energy is lost to the environment. As was done in the prior chapters, the throttling valves in the OFC are assumed to be isenthalpic; mixing chambers and separators are assumed to be isobaric and adiabatic with no work interactions. The gas compressor and turbine are assumed to possess 90% isentropic efficiency, typical of high efficiency air compressor and turbines [26,168,171,172]. The OFC vapor turbines and feed pumps are again assumed to possess 85% isentropic efficiency, as has been done in the preceding analysis.

The power block total 1st law efficiency and utilization efficiency (a nondimensional power output) are defined as the sum of the power generated in the topping and bottoming cycle divided by the energy absorbed from the molten fluoride salt and available exergy in the salt respectively, as shown in eq. (6.2) and (6.3).

$$\eta_I = \frac{W_{Br} + W_{OFC}}{\dot{m}_{salt} c_{salt} \left(T_{hot} - T_{cold} \right)} \tag{6.2}$$

$$\varepsilon = \frac{W_{Brayton} + W_{OFC}}{\dot{m}_{salt} \left(\chi_{hot} - \chi_d \right)} \tag{6.3}$$

In the analysis, the liquid fluoride NAF-$NaBF_4$ salt is modeled as an incompressible liquid with constant specific heat of 1.51kJ/kg·K **[**169**]**. The change in specific enthalpy and entropy from state 1 to 2 for an incompressible liquid with constant specific heat during isobaric heat transfer is $\Delta h_{1\to2} = c_{salt}(T_2 - T_1)$ and $\Delta s_{1\to2} = c_{salt} \ln(T_2/T_1)$, respectively **[**4**]**. The specific exergy change for the liquid fluoride salt then from the hot tank state to the dead state is then given in eq. (6.4),

$$\chi_{hot} - \chi_d = \left(h_{hot} - T_d s_{hot} \right) - \left(h_{cold} - T_d s_d \right) = c_{salt} \left[\left(T_{hot} - T_d \right) - T_d \ln \left(T_{hot} / T_d \right) \right] \tag{6.4}$$

where the subscript *d* denotes the dead state, which is chosen to be at atmospheric pressure and 47°C (~117°F); this temperature was recommended by the CSP group from Sandia National Labs as an assumed heat sink temperature that would allow dry cooling to be feasible **[**184**]**.

6.3.2 Solar collection analysis and total system efficiency

For the solar power tower, the solar efficiency of the system is composed of two parts, the optical efficiency and the receiver efficiency. The optical efficiency η_{opt} quantifies losses due to the imperfect reflective optical path from the primary to secondary concentrator as well as geometric losses from shading or heliostat field blocking. The value quoted in the literature typically ranges from 0.6 to 0.7 depending on the time of day or if an annual average is used [168,171,172]; in this analysis the optical efficiency was taken to be 0.67. The receiver efficiency is a parameter that defines how much of the incoming solar radiation is converted to solar power. For high temperature central receivers, particularly cavity-type receivers, emission or re-radiation losses are the primary loss mechanism as this loss term increases with the receiver temperature T_{rec} to the fourth power **[**168**,**172**]**. Therefore, the receiver efficiency for a high temperature isothermal receiver including emission and natural convection losses can be approximated in eq. (6.5) **[**168**]**,

$$\eta_{rec} = 1 - \frac{\sigma \left(T_{rec}^4 - T_d^4 \right)}{C_{solar} I_{coll}} - \frac{h_{conv} \left(T_{rec} - T_d \right)}{C_{solar} I_{coll}} \tag{6.5}$$

where C_{solar} is the solar concentration ratio, I_{coll} is the collectable solar radiation incident on the receiver per unit area of mirror surface from the heliostats, σ is the Stefan-Boltzmann constant = 5.67×10^{-8}W/m^{2}K^4, and h_{conv} is the convective heat transfer coefficient due to natural convection. Although the actual convective heat transfer coefficient is actually dependent on the fluid properties as well as the receiver dimension and orientation, as an order of magnitude estimate it is taken as 10 W/m^{2}K **[**151**]**. The solar concentration ratio is taken to be 2000 effective suns and I_{coll} is taken to be 300W/m^2 as the annual average solar radiation over all daylight hours per unit area of mirror including optical losses **[**168**]**. While increasing the concentration ratio would improve the receiver efficiency in eq. (6.5), heliostats are quite expensive with the solar

collection system making up about half the initial capital costs of solar power towers [169]; also introducing more heliostats often requires increasing the field density which also reduces the optical efficiency [171]. Therefore, increasing the concentration ratio should be done judiciously to avoid unnecessarily costly systems. It should also be noted that the optical efficiency includes a so-called "collector efficiency factor" that accounts for the temperature difference between the receiver and the liquid molten salt coolant being heated; this built-in-penalty allows the analysis to assume $T_{rec} = T_{hot}$ without losing much accuracy [168]. As mentioned previously, emission losses are by far the largest contribution to receiver losses; recently though, efforts have been made to design and develop non-isothermal, or partitioned, high temperature cavity receivers [185,186]. Emission losses are reduced in these receivers because the fluid is heated sequentially through different partitions in the receiver. The flow into the receiver begins in a partition near the outside rim of the receiver and flows radially inward where there is increasing irradiance flux and higher temperatures; thus the outside partitions serve as a form of thermal shielding for the very hot fluid towards the center of the receiver [172]. Further details on non-isothermal receivers can be found in ref. [172,185,186]

The total system efficiency is determined from the product of the different cycle components as shown in eq. (6.6),

$$\eta_{sys} = \eta_{opt}\eta_{rec}\eta_{PB} \tag{6.6}$$

where η_{PB} is the power block efficiency depending on if the 1st law efficiency of eq. (6.2) or external 2nd law efficiency eq. (6.3) is used. In all cases, T_{cold} was ensured to be above the molten fluoride salt's (NAF-$NaBF_4$) freezing point of 385°C by at least 50°C. Note that the simultaneous optimization of solar collection and power block systems are necessary in order to maximize the efficiency of the system as a whole. In particular, there are several competing effects between the different components of the solar power tower system; for example, high molten salt temperatures increases the power block efficiency based on Carnot considerations, but it reduces the receiver efficiency per eq. (6.5) [172].

6.4 Results and discussion

As mentioned previously, by replacing molten nitrate salt with liquid fluoride salt coolants, the maximum coolant temperatures for the solar power tower can be increased from ~565°C to about 700°C-850°C. In practice, high-temperature metals used in industry also have temperature limits around 850°C and while more unconventional materials could be used, this adds additional costs and complexity to the system. A minimum 15°C temperature difference, or pinch, between streams in all heat exchangers is assumed to be necessary in order facilitate heat transfer. Following the power cycle analysis outlined in section 6.3.1, Fig. 6.4 shows a comparison between the 1st law efficiencies for a power block composed of a Brayton cycle alone and that for a combined Brayton-OFC system at different solar receiver temperatures. Note that by using a combined cycle approach, the maximum power block efficiency achievable at a given receiver temperature increases between 6%-8%. The increase in power block efficiency is particularly pronounced at higher turbine ratios where more net power is generated per unit flow of the liquid fluoride salt. As in chapter 3, this again points to the need for balancing the power block's efficiency with power generation; high efficiencies can be attained at low pressure ratios, but

very little power is generated and correspondingly, higher salt temperatures for the cold tank which would also result in more costly insulation to prevent energy losses to the surroundings in the cold tank and/or lower receiver efficiencies due to higher inlet salt temperature to the receiver.

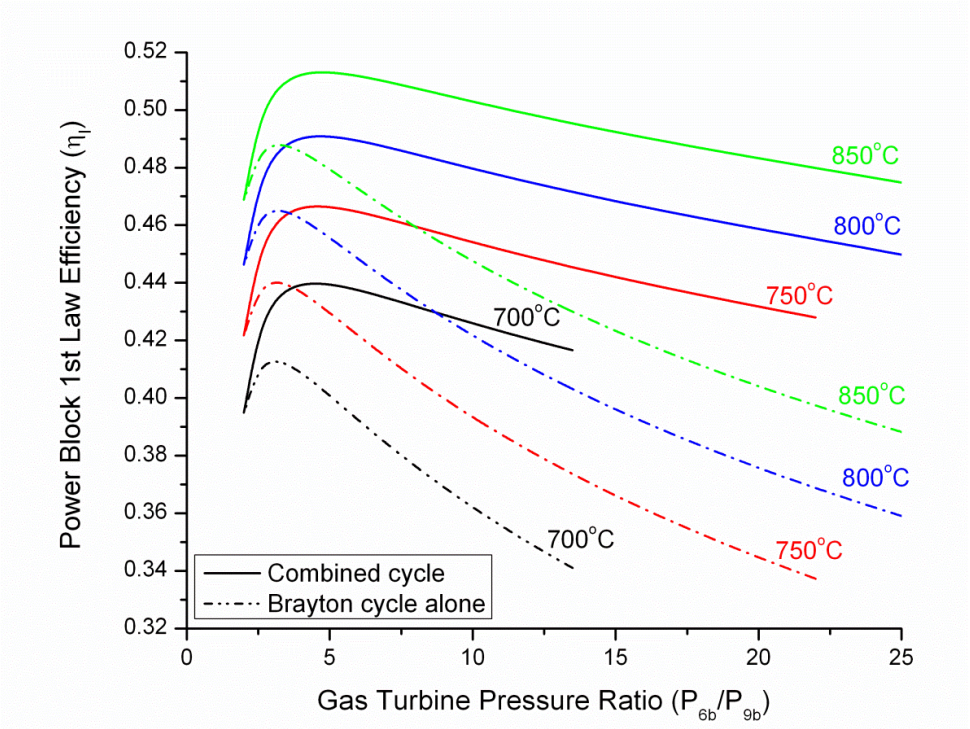

Figure 6.4: Comparison of 1st law efficiencies for a power block composed of the Brayton cycle alone and the combined Brayton-OFC system at different receiver temperatures.

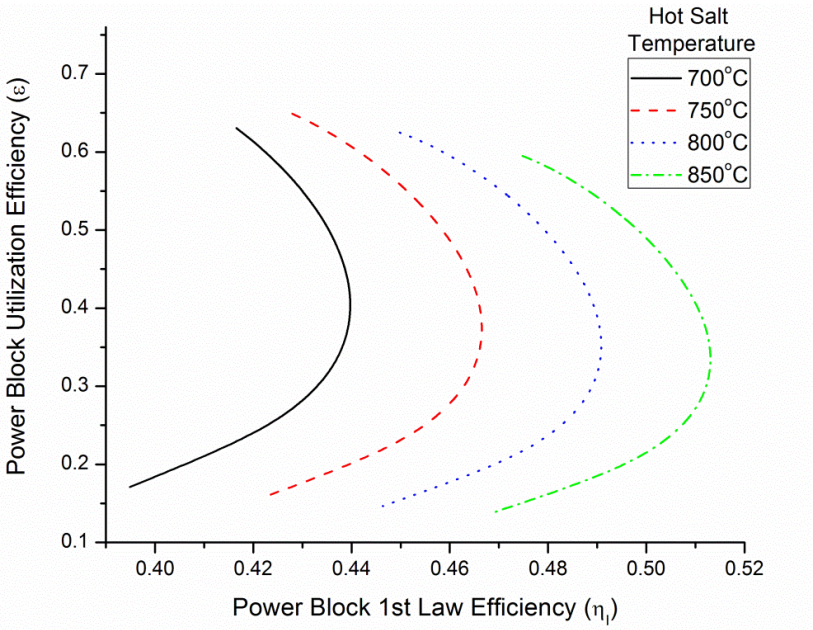

Figure 6.5: Utilization efficiency as a function of the 1st law efficiency for the combined Brayton-OFC system at different receiver temperatures.

Similar to Fig. 3.5, Fig. 6.5 shows a range of operating conditions with which net power output is balanced with 1st law efficiency of the combined Brayton-OFC cycle. It is noted in Fig. 6.5 that the maximum utilization efficiency of the combined cycle seems to decrease with increasing salt temperature after 750°C; but in reality the point of maximum utilization efficiency occurred at higher and higher pressure ratios as the receiver temperature increased. In this study, only pressure ratios up to 25 were examined to keep the maximum pressure in the system practically manageable. If higher pressure ratios were examined, one would see that indeed the maximum utilization efficiency did increase with higher receiver temperatures. In addition, it is noted that the utilization efficiency is a nondimensional parameter power for a given receiver temperature and can be misleading somewhat as it is the ratio of power produced versus potential power producible. As receiver temperatures increase, there is more potential power producible; so it is possible to have higher power generation but lower utilization efficiency, which is also the case for increasing receiver temperature in Fig. 6.5. Results showed that as the receiver temperature increased, the net power generated for the same pressure ratio also increased even though the utilization efficiency may be lower.

The product of the solar efficiency $\eta_{solar} = \eta_{opt}\eta_{rec}$ and the power block efficiency gives the total system efficiency as per eq. (6.6). Fig. 6.6 shows the solar efficiency, maximum power block efficiency optimized to pressure ratio, and the resulting total system efficiency. Note that the power block efficiency is taken as the power block's first law efficiency which is typically used in the literature and in practice for the CSP industry [26,168,171,172].

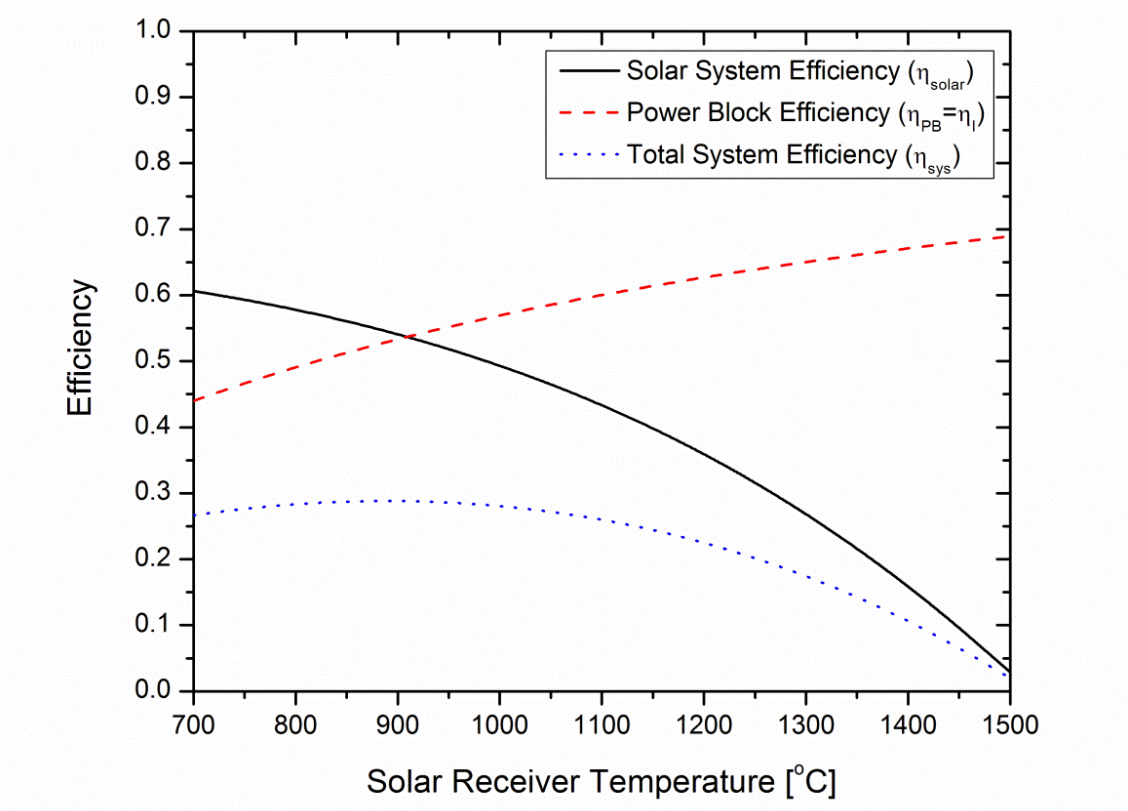

Figure 6.6: Solar power tower and component efficiencies for various solar receiver operating temperatures at concentration ratios of 2000 and using an average annual solar flux.

As previously discussed, optimization of the total system efficiency requires consideration of both the solar collection system and the power block system. As shown in Fig. 6.6, the maximum total system efficiency occurs where the solar and power block efficiency curves intersect at a receiver temperature of approximately 900^{o}C; it is noted that the maximum efficiency is ~0.3 which is comparable to or slightly higher than present high efficiency solar power towers being analyzed in the literature [168,171,172] and over twice the efficiency of many line-focus solar power plants **[**187**]**. This is close to the aforementioned temperature limit of ~850^{o}C for many industrial high-temperature metals **[**169**]**. In Fig. 6.6 and 6.7, it is shown that at higher receiver temperatures above ~1100^{o}C, the combined Brayton-OFC thermal-to-electric conversion efficiency can significantly exceed 60%, the so called "4-minute mile of heat engines." Also shown in Fig. 6.7, by applying a combined Brayton-OFC cycle approach, significantly higher efficiencies are realized over a wide range of solar receiver temperatures.

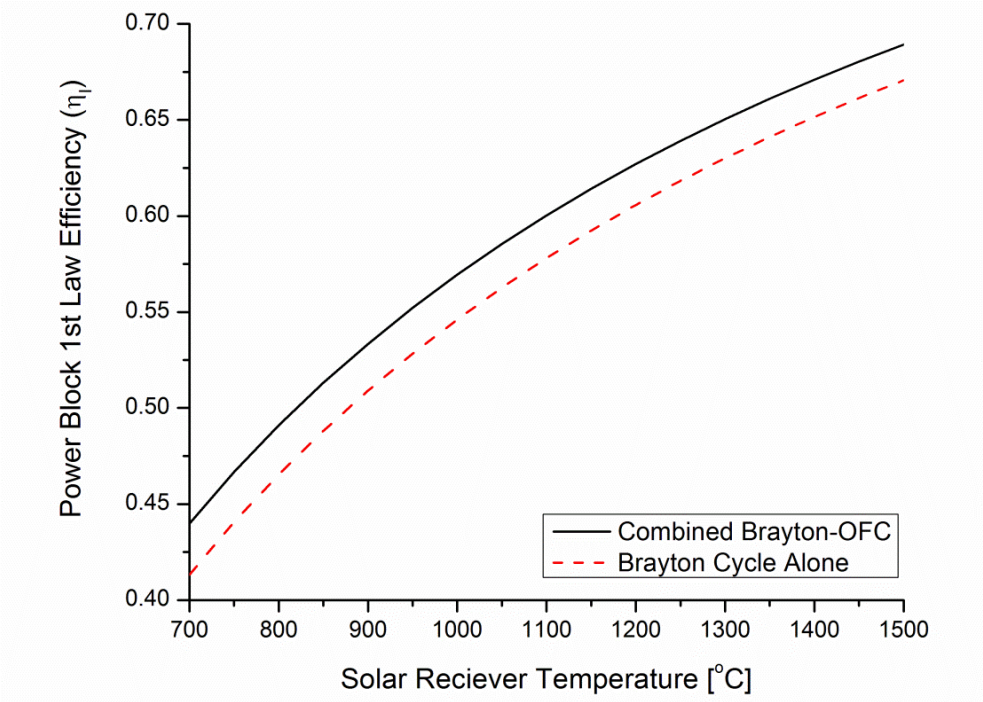

Figure 6.7: Maximum 1st law efficiencies optimized to pressure ratios for combined Brayton-OFC and Brayton cycle alone

Although increased power block efficiencies are possible at higher receiver temperatures, it is also shown in Fig. 6.6 that the solar efficiency becomes to significantly drop as higher and higher receiver temperature approaches due mainly to the radiative emission losses in eq. (6.5). If central receiver designs able to maintain near 90% receiver efficiency are realized even at high temperatures, it would mean considerably higher total system efficiencies. As mentioned previously, although higher receiver efficiencies can be realized through installation of more costly heliostats to increase the concentration ratio; it would be very expensive as well as potentially causing optical efficiencies to decrease due to higher field densities. Research and development into efficient receivers such as the non-isothermal/partitioned receiver which decreases radiative emission losses and are able to transfer the collected solar energy to the coolant yielding much higher receiver efficiencies at high temperatures. In fact, partitioned receivers are able to achieve approximately 80-90% receiver efficiency at temperature of 800-

1300°C compared to only 45-80% receiver efficiency for isothermal receivers [**171**]. Based on this significant difference in receiver efficiencies, further research and development on non-isothermal receivers could be promising for high temperature, efficient solar power towers. In addition to higher receiver temperatures, alternative combined cycle configurations may also lead to higher efficiencies. As mentioned previously, a number of studies have concluded that a simple gas turbine with reheat is more efficient than those with reheat, regeneration, and intercooling in combined cycles using bottoming steam cycles due to higher gas turbine exhaust temperatures. This variation was also investigated here, but results showed the bottoming OFC to not be able to properly utilize the higher temperatures because toluene's critical temperature is 591K, which limits the overall maximum temperature of the bottoming OFC. Unlike the multi-pressure bottoming steam cycles, higher temperatures for the bottoming cycle cannot be realized using a toluene working fluid while still maintaining a subcritical cycle. These results are consistent with those found by Chacartegui et al. **[**26**]**. In cases where simple gas turbines are to be used, it is likely that even a higher temperature working fluid that keeps the cycle subcritical will still not outperform modern multi-pressure steam cycles. Instead, the ORC and OFC seems to be limited to bottoming micro-gas turbines or high efficiency gas turbines that have lower turbine exit temperatures. This area of low power and/or low temperature applications is again where the ORC and OFC seem to have an advantage over modern HRSGs.

6.5 Conclusions

A high-level design of a solar power tower plant is proposed in which the heliostat-central receiver design is used with a liquid-fluoride salt (NaF-NaBF4) that is chemically stable and allows for maximum coolant temperatures significantly above current power tower designs using molten nitrate salts. The proposed power block system is composed of a combined topping Brayton cycle with intercooling, reheat, and regeneration and a bottoming low-temperature modified Organic Flash Cycle. By using a combined cycle design, results showed that the power block efficiency increased by 6%-8% over a range of receiver temperatures. Results showed that a 30% annual average solar-to-electric conversion efficiency is possible using the proposed system design. Although power block efficiencies over 60% are possible, emission losses from isothermal receivers limit the practical operational receiver temperature range. The realization of high efficiency, high temperature receivers operable in the +1000°C temperature range would significantly improve the efficiency of solar power towers and make them much more cost competitive with traditional fuel sources.

7 Conclusions and directions for the future

7.1 Summary of Helmholtz-explicit equations of state employed

The Organic Flash Cycle (OFC) is proposed as a vapor power cycle that could potentially increase net power output and improve the efficiency with which a wide range of finite thermal energy sources are utilized. In this study, modern Helmholtz equations of state such as BACKONE and Span-Wagner multi-parameter equation of state were employed to determine thermodynamic properties for siloxanes (MD4M, D5, MD3M, D6, MM, D4), aromatic hydrocarbons (toluene, ethylbenzene, butylbenzene, o-xylene, m-xylene, p-xylene), alkanes (pentane, butane, cyclopentane, cyclohexane, hexane), and refrigerants (R141b, R113, R123, R245ca). Values of saturated liquid and vapor densities and vapor pressure for these working fluids were calculated using the Helmholtz equations of state and compared to values listed in the NIST Chemistry WebBook. Results showed that maximum deviations were limited to less than ±7.5% for all working fluids, with the percent error typically less than 1%. A comparison of first law efficiencies calculated using the Helmholtz-explicit equations of state for an ideal basic Rankine cycle yielded a percent difference less than ±0.4% compared to calculations using NIST REFPROP 8.0. Results showed the Helmholtz-explicit equations of state to possess suitable accuracy for the vapor cycle analysis in this study. Also by using the Helmholtz equations of state and verified for this study, the number of potential working fluids that can be investigated expands significantly beyond those in the REFPROP library, particularly for working fluids more appropriate for higher temperature applications.

7.2 The OFC and enhancements for applications to intermediate temperature resources

A theoretical investigation on the OFC for intermediate temperature resources was conducted using high accuracy Helmholtz-explicit equations of state for 10 different aromatic hydrocarbon and siloxane working fluids. The premise underlying the OFC design is to improve temperature matching to the source stream, thereby minimizing exergy destruction and losses during heat transfer to the cycle working fluid and increasing net power output. The finite thermal energy reservoir was simulated as a 1kg/s flow of cooling water initially at 300^{o}C. Results showed aromatic hydrocarbons to be the better suited working fluid for the ORC and OFC due to higher power output and less complex turbine designs. The results from the analysis also showed that the single flash OFC achieves comparable utilization efficiencies to the optimized basic ORC. Although the OFC improved heat addition exergetic efficiency, this advantage was effectively negated by irreversibilities introduced during flash evaporation. As a result, a number of modifications to the OFC are proposed including adding a secondary flash stage and replacing the throttling valve with a two-phase expander. Results showed that by splitting the expansion process in the OFC into two steps and combining the liquid stream from flash evaporation in a secondary expansion stage, up to 10% gains in power output above the optimized basic ORC is achievable. The greatest gains in power output were observed when this modification was combined with replacing the throttling valve with a two-phase expander. Results showed that the proposed enhancements had greater effect on the OFC using aromatic hydrocarbon working fluids, increasing the utilization efficiency by 5-20% over the optimized ORC; whereas for siloxanes, the improvement was limited to only 2-4%. Based on an order of magnitude analysis,

results also showed that the OFC and ORC would require comparable heat exchanger surface areas. This has been used as a rough estimate for initial capital costs in many ORC studies; therefore, it was extrapolated that the two systems would also have similar capital costs as well.

7.3 The OFC and enhancements for applications to low temperature resources

The Organic Flash Cycle (OFC) and the proposed enhancements were analyzed for applicability to low temperature resources in the 80°C to 150°C temperature range. Thirteen different alkanes and refrigerants with vapor pressures appropriate for this temperature range were analyzed as potential working fluids. Similar to the intermediate temperature case, the optimized single flash OFC was shown to generate less power per unit flow rate of the thermal reservoir than the optimized ORC. With the proposed modifications from Chapter 4 though, results showed that the OFC can generate well over 60% more power than the optimized ORC for the same finite thermal energy source. Although the modified 2-phase OFC exhibited the highest utilization efficiency of the cycle configurations considered, ultimately the additional power generated must analyzed in respect to the added complexity and costs to the system. The analysis showed that close to 60% increases in utilization efficiency can be achieved in the single flash OFC by simply replacing the throttling valve used during the flash evaporation process with presently available two-phase expanders. The analysis also determined that the minimum temperature difference between streams in the heat exchanger was an important design parameter to consider for low temperature energy resources as even slightly relaxing the pinch temperature can yield significant gains in net power output.

7.4 A high level combined-cycle solar power tower plant design

A combined cycle plant consisting of a topping open air Brayton cycle with intercooling, reheating, and regeneration coupled with a bottoming low temperature modified toluene OFC is proposed for a centralized solar power tower with an isothermal receiver. Liquid-fluoride salt (NaF-NaBF4) is preferred over nitrate salts such that higher coolant temperatures are feasible. Graphite or the fluoride salt itself would serve directly as the storage mechanism during the night or times of solar intermittence. Dry cooling is also preferred as it reduces the water requirements of the plant, a scarce resource in the desert where large solar fields are often constructed. Results showed that a combined cycle design increased power block efficiency by 6-8% as compared to a Brayton cycle alone over a large range of receiver temperatures. From the analysis, a conservative estimate of a 30% total annual average solar-to-electric plant efficiency is possible with the proposed plant layout. Power block efficiencies greater than 60% are also possible, but emission losses from the isothermal central receiver become significant in reducing total system efficiency. The development of efficient solar receivers capable of operating above 1000°C temperature is necessary in order to fully take advantage of the combined cycle concept and yield higher solar-to-electric efficiencies such that high temperature solar thermal can become more cost competitive with traditional fuel sources.

7.5 Future research

Experimental validation of the theoretical results presented in this study through a small scale prototype of the OFC would be a significant milestone in its continued development. Further

research into the design of two-phase expanders specifically for the working fluids proposed in this study would ultimately lead to the high 20-50% gains in utilization efficiency over the optimized ORC that could propel this technology to the physical marketplace. In addition, detailed cost projections and analyses for the plant equipment and the resulting electricity the OFC produces will have huge impact in its actual practicality. Programs such as the Cleantech-to-Market (C2M) initiative sponsored by the Haas Business School at the University of California-Berkeley are thus very important in fostering collaboration between science and business communities to evaluate and promote clean energy technology.

Future research for the OFC could also target new areas of integration in renewable energy systems; one such example is an integrated CSP system with high concentration, high density photovoltaics and solar thermal electricity production using the OFC. Concentrated photovoltaics offer lower cost by reducing the amount of photovoltaic material required for collecting the same amount of solar energy. Using multi-junction and materials able to withstand higher temperatures allows increased robustness and higher efficiency photovoltaic systems. However, for high concentration, densely packed cells, active cooling becomes necessary to remove excess heat in the photovoltaic system such that reasonable solar-to-electric conversion efficiencies are attained and no thermal damage to the cells occurs. Ho et al. [188,189] recently designed and analyzed a two-phase cooling channel operating directly underneath the cells to remove excess heat. In the study, the vapor mass quality was limited to 0.70 at the cooling channel exit to prevent dry out and the correspondingly low heat transfer coefficients that would result. Future research could be geared toward the integration of using the coolant from the cooling channel in the OFC where the flash evaporator is used to bring the two-phase mixture to a saturated vapor for expansion through a turbine. This solar thermal-photovoltaic co-generation scheme could have potentially very high solar-to-electric efficiency. In addition, the coolants utilized in the study by Ho et al. [189] are similar to the refrigerants in this study for the low temperature OFC. Further research into integrated renewable systems such as this could significantly increase the efficiency with which renewables are utilized and certainly warrants further research.

References

[1] C Min, H Lund, LA Rosendahl, and TJ Condra, "Energy efficiency analysis and impact evaluation of the application of thermoelectric power cycle to today's CHP systems," *Applied Energy*, vol. 87, pp. 1231-1238, 2010.

[2] CB Vining, "An inconvenient truth about thermoelectrics," *Nature Materials*, vol. 8, pp. 83-85, 2009.

[3] BCS Incorporated, "Waste Heat Recovery: Technology and Opportunities in U.S. Industry," US Department of Energy - Industrial Technologies Program, 2008.

[4] YA Cengel, *Thermodynamics: An Engineering Approach*, 5th ed. Boston: McGraw Hill, 2006.

[5] MJ Moran and HN Shapiro, *Fundamentals of Enginering Thermodynamics*, 5th ed. Hoboken: John Wiley & Sons Inc, 2004.

[6] AK Gupta, "Advance technologies for clean and efficient energy conversion in power systems," in *Thermal Engineering in Power Systems*, RS Amano and B Sunden, Eds. Southhampton, UK: WIT Press, 2008, ch. 2, pp. 37-70.

[7] WH Wiser, *Energy resources: occurrence, production, conversion, use*. New York, USA: Springer-Verlag, 2000.

[8] J Kern, "Steam Power Plant," in *Energy conversion*, YG Goswami and F Kreith, Eds. Boca Raton, FL: CRC Press, 2008, pp. 8.1-8.16.

[9] T Ho, SS Mao, and R Greif, "Comparison of the Organic Flash Cycle (OFC) to other advanced vapor cycles for intermediate and high temperature waste heat reclamation and solar thermal energy," *Energy [accepted]*.

[10] DL Chase and PT Kehoe, "GE Combined-Cycle Product Line and Performance," General Electric Power Systems, Schenectady, NY, GER-3574G, 2000.

[11] C Casarosa, F Donatini, and A Franco, "Thermoeconomic optimization of heat recovery steam generators operating parameters for combined plants," *Energy*, vol. 29, pp. 389–414, 2004.

[12] A Ragland and W Stenze, "Combined Cycle Heat Recovery Optimization," in *ASME International Joint Power Generation Conference*, Miami Beach, FL, July 23-26, 2000, pp. 1-6.

[13] WB Stine and RW Harrigan, *Solar Energy System Design*. New York: John Wiley & Sons, Inc., 1986.

[14] TC Hung, TY Shai, and SK Wang, "A review of Organic Rankine Cycles (ORCs) for the recovery of low-grade waste heat," *Energy*, vol. 22, pp. 661-667, 1997.

[15] R DiPippo, *Geothermal Power Plants: Principles, Applications, and Case Studies*. Oxford: Elsevier, 2005.

[16] V Ganapathy, *Industrial Boilers and Heat Recovery Steam Generators: Design, Applications, and Calculations*. New York: Marcel Dekker, Inc., 2002.

[17] TJ Marciniak, JL Krazinski, HM Bushby, and EH Buyco, "Comparison of Rankine-cycle power systems: Effects of seven working fluids," Argonne National Laboratory,

ANL/CNSV-TM-87, 1981.

[18] S Quoilin and V Lemort, "Technological and Economical Survey of Organic Rankine Cycle Systems," in *5th European Conference on Economics and Management of Energy in Industry*, Vilamoura, Portugal, 2009.

[19] B Saleh, G Koglbauer, M Wendland, and J Fischer, "Working fluids for low-temperature organic Rankine cycles," *Energy*, vol. 32, pp. 1210-1221, 2007.

[20] BF Tchanche, G Papadakis, G Lambrinos, and A Frangoudakis, "Fluid selection for a low-temperature solar organic Rankine cycle," *Applied Thermal Engineering*, vol. 29, pp. 2468-2476, 2009.

[21] HD Hettiarachchi, M Golubovic, WM Worek, and Y Ikegami, "Optimum design for an Organic Rankine cycle using low-temperature geothermal heat sources," *Energy*, vol. 32, pp. 1698-1706, 2007.

[22] H Chen, DY Goswami, and EK Stefanakos, "A review of thermodynamic cycles and working fluids for the conversion of low-grade heat," *Renewable and Sustainable Energy Reviews*, vol. 14, pp. 3059-3067, 2010.

[23] BF Tchanche, Gr Lambrinos, A Frandoudakis, and G Papdakis, "Low-grade heat conversion into power using organic Rankine cycles - A review of various applications," *Renewable and Sustainable Energy Reviews*, vol. 15, pp. 3963-3979, 2011.

[24] FJ Fernández, MM Prieto, and I Suárez, "Thermodynamic analysis of high-temperature regenerative organic Rankine cyces using siloxanes as working fluids," *Energy*, vol. 36, pp. 5239-5249, 2011.

[25] NA Lai, M Wendland, and J Fischer, "Working fluids for high-temperature organic Rankine cycles," *Energy*, vol. 36, pp. 199-211, 2011.

[26] R Chacartegui, D Sanchez, JM Munoz, and Sanchez T, "Alternative ORC bottoming cycle FOR combined cycle power plants," *Applied Energy*, vol. 86, pp. 2162-2170, 2009.

[27] IH Aljundi, "Effect of dry hydrocarbons and critical point temperature on the efficiencies of organic Rankine cycle," *Renewable Energy*, vol. 4, pp. 1196-1202, 2011.

[28] DA Sunter and VP Carey, "A Thermodynamic Similarity Framework for Assessment of Working Fluids for Solar Rankine Power Generation," *ASME Journal of Solar Engineering*, vol. 132, pp. 041005 (1-8), 2010.

[29] AI Papadopoulos, M Stijepovic, and P Linke, "On the systematic design and selection of optimal working fluids for Organic Rankine Cycles," *Applied Thermal Engineering*, vol. 30, pp. 760-769, 2010.

[30] H Tabor and L Bronicki, "Establishing Criteria for Fluids for Small Vapor Turbines," *SAE Transactions*, vol. 73, pp. 561-575, 1965.

[31] BE Poling, JM Prausnitz, and JP O'Connell, *The Properties of Gases and Liquids*, 5th ed. New York: McGraw Hill, 2001.

[32] BT Liu, KH Chien, and CC Wang, "Effect of working fluids on organic Rankine cycle for waste heat recovery," *Energy*, vol. 29, pp. 1207-1217, 2004.

[33] JVC Vargas and A Bejan, "Thermodynamic optimization of the match between two streams with phase change.," *Energy*, vol. 25, pp. 15-33, 2000.

[34] G Venkatarathnam, G Mokashi, and SS Murthy, "Occurrence of pinch points in condensers and," *International Journal of Refrigeration*, vol. 19, pp. 361-368, 1996.

[35] A Franco and C Casarosa, "On some perspectives for increasing the efficiency of combined cycle power plants," *Energy*, vol. 22, pp. 1501–1518, 2002.

[36] JL Wang, L Zhao, and XD Wang, "A comparative study of pure and zeotropic mixtures in low-temperature solar Rankine cycle," *Applied Energy*, vol. 87, pp. 3366-3373, 2010.

[37] XD Wang and L Zhao, "Analysis of zeotropic mixtures used in low-temperature solar Rankine cycles for power generation," *Solar Energy*, vol. 83, pp. 605-613, 2009.

[38] RS Murugan and PMV Subbarao, "Thermodynamic analysis of Rankine-Kalina combined cycle," *International Journal of Thermodynamics*, vol. 11, pp. 133-141, 2008.

[39] G Angelino and PC Di Paliano, "Multicomponent working fluids for organic Rankine cycles (ORCs)," *Energy*, vol. 23, pp. 449-463, 1998.

[40] C Wu, "Non-azeotropic mixture energy conversion," *Energy Conversion and Management*, vol. 25, pp. 199-206, 1985.

[41] PA Lolos and ED Rogdakis, "A Kalina power cycle driven by renewable energy sources," *Energy*, vol. 34, pp. 457-464, 2009.

[42] OM Ibrahim and SA Klein, "Absorption power cycles," *Energy*, vol. 21, pp. 21-27, 1996.

[43] JM Smith, HC Van Ness, and MM Abbott, *Introduction to chemical engineering thermodynamics*, 7th ed. New York: McGraw-Hill, 2005.

[44] WJ Mulroy, PA Domanski, and DA Didion, "Glide matching with binary and ternary zeotropic refrigerant mixtures Part 1. An experimental study," *International Journal of Refrigeration*, vol. 17, pp. 220-225, 1994.

[45] W Wu, L Zhao, and T Ho, "Experimental investigation on pinch points and maximum temperature differences in a horizontal tube-in-tube evaporator using zeotropic refrigerants," *Energy Conversion and Management*, vol. 56, pp. 22-31, 2012.

[46] G Venkatarathnam and SS Murthy, "Effect of mixture composition ont he formation of pinch points in condensers and evaporators for zeotropic refrigerant mixtures," *International Journal of Refrigeration*, vol. 22, pp. 205-215, 1999.

[47] JR Thome, *Engineering databook III*. Huntsville, AL: Wolverine Tube, Inc, 2010.

[48] VP Carey, *Liquid-Vapor Phase-Change Phenomena*, 2nd ed. New York: Taylor & Francis, 2007.

[49] H Chen, DY Goswami, MM Rahman, and EK Steanakos, "A supercritical Rankine cycle using zeotropic mixture working fluids for the conversion of low-grade heat into power," *Energy*, vol. 36, pp. 549-555, 2010.

[50] AW Crook, *Profiting from low-grade heat: thermodynamic cycles for low-temperature heat sources*. Glasgow: Institution of Electrical Engineers, 1994.

[51] F Heberle, M Preibinger, and D Bruggemann, "Zeotropic mixtures as working fluids in Organic Rankine Cycles for low-enthalpy geothermal resources," *Renewable Energy*, vol. 37, pp. 364-370, 2012.

[52] JJ Bao, L Zhao, and WZ Zhang, "A novel auto-cascade low-temperature solar Rankine cycle system for power generation," *Solar Energy*, vol. 85, pp. 2710-2719, 2011.

[53] YM Zhang, M He, Z Jai, and X Liu, "First law-based thermodynamic analysis on Kalina cycle," *Frontiers of Energy and Power in China*, vol. 2, pp. 145-151, 2008.

[54] HA Mlcak, "An Introduction to the Kalina Cycle," *Proceedings of the International Joint*

Power Generation Conference Vol. 30, vol. ASME International Book No H01077, pp. 1-11, 1996.

[55] AI Kalina, "New Binary Geothermal Power System," in *Proceedings of the International Conference on Geothermal Power Engineering*, Sochi, Russia, 2003, pp. 1-11.

[56] P Bombarda, CM Invernizzi, and C Pietra, "Heat recovery from Diesel engines: A thermodynamic comparison between Kalina and ORC cycles," *Applied Thermal Engineering*, vol. 30, pp. 212-219, 2010.

[57] YM Park and RE Sonntag, "A preliminary study of the Kalina power cycle in connection with a combined cycle system," *International Journal of Energy Research*, vol. 14, pp. 153-162, 1990.

[58] JD Maloney and RC Robertson, "Thermodynamic Study of Ammonia-Water Heat Power Cycles," Oakridge National Laboratory, Report No. 53-8-43, 1953.

[59] S Vijayarghavan, "THERMODYNAMIC STUDIES ON ALTERNATE BINARY WORKING FLUID COMBINATIONS AND CONFIGURATIONS FOR A COMBINED POWER AND COOLING CYCLE," University of Florida, PhD Thesis 2003.

[60] F Xu, DY Goswami, and SS Bhagwat, "A combined power/cooling cycle," *Energy*, vol. 25, pp. 233-246, 2000.

[61] DY Goswami and F Xu, "Analysis of a new thermodynamic cycle for combined power and cooling using low and mid temperature solar collectors," *Journal of Solar Energy Engineering*, vol. 121, pp. 91-97, 1999.

[62] G Tamm, DY Goswami, S Lu, and AA Hasan, "Theoretical and experimental investigation of an ammonia-water power and refrigeration thermodynamic cycle," *Solar Energy*, vol. 76, pp. 217-228, 2004.

[63] AA Hasan, DY Goswami, and S Vijayaraghavan, "First and second law analysis of a new power and refrigeration thermodynamic cycle using solar heat source," *Solar Energy*, vol. 73, pp. 385-393, 2002.

[64] G Tamm, DY Goswami, and S Lu, "Novel combined power and cooling thermodynamic cycle for low temperature heat sources, part I: Theoretical investigation," *Journal of Solar Energy*, vol. 125, pp. 218-222, 2003.

[65] G Tamm and DY Goswami, "Novel combined power and cooling thermodynamic cycle for low temperature heat sources, part II: Experimental investigation," *Journal of Solar Energy*, vol. 125, pp. 223-229, 2003.

[66] S Lu and DY Goswami, "Optimization of a novel combined power/refrigeration thermodynamic cycle," *Journal of Solar Energy*, vol. 125, pp. 212-217, 2003.

[67] S Vijayarghavan and DY Goswami, "Organic working fluids for a combined power and cooling cycle," *Journal of Energy Resources Technology*, vol. 127, pp. 125-130, 2005.

[68] XR Zhang, H Yamaguchi, K Fujima, M Enomoto, and N Sawada, "Study of solar energy powered transcritical cycle using supercritical carbon dioxide," *International Journal of Energy Research*, vol. 30, pp. 1117-1129, 2006.

[69] IK Smith, "Development of the trilateral flash cycle system Part 1: fundamental considerations," *Proceedings of the Institution of Mechanical Enginers, Part A: Journal of Power and Energy*, vol. 207, pp. 179-194, 1993.

[70] EG Feher, "The supercritical thermodynamic power cycle," *Energy Conversion*, vol. 8, pp.

85-90, 1968.

[71] Z Gu and H Sato, "Optimization of cyclic parameters of a supercritical cycle for geothermal power generation," *Energy Conversion and Management*, vol. 42, pp. 1409-1416, 2001.

[72] M Kangolu and YA Cengel, "Retrofitting a geothermal power plant to optimize peformance: a case study," *ASME Journal of Energy Resources Technology*, vol. 121, pp. 295-301, 1999.

[73] Z Gu and H Sato, "Peformance of supercrtiical cycles for geothermal binary design," *Energy Conversion and Management*, vol. 2002, pp. 961-971, 2002.

[74] D Mikielewicz and J Mikielewicz, "A thermodynamic criterion for selection of working fluid forsubcritical and supercritical domestic micro CHP," *Applied Thermal Engineering*, vol. 30, pp. 2357-2362, 2010.

[75] S Karellas and A Schuster, "Supercritical fluid parameters in Organic Rankine Cycle applications," *International Journal of Thermodynamics*, vol. 11, pp. 101-108, 2008.

[76] A Schuster, S Karellas, and R Aumann, "Efficiency optimization potential in supercritical Organic Rankine Cycles," *Energy*, vol. 35, pp. 1033-1039, 2008.

[77] Y Chen, P Lundqvist, A Johansoon, and P Platell, "A comparative study of the carbon dioxide transcritical power cycle compared with an organic Rankine cycle iwth R123 as working fluid in waste heat recovery," *Applied Thermal Engineering*, vol. 26, pp. 2142-2147, 2006.

[78] E Cayer, N Galanis, M Desilets, H Nesreddine, and P Roy, "Analysis of a carbon dioxide transcritical power cycle using a low temperature source," *Applied Energy*, vol. 86, pp. 1055-1063, 2009.

[79] E Cayer, N Galanis, and H Nesreddine, "Parametric study and optimization of a transcritical power cycle using a low temperature source," *Applied Energy*, vol. 87, pp. 1349-1357, 2010.

[80] T Guo, H Wang, and S Zhang, "Comparative analysis of natural and conventional working fluids for use in transcrtical Rankine cycle using low-temperature geothermal source," *International Journal of Energy Research*, vol. 35, pp. 530-544, 2011.

[81] XR Zhang et al., "Analysis of a novel solar energy-powered Rankine cycle for combined power and heat generation using supercritical carbon dioxide," *Renewable Energy*, vol. 31, pp. 1839-1854, 2006.

[82] H Yamaguchi, XR Zhang, K Fujima, M Enomoto, and N Sawada, "Solar energy powered Rankine cycle using supercritical CO2," *Applied Thermal Engineering*, vol. 26, pp. 2345-2354, 2006.

[83] XR Zhang, H Yamaguchi, K Fujima, M Enomoto, and N Sawada, "Theoretical analysis of a thermodynamic cycle for power and heat production using supercritical carbon dioxide," *Energy*, vol. 32, pp. 591-599, 2007.

[84] XR Zhang, H Yamaguchi, and D Uneno, "Experimetnal study on the performance of solar Rankine system using supercrtical CO2," *Renewable Energy*, vol. 32, pp. 2617-2628, 2007.

[85] C Zamfirescu and I Dincer, "Thermodynamic analysis of a novel ammonia-water trilateral Rankine cycle," *Thermochimica Acta*, vol. 477, pp. 7-15, 2008.

[86] J Fischer, "Comparison of trilateral cycles and organic Rankine cycles," *Energy*, vol. 36, pp. 6207-6219, 2011.

[87] IK Smith and R Pitanga Marques Da Silva, "Development of the trilateral flash cycle system. II: Increasing power output with working fluid mixtures," *Proceedings of the Institution of Mechanical Engineers. Part A. Journal of power and energy*, vol. 208, pp. 135-144, 1994.

[88] IK Smith, N Stosic, and CA Aldis, "Development of the trilateral flash cycle system. Part 3: The design of high efficiency two-phase screw expanders," *Proceedings of the Institution of Mechanical Engineers. Part A. Journal of power and energy*, vol. 210, pp. 75-93, 1996.

[89] IK Smith, "Review of the Development of Two-Phase Screw Expanders," in *IMECHE Conference Transactions*, London, England, 1999.

[90] IK Smith and N Stosic, "Prospects for energy conversion efficiency improvements by the use of twin screw two-phase expanders," in *2nd International Heat Power Cycles Conference*, Paris, France, 2001.

[91] IK Smith, N Stosic, and A Kovacevic, "Screw expanders increase output and decrease the cost of geothermal binary power plant systems," *Geothermal Resource Council Transactions*, vol. 29, pp. 787-794, 2005.

[92] EW Lemmon, ML Huber, and MO McLinden, *NIST Standard Reference Database 23: Reference Fluid Thermodynamic and Transport Properties-REFPROP, Version 8.0*. Gaithersburg: National Institute of Standards and Technology, Standard Reference Data Program, 2010.

[93] K Lovegrove and M Dennis, "Solar thermal energy systems in Australia," *International Journal of Environmental Studies*, no. 63, pp. 791-802, 2006.

[94] G Soave, "Equilibrium Constants from a modified Redlich-Kwong Equation of State," *Chemical Engineering Science*, vol. 27, pp. 1197-1203, 1972.

[95] Z Nasri and H Binous, "Applications of the Peng-Robinson Equation of State using MATLAB," *Chemical Engineering Education*, vol. 43, pp. 1-10, 2009.

[96] RC Reid, JM Prausnitz, and BE Poling, *The Properties of Gases and Liquids*, 4th ed. New York: McGraw-Hill Book Company, 1987.

[97] A Muller, J Winkelmann, and J Fischer, "Backone Family of Equations of State: 1. Nonpolar and Polar Pure Fluids," *AIChE Journal*, vol. 42, pp. 1116-1126, 1996.

[98] Wendland M, Fischer J, Muller A, Winkelmann J Weingerl U, "Backone Family of Equations of State: 2. Nonpolar and Polar Fluid Mixtures," *AIChe Journal*, vol. 47, pp. 705-717, 2001.

[99] R Span, *Multiparameter Equations of State: An Accurate Source of Thermodynamic Property Data*. Berlin: Springer, 2000.

[100] R Span and W Wagner, "Equations of state for technical applications. I. Simultanenously optimized function forms for nonpolar and polar fluids.," *International Journal of Thermophysics*, vol. 24, pp. 1-39, 2003.

[101] R Span and W Wagner, "Equations of state for technical applications. II. Results for Nonpolar Fluids.," *International Journal of Thermophysics*, vol. 24, pp. 41-109, 2003.

[102] R Span and W Wagner, "Equations of state for technical applications. III. Results for polar

fluids.," *International Journal of Thermophysics*, vol. 24, pp. 111-162, 2003.

[103] P Colonna, NR Nannan, A Guardone, and EW Lemmon, "Multi-parameter equations of state for selected siloxanes," *Fluid Phase Equilibria*, vol. 244, pp. 193-211, 2006.

[104] P Colonna, NR Nannan, and A Guardone, "Multi-parameter equations of state for siloxanes [(CH3)3-Si-O1/2]2-[O-Si-(CH3)2]i=1,3, and [O-Si-(CH3)2]6," *Fluid Phase Equilbria*, vol. 263, pp. 115-130, 2008.

[105] M Wendland, B Saleh, and J Fischer, "Accurate Thermodynamic Properties from the BACKONE Equation for the Processing of Natural Gas," *Energy & Fuels*, vol. 18, pp. 938-951, 2004.

[106] B Saleh and M Wendland, "Screening of pure fluids as alternative refrigerants," *International Journal of Refrigeration*, vol. 29, pp. 260-269, 2006.

[107] S Calero, M Wendland, and J Fischer, "Description of Alternative Refrigerants with BACKONE Equations," *Fluid Phase Equilibria*, vol. 15, pp. 1-22, 1998.

[108] AL Ngoc, M Wendland, and J Fischer, "Working fluids for high-temperature organic Rankine cycles," *Energy*, vol. 36, pp. 199-211, 2011.

[109] D Chandler, "Introduction to Modern Statistical Mechanics," *Oxford University Press*, 1987.

[110] RT Jacobsen, EW Lemmon, SG Penoncello, Z Shan, and NT Wright, *Heat Transfer Handbook*, Kraus AD Bejan A, Ed. Hoboken: John Wiley & Sons Inc., 2003, vol. 1.

[111] KA Gillis, "Thermodynamic Properties of Seven Gaseous Halogenated Hydrocarbons from Acoustic Measurements: CHCIFCF3, CHF 2CF3, CF3CH3,CHF2CH3, CF3CHFCHF2, CF3CH2CF3, and CHF2CF2CH2F," *International Journal of Thermophysics*, vol. 18, pp. 73-135, 1997.

[112] M Jaeschlke and P Schley, "Ideal-Gas Thermodynamic Properties for Natural-Gas Applications," *International Journal of Thermophysics*, vol. 16, no. 6, pp. 1381-1392, 1995.

[113] D Bucker and W Wagner, "Equation of State for the Thermodynamic Properties of Ethane," *Journal of Physical Chemistry Reference Data*, vol. 35, 2006.

[114] B Saager, "Construction and application of physically based equations of state Part I. Modification of the BACK equation," *Fluid Phase Equilibria*, vol. 72, pp. 41-66, 1992.

[115] B Saager and J Fischer, "Construction and application of physically based equations of state Part II The dipolar and quadrupolar contributions to the Helmholtz energy," *Fluid Phase Equilibria*, vol. 72, pp. 67-88, 1992.

[116] IF Radzyminski and WB Whiting, "Fluid phase stability and equations of state," *Fluid Phase Equilibria*, vol. 34, pp. 101-110, 1987.

[117] J McGarry, "Correlation and Prediction of the Vapor Pressures of Pure Liquids over Large Pressure Ranges," *Industrial and Engineering Chemistry Design and Development* , vol. 22, pp. 313-322, 1983.

[118] DR Defibaugh, ARH Goodwin, G Morrison, and LA Weber, "Thermodynamic properties of 1,l-dichloro-1-fluoroethane (R141b)," *Fluid Phase Equilibria*, vol. 85, pp. 271-284, 1993.

[119] ARH Goodwin, DR Defibaugh, G Morrison, and LA Weber, "The Vapor Pressure of 1, 1-Diehloro-2, 2, 2-Trifluoroethane (R123)," *International Journal of Thermophysics*, vol. 13,

pp. 999-1009, 1992.

[120] MATLAB version 2009b. (2011) fzero. [Online]. http://www.mathworks.com/help/techdoc/ref/fzero.html

[121] PJ Linstrom and WG Mallard. (2011, December) NIST Chemistry WebBook, NIST Standard Reference Database Number 69. National Institute of Technology: Gathersburg. [Online]. http://webbook.nist.gov

[122] C Casci et al., "Heat recovery in a ceramic kiln with an organic Rankine cycle engine," *Heat Recovery Systems*, vol. 1, pp. 125-131, 1981.

[123] H Legmann, "Recovery of industrial heat in the cement industry by the means of the ORC process," in *IEEE 44th Cement Industry Technical Conference*, Jacksonville, FL, 2002, pp. 29-35.

[124] J Wang, Y Dai, and L Gao, "Exergy analyses and parametric optimizations for different cogeneration power plants in cement industry," *Applied Energy*, vol. 86, pp. 941-948, 2009.

[125] E Steinbiss, "Traditional and advanced concepts of waste heat recovery in cement plants," in *Energy efficiency in the cement industry*, J Sirchis, Ed. New York: Elsevier Applied Science, 2005, pp. 52-62.

[126] DA Reay, "Heat recovery - research and development with the European community," *Heat Recovery Systems*, vol. 2, pp. 419-436, 1982.

[127] J Söderman and F Pettersson, "Searching for enhanced energy systems with process integration in pulp and paper industries," *Computer Aided Chemical Engineering*, vol. 14, pp. 1061-1066, 2003.

[128] V Minea, "Using Geothermal Energy and Industrial Waste Heat for Power Generation," in *IEEE Canada Electrical Power Conference*, Montreal, Canada, 2007, pp. 543-549.

[129] NB Desai and S Bandyopadhyay, "Process integration of organic Rankine cycle," *Energy*, vol. 34, pp. 1674-1686, 2009.

[130] K Lovegrove and M Dennis, "Solar thermal energy systems in Australia," *International Journal of Environmental Studies*, vol. 63, pp. 791-802, 2006.

[131] BF Tchanche, GR Lambrinos, A Frangoudakis, and G Papadakis, "Low-grade heat conversion into power using organic Rankine cycle - A review of various applications," *Renewable and Sustainable Energy Reviews*, vol. 15, pp. 3963-3979, 2011.

[132] L Jing, P Gang, and J Jie, "Optimization of low temperature solar thermal electric generation with Organic Rankine Cycle in different area.," *Applied Energy*, vol. 11, pp. 3355-3365, 2010.

[133] PJ Mago, KK Srinivasan, LM Chamra, and C Somayaji, "An examination of exergy destruction in organic Rankine cycles," *International Journal of Energy Research*, vol. 32, pp. 926-938, 2008.

[134] Z Gu and H Sato, "Performance of supercritical cycles for geothermal binary design," *Energy Conversion an dManagement*, vol. 43, pp. 961-971, 2002.

[135] EW Lemmon and R Span, "Short Fundamental Equations of State for 20 Industrial Fluids," *Journal of Chemical Enginering Data*, vol. 51, pp. 785-850, 2006.

[136] Y Dai, J Wang, and L Gao, "Parametric optimization and comparative study of organic Rankine cycle (ORC) for low grade waste heat recovery," *Energy Conversion and*

Management, vol. 50, pp. 576–582, 2009.

[137] N Galanis, E Cayer, P Roy, ES Denis, and M Desilets, "Electricity Generation from Low Temperature Sources," *Journal of Applied Fluid Mechanics*, vol. 2, pp. 55-67, 2009.

[138] I Saavedra, JC Bruno, and A Coronas, "Thermodynamic optimization of organic Rankine cycles at several condensing temperatures: case study of waste heat recovery in a natural gas compressor station," *Proceedings of the Institution of Mechanical Engineers, Part A: Journal of Power and Energy*, vol. 224, pp. 917-930, 2010.

[139] P Colonna, A Guardone, and NR Nannan, "Siloxanes: A new class of candidate Bethe-Zel'dovich-Thompson fluids," *AIP Physics of Fluids*, vol. 19, p. 086102, 2007.

[140] J Chen, Z Yan, G Lin, and B Andresen, "On the Curzon-Ahlborn efficiency and its connection with the efficiencies of real heat engines," *Energy Conversion & Management*, vol. 42, pp. 173-181, 2001.

[141] S Quoilin, S Declaye, and V Lemort, "Expansion machine and fluid selection for the Organic Rankine Cycle," in *7th International Conference on Heat Transfer, Fluid Mechanics, and Thermodynamics*, Antalya, Turkey, July 2010, pp. 19-21.

[142] E Macchi and A Perdichizzi, "Efficiency Prediction for Axial-Flow Turbines Operating with Nonconventional Fluids," *ASME Jour of Engineering for Power*, vol. 103, pp. 718-724, 1981.

[143] C Invernizzi, P Iora, and P Silva, "Bottoming micro-Rankine cycles for micro-gas turbines," *Applied Thermal Engineering*, vol. 27, pp. 100-110, 2007.

[144] G Angelino, C Invernizzi, and E Macchi, "Organic working fluid optimization for space power cycles," in *Modern Research Topics in Aerospace Propulsion*, G Angelino, L DeLuca, and WA Sirignano, Eds. New York: Springer-Verlag, 1991.

[145] KW Li and AP Priddy, *Power Plant System Design*. New York: John wiley & Sons, 1985.

[146] HD Madhawa Hettiarachchi, M Golubovic, WM Worek, and Y Ikegami, "Optimum design criteria for an Organic Rankine cycle using low-temperature geothermal heat sources," *Energy*, vol. 32, pp. 1698–1706, 2007.

[147] Z Shengjun, W Huaixin, and G Tao, "Performance comparison and parametric optimization of subcritical Organic Rankine Cycle (ORC) and transcritical power cycle system for low-temperature geothermal power generation," *Applied Energy*, vol. 88, pp. 2740–2754, 2011.

[148] M Aslam Siddiqi and B Atakan, "Investigation of the Criteria for Fluid Selection in Rankine Cycles for Waste Heat Recovery," *International Journal of Thermodynamics*, vol. 14, pp. 117-123, 2011.

[149] A Schuster, S Karellas, E Kakaras, and H Spliethoff, "Energetic and economic investigation of Organic Rankine Cycle applications," *Applied Thermal Engineering*, vol. 29, pp. 1809–1817, 2009.

[150] A Abie Lakew and O Bolland, "Working fluids for low-temperature heat source," *Applied Thermal Engineering*, vol. 30, pp. 1262–1268, 2010.

[151] FP Incropera and DP DeWitt, *Fundamentals of Heat and Mass Transfer* , 5th ed. Hoboken: John Wiley & Sons, 2002.

[152] AC McMahan, "Design and Optimization of Organic Rankine Cycle Solar-Thermal Powerplants," University of Wisconsin-Madison, MS Thesis 2006.

[153] H Hjartarson, "Waste Heat Utilization at Elkem Ferrosilicon Plant in Iceland," University of Iceland, MS Thesis 2009.

[154] JJ Brasz, V Shistla, N Stosic, and IK Smith, "Development of a twin-screw expressor as a throttle valve replacement for water cooled chillers," in *Proceedings of the 15th International Compressor Conference*, Purdue, IN, 2000.

[155] MA Barclay and CC Yang, "Offshore LNG: The Perfect Starting Point for the 2-Phase Expander?," in *Offshore Technology Conference*, Houston, TX, 2006.

[156] R DiPippo, "Ideal thermal efficiency for geothermal binary plants," *Geothermics*, vol. 36, pp. 276-285, 2007.

[157] L Wei, Y Zhang, Y Mu, X Yang, and X Chen, "Efficiency Improving Strategies of Low-Temperature Heat Conversion Systems Using Organic Rankine Cycle: An Overview," *Energy Sources, Part A*, vol. 33, pp. 869-878, 2011.

[158] O Bailey and E Worrell, "Clean Energy Technologies: A Preliminary Inventory of the Potential for Electricity Generation," *Lawrence Berkeley National Laboratory*, vol. LBNL-57451, pp. 1-37, 2005.

[159] B Sternlicht, "Waste energy recover: an excellent investment opportunity," *Energy Conversion and Management*, vol. 22, pp. 361-373, 1982.

[160] TC Hung, SK Wang, CH Kuo, BS Pei, and KF Tsai, "A study of organic working fluids on system efficiency of an ORC using low-grade energy sources," *Energy*, vol. 35, pp. 1403-1411, 2010.

[161] AM Delgado-Torres and L Garcia-Rodriguez, "Analysis and optimization of the low0temperature solar organic Rankine cycle (ORC)," *Energy Conversion and Management*, vol. 51, pp. 2846-2856, 2010.

[162] G Restrepo, M Weckert, R Bruggemann, S Gerstmann, and H Frank, "Ranking of Refrigerants," *Environmental Science & Technology*, vol. 42, pp. 2925-2930, 2008.

[163] WC Andersen and TJ Bruno, "Rapid Screening of Fluids for Chemical Stability in Organic Rankine Cycle Applications," *Industrial and Engineering Chemistry Research*, vol. 44, pp. 5560-5566, 2005.

[164] KH Aboul-Fotouh and KE Starling, "Use of a generalized modified BWR equation of state for halogenated hydrocarbon saturated thermodynamic properties," *Proceedings of the Oklahoma Academy of Science*, vol. 58, pp. 77-80, 1978.

[165] SA Kalogirou, "Solar thermal collectors and applications," *Progress in Energy and Combustion Science*, vol. 30, pp. 231-295, 2004.

[166] D Mills, "Advances in solar thermal electricity technology," *Solar Energy*, vol. 76, pp. 19-31, 2004.

[167] D Rotman, "Chasing the Sun," *Technology Review*, pp. 44-51, July/August 2009.

[168] N Fraidenraich, JM Gordon, and C Tiba, "Optimization of gas-turbine combined cycles for solar energy and alternative-fuel power generation," *Solar Energy*, vol. 48, pp. 301-307, 1992.

[169] CW Forsberg, PF Peterson, and H Zhao, "High-Temperature Liquid-Fluoride-Salt Closed-Brayton-Cycle Solar Power Towers," *ASME Journal of Solar Energy Engineering*, vol. 129, pp. 141-146, 2007.

[170] B Facchini, D Fiaschi, and G Manfrida, "Exergy analysis of combined cycles using latest

generation gas turbines," *J. Eng. Gas Turbines Power*, vol. 122, pp. 233-238, 2000.

[171] A Segal and M Epstein, "Optimized working temperatures of a solar central receiver," *Solar Energy*, vol. 75, pp. 503-510, 2003.

[172] A Kribus, "A high-efficeincy triple cycle for solar power generation," *Solar Energy*, vol. 72, pp. 1-11, 2002.

[173] JM Muñoz de Escalona, D Sánchez, R Chacartegui, and T Sánchez, "Part-load analysis of gas turbine & ORC combined cycles," *Applied Thermal Engineering*, vol. 36, pp. 63-72, 2012.

[174] AL Polyzakis, C Koroneos, and G Xydis, "Optimum gas turbine cycle for combined cycle power plant," *Energy Conversion & Management*, vol. 49, pp. 551-563, 2008.

[175] MA da Cunha Alves et al., "An insight on intercooling and reheat gas turbine cycles," *Proceedings of the Institution of Mechanical Engineers, Part A: Journal of Power and Energy*, vol. 215, pp. 163-171, 2001.

[176] T Heppenstall, "Advanced gas turbine cycles for power generation: a critical review," *Applied Thermal Engineering*, vol. 18, pp. 837-846, 1998.

[177] MA El-Masri, "On Thermodynamic of Gas-Turbine Cycles: Part 1 - Second Law Analysis of Combined Cycles," *ASME Journal of Engineering for Gas Turbines and Power*, vol. 107, pp. 880-889, 1985.

[178] W Xiang and Y Chen, "Performance improvement of combined cycle power plant based on the optimization of the bottom cycle and heat recuperation," *Journal of Thermal Science*, vol. 16, pp. 84-89, 2006.

[179] YSH Najjar and AB Radhwan, "Cogeneration by combining gas turbine engine with Organic Rankine Cycle," *Heat Recovery Systems and CHP*, vol. 8, pp. 211-219, 1988.

[180] PJ Mago and R Luck, "Energetic and exergetic analysis of waste heat recovery from a microturbine using Organic Rankine cycles," *International Journal of Energy Research*, vol. (Available Online), 2012.

[181] MJ Wagner and C Kutscher, "The Impact of Hybrid Wet/Dry Cooling on Concentrating Solar Power Plant Performance," in *ASME 2010 4th International Conference on Energy Sustainability, Volume 2*, Phoenix, AZ, USA, 2010, pp. 675-682.

[182] R Kurz, "Introduction to Gas Turbines & Applications (Solar Turbines)," in *EPA National CHP Turbine Technology and Regulatory forum*, San Diego, CA, March 5-6 2003.

[183] H Gurgenci, "Performances of Organic Rankine Cycles under part-load and off design conditions," *Solar Energy*, vol. 36, pp. 45-51, 1986.

[184] CSP Group Sandia National Labs, "Solar Thermal Energy Research," in *Sandia National Laboratory Science and Engineering Exposition 2011*, Albuquerque, New Mexico, October 31, 2011, October.

[185] A Kribus et al., "A multistage solar receiver: the route to high temperature," *Solar Energy*, vol. 67, pp. 3-11, 2000.

[186] H Ries, A Kribus, and J Karni, "Non-isothermal receivers," *Journal of Solar Energy Engineering*, vol. 117, pp. 259-261, 1995.

[187] JF Kreider, "Perforamce of a large solar-thermal electric power plant in the USA," in *Proceedings of the 3rd Sede Boqer Syposium on Solar Electricity Production*, Sede Boqer, Israel, 1988, pp. 53-81.

[188] T Ho, SS Mao, and R Greif, "Improving efficiency of high-concentrator photovoltaics by cooling with two-phase forced convection," *International Journal of Energy Research*, vol. 34, pp. 1257-1271, 2010.

[189] T Ho, SS Mao, and R Greif, "The impact of cooling on cell temperature and the practical solar concentration limits for photovoltaics," *International Journal of Energy Research*, vol. 35, pp. 1250-1257, 2011.

[190] A Franco and C Casarosa, "On some perspectives for increasing the efficiency of combined cycle power plants," *Applied Thermal Engineering*, vol. 22, pp. 1501-1518, 2002.

A. Appendix A

Table A.1 – Constants for nonpolar attractive contribution to reduced Helmholtz energy for eq. (2.23) **[**97**]**.

I	c_i	N_i	m_i	j_i	l_i
1	7.51342935250E-03	-5	1	1	-
2	1.66059022800E-01	-4	2	-4	-
3	-1.76690332000E-01	-4	2	-3	-
4	1.41999966510E-03	-3	4	4	-
5	4.43330593900E-07	-3	10	-1	-
6	-1.57318745200E+00	-2	1	0	-
7	-6.25563851820E-02	-2	2	4	-
8	-7.31417150050E-02	-2	3	-3	-
9	1.65829136210E-02	-2	4	-4	-
10	1.39207317570E-01	-1	1	-2	-
11	1.92604241460E+00	-1	2	-1	-
12	-1.64912664400E+01	-1	2	1	-
13	3.04735094200E+01	-1	2	2	-
14	-2.11296527240E+01	-1	2	3	-
15	5.16778479720E+00	-1	2	4	-
16	-1.78840356100E-05	-1	8	4	-
17	-3.56902553030E-02	0	2	-4	-
18	4.31670708510E-02	0	3	-2	-
19	-4.01161732060E-03	1	4	-4	-
20	-2.92088671940E-01	-4	1	0	1
21	-4.12740219040E-01	-14	2	-3	2
22	4.00933667750E-01	-14	2	-2	2
23	-9.64315905460E-02	-12	2	4	2
24	2.19417397800E-02	-10	5	-1	2
25	-4.30641503620E-02	-8	1	4	2
26	7.19458390920E-02	-6	2	4	2
27	2.43870901150E-03	-4	8	4	2
28	-4.64644336320E-02	-2	1	1	2

The constants in eq. (2.23) are then determined by the following **[**99**]**:

$n_i = c_i \varphi^{j_i}$, where φ is the substance's anisotropy parameter.

$t_i = -n_i / 2;\ d_i = m_i;\ l_i = p_i$

Table A.2 – Constants for dipole interactions contribution to reduced Helmholtz energy for eq. (2.26) [97,115].

i	c_i	N_i	m_i	k_i	o_i
1	-4.23652173318E-02	-5	2	5	1
2	2.04459397242E-02	-8	2	6	1
3	6.64266837321E-02	-4	2	7	1
4	-3.24168341478E-02	-3	2	7	1
5	-7.41263275720E-03	-10	2	9	1
6	-1.60855507113E-02	-7	2	9	1
7	4.35623305093E-03	-10	2	11	1
8	-1.05933370736E-04	-11	2	15	1
9	-1.32000046519E-06	-15	2	18	1
10	8.38157718194E-06	-10	3	18	1
11	1.09144074057E-02	-2	2	5	0
12	2.57960188278E-02	-2	3	5	0
13	-5.44140085185E-04	-1	6	5	0
14	3.49568484468E-03	-5	2	6	0
15	-4.21407562467E-02	-3	3	6	0
16	-7.45992658113E-03	-1	3	6	0
17	1.46102252152E-04	1	6	6	0
18	5.66611094911E-04	-9	2	7	0
19	-3.78643890614E-03	-7	2	7	0
20	-3.65824539450E-02	-2	2	7	0
21	1.69287932475E-02	-1	2	7	0
22	6.63866480778E-03	-5	3	7	0
23	2.94409406715E-02	-2	3	7	0
24	-1.12110434947E-02	-1	3	7	0
25	-1.82144939032E-06	-8	10	7	0
26	7.58594753989E-08	-5	16	7	0
27	-2.16942306418E-05	1	4	8	0
28	-2.74025042954E-06	-4	9	10	0

The constants in eq. (2.26) are then determined by the following **[**99**]**:

$n_i = c_i \left(\mu^{*2}\right)^{k_i/4}$, where μ^{*2} is the substance's reduced dipole moment.

$t_i = -n_i / 2;\ d_i = m_i / 2;\ g_i = o_i$

Table A.3 - Constants for quadrupole interactions contribution to reduced Helmholtz energy for eq. (2.27) [97,115].

i	c_i	N_i	m_i	k_i	o_i
1	-4.12154280896E-03	-8	2	11	1
2	3.55780441736E-03	-6	2	12	1
3	-8.88093798389E-04	-4	2	13	1
4	9.73791559609E-05	-10	2	16	1
5	-6.04233719326E-08	-20	2	19	1
6	-3.04478633146E-05	-8	2	20	1
7	-3.78930196337E-04	-3	8	7	0
8	-2.75388267352E-02	-3	2	8	0
9	1.18301888420E-02	-2	2	8	0
10	-2.83451230562E-03	0	2	8	0
11	-5.67703874828E-05	-5	8	8	0
12	3.14708573212E-03	-1	2	9	0
13	9.63786052569E-04	-3	5	10	0
14	-1.27591002424E-03	-1	5	10	0
15	3.63746463238E-04	0	5	10	0
16	3.01067943096E-05	0	8	10	0
17	2.91778231128E-07	-10	7	18	0

The constants in eq. (2.27) are then determined by the following **[**99**]**:

$n_i = c_i \left(Q^{*2}\right)^{k_i/4}$, where Q^{*2} is the substance's reduced quadrupole moment.

$t_i = -n_i / 2;\ d_i = m_i / 2;\ g_i = o_i$

Table A.4 – Constants for eq. (2.35) to calculate the residual component of reduced Helmholtz energy in Span-Wagner equation for non-polar or weakly polar molecules and siloxanes [101,103,104].

i	t_i	d_i	p_i
1	0.250	1	-
2	1.125	1	-
3	1.500	1	-
4	1.375	2	-
5	0.250	3	-
6	0.875	7	-
7	0.625	2	1
8	1.750	5	1
9	3.625	1	2
10	3.625	4	2
11	14.5	3	3
12	12.0	4	3

Table A.5 – Constants for eq. (2.35) to calculate the residual component of reduced Helmholtz energy in Span-Wagner equation for non-polar or weakly polar molecules and siloxanes **[**102**]**.

i	t_i	d_i	p_i
1	0.250	1	-
2	1.250	1	-
3	1.500	1	-
4	0.250	3	-
5	0.875	7	-
6	2.375	1	1
7	2.000	2	1
8	2.125	5	1
9	3.500	1	2
10	6.50	1	2
11	4.75	4	2
12	12.5	2	3

Table A.6 – Approximate maximum uncertainties in equations of state used in NIST REFPROP 8.0 **[**92**]**

Working Fluid	Uncertainty in Density ρ	Uncertainty in Vapor Pressure P_{sat}
toluene	0.05% to 0.5%	0.3%
pentane	0.2% to 0.5%	0.2%
butane	0.02% to 0.4%	0.5%
cyclohexane	0.1%	0.1%
hexane	0.2% to 0.5%	0.2%
R113	0.2%	0.3%
R123	0.1%	0.1%
R141b	0.2% to 0.5%	0.2%
R245ca	0.07%	0.26%

B. Appendix B

To determine thermodynamics properties from temperature, density, Helmholtz energy, and its derivatives, the combined first and second law of thermodynamics **[**4**]**,

$$du = Tds - PdV = Tds + P\rho^{-2}d\rho \tag{B.1}$$

and the definition of Helmholtz free energy and its derivative are shown **[**4**]**.

$$\begin{aligned} a &= u - Ts \\ da &= du - Tds - sdT = -sdT + P\rho^{-2}d\rho \end{aligned} \tag{B.2}$$

Pressure, entropy and enthalpy can be determined from the above equations. From eq. (B.2), pressure is shown in eq. (B.3) and entropy is shown in eq. (B.4).

$$P = \rho^2 \left(\frac{\partial a}{\partial \rho} \right)_T \tag{B.3}$$

$$s = -\left(\frac{\partial a}{\partial T} \right)_\rho \tag{B.4}$$

The definition of enthalpy is given in eq. (B.5) **[**4**]**.

$$h = u + PV = u + P\rho^{-1} \tag{B.5}$$

The Helmholtz energy, density, and temperature are now replaced with its reduced forms.

$$\begin{aligned} \alpha &= a / RT \\ \tau &= T_0 / T \\ \delta &= \rho / \rho_0 \end{aligned} \tag{B.6}$$

For pressure, eq. (B.3) now becomes eq. (B.7)

$$P = \rho^2 \left(\frac{\partial a}{\partial \rho} \right)_T = \left(\rho_0{}^2 \delta^2 \right) \left(\frac{1}{\rho_0} \frac{\partial \left[\alpha RT \right]}{\partial \delta} \right)_\tau = \rho_0 \delta^2 RT \left(\frac{\partial \alpha}{\partial \delta} \right)_\tau = \rho \delta RT \left(\frac{\partial \alpha}{\partial \delta} \right)_\tau \tag{B.7}$$

and entropy from eq. (B.4) becomes eq. (B.8).

$$s = -\left(\frac{\partial a}{\partial T} \right)_\rho = -\left(\frac{\partial \left(\alpha RT \right)}{\partial T} \right)_\rho = -RT \left(-\frac{\tau^2}{T_0} \frac{\partial \alpha}{\partial \tau} \right)_\delta - R\alpha = R\tau \left(\frac{\partial \alpha}{\partial \tau} \right)_\delta - R\alpha \tag{B.8}$$

For enthalpy, eq. (B.2) is combined with eq. (B.7) and eq. (B.8) to give

$$h = u + P\rho^{-1} = a + Ts + P\rho^{-1} = RT \left[\tau \left(\frac{\partial \alpha}{\partial \tau} \right)_\delta + \delta \left(\frac{\partial \alpha}{\partial \delta} \right)_\tau \right] \tag{B.9}$$